frontiers | Research Topics

Brain connectivity, dynamics, and complexity

Edited by
Stephen José Hanson, Ruben Sanchez-Romero, Pedro Antonio Valdes-Sosa and Bharat B. Biswal

Published in
Frontiers in Human Neuroscience
Frontiers in Computational Neuroscience

ISSN 1664-8714
ISBN 978-2-8325-2891-4
DOI 10.3389/978-2-8325-2891-4

About Frontiers

Frontiers is more than just an open access publisher of scholarly articles: it is a pioneering approach to the world of academia, radically improving the way scholarly research is managed. The grand vision of Frontiers is a world where all people have an equal opportunity to seek, share and generate knowledge. Frontiers provides immediate and permanent online open access to all its publications, but this alone is not enough to realize our grand goals.

Frontiers journal series

The Frontiers journal series is a multi-tier and interdisciplinary set of open-access, online journals, promising a paradigm shift from the current review, selection and dissemination processes in academic publishing. All Frontiers journals are driven by researchers for researchers; therefore, they constitute a service to the scholarly community. At the same time, the *Frontiers journal series* operates on a revolutionary invention, the tiered publishing system, initially addressing specific communities of scholars, and gradually climbing up to broader public understanding, thus serving the interests of the lay society, too.

Dedication to quality

Each Frontiers article is a landmark of the highest quality, thanks to genuinely collaborative interactions between authors and review editors, who include some of the world's best academicians. Research must be certified by peers before entering a stream of knowledge that may eventually reach the public - and shape society; therefore, Frontiers only applies the most rigorous and unbiased reviews. Frontiers revolutionizes research publishing by freely delivering the most outstanding research, evaluated with no bias from both the academic and social point of view. By applying the most advanced information technologies, Frontiers is catapulting scholarly publishing into a new generation.

What are Frontiers Research Topics?

Frontiers Research Topics are very popular trademarks of the *Frontiers journals series*: they are collections of at least ten articles, all centered on a particular subject. With their unique mix of varied contributions from Original Research to Review Articles, Frontiers Research Topics unify the most influential researchers, the latest key findings and historical advances in a hot research area.

Find out more on how to host your own Frontiers Research Topic or contribute to one as an author by contacting the Frontiers editorial office: frontiersin.org/about/contact

Brain connectivity, dynamics, and complexity

Topic editors

Stephen José Hanson — The State University of New Jersey, United States
Ruben Sanchez-Romero — Rutgers University, United States
Pedro Antonio Valdes-Sosa — University of Electronic Science and Technology of China, China
Bharat B. Biswal — Department of Biomedical Engineering, Newark College of Engineering, New Jersey Institute of Technology, United States

Citation

Hanson, S. J., Sanchez-Romero, R., Valdes-Sosa, P. A., Biswal, B. B., eds. (2023). *Brain connectivity, dynamics, and complexity*. Lausanne: Frontiers Media SA. doi: 10.3389/978-2-8325-2891-4

Table of contents

05 Editorial: Brain connectivity, dynamics, and complexity
Stephen José Hanson and Ruben Sanchez-Romero

07 Distinct and Dissociable EEG Networks Are Associated With Recovery of Cognitive Function Following Anesthesia-Induced Unconsciousness
Alexander Rokos, Bratislav Mišić, Kathleen Berkun, Catherine Duclos, Vijay Tarnal, Ellen Janke, Paul Picton, Goodarz Golmirzaie, Mathias Basner, Michael S. Avidan, Max B. Kelz, George A. Mashour and Stefanie Blain-Moraes

20 Multifractal Functional Connectivity Analysis of Electroencephalogram Reveals Reorganization of Brain Networks in a Visual Pattern Recognition Paradigm
Orestis Stylianou, Frigyes Samuel Racz, Keumbi Kim, Zalan Kaposzta, Akos Czoch, Andriy Yabluchanskiy, Andras Eke and Peter Mukli

33 Resting-State Functional Connectivity in the Dorsal Attention Network Relates to Behavioral Performance in Spatial Attention Tasks and May Show Task-Related Adaptation
Björn Machner, Lara Braun, Jonathan Imholz, Philipp J. Koch, Thomas F. Münte, Christoph Helmchen and Andreas Sprenger

45 The Relationship Between Default Mode and Dorsal Attention Networks Is Associated With Depressive Disorder Diagnosis and the Strength of Memory Representations Acquired Prior to the Resting State Scan
Skye Satz, Yaroslav O. Halchenko, Rachel Ragozzino, Mora M. Lucero, Mary L. Phillips, Holly A. Swartz and Anna Manelis

57 Quantification of Kuramoto Coupling Between Intrinsic Brain Networks Applied to fMRI Data in Major Depressive Disorder
Lena G. Bauer, Fabian Hirsch, Corey Jones, Matthew Hollander, Philipp Grohs, Amit Anand, Claudia Plant and Afra Wohlschläger

71 Functional Connectivity and Complexity in the Phenomenological Model of Mild Cognitive-Impaired Alzheimer's Disease
Surya Das and Subha D. Puthankattil

82 Brain fingerprints along the language hierarchy
Juan Zhang, Liping Zhuang, Jiahao Jiang, Menghan Yang, Shijie Li, Xiangrong Tang, Yingbo Ma, Lanfang Liu and Guosheng Ding

94 Dissociation of categorical and coordinate spatial relations on dynamic network organization states
Xin Hao, Zhencai Chen, Taicheng Huang, Yiying Song, Xiangzhen Kong and Jia Liu

106 The music of the hemispheres: Cortical eigenmodes as a physical basis for large-scale brain activity and connectivity patterns
Eli J. Müller, Brandon R. Munn, Kevin M. Aquino, James M. Shine and Peter A. Robinson

113 Dynamic Effective Connectivity using Physiologically informed Dynamic Causal Model with Recurrent Units: A functional Magnetic Resonance Imaging simulation study
Sayan Nag and Kamil Uludag

frontiers | Frontiers in Human Neuroscience

TYPE Editorial
PUBLISHED 19 June 2023
DOI 10.3389/fnhum.2023.1232224

OPEN ACCESS

EDITED AND REVIEWED BY
Sébastien Hélie,
Purdue University, United States

*CORRESPONDENCE
Stephen José Hanson
jose@rubic.rutgers.edu
Ruben Sanchez-Romero
ruben.saro@gmail.com

RECEIVED 31 May 2023
ACCEPTED 09 June 2023
PUBLISHED 19 June 2023

CITATION
Hanson SJ and Sanchez-Romero R (2023) Editorial: Brain connectivity, dynamics, and complexity. *Front. Hum. Neurosci.* 17:1232224. doi: 10.3389/fnhum.2023.1232224

Editorial: Brain connectivity, dynamics, and complexity

Stephen José Hanson[1]* and Ruben Sanchez-Romero[2]*

[1]Rutgers, The State University of New Jersey, New Brunswick, NJ, United States, [2]Rutgers University, Newark, NJ, United States

KEYWORDS

computational neuroscience, brain connectivity, complexity, information theory, dynamics

Editorial on the Research Topic
Brain connectivity, dynamics, and complexity

The contributions in this Research Topic collectively explore the nature of functional brain connectivity and its relation to cognition, emphasizing shared mechanisms and brain complexity. Results presented here reveal common themes in how the brain dynamically reorganizes and adapts to task- and disease-related perturbations.

Some of the contributions present a variety of theoretical and methodological approaches to studying the relationship between connectivity, dynamics, and complexity. The articles include a novel multi-fractal functional connectivity estimation to track changes during visual pattern recognition (Stylianou et al.), a dimensionality reduction technique to facilitate comparisons of oscillatory patterns across task paradigms and modalities (Müller et al.), a new adaptation of the dynamic causal modeling (DCM) approach to capture connectivity changes during more ecological tasks such as movie watching (Nag and Uludag), a new connectivity method based on the Kuramoto model of coupled oscillators applied to network-level fMRI data (Bauer et al.), and a framework to study the relationship between functional connectivity and complexity (Das and Puthankattil).

From an application perspective, contributions focus on the study of the large-scale cortical networks supporting cognition, in health and disease, including navigation subnetworks representing different types of spatial relation representations (Hao et al.), changes in individual differences along the language network hierarchy and their potential as biomarkers (Zhang et al.), the adaptation of the dorsal attention network to demands of a spatial attention task (Machner et al.), the relationship between memory, depression, and inter-network connectivity (Satz et al.), and the recovery of cognitive functions and related task networks after anesthesia (Rokos et al.).

We consider that the integration of these studies has the potential to advance our understanding of common principles governing the dynamic and complex relationship between brain connectivity and cognition.

Author contributions

All authors listed have made a substantial, direct, and intellectual contribution to the work and approved it for publication.

Conflict of interest

The authors declare that the research was conducted in the absence of any commercial or financial relationships that could be construed as a potential conflict of interest.

Publisher's note

frontiers in Human Neuroscience

ORIGINAL RESEARCH
published: 14 September 2021
doi: 10.3389/fnhum.2021.706693

Distinct and Dissociable EEG Networks Are Associated With Recovery of Cognitive Function Following Anesthesia-Induced Unconsciousness

*Alexander Rokos[1], Bratislav Mišić[2], Kathleen Berkun[3], Catherine Duclos[4], Vijay Tarnal[5], Ellen Janke[5], Paul Picton[5], Goodarz Golmirzaie[5], Mathias Basner[6], Michael S. Avidan[7], Max B. Kelz[8], George A. Mashour[5] and Stefanie Blain-Moraes[4]**

[1]Integrated Program in Neuroscience, McGill University, Montreal, QC, Canada, [2]Neurology and Neurosurgery, McGill University, Montreal, QC, Canada, [3]Cognitive Science, McGill University, Montreal, QC, Canada, [4]School of Physical and Occupational Therapy, McGill University, Montreal, QC, Canada, [5]Department of Anesthesiology, Center of Consciousness Science, University of Michigan Medical School, Ann Arbor, MI, United States, [6]Department of Psychiatry, Perelman School of Medicine, University of Pennsylvania, Philadelphia, PA, United States, [7]Department of Anesthesiology, Washington University School of Medicine, St. Louis, WA, United States, [8]Deparment of Anesthesiology, Perelman School of Medicine, University of Pennsylvania, Philadelphia, PA, United States

OPEN ACCESS

Edited by:
Ruben Sanchez-Romero,
Rutgers University, United States

Reviewed by:
Minji Lee,
Korea University, South Korea
Jesús Javier Ballesteros Carrasco,
Massachusetts General Hospital, United States
Sarah Eagleman,
Stanford University, United States

***Correspondence:**
Stefanie Blain-Moraes
stefanie.blain-moraes@mcgill.ca

Specialty section:
This article was submitted to Cognitive Neuroscience, a section of the journal Frontiers in Human Neuroscience

Received: 07 May 2021
Accepted: 20 August 2021
Published: 14 September 2021

Citation:
Rokos A, Mišić B, Berkun K, Duclos C, Tarnal V, Janke E, Picton P, Golmirzaie G, Basner M, Avidan MS, Kelz MB, Mashour GA and Blain-Moraes S (2021) Distinct and Dissociable EEG Networks Are Associated With Recovery of Cognitive Function Following Anesthesia-Induced Unconsciousness. Front. Hum. Neurosci. 15:706693. doi: 10.3389/fnhum.2021.706693

The temporal trajectories and neural mechanisms of recovery of cognitive function after a major perturbation of consciousness is of both clinical and neuroscientific interest. The purpose of the present study was to investigate network-level changes in functional brain connectivity associated with the recovery and return of six cognitive functions after general anesthesia. High-density electroencephalograms (EEG) were recorded from healthy volunteers undergoing a clinically relevant anesthesia protocol (propofol induction and isoflurane maintenance), and age-matched healthy controls. A battery of cognitive tests (motor praxis, visual object learning test, fractal-2-back, abstract matching, psychomotor vigilance test, digital symbol substitution test) was administered at baseline, upon recovery of consciousness (ROC), and at half-hour intervals up to 3 h following ROC. EEG networks were derived using the strength of functional connectivity measured through the weighted phase lag index (wPLI). A partial least squares (PLS) analysis was conducted to assess changes in these networks: (1) between anesthesia and control groups; (2) during the 3-h recovery from anesthesia; and (3) for each cognitive test during recovery from anesthesia. Networks were maximally perturbed upon ROC but returned to baseline 30–60 min following ROC, despite deficits in cognitive performance that persisted up to 3 h following ROC. Additionally, during recovery from anesthesia, cognitive tests conducted at the same time-point activated distinct and dissociable functional connectivity networks across all frequency bands. The results highlight that the return of cognitive function after anesthetic-induced unconsciousness is task-specific, with unique behavioral and brain network trajectories of recovery.

Keywords: brain networks, functional connectivity, electroencephalography, cognitive function, anesthesia, partial least squares

INTRODUCTION

Following the loss of consciousness from anesthesia, the brain can reconstitute its diverse range of cognitive functions, ranging from sensorimotor function to reasoning and logic, to memory. Although neural patterns associated with loss and recovery of consciousness have been characterized using functional brain dynamics and connectivity patterns (John et al., 2001; Lee et al., 2013; Blain-Moraes et al., 2015; Mashour and Hudetz, 2018), the neurocognitive trajectories associated with the reconstitution of cognition after anesthesia-induced unconsciousness are poorly understood. This can be attributed to the challenges associated with studying the neural correlates of the recovering brain after the clinical or experimental administration of general anesthesia. Previous studies have used cognitive tests administered pre– and post-anesthesia to compare recovery times from different anesthetics (Långsjö et al., 2005), and to track the recovery times of various cognitive functions (N'Kaoua et al., 2002; Allampati et al., 2019). However, in these clinical studies with surgical patients, it is difficult to dissociate the effects of general anesthesia from the surgical intervention, which can adversely affect cognition through pain, inflammation, and analgesic confounds. In most experimental studies that isolate the effects of general anesthesia alone in healthy volunteers, the anesthetic protocols either just cross the threshold of unresponsiveness (Långsjö et al., 2005; Purdon et al., 2013; Blain-Moraes et al., 2015; Chennu et al., 2016; Scheinin et al., 2021), or induce a more profound unconsciousness for a short period of time (Banks et al., 2020). While these experimental anesthetic protocols may be suitable for modeling light sedation procedures (Allampati et al., 2019), they do not model general anesthesia for a major surgery, which animal studies have suggested can immediately and persistently impair cognition in the post-anesthetic period (Valentim et al., 2008; Carr et al., 2011; Avidan and Evers, 2016; Jiang et al., 2017). To study the neurocognitive recovery profiles under these circumstances, a protocol relevant to major surgery is required.

To address these limitations, we developed a protocol for healthy volunteers using a clinically relevant anesthetic regimen to induce unconsciousness without surgical intervention (Maier et al., 2017). High-density electroencephalography (EEG) was recorded during the administration of the anesthetic (15 min induction through propofol, 3 h maintenance with isoflurane), through the recovery of consciousness, and continued for 3 h after emergence. Isoflurane anesthesia is a halogenated ether and was selected over other anesthetics for its heterogenous molecular targets, which have a more profound effect on neural dynamics through multiple neurotransmitter receptor and channel systems. As a result, it has a slower offset in comparison to other anesthetics, theoretically providing the best opportunity to observe the differential recovery of cognitive function (Hemmings et al., 2019). Previous analysis of these data used source-localized spectral analysis, functional connectivity, and graph-theoretical approaches to characterize brain patterns during the recovery of consciousness and cognitive functions (Blain-Moraes et al., 2017). While global network efficiency distinguished between states of consciousness, it did not track the return of various cognitive functions. Conversely, alpha power in the superior parietal lobule only returned to baseline 90-min after recovery of consciousness, paralleling mean discharge-readiness times in the recovery room (Mashour et al., 2012). This source-localized spectral characteristic may be a biomarker for functional brain network recovery after anesthesia; however, the specific network mechanisms underlying the recovery of individual cognitive functions remain unknown. Two families of intrinsic coupling have been used to investigate the brain connectome using neurophysiological data: envelope coupling (also referred to as amplitude coupling) and phase coupling (Engel et al., 2013). Previous analyses of this dataset have shown that phase coupling, specifically, weighted phase lag index (wPLI) for the assessment of brain functional connectivity (Vinck et al., 2011), can characterize anesthetic-related changes in brain network function (Blain-Moraes et al., 2017; Duclos et al., 2021). We hypothesized that brain networks calculated with wPLI would similarly reveal anesthetic-related changes in cognitive function after recovery of consciousness.

Thus, the objective of the present study was to investigate network-level changes in functional brain connectivity associated with the recovery and return of six cognitive functions after anesthesia: attention, sensorimotor function, memory, reasoning and logic, abstract thinking, and maximal speed of cognitive processing. Since source localization or neuroimaging was not used in this study, the term "network" denotes a pattern of EEG- based functional connectivity. Multivariate partial least squares (PLS) analysis was applied to behavioral cognitive assessments and functional connectivity networks derived from EEG, testing the hypothesis that distinct networks could be associated with the return of specific cognitive functions following deep general anesthesia.

MATERIALS AND METHODS

This study was conducted at the University of Michigan Medical School and approved by the Institutional Review Board (HUM0071578); written consent was obtained from all participants.

Study Population

Participants in this study were the subset of 20 healthy volunteers from the Reconstructing Consciousness and Cognition (ReCCognition) study (NCT01911195) evaluated at the University of Michigan who were selected because they underwent EEG recording with a 128-channel montage. The full protocol for this investigation has been published (Maier et al., 2017). All participants were class 1 physical status according to the American Society of Anesthesiologists, between 20 and 40 years of age, and had a body mass index of <30. Participants were excluded if they were pregnant, had a history of obstructive sleep apnea, reactive airway, gastroesophageal reflux, asthma, epilepsy, neuropsychiatric disorders, history or current use of psychotropic medications, cardiac conduction abnormalities, history of adverse reactions to anesthesia as well as family history of neurologic, psychiatric, or adverse reactions to anesthesia.

Pregnancy and illicit drug use were ruled out with both urine and blood analyses.

Experimental Protocol

Participants were randomized to one of two groups: general anesthesia with propofol and isoflurane, or wakefulness.

Anesthesia Group

Participants in the anesthesia group (n = 10) were brought into the Operating Room, where they were outfitted with a 128-channel EEG system (Electrical Geodesics, Inc., Eugene, OR, USA), and standard anesthesia monitors (electrocardiogram, non-invasive blood pressure cuff, pulse oximeter). In a seated position, participants completed a computerized neurocognitive test battery comprised of six independent cognitive tests (session 1). Upon completion, participants were moved to a supine position, and anesthesia was induced with a stepwise increase in propofol: 100 μg/kg/min for 5 min; 200 μg/kg/min for 5 min; 300 μg/kg/min for 5 min. During induction, participants followed a series of auditory commands delivered every 30 s to squeeze their right or left hand twice (right or left randomly delivered). Loss of consciousness (LOC) was defined as the first time the participant failed to respond to two consecutive commands. After induction, unconsciousness was maintained by inhaling 1.3 age-adjusted minimum alveolar concentration (MAC)—the concentration required to prevent movement in response to surgical stimuli in 50% of the population—of isoflurane. After 3 h, isoflurane was discontinued, and participants again listened to the same series of auditory commands every 30 s. Recovery of consciousness (ROC) was defined as the first time the participant responded to two consecutive auditory commands. At ROC, defined as t = 0, participants were returned to a seated position and repeated the computerized neurocognitive test battery (session 2). Neurocognitive testing was repeated at t = 30, 60, 90, 120, 150 and 180 min (sessions 3–8; **Figure 1A**).

Control Group

Participants in the control group (n = 10) were brought into a quiet room, where they were outfitted with the same EEG system as the Anesthesia group, n = 1 with 64 channels and n = 9 with 128 channels. This group followed the same experimental protocol, however, instead of being anesthetized, these participants remained awake by reading or watching television. They were instructed to avoid napping and were monitored by a research assistant to ensure compliance (**Figure 1B**).

Neurocognitive Testing

During each of the eight neurocognitive testing sessions, participants completed a series of six computerized tests selected from the Cognition test battery (Basner et al., 2015) that reflect a broad range of cognitive domains, ranging from sensory-motor speed to complex executive functions. The test order was randomized across subjects, but each subject received the tests in the same order across sessions. We briefly describe the six tests chosen for this study in **Table 1**; for full details, see Maier et al. (2017).

TABLE 1 | Neurocognitive tests within one testing session (Basner et al., 2015).

Cognitive function	Test	Description	Mean duration (seconds)
Sensorimotor speed	Motor Praxis (MP)	Sensorimotor speed was measured by asking participants to click on 20 consecutive squares that appear randomly on the screen (Basner et al., 2015), each successive square was smaller and thus more difficult to track.	39.60 ± 29.25
Spatial learning and memory	Visual Object Learning Test (VOLT)	This task measured the participant's memory for complex figures by asking them to memorize 10 three-dimensional figures. Participants were then asked to distinguish the 10 memorized objects from a larger set of 20.	112.91 ± 24.22
Working memory	Fractal-2-Back (F2B)	Participants looked at a sequential 750 ms display of 62 fractal objects and were asked to press the spacebar when the current stimulus matched that displayed two figures before.	126.15 ± 13.21
Abstraction, concept formation	Abstract Matching (AM)	This test required participants to discern general rules from discrete examples, measuring executive function dependent on abstraction and concept formation. Participants were shown two pairs of objects that varied by perceptual dimensions and were asked to classify a target object as belonging to one of the two pairs.	118.46 ± 53.63
Vigilant attention	Psychomotor Vigilance Test (PVT)	This 3-min version of the PVT records reaction times to visual stimuli that occur at random inter-stimulus intervals. Subjects were instructed to monitor a box on the screen, and hit the space bar as fast as possible once a millisecond counter appears in the box and starts incrementing.	201.37 ± 19.62
Visual search, spatial memory, paired associate learning, sensory-motor speed	Digital Symbol Substitution Test (DSST)	Participants were required to refer to a displayed legend to decode specific symbols with each of the numbers from 1 to 9; during testing, a symbol appeared on the screen, and participants were asked to select the corresponding number as quickly as possible. The test duration was fixed at 90 s, and the legend key was randomly reassigned with each administration.	110.85 ± 29.24

Electroencephalography Data Acquisition and Preprocessing

After fitting each participant with a 64- or 128-channel electrode net, impedances were brought to below 50 kΩ as per manufacturer recommendations. Data were sampled at 500 Hz, and all channels were referenced to the vertex. Throughout each recording, an investigator experienced in reading EEG visually monitored the data to ensure signal integrity. EEG data was bandpass filtered between 0.1 and 50 Hz and re-referenced to an average reference. Epochs and channels identified as containing non-physiological artifacts were removed. Independent component analysis (ICA) was used to remove electrooculogram (EOG) artifacts. Data were segmented by each of the six cognitive tests, within each of the eight recording sessions, for a total of 48 epochs per participant. Participants with too much electrophysiological noise or an incomplete set of neurocognitive tests were eliminated from the participant pool, yielding a final analysis sample of $n = 8$ for the Anesthesia group and $n = 6$ for the Control group. To facilitate the comparison of EEG networks across participants, the set of scalp electrodes common to all participants after data cleaning were identified, yielding a final set of 94 EEG channels that were used in the subsequent analyses.

Electroencephalographic Network Analysis

We divided the EEG signal into five frequency bands—delta (1–4 Hz), theta (4–8 Hz), alpha (8–13 Hz), beta (13–30 Hz), and gamma (30–50 Hz)—using Butterworth band-pass filtering. We then constructed a functional brain network for each frequency band within each analysis epoch using the weighted phase lag index (WPLI; Vinck et al., 2011), which reduces the effects of EEG volume conduction.

$$wPLI_{ij} = \frac{\left|E\left\{J\left(C_{ij}\right)\right\}\right|}{E\left\{\left|J\left(C_{ij}\right)\right|\right\}} = \frac{\left|E\left\{\left|J\left(C_{ij}\right)\right| sgn\left(J\left(C_{ij}\right)\right)\right\}\right|}{E\left\{\left|J\left(C_{ij}\right)\right|\right\}} \quad (1)$$

where $J(C_{ij})$ is the imaginary part of cross-spectrum C_{ij} between signals i and j. The cross-spectrum C_{ij} is defined as $Z_i Z_j^*$, where Z_i is the complex value Fourier spectra of signal i and Z_j^* is the complex conjugate of Z_j. WPLI ranges between 0 and 1: when the phase of one signal always leads or lags that of the other (i.e., if $\Pr\{sgn(J(C_{ij}))=1 \text{ or } -1\}$), then $WPLI_{ij}$ equals 1; when the phase lead and lag relationship between the two signals is random, then $WPLI_{ij}$ equals 0.

Partial Least Squares (PLS) Analysis

Changes in functional connectivity patterns across the groups and conditions were assessed using mean-centering Partial Least Squares (PLS) analysis (McIntosh and Mišić, 2013). This multivariate technique detects the combination of groups/conditions and spatiotemporal patterns of neural activity that optimally relate to each other. This analysis enabled the isolation of networks of functional connectivity that collectively covaried with experimental manipulations. It also enabled the identification of the dominant, data-driven patterns without needing to specify *a priori* hypotheses about the differentiation between groups and conditions, or the specific spatiotemporal profiles of these differences.

PLS can be used to relate two "blocks" or sets of variables to each other (McIntosh and Lobaugh, 2004). We conducted three variations of the PLS analysis, contrasting: (1) WPLI matrices of the anesthesia and control groups during cognitive tests; (2) WPLI matrices of all testing sessions and all cognitive tests within only the anesthesia group; and (3) WPLI matrices from different sessions within a single cognitive task, within only the anesthesia group. The first variation assessed if changes in functional connectivity networks over time were significantly different between control and anesthesia groups. This analysis included WPLI matrices from all participants (anesthesia and control), all frequency bandwidths, and all analysis epochs (eight sessions, six cognitive tests). The second variation identified networks of functional connectivity that related to the recovery of cognitive function after anesthetic-induced unconsciousness. This analysis included WPLI matrices from only the anesthesia group, all five frequency bandwidths, and all analysis epochs (eight sessions, six cognitive tests). The third variation identified networks that differentiated the time-varying recovery of each of the six cognitive tests. Separate PLS analyses were conducted for each of the six cognitive tests. Each variation three analysis included WPLI matrices from the anesthesia group only, a single frequency band, all sessions, and a single cognitive test.

For each variation of the PLS analysis, the covariance matrix between the two sets of variables was computed, and decomposed into mutually orthogonal "latent variables" using singular value decomposition (SVD; Eckart and Young, 1936). Each latent variable was expressed as a vector of design weightings, a vector of functional connectivity weightings, and a scalar singular value (s). The two vectors reflect a symmetrical relationship between the experimental design component most related to the differing functional connectivity values on the one hand, and the optimal (in the least squares sense) network of connectivity related to the identified experimental design components on the other. In other words, the elements of the design weighting vectors represent a contrast of maximal covariance between groups and/or conditions, while the functional connectivity weightings represent a pattern of WPLI connections and frequencies that maximally expressed that contrast. The singular value reflects the covariance between the design variables (groups and conditions) and functional connectivity variables (WPLI) that are captured by each latent variable. The effect size ranges from 0 to 100% and reflects the proportion of cross block covariance accounted for by each latent variable. It is calculated as the ratio of the square of its singular value to the sum of all squared singular values derived from the decomposition (Berman et al., 2014; Mišić et al., 2016). A design salience (optimal contrast) is depicted for each latent variable. This variable ranges from −1 to +1 and represents the overall multivariate pattern of covariance attributable to each condition (design weighting). The design saliences across all conditions of any given contrast sum to zero.

The statistical significance of each latent variable (i.e., each design salience contrast) was determined using permutation tests. The group and condition labels of the WPLI matrices were randomly permuted and the new data were subjected to SVD

as described above, yielding a new set of singular values. These singular values were associated with the null hypothesis that there is no association between the EEG functional connectivity matrix and the group or condition. This procedure was repeated 500 times to generate a sampling distribution of singular values under the null hypothesis. The p-value for each latent variable was estimated as the probability that singular values from the distribution of permuted samples exceeded that from the original non-permuted data.

The reliability of the spatiotemporal patterns associated with each effect was estimated by calculating the standard errors of each functional connectivity weighting using bootstrap resampling (Efron and Tibshirani, 1986). Bootstrap samples were generated by randomly sampling participants with replacement, while their group and condition assignments were preserved, and subjecting the new data to SVD as described above. This process was repeated 500 times, generating a bootstrap distribution for each functional connectivity weighting. The goal of this process was to identify weightings that were stable regardless of which participants were included in the sample. Bars that possessed 95% confidence intervals that did not contain 0 were considered driving factors in the latent variable (i.e., significant and reliable contributors to the design salience) and have been marked with $*$ in the figures.

The magnitude and stability of the connectivity of each pair of electrodes to the overall network were assessed by calculating the bootstrap ratio (b_i), defined as the functional connectivity weighting divided by its bootstrap-estimated error. If we assume that the bootstrap distribution is approximately unit normal (Efron and Tibshirani, 1986), the bootstrap ratios are approximately equivalent to a Z-score. Bootstrap ratios were thresholded at the 99% confidence interval to generate a network of functional connectivities between EEG electrodes that reliably express the statistical effect (pattern of functional connectivity variance) captured by the latent variable. Positive bootstrap ratios indicate that the associated functional connectivity network expresses the contrast in the depicted orientation whereas negative bootstrap ratios indicate that the network expresses the contrast in the opposite orientation (Mišić et al., 2016).

Statistical Analysis

In order to compare cognitive recovery trajectories across participants, scores for all cognitive tests were normalized to 0 (performance at baseline). Normalized scores for each cognitive test were averaged for each recording session across anesthesia and control groups. To determine if there was a significant change in performance across the experimental sessions, a repeated-measures analysis of variance (ANOVA) with a Greenhouse-Geisser correction was performed for each cognitive test, with differences considered significant at $p < 0.05$. To assess when performance on each cognitive test returned to baseline, *post hoc* pairwise t-tests tests using the Bonferroni correction were used to identify the sessions with significantly different cognitive scores; recovery of performance was marked at the first session where scores were not significantly different from baseline.

RESULTS

Temporal Recovery of Cognitive Performance Varies by Task After Anesthesia-Induced Unconsciousness

Upon recovery from anesthesia-induced unconsciousness, performance scores significantly decreased from baseline for all cognitive tests, with the exception of Abstract Matching. Performance on the remaining five cognitive tests returned to

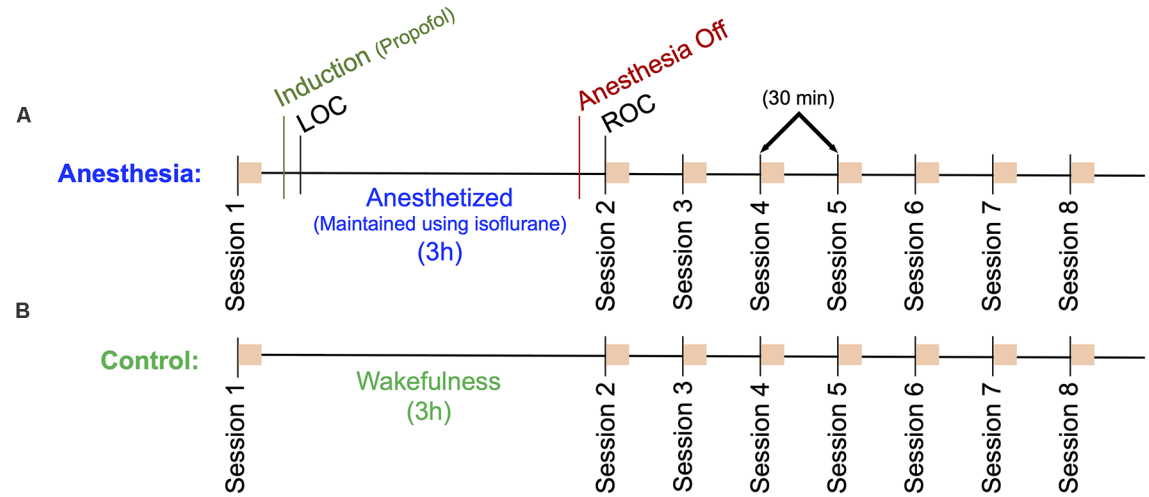

FIGURE 1 | Outline of the experimental protocol. Eight sessions consisting of a battery of six neurocognitive tests are indicated as orange squares. **(A)** Anesthesia group protocol. A baseline cognitive test battery (Session 1) was followed by a 15-min propofol induction and a 3 h anesthesia using isoflurane. Session 2 cognitive tests commenced immediately upon recovery of consciousness (ROC), sessions 3–8 followed at 30-min intervals. **(B)** Control group protocol. A baseline cognitive test battery (Session 1) followed by a 3-h period of wakefulness, where participants read a book, watched a movie, or engaged in other wakeful behavior. Sessions 2–8 were then completed at 30 min intervals. High density EEG was recorded throughout the protocol for both groups.

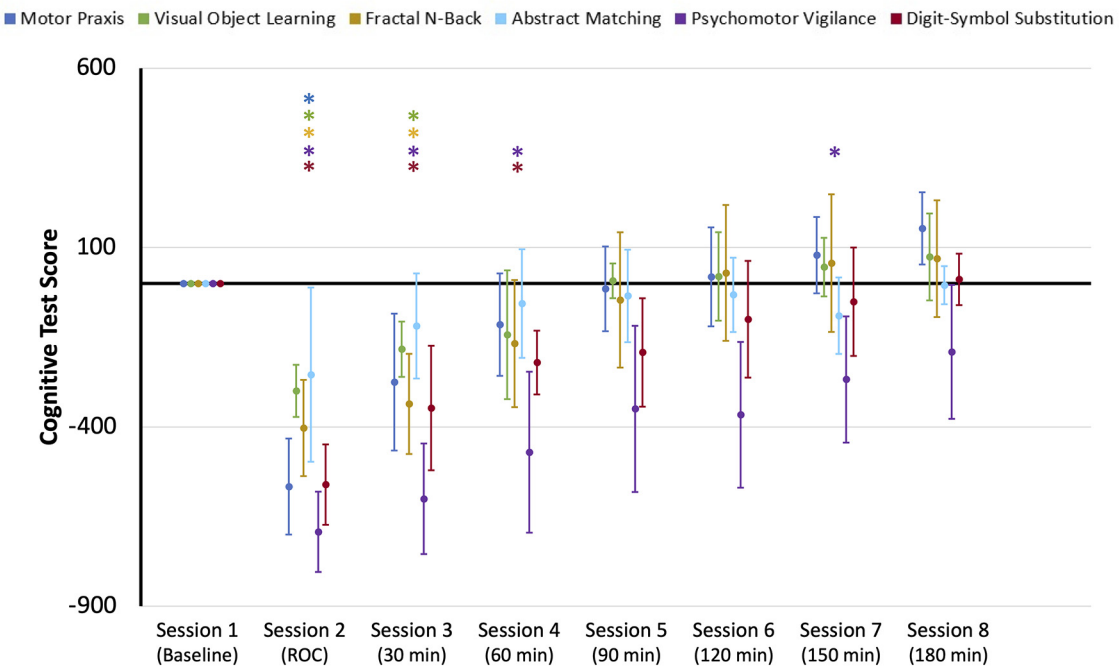

FIGURE 2 | Cognitive test performance scores for the eight sessions of the neurocognitive test battery: baseline, upon recovery of consciousness (ROC), and at six 30-min intervals for 3 h post-ROC. Scores were normalized to baseline performance (0). Error bars indicate standard deviation, and * indicates sessions where scores for each cognitive test were significantly different from baseline.

baseline at varying rates (**Figure 2**). Motor Praxis scores returned within 30 min; Visual Object Learning and Fractal-n-Back scores returned within 60 min; Psychomotor Vigilance and Digital-Symbol Substitution Task scores returned within 90 min. In the control group, a significant difference in performance scores was only found for the VOLT test at session eight compared to session one (**Supplementary Figure 1**), demonstrating that the changes observed in the experimental group were a direct result of anesthesia-induced unconsciousness, and not related to fatigue or learning effects. These results parallel the cognitive recovery trajectories of participants in the full ReCCognition study, wherein 30 individuals showed differential recovery times following anesthesia of the speed and accuracy of tasks associated with attention, complex scanning and visual tracking, working memory, and executive function (Mashour et al., 2020).

Networks Associated With Cognition Are Significantly Altered After Anesthesia

The first variation of the PLS analysis assessed if changes in cognitive networks over time were significantly different between control and anesthesia groups. Three latent variables (LV) emerged as significant (LV1: $p < 0.0005$, effect size (ES) = 87%, LV2: $p = 0.04$, $ES = 3\%$, LV3: $p = 0.03$, $ES = 0.003\%$). As latent variables 2 and 3 only accounted for 3% and 0.003% of the cross block covariance (as determined by effect size calculations) respectively, they were excluded from subsequent analysis.

Latent variable 1 was associated with a network that significantly differentiated anesthesia and control groups (**Figure 3**). Functional connectivity networks in the control group had negatively loaded design weightings, while those in the anesthesia group had predominantly positively loaded design weightings. This contrast captures a functional connectivity network that maximally varied between the control and anesthesia groups across all testing sessions and demonstrates that networks activated during each cognitive task are significantly altered after a period of profound anesthesia-induced unconsciousness. The anesthesia group also expressed a significant session × task interaction, which was not observed in the control group. This interaction was driven by the large contrast in networks across all tasks upon recovery of consciousness, indicating that cognitive networks are maximally altered at this point in the recovery trajectory.

Networks Activated by Cognitive Tasks Return to Their Baseline State 30–60 min Following Recovery of Consciousness

One latent variable emerged as significant (LV1: $p = < 0.0005$; $ES = 74\%$) in the second variation of PLS analysis (i.e., anesthesia only), which identified the functional connectivity network that maximally varied across the recovery of cognitive function after anesthetic-induced unconsciousness. The design salience associated with this latent variable is positively loaded and significantly different from baseline across all cognitive tasks immediately upon recovery of consciousness (session 2) indicating that the multivariate pattern of covariance

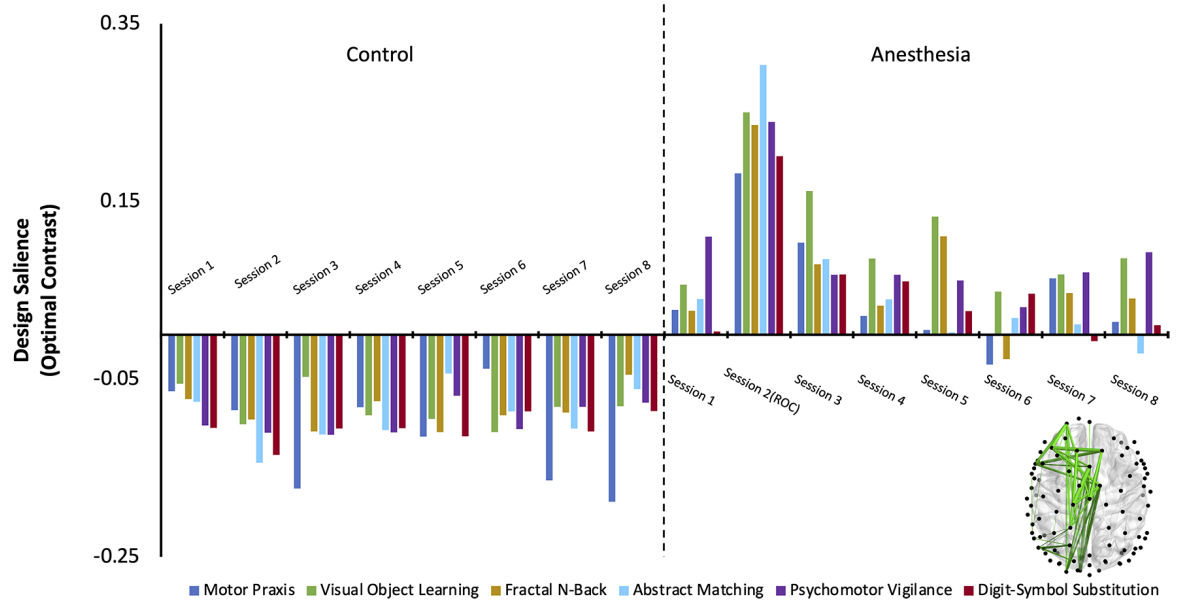

FIGURE 3 | The dominant latent variable (LV = 1) capturing the network of maximal functional connectivity covariance between groups (Control and Anesthesia) across all eight testing sessions and all six cognitive tasks (PLS analysis, variation 1). Permutation testing confirmed the statistical significance of the entire design salience ($p < 0.0005$), and the attributable proportion of cross block covariance (ES) was calculated to be 87%. Connections that reliably express the contrast were identified using bootstrap ratios thresholded at 99% (see "Materials and Methods" section) and are mapped on the brain.

is maximally attributable to this testing session (i.e., the maximal variance in the WPLI of the associated network is seen immediately upon recovery of consciousness). Bootstrap ratios for the associated network are positive, indicating that the functional connectivity within the associated network is stronger at this stage of recovery relative to baseline (the network expresses the contrast in the depicted orientation). The non-zero confidence intervals associated with each cognitive task at this testing session indicate that this condition (session 2) most reliably drives/expresses the multivariate contrast seen within participants exposed to anesthesia.

Brain networks associated with each cognitive task are not differentiable from the baseline state at sessions 3 and 4 (**Figure 4A**). Thus, networks associated with all six cognitive tasks returned to their baseline pattern between 30 min and 1 h following recovery of consciousness. While the networks associated with some cognitive tests expressed a significant, negatively loaded design salience between sessions 5–8, no changes were consistent over consecutive sessions.

Across all five frequency bandwidths, changes in cognitive networks post-ROC were most robustly expressed in delta, theta, and alpha, with functional connectivity in theta having the highest bootstrap ratios (**Figure 4B**). This indicates that networks isolated from the theta band (**Figure 4C**) most reliably express the contrast captured in this latent variable across sessions following exposure to anesthesia. The salience network associated with theta demonstrates that the disruption of inter-hemispheric, long-range connectivity is associated with the significant changes in cognitive function immediately upon recovery of consciousness (session 2).

Recovery of Cognitive Functions Activates Distinct and Dissociable Networks

The third variation of PLS analysis identified functional connectivity networks that maximally varied across testing sessions (i.e., across recovery from anesthesia). These contrasts differentiated the time-varying recovery of each cognitive test. Within alpha and theta bandwidths, one latent variable was significant for each cognitive test, indicating that significant changes occurred in patterns of networks associated with each cognitive test over the eight testing sessions (**Figure 5A**, **Figure 6A**). The effect size for all cognitive tests is high (**Table 2**), indicating that a large proportion of the cross block covariance is captured by the latent variable. The Motor Praxis Task has a relatively lower effect size (alpha *ES* = 61%, theta *ES* = 68%) compared to the other five tasks. In this task, other patterns of network changes account for a large degree of the variability expressed by the network across time in addition to the pattern captured by the significant latent variable.

Design saliences and thresholded associated functional connectivity networks corresponding to each cognitive test in the alpha bandwidth are presented in **Figure 5**, and those for the theta bandwidth in **Figure 6**. Data associated with the latent variables for delta, beta, and gamma bandwidth are included in **Supplementary Figures 2–4**. Across all analyses, the largest contrast in design salience occurs at session two, immediately upon recovery from anesthesia-induced unconsciousness.

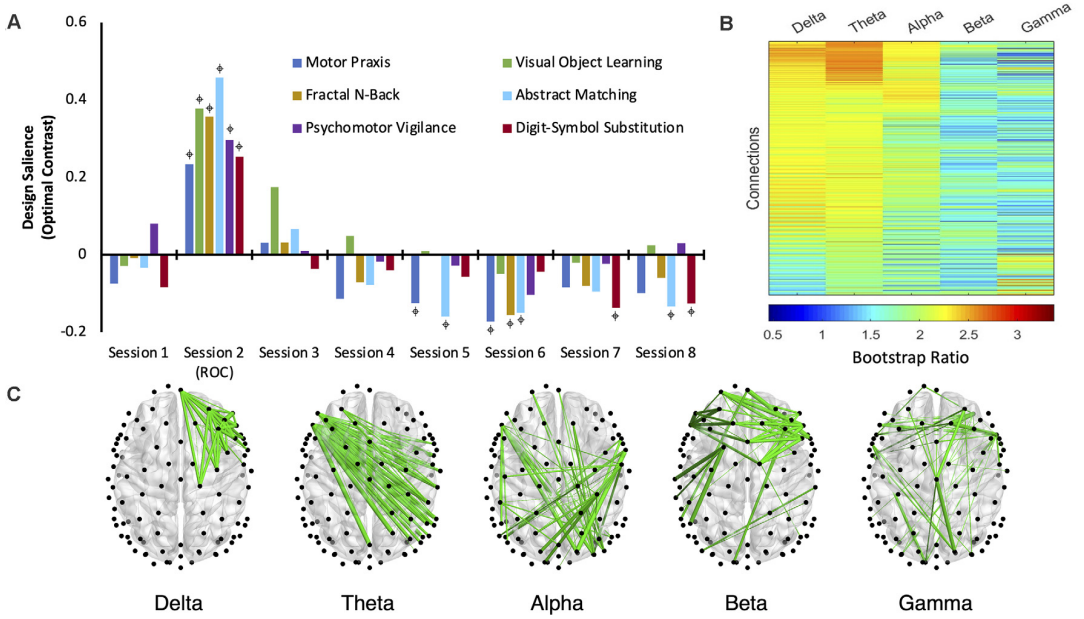

FIGURE 4 | The dominant latent variable (LV = 1) capturing the network of maximal functional connectivity covariance across the anesthetic protocol (five frequency bands, eight cognitive testing sessions, consisting of six cognitive tasks; PLS analysis, variation 2). **(A)** Permutation testing identified a significant design salience (optimal contrast) that captured a session × task interaction depicting the maximal covariance of function related to the recovery of cognitive function after anesthetic-induced unconsciousness ($p < 0.0005$) with an attributable proportion of cross block covariance (ES) of 74%. ϕ = non-zero bootstrap-estimated 95% confidence interval. **(B)** Bootstrap ratios (BSRs) for each connection (pair of electrodes) associated with each frequency band. The higher the BSR magnitude, the more reliably the connection expressed the contrast in its present orientation (see "Materials and Methods" section). **(C)** The top 1% of connections that reliably express the contrast, determined by thresholding the BSRs.

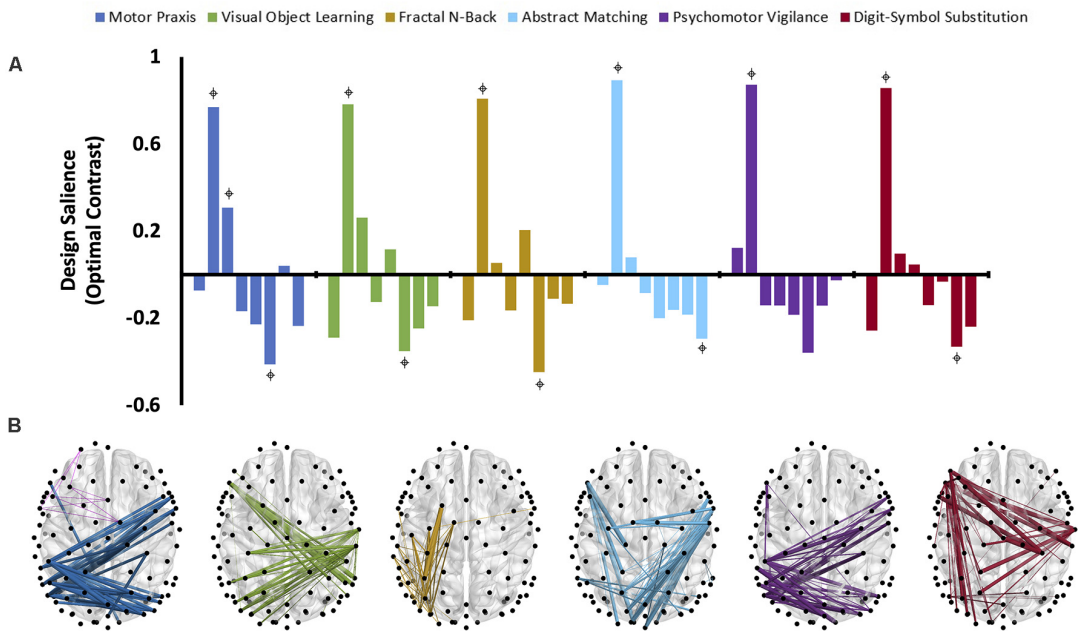

FIGURE 5 | The dominant latent variables (LV = 1 in all cases) capturing the distinct networks of maximal functional connectivity covariance across all eight cognitive testing sessions corresponding to each cognitive task in the alpha bandwidth (PLS analysis, variation 3). **(A)** Design saliences associated with network changes for each cognitive test across all eight sessions, where each bar corresponds to a single cognitive testing session. ϕ = non-zero bootstrap-estimated 95% confidence interval. Permutation-estimated *p*-values and proportions of attributable cross block covariance (ES) associated with the significant latent variable are included in **Table 2**. **(B)** The top 1% of connections corresponding to each cognitive test that reliably express the contrast, determined by thresholding the bootstrap ratios.

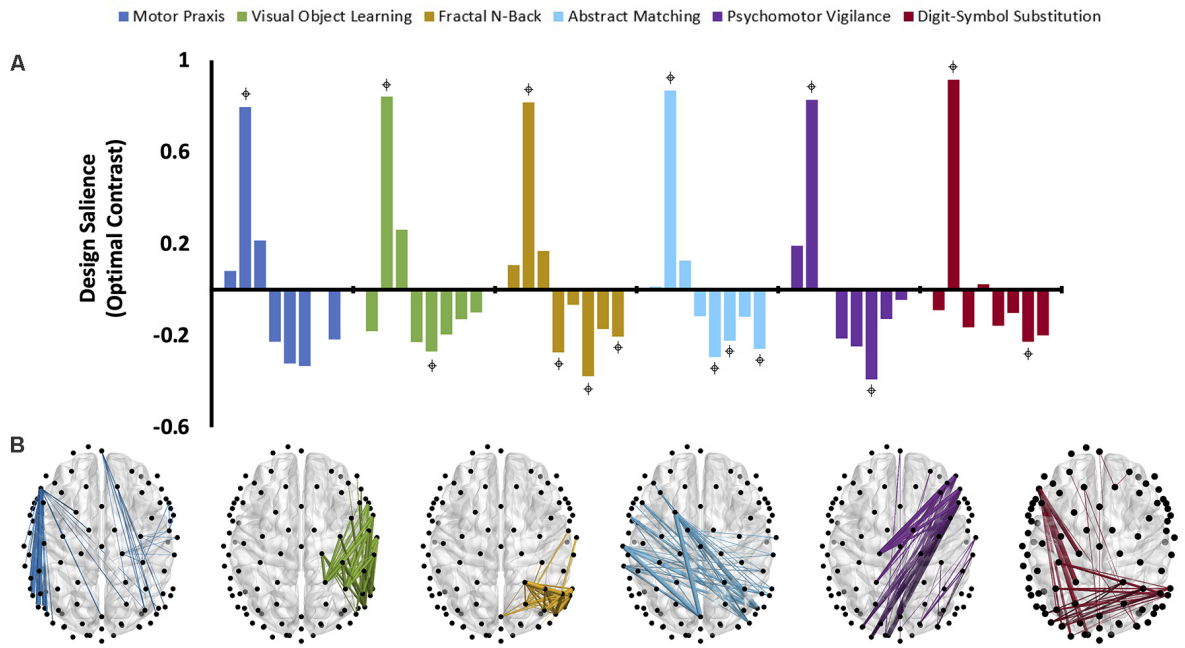

FIGURE 6 | The dominant latent variables (LV = 1 in all cases) capturing the distinct networks of maximal functional connectivity covariance across all eight cognitive testing sessions corresponding to each cognitive task in the theta bandwidth (PLS analysis, variation 3). **(A)** Design saliences associated with network changes for each cognitive test across all eight sessions, where each bar corresponds to a single cognitive testing session. ϕ = non-zero bootstrap-estimated 95% confidence interval. Permutation-estimated *p*-values and proportions of attributable cross block covariance (ES) associated with the significant latent variable are included in **Table 2**. **(B)** The top 1% of connections corresponding to each cognitive test that reliably express the contrast, determined by thresholding the bootstrap ratios.

Bootstrapping provided 95% confidence intervals that were consistently non-zero at session two across all cognitive tasks and frequency bands. As expected, this indicates that each of these distinct cognitive networks is maximally altered upon recovery of consciousness and that this session is reliably, and significantly, contributing to the multivariate pattern of covariance. The congruent directionality of the design salience weightings (positively loaded) and bootstrap ratios (positive values) upon recovery of consciousness indicates that functional connectivity within these distinct networks is significantly stronger than at baseline. This may suggest that these networks play a significant role in the recovery of the specific cognitive function associated with the cognitive test driving the contrast. Strikingly, the alpha and theta networks associated with cognitive recovery are distinct across each of the six cognitive tests (**Figure 5B**, **Figure 6B**). In the alpha bandwidth, all tasks except the Psychomotor Vigilance Test have a significant negative contrast during one session post-ROC (**Figure 5A**). In the theta bandwidth, all tasks except the Motor Praxis Task have one to three sessions that express significant negative contrast post-ROC (**Figure 6A**). Given that the bootstrap ratios were positive values, the negatively loaded design salience bars can be interpreted as significantly weaker functional connectivity within the associated networks at this point in recovery relative to baseline and to the significantly positive design saliences seen at session 2.

DISCUSSION

In this study with healthy adults exposed to a clinically relevant anesthesia regimen, we demonstrated that six distinct cognitive functions follow different temporal trajectories of recovery following anesthesia, with certain cognitive functions returning to baseline only 90–180 min following the recovery of consciousness. These results were supported by a larger study of 60 individuals (including those in this study) showing that the rates of recovery statistically differed among cognitive domains upon recovery from anesthetic-induced unconsciousness (Mashour et al., 2020). Importantly, we found that brain networks associated with cognitive tasks are significantly altered after a period of profound anesthesia-induced unconsciousness, return to their baseline state 30–60 min following recovery of consciousness, and are distinct and dissociable across various cognitive functions.

Globally, the results from several variations of the PLS analysis reflect well-known effects of anesthesia, namely, the impairment and gradual recovery of cognitive functions following anesthetic-induced unconsciousness (Larsen et al., 2000; Chen et al., 2001). The results from our data-driven multivariate EEG analysis provide evidence for network-level disturbances that accompany the anesthetic-induced change in cognitive function. Like cognitive task performance, the brain networks are maximally altered immediately upon recovery of consciousness. Although network-level alterations return to baseline 30–60 min

TABLE 2 | Partial Least Squares (PLS) variation three permutation and bootstrapping results for alpha and theta bands.

Cognitive test	Latent variable 1 *p* - value (design salience statistical significance) and effect size (proportion of cross block covariance captured)
Motor Praxis (MP)	Alpha: $p = 0.006$, $ES = 61\%$ Theta: $p = 0.008$, $ES = 68\%$
Visual Object Learning Test (VOLT)	Alpha: $p = 0.008$, $ES = 80\%$ Theta: $p = 0.002$, $ES = 90\%$
Fractal-2-Back (F2B)	Alpha: $p = 0.002$, $ES = 84\%$ Theta: $p < 0.0005$, $ES = 93\%$
Abstract Matching (AM)	Alpha: $p < 0.0005$, $ES = 91\%$ Theta: $p < 0.0005$, $ES = 95\%$
Psychomotor Vigilance Test (PVT)	Alpha: $p = 0.008$, $ES = 87\%$ Theta: $p = 0.002$, $ES = 92\%$
Digital Symbol Substitution Test (DSST)	Alpha: $p = 0.002$, $ES = 81\%$ Theta: $p = 0.008$, $ES = 91\%$

following ROC, cognitive test performance did not recover until 90–180 post-ROC. These findings are consistent with our previous analyses of this dataset, which have shown that after ROC, neurophysiological characteristics such as source-localized alpha power and graph theory characteristics of brain networks return to baseline prior to the full recovery of cognitive functions (Blain-Moraes et al., 2017).

Functional connectivity in theta bandwidth was most strongly associated with brain network contrasts in the 3 h after recovery of consciousness, with long-range interhemispheric connections expressing maximal contrast immediately upon recovery of consciousness. These findings add to the large body of literature demonstrating anesthetic suppression of long-range functional connectivity (Boveroux et al., 2010; Schröter et al., 2012; Barttfeld et al., 2015). Moreover, theta band activity in frontal electrodes has been positively linked to working memory demand (Sauseng et al., 2005; Grunwald et al., 2014), and theta oscillations are implicated in the coordination and integration of various cognitive processes during working memory intensive tasks (Sarnthein et al., 1998; Sauseng et al., 2010). We, therefore, suggest that the increased theta connectivity network observed during cognitive tests performance following recovery of consciousness may represent increased recruitment of cognitive resources to compensate for the major perturbation of anesthesia. Networks isolated from the alpha bandwidth also reliably express the contrast across sessions following exposure to anesthesia. As alpha band oscillations have been related to the inhibition of brain activities that are not involved in a cognitive task (Klimesch et al., 2007; Jensen and Mazaheri, 2010; Uusberg et al., 2013), it is possible that the alpha recovery network maximizes a limited cognitive reserve by suppressing brain activities that are not required for the specific cognitive task. These results may reflect the complementary and compensatory roles of theta and alpha recovery networks in response to anesthesia-induced perturbations in cognitive functioning.

PLS analysis of the functional connectivity networks associated with specific cognitive tests across recovery from anesthesia isolated distinct and dissociable networks for each cognitive activity across all frequency bands. For example, in the alpha bandwidth, the motor praxis and psychomotor vigilance tasks were similarly associated with inter-hemisphere parietal connections and long-range right frontal to left parietal connections, while the visual object learning task was associated with similar parietal, but left frontal to right parietal long–range connections. The fractal n-back task was associated with short-range connections in the left parietal, temporal and occipital regions. Long-range connections associated with the abstract matching task converge in parietal regions, while long-range connections associated with the digital symbol substitution task converged in the left frontal regions. Strikingly, these networks do not overlap with the canonical network associated with specific cognitive functions [e.g., the VOLT primarily activates the frontal and bilateral anterior medial temporal cortices and the hippocampus (Jackson and Schacter, 2004); PVT recruits the prefrontal cortex, motor cortex, inferior parietal cortex and visual cortex (Basner et al., 2015)]. This does not necessarily indicate that these canonical networks are inactive. Rather, as PLS analysis foregrounds the contrast in networks across conditions, this indicates that the canonical networks exhibit similar levels of connectivity across the 3 h following recovery of consciousness. In other words, the changes in cognitive task performance in the 3 h post-ROC are not associated with changes in the strength or number of functional connections of the networks typically associated with these cognitive activities. Therefore, the present results, which show that specific networks are differentially activated according to cognitive tasks after recovery from anesthetic-induced unconsciousness, must be interpreted carefully. One possibility is that these networks reflect an adaptive, compensatory network associated with cognitive reserve: non-traditional cognitive networks that are recruited to maintain cognitive function when traditional networks are disrupted (Barulli and Stern, 2013). Another possibility is that these networks are inappropriately recruited for the cognitive task as the brain recovers from the functional connectivity disruption of anesthesia (Barttfeld et al., 2015). Indeed, each network also exhibits a negative salience 60–90 min post recovery of consciousness, potentially indicating an inhibition of these networks once baseline functional connectivity patterns are restored. This timeline is congruent with our prior findings that source-localized alpha power returns to baseline levels within 90 min of recovery of consciousness (Blain-Moraes et al., 2017), and with results from a large randomized control trial assessing different methods of monitoring intraoperative awareness, where mean discharge-readiness times in the recovery room were approximately 95 min (Mashour et al., 2012). Finally, these network changes may reflect residual effects of the prolonged exposure to anesthesia. Loss and recovery of consciousness associated with general anesthesia have been posited to be governed by the principle of "neural inertia", a neurobiological process that maintains aroused and anesthetized states, and creates resistance to behavioral state transitions (Friedman et al., 2010). It is likely that, upon recovery of consciousness, the brain's neural inertia maintains many of the network properties that existed immediately prior to the moment of return of behavioral responsiveness. As a result of this neural inertia, the major difference in functional connectivity networks observed during the cognitive tests conducted immediately upon recovery of

consciousness may also reflect the characteristics of the networks involved in the return of consciousness.

Our study design offers a unique opportunity to examine isolated brain networks associated with specific cognitive functions. In healthy human studies, the assessment of functional connectivity patterns associated with higher-order cognitive tasks, such as executive function, is typically confounded by concomitant cognitive functions, such as attention. In this study, cognitive task performance is differentially affected by anesthesia, particularly in the minutes immediately after ROC. Loosely, anesthesia performs a temporal separation of cognitive function performance much like gel electrophoresis separates molecules, enabling us to individually examine the component parts. The fact that these isolated cognitive functional connectivity networks do not map onto canonical networks may prompt a reconsideration of the relationship between functional connectivity and cognition. Indeed, anesthesia has been successfully used as a tool to re-examine the relationship of functional connectivity to brain-based phenomena. In a recent study, cholinergic stimulation of the prefrontal cortex induced wakefulness in a rat model, despite continuous exposure to general anesthesia (Pal et al., 2020). Surprisingly, functional connectivity remained suppressed during the induced wakeful period in the presence of anesthetics, which suggested that the level of consciousness can be dissociated from cortical connectivity. Similarly, the findings of this study suggest that functional connectivity patterns may be dissociable from cognitive tasks and could prompt a reevaluation of the role of these connectivity measures in cognition.

This study has several limitations. First, the number of participants in the study is relatively low (n = 14). The results of PLS analysis are sensitive to signal/noise ratio (Cramer, 1993), which is decreased in this sample size by the high inter-subject variability of brain network activity after recovery from anesthetic-induced unconsciousness. However, the latent variables for variations one and two of the analysis accounted for 87% and 74% of the network covariance respectively, indicating the robustness of these results despite the smaller sample size. In the third variation of the PLS analysis, which identified networks that differentiated the time-varying recovery of each cognitive test, networks associated with motor praxis (theta and alpha) and visual object learning (alpha) explained less than 70% of the covariance. While the results are statistically significant, the latent networks associated with these cognitive tests should be interpreted with caution. Second, we use a single measure of functional connectivity—wPLI—to assess the functional coupling of brain networks during cognitive tests. Although we chose this measure due to its robustness against volume conduction (Vinck et al., 2011), this may bias our results, as other types of phase-based connectivity or families of connectivity (e.g., envelope-based connectivity) may identify different coupling patterns across cognitive tasks. For example, several recent studies have demonstrated that envelope- and phase-based measures of functional connectivity capture different and complementary relationships between brain regions, especially in the networks related to loss and recovery of consciousness (Siems and Siegel, 2020; Duclos et al., 2021). wPLI also only provides information about the strength, not the direction, of functional coupling, which may be investigated with other connectivity metrics such as directed phase lag index (Stam and van Straaten, 2012). Third, our functional connectivity networks were constructed based on sensor-level EEG data, with the nodes of the networks constrained to the fixed electrode positions of the EEG net. The data were not source localized, limiting the conclusions that can be drawn about the specific brain regions implicated in the networks associated with the recovery of cognitive function presented in our results. Finally, across all PLS analysis variations, the largest contrast was uniformly driven by the cognitive testing period immediately succeeding recovery of consciousness. While these results align with our expectation of maximal impairment upon return of responsiveness, the magnitude of this contrast dwarfs the subsequent sessions, potentially masking more subtle network changes that accompany the return to baseline cognitive performance up to 3 h after recovery of consciousness.

The present study investigated EEG network-level changes in functional connectivity associated with the recovery of six cognitive functions following a clinically relevant anesthesia regimen. Brain networks associated with cognitive tests were significantly altered in patients recovering from anesthesia compared to control subjects. Across 3 h post-ROC, the cognitive networks of participants recovering from anesthesia were most significantly altered in the theta bandwidth, particularly in long-range interhemispheric connections. Finally, different cognitive functions were associated with distinct and dissociable brain network changes across the 3-h recovery period. Collectively, these results demonstrate that cognitive functions have distinct temporal and network-level patterns of reconstitution following an anesthetic-induced loss of consciousness. Future studies should aim to validate these findings with neuroimaging techniques with an appropriate spatial resolution to identify the specific brain regions involved in the reconstitution of each cognitive activity following anesthesia.

DATA AVAILABILITY STATEMENT

The raw data supporting the conclusions of this article will be made available by the authors, without undue reservation.

ETHICS STATEMENT

The studies involving human participants were reviewed and approved by University of Michigan Medical School. The patients/participants provided their written informed consent to participate in this study.

AUTHOR CONTRIBUTIONS

MA, MK, and GM conceived and designed the study. MB designed the cognitive tests and extracted cognitive test data. SB-M and GG acquired EEG data. VT, EJ, PP, GG, and GM served as the clinical anesthesiologists. AR and KB analyzed the data. AR, BM, CD, SB-M, and GM interpreted the data. AR, CD, and SB-M wrote the manuscript. All

authors contributed to critical review of the manuscript. All authors contributed to the article and approved the submitted version.

FUNDING

This work was supported by the James S. McDonnell Foundation, St. Louis, MO (GM, MK, and MA); and the Natural Science and Engineering Research Council (NSERC) of Canada (SB-M, RGPIN-2016-03817).

SUPPLEMENTARY MATERIAL

The Supplementary Material for this article can be found online at: https://www.frontiersin.org/articles/10.3389/fnhum.2021.706693/full#supplementary-material.

REFERENCES

Allampati, S., Wen, S., Liu, F., and Kupec, J. T. (2019). Recovery of cognitive function after sedation with propofol for outpatient gastrointestinal endoscopy. *Saudi. J. Gastroenterol.* 25, 188–193. doi: 10.4103/sjg.SJG_369_18

Avidan, M. S., and Evers, A. S. (2016). The fallacy of persistent postoperative cognitive decline. *Anesthesiology* 124, 255–258. doi: 10.1097/ALN.0000000000000958

Banks, M. I., Krause, B. M., Endemann, C. M., Campbell, D. I., Kovach, C. K., Dyken, M. E., et al. (2020). Cortical functional connectivity indexes arousal state during sleep and anesthesia. *NeuroImage* 211:116627. doi: 10.1016/j.neuroimage.2020.116627

Barttfeld, P., Uhrig, L., Sitt, J. D., Sigman, M., Jarraya, B., and Dehaene, S. (2015). Signature of consciousness in the dynamics of resting-state brain activity. *Proc. Natl. Acad. Sci. U S A* 112, 887–892. doi: 10.1073/pnas.1418031112

Barulli, D., and Stern, Y. (2013). Efficiency, capacity, compensation, maintenance, plasticity: emerging concepts in cognitive reserve. *Trends Cogn. Sci.* 17, 502–509. doi: 10.1016/j.tics.2013.08.012

Basner, M., Savitt, A., Moore, T. M., Port, A. M., McGuire, S., Ecker, A. J., et al. (2015). Development and validation of the cognition test battery for spaceflight. *Aerosp. Med. Hum. Perform.* 86, 942–952. doi: 10.3357/AMHP.4343.2015

Berman, M. G., Misic, B., Buschkuehl, M., Kross, E., Deldin, P. J., Peltier, S., et al. (2014). Does resting-state connectivity reflect depressive rumination? a tale of two analyses. *Neuroimage* 103, 267–279. doi: 10.1016/j.neuroimage.2014.09.027

Blain-Moraes, S., Tarnal, V., Vanini, G., Alexander, A., Rosen, D., Shortal, B., et al. (2015). Neurophysiological correlates of sevoflurane-induced unconsciousness. *Anesthesiology* 122, 307–316. doi: 10.1097/ALN.0000000000000482

Blain-Moraes, S., Tarnal, V., Vanini, G., Bel-Behar, T., Janke, E., Picton, P., et al. (2017). Network efficiency and posterior alpha patterns are markers of recovery from general anesthesia: a high-density electroencephalography study in healthy volunteers. *Front. Hum. Neurosci.* 11:328. doi: 10.3389/fnhum.2017.00328

Boveroux, P., Vanhaudenhuyse, A., Bruno, M.-A., Noirhomme, Q., Lauwick, S., Luxen, A., et al. (2010). Breakdown of within- and between-network resting state functional magnetic resonance imaging connectivity during propofol-induced loss of consciousness. *Anesthesiology* 113, 1038–1053. doi: 10.1097/ALN.0b013e3181f697f5

Carr, Z. J., Torjman, M. C., Manu, K., Dy, G., and Goldberg, M. E. (2011). Spatial memory using active allothetic place avoidance in adult rats after isoflurane anesthesia: a potential model for postoperative cognitive dysfunction. *J. Neurosurg. Anesthesiol.* 23, 138–145. doi: 10.1097/ANA.0b013e3182049f19

Chen, X., Zhao, M., White, P. F., Li, S., Tang, J., Wender, R. H., et al. (2001). The recovery of cognitive function after general anesthesia in elderly patients: a comparison of desflurane and sevoflurane. *Anesth. Analg.* 93, 1489–1494. doi: 10.1097/00000539-200112000-00029

Chennu, S., O'Connor, S., Adapa, R., Menon, D. K., and Bekinschtein, T. A. (2016). Brain connectivity dissociates responsiveness from drug exposure during propofol-induced transitions of consciousness. *PLoS Comput. Biol.* 12:e1004669. doi: 10.1371/journal.pcbi.1004669

Cramer, R. D. (1993). Partial least squares (PLS): its strengths and limitations. *Perspect. Drug Discov. Des.* 1, 269–278. doi: 10.1007/BF02174528

Duclos, C., Maschke, C., Mahdid, Y., Berkun, K., da Silva Castanheira, J., Tarnal, V., et al. (2021). Differential classification of states of consciousness using envelope- and phase-based functional connectivity. *Neuroimage* 237:118171. doi: 10.1016/j.neuroimage.2021.118171

Eckart, C., and Young, G. (1936). The approximation of one matrix by another of lower rank. *Psychometrika* 1, 211–218. doi: 10.1007/BF02288367

Efron, B., and Tibshirani, R. (1986). Bootstrap methods for standard errors, confidence intervals and other measures of statistical accuracy. *Stat. Sci.* 1, 54–75. doi: 10.1214/ss/1177013815

Engel, A. K., Gerloff, C., Hilgetag, C. C., and Nolte, G. (2013). Intrinsic coupling modes: multiscale interactions in ongoing brain activity. *Neuron* 80, 867–886. doi: 10.1016/j.neuron.2013.09.038

Friedman, E. B., Sun, Y., Moore, J. T., Hung, H.-T., Meng, Q. C., Perera, P., et al. (2010). A conserved behavioral state barrier impedes transitions between anesthetic-induced unconsciousness and wakefulness: evidence for neural inertia. *PLoS One* 5:e11903. doi: 10.1371/journal.pone.0011903

Grunwald, M., Weiss, T., Mueller, S., and Rall, L. (2014). EEG changes caused by spontaneous facial self-touch may represent emotion regulating processes and working memory maintenance. *Brain Res.* 1557, 111–126. doi: 10.1016/j.brainres.2014.02.002

Hemmings, H. C., Riegelhaupt, P. M., Kelz, M. B., Solt, K., Eckenhoff, R. G., Orser, B. A., et al. (2019). Towards a comprehensive understanding of anesthetic mechanisms of action: a decade of discovery. *Trends Pharmacol. Sci.* 40, 464–481. doi: 10.1016/j.tips.2019.05.001

Jackson, O., and Schacter, D. L. (2004). Encoding activity in anterior medial temporal lobe supports subsequent associative recognition. *Neuroimage* 21, 456–462. doi: 10.1016/j.neuroimage.2003.09.050

Jensen, O., and Mazaheri, A. (2010). Shaping functional architecture by oscillatory alpha activity: gating by inhibition. *Front. Hum. Neurosci.* 4:186. doi: 10.3389/fnhum.2010.00186

Jiang, S., Miao, B., and Chen, Y. (2017). Prolonged duration of isoflurane anesthesia impairs spatial recognition memory through the activation of JNK1/2 in the hippocampus of mice. *Neuroreport* 28, 386–390. doi: 10.1097/WNR.0000000000000760

John, E. R., Prichep, L. S., Kox, W., Valdés-Sosa, P., Bosch-Bayard, J., Aubert, E., et al. (2001). Invariant reversible QEEG effects of anesthetics. *Conscious. Cogn.* 10, 165–183. doi: 10.1006/ccog.2001.0507

Klimesch, W., Sauseng, P., and Hanslmayr, S. (2007). EEG alpha oscillations: the inhibition-timing hypothesis. *Brain Res. Rev.* 53, 63–88. doi: 10.1016/j.brainresrev.2006.06.003

Långsjö, J. W., Maksimow, A., Salmi, E., Kaisti, K., Aalto, S., Oikonen, V., et al. (2005). S-ketamine anesthesia increases cerebral blood flow in excess of the metabolic needs in humans. *Anesthesiology* 103, 258–268. doi: 10.1097/00000542-200508000-00008

Larsen, B., Seitz, A., and Larsen, R. (2000). Recovery of cognitive function after remifentanil-propofol anesthesia: a comparison with desflurane and sevoflurane anesthesia. *Anesth. Analg.* 90, 168–174. doi: 10.1097/00000539-200001000-00035

Lee, U., Ku, S., Noh, G., Baek, S., Choi, B., and Mashour, G. A. (2013). Disruption of frontal-parietal communication by ketamine, propofol and sevoflurane. *Anesthesiology* 118, 1264–1275. doi: 10.1097/ALN.0b013e31829103f5

Maier, K. L., McKinstry-Wu, A. R., Palanca, B. J. A., Tarnal, V., Blain-Moraes, S., Basner, M., et al. (2017). Protocol for the reconstructing human consciousness and cognition (ReCCognition) study. *Front. Hum. Neurosci.* 11:284. doi: 10.3389/fnhum.2017.00284

Mashour, G. A., and Hudetz, A. G. (2018). Neural correlates of unconsciousness in large-scale brain networks. *Trends Neurosci.* 41, 150–160. doi: 10.1016/j.tins.2018.01.003

Mashour, G. A., Palanca, B. J. A., Basner, M., Li, D., Wang, W., Blain-Moraes, S., et al. (2020). Recovery of consciousness and cognition after general anesthesia in humans. *bioRxiv* [Preprint]. doi: 10.1101/2020.05.28.121269

Mashour, G. A., Shanks, A., Tremper, K. K., Kheterpal, S., Turner, C. R., Ramachandran, S. K., et al. (2012). Prevention of intraoperative awareness with explicit recall in an unselected surgical population: a randomized comparative effectiveness trial. *Anesthesiology* 117, 717–725. doi: 10.1097/ALN.0b013e31826904a6

McIntosh, A. R., and Lobaugh, N. J. (2004). Partial least squares analysis of neuroimaging data: applications and advances. *Neuroimage* 23, S250–S263. doi: 10.1016/j.neuroimage.2004.07.020

McIntosh, A. R., and Mišić, B. (2013). Multivariate statistical analyses for neuroimaging data. *Annu. Rev. Psychol.* 64, 499–525. doi: 10.1146/annurev-psych-113011-143804

Mišić, B., Dunkley, B. T., Sedge, P. A., Da Costa, L., Fatima, Z., Berman, M. G., et al. (2016). Post-traumatic stress constrains the dynamic repertoire of neural activity. *J. Neurosci.* 36, 419–431. doi: 10.1055/s-0041-1728230

N'Kaoua, B., Véron, A.-L. H., Lespinet, V. C., Claverie, B., and Sztark, F. (2002). Time course of cognitive recovery after propofol anaesthesia: a level of processing approach. *J. Clin. Exp. Neuropsychol.* 24, 713–719. doi: 10.1076/jcen.24.6.713.8401

Pal, D., Li, D., Dean, J. G., Brito, M. A., Liu, T., Fryzel, A. M., et al. (2020). Level of consciousness is dissociable from electroencephalographic measures of cortical connectivity, slow oscillations and complexity. *J. Neurosci.* 40, 605–618. doi: 10.1523/JNEUROSCI.1910-19.2019

Purdon, P. L., Pierce, E. T., Mukamel, E. A., Prerau, M. J., Walsh, J. L., Wong, K. F. K., et al. (2013). Electroencephalogram signatures of loss and recovery of consciousness from propofol. *Proc. Natl. Acad. Sci. U S A* 110, E1142–E1151. doi: 10.1073/pnas.1221180110

Sarnthein, J., Petsche, H., Rappelsberger, P., Shaw, G. L., and von Stein, A. (1998). Synchronization between prefrontal and posterior association cortex during human working memory. *Proc. Natl. Acad. Sci. U S A* 95, 7092–7096. doi: 10.1073/pnas.95.12.7092

Sauseng, P., Griesmayr, B., Freunberger, R., and Klimesch, W. (2010). Control mechanisms in working memory: a possible function of EEG theta oscillations. *Neurosci. Biobehav. Rev.* 34, 1015–1022. doi: 10.1016/j.neubiorev.2009.12.006

Sauseng, P., Klimesch, W., Schabus, M., and Doppelmayr, M. (2005). Fronto-parietal EEG coherence in theta and upper alpha reflect central executive functions of working memory. *Int. J. Psychophysiol.* 57, 97–103. doi: 10.1016/j.ijpsycho.2005.03.018

Scheinin, A., Kantonen, O., Alkire, M., Långsjö, J., Kallionpää, R. E., Kaisti, K., et al. (2021). Foundations of human consciousness: imaging the twilight zone. *J. Neurosci.* 41, 1769–1778. doi: 10.1523/JNEUROSCI.0775-20.2020

Schröter, M. S., Spoormaker, V. I., Schorer, A., Wohlschläger, A., Czisch, M., Kochs, E. F., et al. (2012). Spatiotemporal reconfiguration of large-scale brain functional networks during propofol-induced loss of consciousness. *J. Neurosci.* 32, 12832–12840. doi: 10.1038/s41557-021-00770-7

Siems, M., and Siegel, M. (2020). Dissociated neuronal phase- and amplitude-coupling patterns in the human brain. *Neuroimage* 209:116538. doi: 10.1016/j.neuroimage.2020.116538

Stam, C. J., and van Straaten, E. C. W. (2012). Go with the flow: use of a directed phase lag index (dPLI) to characterize patterns of phase relations in a large-scale model of brain dynamics. *Neuroimage* 62, 1415–1428. doi: 10.1016/j.neuroimage.2012.05.050

Uusberg, A., Uibo, H., Kreegipuu, K., and Allik, J. (2013). EEG alpha and cortical inhibition in affective attention. *Int. J. Psychophysiol.* 89, 26–36. doi: 10.1016/j.ijpsycho.2013.04.020

Valentim, A. M., Alves, H. C., Olsson, I. A. S., and Antunes, L. M. (2008). The effects of depth of isoflurane anesthesia on the performance of mice in a simple spatial learning task. *J. Am. Assoc. Lab Anim. Sci.* 47, 16–19.

Vinck, M., Oostenveld, R., van Wingerden, M., Battaglia, F., and Pennartz, C. M. A. (2011). An improved index of phase-synchronization for electrophysiological data in the presence of volume-conduction, noise and sample-size bias. *Neuroimage* 55, 1548–1565. doi: 10.1016/j.neuroimage.2011.01.055

Conflict of Interest: The authors declare that the research was conducted in the absence of any commercial or financial relationships that could be construed as a potential conflict of interest.

Publisher's Note: All claims expressed in this article are solely those of the authors and do not necessarily represent those of their affiliated organizations, or those of the publisher, the editors and the reviewers. Any product that may be evaluated in this article, or claim that may be made by its manufacturer, is not guaranteed or endorsed by the publisher.

frontiers in Human Neuroscience

ORIGINAL RESEARCH
published: 18 October 2021
doi: 10.3389/fnhum.2021.740225

Multifractal Functional Connectivity Analysis of Electroencephalogram Reveals Reorganization of Brain Networks in a Visual Pattern Recognition Paradigm

Orestis Stylianou[1,2], Frigyes Samuel Racz[1], Keumbi Kim[1], Zalan Kaposzta[1], Akos Czoch[1], Andriy Yabluchanskiy[3,4,5], Andras Eke[1,6] and Peter Mukli[1,3]**

[1] Department of Physiology, Semmelweis University, Budapest, Hungary, [2] Institute of Translational Medicine, Semmelweis University, Budapest, Hungary, [3] Vascular Cognitive Impairment and Neurodegeneration Program, Department of Biochemistry and Molecular Biology, Oklahoma Center for Geroscience and Healthy Brain Aging, The University of Oklahoma Health Sciences Center, Oklahoma City, OK, United States, [4] The Peggy and Charles Stephenson Cancer Center, The University of Oklahoma Health Sciences Center, Oklahoma City, OK, United States, [5] Department of Health Promotion Sciences, College of Public Health, The University of Oklahoma Health Sciences Center, Oklahoma City, OK, United States, [6] Department of Radiology and Biomedical Imaging, Yale University School of Medicine, New Haven, CT, United States

OPEN ACCESS

Edited by:
Pedro Antonio Valdes-Sosa, University of Electronic Science and Technology of China, China

Reviewed by:
Olga Mikhailovna Bazanova, State Research Institute of Neuroscience and Medicine, Russia
Xi Zhu, Columbia University, United States

***Correspondence:**
Peter Mukli
mukli.peter@med.semmelweis-univ.hu
Andras Eke
eke.andras@med.semmelweis-univ.hu

Specialty section:
This article was submitted to Cognitive Neuroscience, a section of the journal Frontiers in Human Neuroscience

Received: 12 July 2021
Accepted: 23 September 2021
Published: 18 October 2021

Citation:
Stylianou O, Racz FS, Kim K, Kaposzta Z, Czoch A, Yabluchanskiy A, Eke A and Mukli P (2021) Multifractal Functional Connectivity Analysis of Electroencephalogram Reveals Reorganization of Brain Networks in a Visual Pattern Recognition Paradigm. Front. Hum. Neurosci. 15:740225. doi: 10.3389/fnhum.2021.740225

The human brain consists of anatomically distant neuronal assemblies that are interconnected via a myriad of synapses. This anatomical network provides the neurophysiological wiring framework for functional connectivity (FC), which is essential for higher-order brain functions. While several studies have explored the scale-specific FC, the scale-free (i.e., multifractal) aspect of brain connectivity remains largely neglected. Here we examined the brain reorganization during a visual pattern recognition paradigm, using bivariate focus-based multifractal (BFMF) analysis. For this study, 58 young, healthy volunteers were recruited. Before the task, 3-3 min of resting EEG was recorded in eyes-closed (EC) and eyes-open (EO) states, respectively. The subsequent part of the measurement protocol consisted of 30 visual pattern recognition trials of 3 difficulty levels graded as Easy, Medium, and Hard. Multifractal FC was estimated with BFMF analysis of preprocessed EEG signals yielding two generalized Hurst exponent-based multifractal connectivity endpoint parameters, $H(2)$ and ΔH_{15}; with the former indicating the long-term cross-correlation between two brain regions, while the latter captures the degree of multifractality of their functional coupling. Accordingly, $H(2)$ and ΔH_{15} networks were constructed for every participant and state, and they were characterized by their weighted local and global node degrees. Then, we investigated the between- and within-state variability of multifractal FC, as well as the relationship between global node degree and task performance captured in average success rate and reaction time. Multifractal FC increased when visual pattern recognition was administered with no differences regarding difficulty level. The observed regional heterogeneity was greater for ΔH_{15} networks compared to $H(2)$ networks. These results show that reorganization of scale-free coupled dynamics takes place during visual pattern recognition independent of difficulty level. Additionally, the observed regional

variability illustrates that multifractal FC is region-specific both during rest and task. Our findings indicate that investigating multifractal FC under various conditions – such as mental workload in healthy and potentially in diseased populations – is a promising direction for future research.

Keywords: multifractal, functional connectivity, brain networks, electroencephalography, visual pattern recognition

INTRODUCTION

The human brain is a complex system encompassing spatially distinct neuronal populations interconnected via an intricate axonal grid. Functional brain networks emerge within this anatomical circuitry, which provides the neurophysiological basis for higher-order brain functions (Van Hoesen, 1993). For instance, visual pattern recognition requires coordinated interactions among disparate brain regions such as the visual cortex, where primary processing, and the association areas in the parietal and frontal cortices, where high-level cognitive evaluation takes place (Van Hoesen, 1993; Kandel et al., 2012). Based on the hypothesis that regions that exhibit statistically similar dynamics are functionally coupled, functional neuroimaging methods allowed the reconstruction of functional connectivity (FC) in the brain under cognitive (Friston et al., 1993) and motor (Biswal et al., 1995) tasks. A paradigm shift regarding resting-state studies occurred after discovering that even in the absence of external stimuli the brain is organized in resting-state networks (RSNs) (Raichle et al., 2001). This resting-state neural architecture is altered during task through a series of activations and deactivations of brain regions (Fox et al., 2005). Accordingly, we believe that studying the brain under mental workload could reveal valuable information.

Due to its high spatial resolution, functional magnetic resonance imaging (fMRI) has been commonly favored as the gold standard imaging technique for detecting task-related changes of FC (Fox et al., 2005; Krienen et al., 2014; Di et al., 2015; Elton and Gao, 2015; Kaufmann et al., 2017). Nevertheless, the low sampling frequency and the physical constraints of the fMRI systems present themselves as limitations when more elaborate experimental paradigms are designed. Albeit at the cost of a lower anatomical resolution, these limitations can be overcome using electroencephalography (EEG) owing to its high sampling rate and easy-to-use instrumentation. This led to numerous task-related EEG studies, ranging from traditional tasks like n-back (Hou et al., 2018; Kaposzta et al., 2021) and face perception (Yang et al., 2015) to more complex designs like urban navigation (Skroumpelou et al., 2015). By using a visual pattern recognition paradigm, Racz et al. demonstrated an increase in scale-specific FC during task (Racz et al., 2017); though, in that study the scale-free aspect of the connections was not taken into consideration.

Various statistical approaches have been applied and/or developed for characterizing the linear and nonlinear aspects of the coupled neural activities (Bastos and Schoffelen, 2016). A common limitation of these methods is that they capture interdependence on a single scale, despite the fact that the scale-free (or fractal) nature of the connections has already been demonstrated in various modalities such as EEG (Wang and Zhao, 2012; Stylianou et al., 2021), fMRI (Ciuciu et al., 2014) and magnetoencephalography (Achard et al., 2008). The univariate scale-free behavior of neural dynamics has already been shown both regionally (Popivanov et al., 2006) and globally (Stam and de Bruin, 2004). While estimating FC at a given time scale reflect the coupling between oscillatory (narrowband) components at specific cross-spectrum frequencies, our current approach assumes a significant scale-free (broadband) component of the cross-spectrum; a signature of statistical dependency spanning a broad range of frequencies (scales). Moreover, the true multifractal nature of coupled dynamics was recently validated in resting-state EEG (Stylianou et al., 2021). Scale-free FC estimators allow for capturing how the long-term memory and multifractality of the coupled dynamics are spatially distributed across brain networks; topological aspects that otherwise would remain obscured. Visual pattern recognition requires sustained interaction between brain regions involved in the processing of the visual information, which can be captured as increased cross-correlations (long-term memory) in the functional connections. Furthermore, cognitive stimulation implies a shift in FC that is typically governed by complex nonlinear dynamics (Rabinovich and Muezzinoglu, 2010; Werner, 2010), which might alter the multifractal profile of FC. To the best of our knowledge, this is the first study investigating the task-related network reorganization using multifractal connectivity analysis.

In the current study, we examined the task-related reorganization of FC by applying a bivariate, focus-based adaptation of multifractal analysis on EEG records. The task of choice was a complex pattern recognition paradigm, which has previously shown its utility in increasing FC in the prefrontal cortex (Racz et al., 2017). Our primary objectives were: (i) to test the hypothesis that shifts in scale-free coupled dynamics would occur during the transition from rest to task; and (ii) to examine the localization of multifractal FC within each mental state. Our secondary aim was to assess the relationship between cognitive performance and brain network measures reconstructed from scale-free FC estimators.

MATERIALS AND METHODS

Participants

Fifty-eight young, healthy volunteers (24.2 ± 3.4 years of age, 28 females, 9 left-handed) with no history of psychiatric/neurological illness were recruited for the study. Participants were instructed to have a good night's sleep before the day of the experiment. All subjects provided written informed consent prior to the measurement. The study was designed and carried out in accordance with the Declaration of Helsinki and

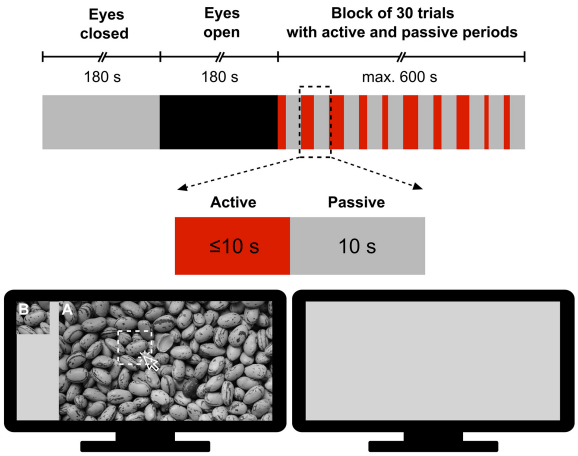

FIGURE 1 | Measurement protocol for obtaining electroencephalography records during resting states and subsequent visual pattern recognition. First, resting-state recordings were made in 180 s periods with eyes closed and eyes open, respectively. Then, the subject performed a pattern recognition task in a block of 30 trials, each consisting of a 10 s or less of active period and a 10 s passive period. In the active period, participants were presented a large-size image **(A)** and its cropped sub-region **(B)** and were required to click on **(A)** at the position of **(B)** if found *(The picture of* **Figure 1** *was taken from https://alphacoders.com/users/profile/97828)*.

was approved by the Regional and Institutional Committee of Science and Research Ethics of Semmelweis University (approval number: 2020/6).

Measurement Protocol

All measurements took place in the Department of Physiology at Semmelweis University in a quiet room under subdued ambient illumination. During the measurement, participants were seated comfortably in a chair in front of a computer monitor at an approximate distance of 0.8 m from the screen and were instructed to refrain from moving and facial expressions as much as possible. The measurement protocol was designed and implemented in MATLAB (version 2012, Mathworks, Natick, MA, United States) according to a pattern recognition paradigm modified after Racz et al. (2017). The session started with a 3-min eyes-closed (EC) period serving as a baseline, followed by a 3-min eyes-open (EO) resting-state period, as a control for the task state. Then, participants were engaged in a visual pattern recognition paradigm consisting of a block of 30 trials with active and passive periods (**Figure 1**). Specifically, in the active period of a trial, the subject was allowed a maximum of 10 s to identify a sub-region of a grayscale image by clicking on its assumed location; at that point, the active period was terminated. The active period was immediately followed by a passive (task-free) period, during which a gray background was displayed for 10 s. In this stimulation paradigm, a pool of 6 different grayscale images was permutated. Each of them was shown 5 times in total – with a different sub-region to be identified in each case – thus yielding a total of $6 \times 5 = 30$ trials. To investigate the impact of difficulty level, images were sorted into Easy, Medium and Hard categories with 2 images in each. Their classification was based on their complexity, defined as the file size ratio of compressed/uncompressed images [cf. Equation 1 in Yu and Winkler (2013)]. The order of the 30 trials was randomized with a different permutation sequence for each participant. The following metrics characterized the performance during pattern recognition: (i) reaction time, defined as the time between the beginning of the image presentation and response (left mouse click on the image) and (ii) success, defined as 1 if the participant correctly identified the sub-region's location and 0 otherwise. When the subject did not respond, the trial was considered a failure (success = 0) and the reaction time was set to 10 s.

Data Acquisition

EEG signals were recorded by a wireless Emotive Epoc+ device and its corresponding EmotivPRO software (Emotiv Systems Inc., San Francisco, CA, United States). After ensuring low electrical impedance (<20 kΩ), EEG signals from 14 brain regions (10–20 standard montage locations: AF3, AF4, F3, F4, F7, F8, FC5, FC6, T7, T8, P7, P8, O1, and O2) were recorded, at a 128 Hz sampling rate[1]. CMS and DRL electrodes at left and right mastoid processes were used as reference.

Preprocessing

The EEG device applied built-in band-pass (0.2–45 Hz, digital 5th order Sinc) and notch (50 and 60 Hz) filters to the raw data. To maximize the artifact-detection capacity of independent component analysis (ICA), first we performed wavelet-enhanced ICA (wICA) (Rong-Yi and Zhong, 2005; Gabard-Durnam et al., 2018). The purpose of wICA was to exclude wavelet components with coefficients higher than a certain threshold, resulting in the removal of high amplitude spikes. Subsequently, we manually excluded non-brain components, as ICA isolated them. wICA was performed in an automated manner, while the EEGLAB toolbox (Delorme and Makeig, 2004) was used for manual ICA.

Estimation of Multifractal Functional Connectivity

The scale-free coupled dynamics were estimated with bivariate focus-based multifractal analysis (BFMF), introduced by Mukli and colleagues (Mukli et al., 2018). The applicability of BFMF for multifractal FC estimation was demonstrated previously (Stylianou et al., 2021). Here we only provide a summary of the method, while further details are found in the references mentioned above. The scaling function S_{XY} (**Figure 2**) of two EEG time series (X and Y) of length L datapoints can be calculated as:

$$S_{XY}(q,s) = \left(\frac{1}{N_s} \sum_{v=1}^{N_s} |cov_{XY}(v,s)|^q \right)^{1/q}, \quad (1)$$

where N_s denotes the number of bridge-detrended, non-overlapping windows of size s ($s = 2^n$ with n being integers ranging from 2 to 8) indexed by v. The statistical moment order

[1] 18 recordings were carried out at 256 Hz sampling rate which were downsampled to 128 Hz prior to further preprocessing.

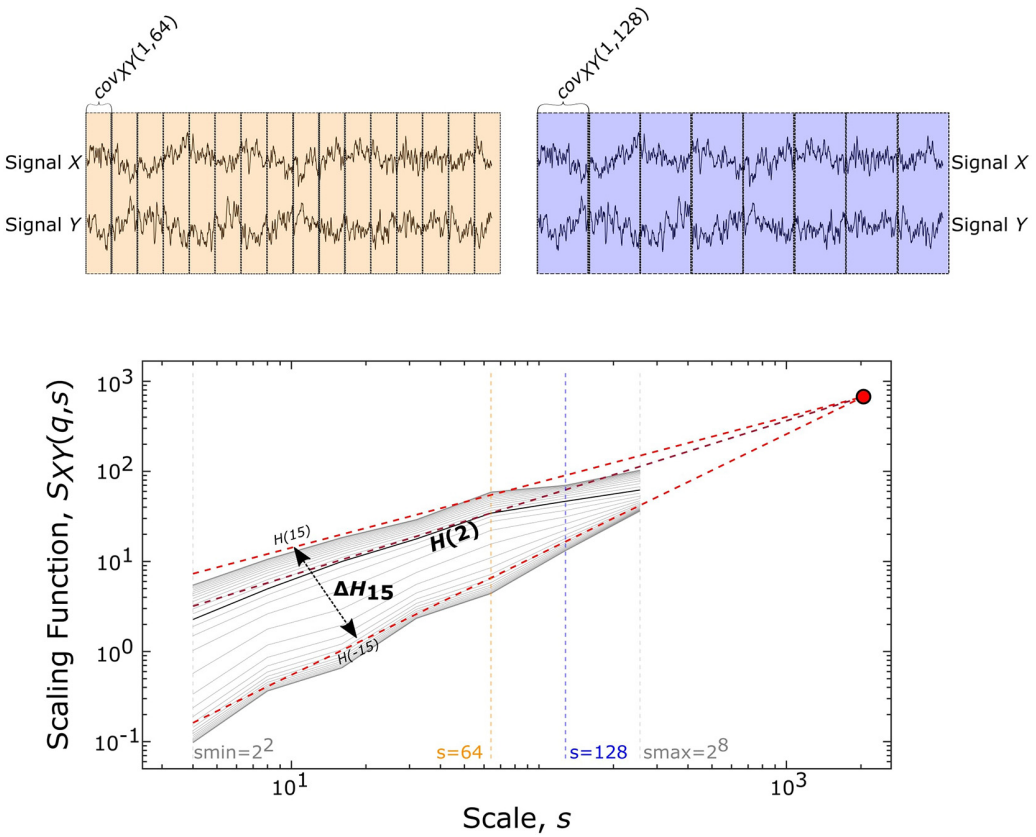

FIGURE 2 | Multifractal time series analysis and its endpoint parameters. On the upper panels, a representative pair of 2048 datapoint-long EEG segments (from Subject01) is displayed along with the windowing scheme for a smaller (s = 64, shown in yellow) and larger (s = 128, shown in purple) scale, which illustrates the calculation of covariance scaling function [$S_{XY}(q,s)$ displayed in the lower panel] according to Eq. 1. The *Focus* (red disk) is used as a reference point when simultaneously fitting linear models in the log-log transform of the $S_{XY}(q,s)$ vs s, the essential step of BFMF. The slope of each linear regression line represents the generalized Hurst exponent [$H(q)$] (shown for q = −15, +2, +15). $H(2)$ describes the long-term cross-correlation between the signals X and Y, while the degree of multifractality (ΔH_{15}) is captured in the difference between $H(q)$ values at the extreme [i.e., minimal (–15) and maximal (15)] statistical moments.

(q) ranges from −15 to 15 with increments of 1 and the window-wise covariance between simultaneous s-size segments of X and Y is denoted by $cov_{XY}(v, s)$. When q = 0, the scaling function takes the form:

$$S_{XY}(0, s) = e^{\left[\frac{1}{2N_s}\sum_{v=1}^{N_s}\ln\left(\left|cov_{XY}(v,s)\right|\right)\right]} \quad (2)$$

In the special case when the whole segment is used for obtaining the scaling function [$S_{XY}(q,L)$], the sum in Eq. 1 becomes independent of q and thus, the scaling function values of all moments converge to a so-called *Focus*. This *Focus* serves as a reference point when regressing for the log[$S_{XY}(q,s)$] vs log[s] relationship for every q simultaneously. In contrast with the standard approach where separate q-wise assessments of the power-law relationship are applied, fitting all statistical moments simultaneously results in a more robust analysis (Mukli et al., 2015). This is achieved by enforcing the monotonous decay of regression slopes, which represent the generalized, q-dependent bivariate Hurst-exponent function $H(q)$. The special case of $H(2)$ depicts the global long-term cross-correlation in the coupled dynamics underlying the functional connection. If this bivariate $H(2)$ is greater than 0.5, then there is functional coupling exhibiting long-term memory. $H(2)$ = 0.5 indicates uncorrelated, uncoupled dynamics, while $H(2)$ < 0.5 demonstrates anticorrelated coupling (Eke et al., 2002; Kristoufek, 2014). ΔH_{15}, calculated as $H(-15)$-$H(15)$, captures the degree of multifractality, an indicator of the q-wise dependence of the scaling function on large and small covariances. The whole segment of each trial (active section + 10 s of passive period) was analyzed with BFMF. As for the resting-state conditions, 9 non-overlapping segments of 20 s for each of the EC and EO states were analyzed. To remove the effect of different time lengths due to various response times, we also performed analyses adjusted to the length of time series (see **Supplementary Material**).

Assessing Multifractality

A series of statistical tests evaluated the true scale-free nature of the connections. In short, the purpose of these tests was to: (i) validate the power-law relationship of the connection both in the frequency and time domains (spectral slope and detrended cross-correlation coefficient tests, respectively),

(ii) distinguish true from spurious multifractality (phase randomization and shuffling tests), and (iii) determine if the emerging coupling between the two processes is genuine or only reflects a mere autocorrelation within each EEG signal (bivariate-univariate Hurst comparison). This series of tests reveal the qualitative nature of bivariate multifractality, which is assessed independently from its quantitative changes in this study. The complete account of the testing procedure followed in this study was reported elsewhere (Stylianou et al., 2021). We expanded the test yielding a distinction between extrinsic and intrinsic multifractality referred to as bivariate-univariate Hurst comparison. In our previous paper, only the inequality between the bivariate Hurst exponent and the mean of the univariate Hurst exponents comprising the connection was tested (Stylianou et al., 2021). In the present study, we considered a bivariate-univariate Hurst comparison test successful only when the bivariate $H(2)$ was lower than the mean of its univariate $H(2)$. This choice was made based on the fact that bivariate $H(2)$ can exceed the mean of univariate $H(2)$ only due to the finite length or non-normal distribution of the time series (Kristoufek, 2015a, 2016).

Brain Network Construction

We then proceeded with reconstructing functional networks and analyzing their architecture. For each subject, we isolated 48 different EEG segments (9 EC, 9 EO, 10 Easy, 10 Medium and 10 Hard). For each connection, the $H(2)$ and ΔH_{15} values obtained in the 5 different states were averaged, resulting in 5 different values per subject. Altogether, 5-5 (i.e., fully connected) networks (EC, EO, Easy, Medium, Hard) were reconstructed for every subject, based on either their $H(2)$ or ΔH_{15} values. In these analyses, we used untresholded networks as we did in our previous studies of EEG-based functional connectivity (Racz et al., 2018, 2019, 2020; Kaposzta et al., 2021). We characterized network topology via the local (D) and global ($\overline{D}$) weighted node degrees from the $H(2)$ and ΔH_{15} values of each connection, since earlier we found that in small networks, clustering coefficient and efficiency were highly correlated with node degree (Kaposzta et al., 2021). D represents the total connection strength of a node, while $\overline{D}$ (the average of all D) is an indicator of the network's interconnectivity[2]. The calculations of D and $\overline{D}$ were carried out using functions of the Brain Connectivity Toolbox (Rubinov and Sporns, 2010).

Statistical Evaluation

We evaluated between-states (e.g., Hard vs EC) and within-states (e.g., O1 vs O2 in EO) differences for both $H(2)$ and ΔH_{15} networks. To rule out that the observed differences could be attributed to opening of the eyes, we included both resting-state periods in the statistical evaluation. Therefore, the between-states comparisons consisted of global $\overline{D}$ and local D comparisons of the 5 different states (EC, EO, Easy, Medium, Hard). Since the normality assumption (Lilliefors test) was not satisfied for all distributions, we used the non-parametric Friedman test. Subsequently, paired comparisons were used to identify specific pairwise differences. If any of the two populations under investigation were non-normally distributed, Wilcoxon signed-rank test was carried out. If both distributions were normal, a paired sample t-test was used. Benjamini-Hochberg (BH) correction (with $\alpha = 0.05$) (Benjamini and Hochberg, 1995) was used to adjust for multiple testing. Then, we investigated the regional differences within every state's local D (i.e., 91 comparisons for each of the 5 states). The same statistical tests as in the between-states comparisons were utilized. Moreover, we estimated Kendall's coefficient of concordance (W) of D for both $H(2)$ and ΔH_{15} networks for each state.

We also contrasted the average success rate (SR) and average reaction time (RT) between the 3 difficulty levels, applying the same statistical pipeline as described above. Then we investigated the plausible relationships between performance metrics and network architecture since scale-free FC and behavioral variables have already been shown to correlate (Ciuciu et al., 2014). In that, we examined the effect of FC on task performance by calculating the Spearman's rank correlation (r) between SR-$\overline{D}$ and RT-$\overline{D}$ for each difficulty level. Every step of our analytical pipeline was implemented in MATLAB (version 2012, Mathworks, Natick, MA, United States).

RESULTS

Qualitative Assessment of Bivariate Multifractal Character

Table 1 summarizes the percentage of connections passing each multifractal test. The 5 different states showed similar success rates in the spectral slope, phase randomization and ΔH_{15} part of shuffling tests (the latter comparing the original ΔH_{15} with that of shuffled surrogates). On the other hand, the rest states exhibited higher success rates in the bivariate-univariate Hurst comparison test and passed the detrended cross-correlation coefficient tests more frequently. Finally, comparing the original $H(2)$ with that of shuffled surrogates had a higher success rate in the task states. As a result, more connections showed scale-free characteristics in the rest states (**Table 2**).

TABLE 1 | Success rate of multifractality tests at the subject level (mean ± standard deviation).

	Tests					
	PL	**PR**	**SΔH_{15}**	**S-$H(2)$**	**DCCC**	**Biv-Univ**
EC	92 ± 7%	96 ± 4%	99 ± 2%	70 ± 18%	93 ± 4%	85 ± 18%
EO	94 ± 3%	96 ± 6%	98 ± 4%	76 ± 16%	93 ± 4%	86 ± 15%
Easy	93 ± 2%	97 ± 4%	99 ± 2%	90 ± 8%	64 ± 19%	65 ± 17%
Medium	94 ± 2%	97 ± 4%	99 ± 2%	90 ± 9%	65 ± 16%	68 ± 18%
Hard	94 ± 2%	97 ± 3%	99 ± 2%	89 ± 9%	62 ± 17%	73 ± 16%

PL, power-law test; PR, phase randomization test; S-ΔH_{15}, ΔH_{15} part of the shuffling test; S-H(2), H(2) part of the shuffling test; DCCC, detrended cross-correlation coefficient test; Biv-Univ, bivariate-univariate Hurst comparison.

[2] D $\sum_{i=1}^{n} c_i$ where n represents all possible edges of a node, while c_i is the strength [either $H(2)$ or ΔH_{15}] of the ith connection. $\overline{D} = \frac{\sum_{j=1}^{N} D_j}{N}$ where N represents all nodes of the network, while ${D_j}^W$ is the weighted degree of the jth node.

TABLE 2 | Percentage of connections, at the subject level (mean ± standard deviation), that passed all multifractality assessment tests.

	State				
	EC	**EO**	**Easy**	**Medium**	**Hard**
***H*(2)**	48 ± 13%	55 ± 12%	31 ± 10%	34 ± 10%	35 ± 9%
ΔH_{15}	46 ± 13%	53 ± 12%	30 ± 10 %	33 ± 10%	34 ± 9%

Effect of Brain State on Multifractal Connectivity

The Friedman tests indicated a significant effect of state ($p < 0.01$), and post hoc pairwise comparisons revealed that the rest states (EC, EO) were characterized by lower $\overline{D}$ compared to the task states (Easy, Medium, Hard) (**Figures 3**, **4**). Additionally, we found higher $\overline{D}$ during EO compared to EC, for both $H(2)$ and ΔH_{15} networks. A similar motif emerged in the local level comparisons, with the D of several nodes being significantly different between the rest and task states, as well as between EC and EO for both networks (**Figure 5**).

As seen in **Figure 3**, the $H(2)$ networks had higher FC in the frontal regions, while higher values of ΔH_{15} were observed in the occipital cortex. This regional variability was statistically validated by the within-state comparisons, which showed significant differences within all 5 tasks, for both $H(2)$ and ΔH_{15} networks. We also observed that if the D of two nodes in the ΔH_{15} network were statistically different, there was a high chance of the equivalent nodes being statistically different in the $H(2)$ network as well, while the opposite did not occur. This can be easily visualized by the abundance of blue [both $H(2)$ and ΔH_{15} significant] and orange (only ΔH_{15} significant), in contrast to the sparse red [only $H(2)$ significant] boxes in **Figure 6**. Moreover, small subject concordance appeared only in the ΔH_{15} networks; on the contrary, no subject agreement was found in the $H(2)$ networks (**Table 3**).

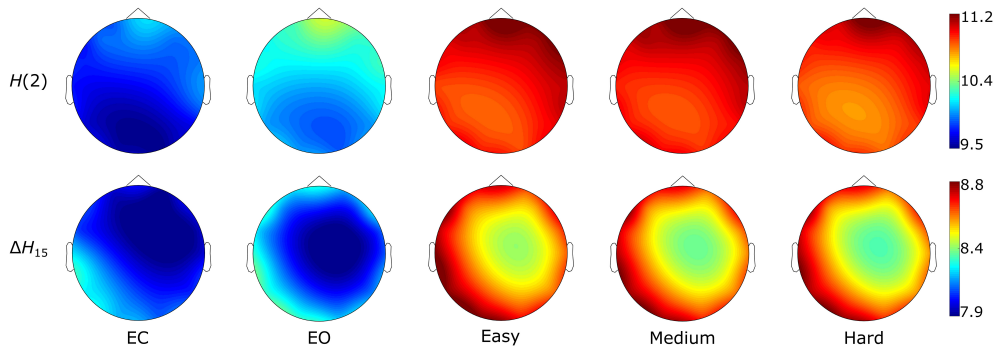

FIGURE 3 | State-dependent weighted node degree topology of $H(2)$ and ΔH_{15} brain networks. The color bars represent the values of the local node degrees.

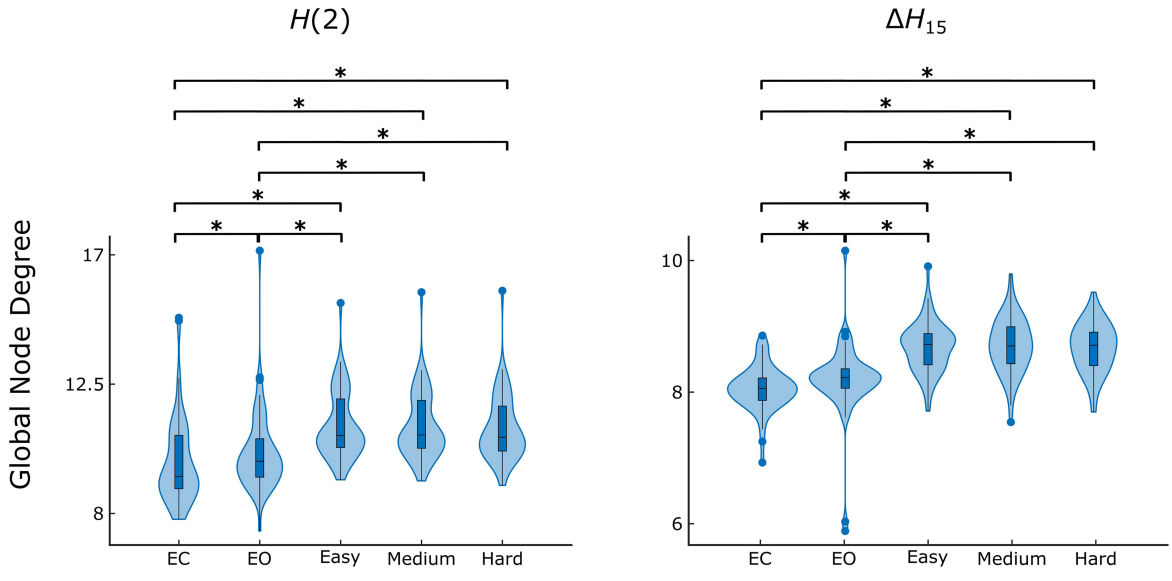

FIGURE 4 | State-dependent weighted global node degree distribution of $H(2)$ and ΔH_{15} brain networks. Significance marked by asterisk (*). Figure was created using Gramm (Morel, 2018).

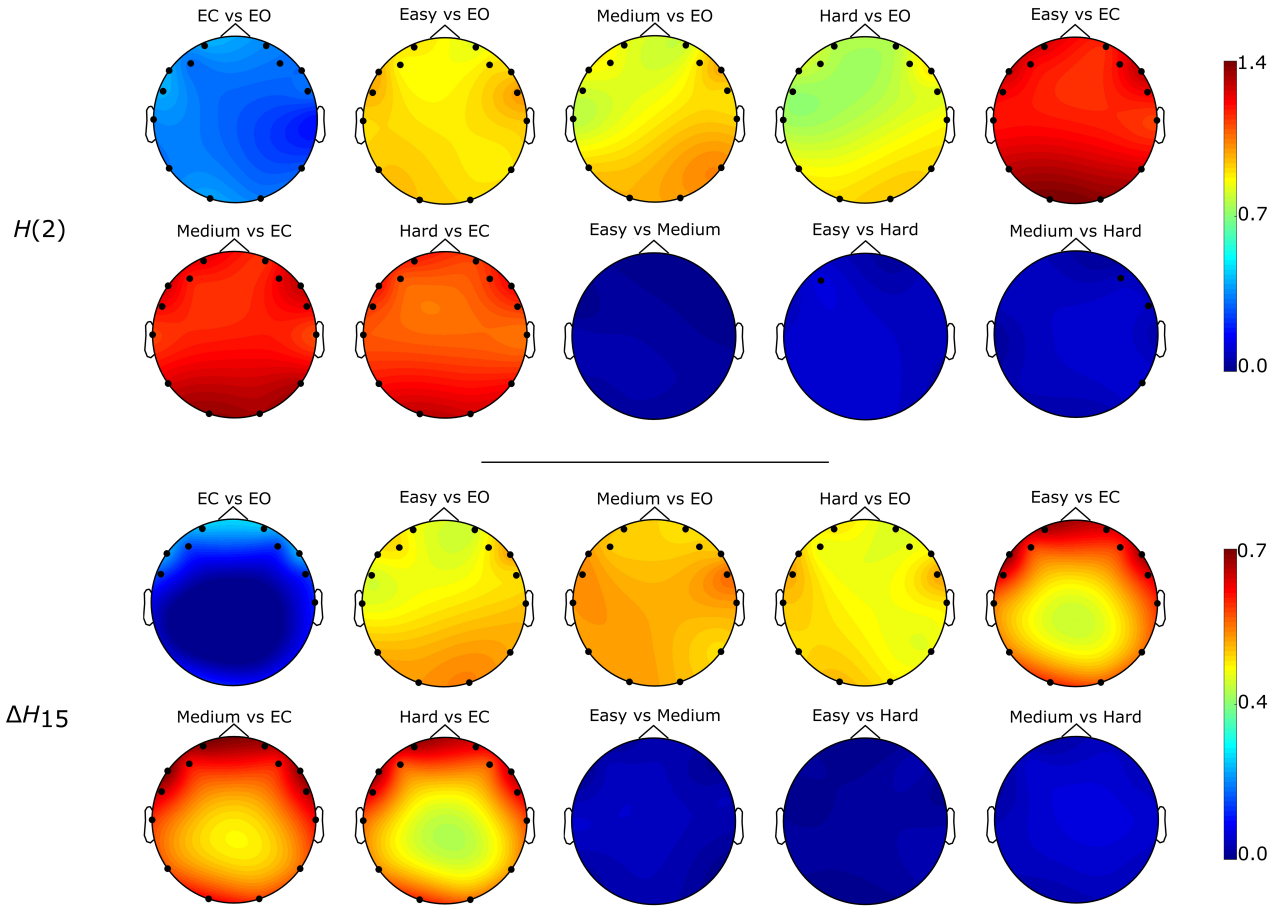

FIGURE 5 | Localization of significantly different weighted node degrees for every between state comparison of the $H(2)$ and ΔH_{15} brain networks. The colormap is based on the absolute difference of the node degrees of the states under investigation (e.g., $|D_{O2,EC} - D_{O2,EO}|$). Only the significantly different nodes are shown.

Cognitive Performance and Its Correlates With Functional Connectivity

The comparison of difficulty levels indicated a significant decrease of SR in the Hard state. RT was also statistically different between the 3 difficulty levels, with Easy having the fastest response and Hard having the slowest (**Figure 7**). Furthermore, significant ($p < 0.05$) positive correlations were found between RT and $\overline{D}$ of the ΔH_{15} networks during Easy and Hard (**Figure 8**). After BH correction, these correlations were rendered not significant.

DISCUSSION

This study investigated the scale-free coupled dynamics of brain activity in resting state and during a visual pattern recognition task of various difficulty levels. We employed two FC estimators derived from bivariate focused-based multifractal analysis, namely $H(2)$ and ΔH_{15}. They were used for constructing brain networks based on their multifractal connectivity for both rest and task conditions. Our findings show that: (i) the local and global functional connectivity measures increased during task when compared to resting conditions, indicating a reorganization of brain networks, and (ii) there was a substantial regional variability within the 5 different states. However, significant correlations were found only between the global node degree and average reaction time during Easy and Hard tasks in the ΔH_{15}-networks.

After acquiring the BFMF measures, $H(2)$ and ΔH_{15}, it was essential to perform an array of multifractality assessment tests since by default not all functional connections – or in general, not all dynamic processes – can be assumed to have multifractal character. Our tests showed that a considerable fraction of the connections had true multifractal characteristics (**Table 1**). Similar success rates have been found in the resting state previously (Stylianou et al., 2021). Despite the different channel density of the EEG devices and the different sampling populations, similar results were obtained in these studies, concluding that coupled dynamics between cortical regions are indeed multifractal during rest. The extent of multifractality decreased during task, as indicated by the lower number of connections passing our multifractality assessment tests (**Table 2**). To the best of our knowledge, this is the first study demonstrating the true multifractal nature of coupled dynamics

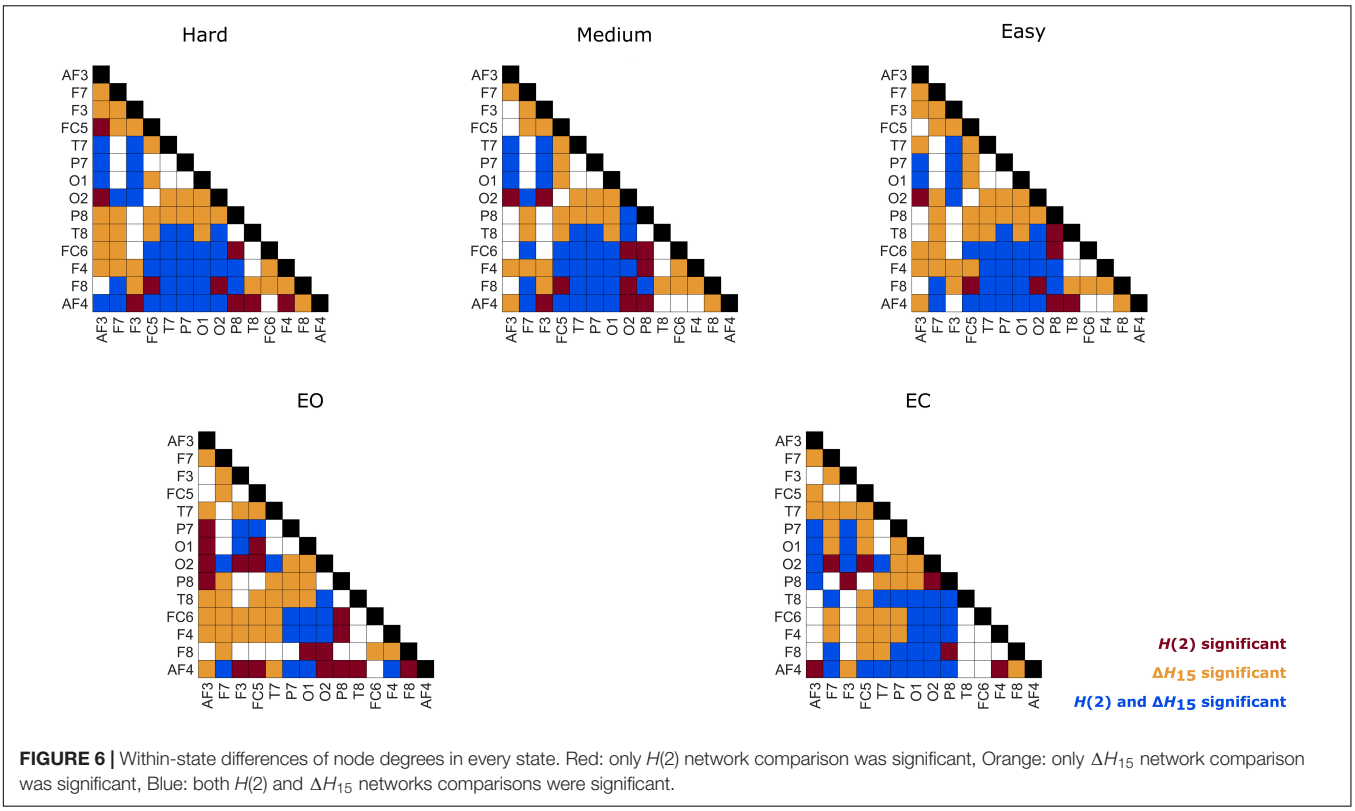

FIGURE 6 | Within-state differences of node degrees in every state. Red: only $H(2)$ network comparison was significant, Orange: only ΔH_{15} network comparison was significant, Blue: both $H(2)$ and ΔH_{15} networks comparisons were significant.

TABLE 3 | State-dependent subject concordance, as captured by Kendall's W.

	State				
	EC	**EO**	**Easy**	**Medium**	**Hard**
$H(2)$	0.10	0.09	0.09	0.12	0.11
ΔH_{15}	0.24	0.15	0.25	0.24	0.26

during complex mental tasks. This provides an opportunity to reveal novel aspects of rest and task states using BFMF by obtaining information that would have remained hidden otherwise [for a demonstration, see the **Supplementary Material** in Stylianou et al. (2021)].

The higher node degree in the fully connected (i.e., unthresholded) $H(2)$ and ΔH_{15} networks during task corresponds to increased $H(2)$ and ΔH_{15} values of the connections. The high values of $H(2)$ indicate a relative shift of the coupled dynamics toward lower frequency components. This greater long-term memory reflects a stronger coupling between the probed regions of the brain cortex. Conversely, Ciuciu and colleagues found a shift of scale-free coupled fluctuations in fMRI-BOLD signals toward the higher frequencies (i.e., decreasing Hurst-exponent), accompanied by a decrease in connectivity between resting-state networks during a motor task (Ciuciu et al., 2014). While the signs of changes were opposite, both studies showed a positive association between $H(2)$ and FC change during task. This difference could possibly be attributed to the differences in imaging modality and stimulation paradigm, which should be further investigated in future studies. Moreover, based on the elevated ΔH_{15} values of the connections, we can conclude that the coupling between recorded EEG signals transitioned into a state with increased multifractal strength suggesting increased nonlinearity (Ashkenazy et al., 2003). Multifractal dynamics are characterized by increased dependency between different time scales. As time scale relates to frequency, one such model is formulated by assuming a relationship between the phase of lower frequencies and the amplitude of higher frequencies (He et al., 2010). In that, a stronger phase-amplitude coupling is associated with higher nonlinearity as captured by increased ΔH_{15} (Ashkenazy et al., 2003). Taken together, BFMF reveals that task induces a redistribution of the long-term cross-correlation in coupled dynamics as indicated by higher Hurst exponent and renders them more interdependent across different time scales as manifested by increased ΔH_{15}. The more pronounced multifractal character of the connections can possibly be attributed to the recruitment of excitatory/inhibitory feedback loops (Poil et al., 2012) during task, whose transient is typically characterized by nonlinear dynamics (Rabinovich and Muezzinoglu, 2010). The elevated coupling [increased $H(2)$] and feedback loops (increased ΔH_{15}) that take place in this visual pattern recognition paradigm can be ascribed to the enhanced cooperation of distant brain areas involved in various aspects of visual processing, such as recalling short-term memory and making visual comparisons.

Both $H(2)$ and ΔH_{15} networks showed a significantly increased connectivity in task states compared to EO and EC, captured in their global and local weighted node degrees

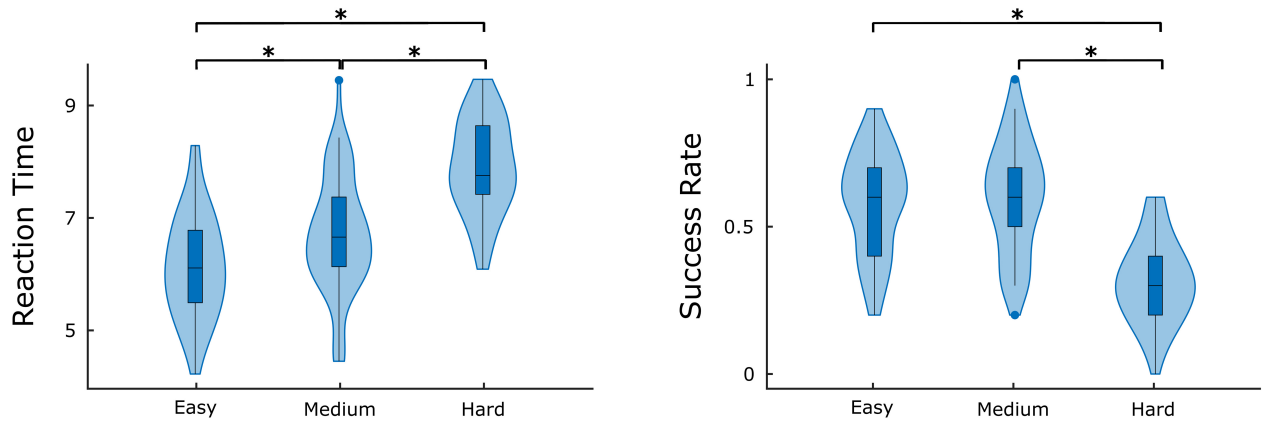

FIGURE 7 | Average success rate and reaction time for different difficulty levels. Significant differences are marked by asterisk (*). Figure was created using Gramm (Morel, 2018).

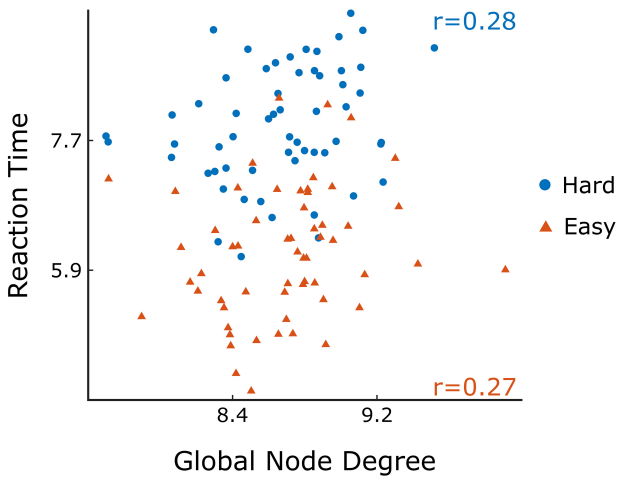

FIGURE 8 | Scatter plots of the reaction time vs global node degree for Easy (orange) and Hard (blue) task in ΔH_{15} networks and their Spearman's correlation (r). Figure was created using Gramm (Morel, 2018).

(**Figures 3–5**). Our results agree with the findings of a previous functional near-infrared spectroscopy study using a very similar cognitive paradigm. Racz et al. found global weighted node degree increased in the prefrontal cortex during task (Racz et al., 2017), using the scale-specific Pearson's correlation as FC estimator. Based on these two studies, it appears that both the scale-free and scale-specific connectivity of the brain increases during visual pattern recognition. This indicates that a significant reorganization of functional brain networks takes place in response to increased mental workload. Nevertheless, definite conclusions cannot be drawn due to the different modalities (EEG vs functional near-infrared spectroscopy). It is also noteworthy that FC increased during the transition from EC to EO. Since considerable brain capacity is devoted to visual processing, opening the eyes should substantially increase brain network activity. Thus, the observed higher node degrees during EO are consistent with the manifestation of increased mental workload. It should be recalled that a shift to higher frequencies characterizes cortical desynchronization during EO, contrasting with the earlier interpretation of increased $H(2)$ (i.e., shift to lower frequencies). We speculate that scale-free and oscillatory components of coupled electrophysiological activity have different origins and could be affected by the opening of the eyes differently. Previously, we have demonstrated that the global multifractal dynamics of FC are affected by the EC-EO transition (Racz et al., 2018), our present study extends these findings by revealing the local alterations in scale-free coupled dynamics (**Figure 5**). Still, the mental workload of EO was not as substantial as that of the pattern recognition task, since the node degrees of the EO networks differed significantly from those of the task states. On the other hand, the 3 task states (Easy, Medium and Hard) had statistically similar node degrees (**Figures 3–5**), even though the cognitive stimulation paradigm showed a lower success rate for more complex images (**Figure 7**). Similar results were found in an n-back EEG study (Kaposzta et al., 2021), in which there was no significant difference in the density, clustering coefficient and efficiency of the 2-back and 3-back brain networks. In this n-back study, the network measures decreased during task, which is in contrast with the current findings of increased FC. This apparent controversy in FC alterations between tasks has already been noticed, with n-back being the most different from the rest of the studied task conditions (Krienen et al., 2014). The use of different FC estimators could have impacted the reported results as well. Moreover, for both BFMF measures, the within-state comparisons showed apparent regional variability (**Figure 6**), similarly to our previous results (Stylianou et al., 2021). In that, we saw that the degree of multifractality (ΔH_{15}) varied more than the long-term cross-correlation [$H(2)$] across the brain, in all states. Additionally, significant differences in the long-term cross-correlation were accompanied by changes in the degree of multifractality, in most cases. A possible explanation could be that multifractality results from more complex dynamics

(Tel, 1988) which tend to vary more from region to region. On the other hand, this contradicts the findings of our previous resting-state study, where $H(2)$ values varied the most [cf. Table 2 in Stylianou et al. (2021)]. The different electrode densities of the EEG system used in these two studies (62 vs 14 channels) could well account for the observed differences. Nonetheless, these two studies indicate that scale-free coupled dynamics do not emerge homogenously in the brain, neither in rest nor in task states, which is a motivation for further studying the multifractal properties of FC at higher spatial resolution. Furthermore, small subject concordance within the different states was observed only for the ΔH_{15} network (**Table 3**). This agrees with a previous study (Mueller et al., 2013), which found inter-subject FC variation localized mainly in the high-order association cortices in the frontal and parietal lobes, i.e., regions strongly overlapping with those we recorded EEG from.

As to the performance metrics, the Easy state was associated with faster RT than the Medium and Hard states, while significant differences in the SR were observed only between Easy-Hard and Medium-Hard (**Figure 7**). Even though no significant differences in the SR were observed between Easy-Medium, the RT during the Medium task was longer. We believe that a significant difference in the SR between Easy-Medium could be found by including a larger or more diverse population sample in future studies. Furthermore, no significant associations were found between the global node degrees and performance metrics (SR and RT), with the exception of positive correlations between RT and $\overline{D}$ in the Easy and Hard states of the ΔH_{15} networks. Similarly, in another EEG n-back study, network measures were found significantly correlated only with RT, and not with SR (Dai et al., 2017). This suggests that lower multifractality corresponds to faster pattern recognition, while the subject's SR remains independent of scale-free coupled dynamics. These correlations did not remain significant after BH correction, suggesting that a larger, more representative sample of the population could potentially reveal significant correlations even after BH correction.

Our results derived from the main analytical pipeline are supported by further analysis accounting for the slightly different length of analyzed signals from the task states (**Supplementary Material**). Because the multifractal profile of a time series is influenced by its length (Grech and Pamuła, 2012; Rak and Grech, 2018), we anticipated a similar effect on our bivariate multifractal analysis (Kristoufek, 2015b); thus, we re-analyzed our dataset in a pipeline adjusted to the different lengths of analyzed pair of time series based on the different response times. The results agree with our primary analysis, indicating that the slightly varying signal length had no effect on the observed patterns. We also compared the $\overline{D}$ of every state after excluding connections that did not pass our multifractality assessment tests. While significant differences were found between rest and task states, they were of the opposite direction, i.e., $\overline{D}$ decreased during task (**Supplementary Figure 1**), which can be explained by the larger number of connections that passed our tests during rest (**Table 2**). However, there was great inconsistency among the multifractality assessment tests for every connection and task (e.g., out of the 10 Hard segments, the connection AF4-AF3 might have passed the test in only 4 of them). In order to avoid any bias, our main analysis focused on unthresholded networks. Additionally, the thresholded analysis showed significant positive correlations between $\overline{D}$-RT in the Easy and Medium states for both $H(2)$ and ΔH_{15} networks, warranting further investigation in future studies (**Supplementary Figure 2**). While a growing number of publications investigates the FC-related differences between the two sexes (Zhang et al., 2018; Ýçer et al., 2020), we found no significant sex-related differences in network architecture. Since the studies mentioned above had higher spatial resolution (higher density EEG or fMRI recordings), we believe that future experiments with higher number of EEG channels might be able to reveal such differences. As to the effect of handedness, no significant differences in $\overline{D}$ were identified between the left- and right-handed participants in any state (EC, EO, Easy, Medium, Hard) or network [$H(2)$ and ΔH_{15}]. To assess the test-retest reliability, 5 of our subjects repeated the same experiment a few months later. No significant differences were found in the SR and RT between the two sessions, suggesting that our experimental paradigm can be used in further reproducibility studies. Finally, we found a moderate concordance between $H(2)$ and ΔH_{15} values for every subject (**Supplementary Table 1**), indicating a relatively constant multifractal character of the connections. Further details of these analyses can be found in the **Supplementary Material**.

Future developments based on this study should consider the following shortcomings. Despite its sample size, the subject cohort of our study might not have been representative of the general population, thus limiting us in drawing more general conclusions. All participants were young, healthy and educated, university students or graduates. Differences observed in the multifractal FC during task could be augmented or attenuated if a larger cohort of volunteers participated. The recorded EEG signals might be affected by scalp muscle contraction (especially at the frontal and temporal sites), as shown previously (Goncharova et al., 2003). Since the spectral characteristics of electromyographic signals considerably overlap with EEG, part of the results could be attributed to activity of motor units rather than changes in local field potentials in the brain cortex. Nonetheless, independent component analysis can remove a significant part of these electromyographic contaminations (Yilmaz et al., 2019). Additionally, task-related EEG changes are not greatly affected by muscle contractions (Boytsova et al., 2016). Because during diverse tasks different brain network architectures emerge (Krienen et al., 2014), the construction of more extensive cognitive stimuli with several different paradigms should be considered. Studies found that FC changed as subjects repeated and thus learned a task (Lewis et al., 2009; Bassett et al., 2011), which warrants that our future experiments investigate the effect of learning. Additionally, the bimodality phenomenon observed in univariate focus-based multifractal analysis (Nagy et al., 2017) can be extended to the multifractal covariance scaling function with multiple scaling ranges.

As to future perspectives, it will be interesting to see the discriminatory power of multifractal FC between rest and task states at the individual level, which was beyond the scope of this study. In future studies, we intend to investigate the rest-state classification performance of BFMF compared to other measures of brain network dynamics (Racz et al., 2020). To reveal mechanistic background of scale-free coupled dynamics, further clinical trials and animal models are needed using anesthetics, antipsychotics, antiparkinsonian and other medications (Nasrallah et al., 2017). On a final note, a promising field where such visual pattern recognition task could be advantageous is in attention deficit hyperactivity disorder (ADHD) research, where brain network alterations during spatial working memory tasks have already been revealed (Jang et al., 2020).

CONCLUSION

In the present study, we reconstructed brain networks from measures of scale-free coupled dynamics in resting states and during a visual pattern recognition task estimated by our novel bivariate multifractal analytical algorithm. Initially, we showed that our method could capture true multifractal coupled dynamics that varied across different brain regions. Additionally, we saw an increase in functional connectivity during the transition from rest (EC and EO) to task states, which was however, independent of task difficulty. We also found higher functional connectivity when the participants transitioned from EC to EO. These findings could well facilitate future research of scale-free functional connectivity studies with complex experimental designs in healthy and diseased populations.

DATA AVAILABILITY STATEMENT

The raw data supporting the conclusions of this article will be made available by the authors, without undue reservation.

ETHICS STATEMENT

The studies involving human participants were reviewed and approved by Regional and Institutional Committee of Science and Research 111 Ethics of Semmelweis University (approval number: 2020/6). The patients/participants provided their written informed consent to participate in this study.

AUTHOR CONTRIBUTIONS

OS implemented the analytical framework, contributed to experiment design, performed experiments, data analysis and interpretation, and wrote the first draft of the manuscript. FR performed experiments and contributed to experiment design, data analysis, and manuscript development. KK, ZK, and AC performed experiments and contributed to data analysis. AY contributed to manuscript development. AE provided conceptual guidance and supervision throughout the study. PM developed the code for BFMF, specified the concept and aims of the study and contributed to experiment design. All authors contributed to reviewing the manuscript and approved its final version.

FUNDING

FR and PM acknowledge financial support from the "Development of Scientific Workshops for Medical, Health Sciences and Pharmaceutical Training" Project (EFOP-3.6.3-VEKOP-16-2017-00009). AY and PM acknowledge financial support from the "the Cellular and Molecular GeroScience CoBRE (P20GM125528, sub#5337)".

SUPPLEMENTARY MATERIAL

The Supplementary Material for this article can be found online at: https://www.frontiersin.org/articles/10.3389/fnhum.2021.740225/full#supplementary-material

REFERENCES

Achard, S., Bassett, D. S., Meyer-lindenberg, A., and Bullmore, E. (2008). Fractal connectivity of long-memory networks. *Phys. Rev. E Stat. Nonlin. Soft Matter Phys.* 77(3 Pt 2):036104. doi: 10.1103/PhysRevE.77.036104

Ashkenazy, Y., Havlin, S., Ivanov, P. C., Peng, C.-K., Schulte-Frohlinde, V., and Stanley, H. E. (2003). Magnitude and sign scaling in power-law correlated time series. *Physica A* 323, 19–41. doi: 10.1016/S0378-4371(03)00008-6

Bassett, D. S., Wymbs, N. F., Porter, M. A., Mucha, P. J., Carlson, J. M., and Grafton, S. T. (2011). Dynamic reconfiguration of human brain networks during learning. *Proc. Natl. Acad. Sci. U. S. A.* 108, 7641–7646. doi: 10.1073/pnas.1018985108

Bastos, A. M., and Schoffelen, J. M. (2016). A tutorial review of functional connectivity analysis methods and their interpretational pitfalls. *Front. Syst. Neurosci.* 9:175. doi: 10.3389/fnsys.2015.00175

Benjamini, Y., and Hochberg, Y. (1995). Controlling the false discovery rate: a practical and powerful approach to multiple testing. *J. R. Stat. Soc. Ser. B (Methodol.).* 57, 289–300. doi: 10.1111/j.2517-6161.1995.tb02031.x

Biswal, B., Zerrin Yetkin, F., Haughton, V. M., and Hyde, J. S. (1995). Functional connectivity in the motor cortex of resting human brain using echo-planar mri. *Magn. Reson. Med.* 34, 537–541. doi: 10.1002/mrm.1910340409

Boytsova, J. A., Danko, S. G., and Medvedev, S. V. (2016). When EMG contamination does not necessarily hide high-frequency EEG: scalp electrical recordings before and after Dysport injections. *Exp. Brain Res.* 234, 3091–3106. doi: 10.1007/s00221-016-4708-3

Ciuciu, P., Abry, P., and He, B. J. (2014). Interplay between functional connectivity and scale-free dynamics in intrinsic fMRI networks. *Neuroimage* 95, 248–263. doi: 10.1016/j.neuroimage.2014.03.047

Dai, Z., de Souza, J., Lim, J., Ho, P. M., Chen, Y., Li, J., et al. (2017). EEG cortical connectivity analysis of working memory reveals topological reorganization in theta and alpha bands. *Front. Hum. Neurosci.* 11:237. doi: 10.3389/fnhum.2017.00237

Delorme, A., and Makeig, S. (2004). EEGLAB: an open source toolbox for analysis of single-trial EEG dynamics including independent component analysis. *J. Neurosci. Methods* 134, 9–21. doi: 10.1016/j.jneumeth.2003.10.009

Di, X., Fu, Z., Chan, S. C., Hung, Y. S., Biswal, B. B., and Zhang, Z. (2015). Task-related functional connectivity dynamics in a block-designed visual experiment. *Front. Hum. Neurosci.* 9:543. doi: 10.3389/fnhum.2015.00543

Eke, A., Herman, P., Kocsis, L., and Kozak, L. R. (2002). Fractal characterization of complexity in temporal physiological signals. *Physiol. Meas.* 23, R1–R38. doi: 10.1088/0967-3334/23/1/201

Elton, A., and Gao, W. (2015). Task-related modulation of functional connectivity variability and its behavioral correlations. *Hum. Brain Mapp.* 36, 3260–3272. doi: 10.1002/hbm.22847

Fox, M. D., Snyder, A. Z., Vincent, J. L., Corbetta, M., Van Essen, D. C., and Raichle, M. E. (2005). The human brain is intrinsically organized into dynamic, anticorrelated functional networks. *Proc. Natl. Acad. Sci. U. S. A.* 102, 9673–9678. doi: 10.1073/pnas.0504136102

Friston, K. J., Frith, C. D., Liddle, P. F., and Frackowiak, R. S. J. (1993). Functional connectivity: the principal-component analysis of large (PET) data sets. *J. Cereb. Blood Flow Metab.* 13, 5–14. doi: 10.1038/jcbfm.1993.4

Gabard-Durnam, L. J., Mendez Leal, A. S., Wilkinson, C. L., and Levin, A. R. (2018). The harvard automated processing pipeline for electroencephalography (HAPPE): standardized processing software for developmental and high-artifact data. *Front. Neurosci.* 12:97. doi: 10.3389/fnins.2018.00097

Goncharova, I. I., McFarland, D. J., Vaughan, T. M., and Wolpaw, J. R. (2003). EMG contamination of EEG: spectral and topographical characteristics. *Clin. Neurophysiol.* 114, 1580–1593. doi: 10.1016/S1388-2457(03)00093-2

Grech, D., and Pamuła, G. (2012). Multifractal background noise of monofractal signals. *Acta Phys. Pol. A* 121, B–34–B–39. doi: 10.12693/APhysPolA.121.B-34

He, B. J., Zempel, J. M., Snyder, A. Z., and Raichle, M. E. (2010). The temporal structures and functional significance of scale-free brain activity. *Neuron* 66, 353–369. doi: 10.1016/j.neuron.2010.04.020

Hou, F., Liu, C., Yu, Z., Xu, X., Zhang, J., Peng, C.-K., et al. (2018). Age-related alterations in electroencephalography connectivity and network topology during n-back working memory task. *Front. Hum. Neurosci.* 12:484. doi: 10.3389/fnhum.2018.00484

Ýçer, S., Acer, Ý, and Baş, A. (2020). Gender-based functional connectivity differences in brain networks in childhood. *Comput. Methods Programs Biomed.* 192:105444. doi: 10.1016/j.cmpb.2020.105444

Jang, K.-M., Kim, M.-S., and Kim, D.-W. (2020). The dynamic properties of a brain network during spatial working memory tasks in college students with ADHD traits. *Front. Hum. Neurosci.* 14:580813. doi: 10.3389/fnhum.2020.580813

Kandel, E. R., Schwartz, J. H., and Jessell, T. M. (2012). *Principles of Neural Science*. New York, NY: McGraw-Hill Professional Pub.

Kaposzta, Z., Stylianou, O., Mukli, P., Eke, A., and Racz, F. S. (2021). Decreased connection density and modularity of functional brain networks during n-back working memory paradigm. *Brain Behav.* 11:116. doi: 10.1002/brb3.1932

Kaufmann, T., Alnæs, D., Brandt, C. L., Doan, N. T., Kauppi, K., Bettella, F., et al. (2017). Task modulations and clinical manifestations in the brain functional connectome in 1615 fMRI datasets. *Neuroimage* 147, 243–252. doi: 10.1016/j.neuroimage.2016.11.073

Krienen, F. M., Thomas Yeo, B. T., and Buckner, R. L. (2014). Reconfigurable task-dependent functional coupling modes cluster around a core functional architecture. *Philos. Trans. R. Soc. B Biol. Sci.* 369:20130526. doi: 10.1098/rstb.2013.0526

Kristoufek, L. (2014). Spectrum-based estimators of the bivariate hurst exponent. *Phys. Rev. E* 90:062802. doi: 10.1103/PhysRevE.90.062802

Kristoufek, L. (2015a). Can the bivariate hurst exponent be higher than an average of the separate hurst exponents? *Physica A* 431, 124–127. doi: 10.1016/j.physa.2015.02.086

Kristoufek, L. (2015b). Finite sample properties of power-law cross-correlations estimators. *Physica A* 419, 513–525. doi: 10.1016/j.physa.2014.10.068

Kristoufek, L. (2016). Power-law cross-correlations estimation under heavy tails. *Commun. Nonlinear Sci. Numer. Simul.* 40, 163–172. doi: 10.1016/j.cnsns.2016.04.010

Lewis, C. M., Baldassarre, A., Committeri, G., Romani, G. L., and Corbetta, M. (2009). Learning sculpts the spontaneous activity of the resting human brain. *Proc. Natl. Acad. Sci.* 106, 17558–17563. doi: 10.1073/pnas.0902455106

Morel, P. (2018). Gramm: grammar of graphics plotting in Matlab. *J. Open Source Softw.* 3:568. doi: 10.21105/joss.00568

Mueller, S., Wang, D., Fox, M. D., Yeo, B. T. T., Sepulcre, J., Sabuncu, M. R., et al. (2013). Individual variability in functional connectivity architecture of the human brain. *Neuron* 77, 586–595. doi: 10.1016/j.neuron.2012.12.028

Mukli, P., Nagy, Z., and Eke, A. (2015). Multifractal formalism by enforcing the universal behavior of scaling functions. *Physica A* 417, 150–167. doi: 10.1016/j.physa.2014.09.002

Mukli, P., Nagy, Z., Racz, F. S., Herman, P., and Eke, A. (2018). Impact of healthy aging on multifractal hemodynamic fluctuations in the human prefrontal cortex. *Front. Physiol.* 9:1072. doi: 10.3389/fphys.2018.01072

Nagy, Z., Mukli, P., Herman, P., and Eke, A. (2017). Decomposing multifractal crossovers. *Front. Physiol.* 8, 533. doi: 10.3389/fphys.2017.00533

Nasrallah, F. A., Singh, K. K. D. R., Yeow, L. Y., and Chuang, K.-H. (2017). GABAergic effect on resting-state functional connectivity: dynamics under pharmacological antagonism. *Neuroimage* 149, 53–62. doi: 10.1016/j.neuroimage.2017.01.040

Poil, S.-S., Hardstone, R., Mansvelder, H. D., and Linkenkaer-Hansen, K. (2012). Critical-state dynamics of avalanches and oscillations jointly emerge from balanced excitation/inhibition in neuronal networks. *J. Neurosci.* 32, 9817–9823. doi: 10.1523/JNEUROSCI.5990-11.2012

Popivanov, D., Stomonyakov, V., Minchev, Z., Jivkova, S., Dojnov, P., Jivkov, S., et al. (2006). Multifractality of decomposed EEG during imaginary and real visual-motor tracking. *Biol. Cybern.* 94, 149–156. doi: 10.1007/s00422-005-0037-5

Rabinovich, M. I., and Muezzinoglu, M. K. (2010). Nonlinear dynamics of the brain: emotion and cognition. *Phys. Uspekhi* 53, 357–372. doi: 10.3367/UFNe.0180.201004b.0371

Racz, F. S., Mukli, P., Nagy, Z., and Eke, A. (2017). Increased prefrontal cortex connectivity during cognitive challenge assessed by fNIRS imaging. *Biomed. Opt. Express* 8:3842. doi: 10.1364/BOE.8.003842

Racz, F. S., Stylianou, O., Mukli, P., and Eke, A. (2018). Multifractal dynamic functional connectivity in the resting-state brain. *Front. Physiol.* 9:1704. doi: 10.3389/fphys.2018.01704

Racz, F. S., Stylianou, O., Mukli, P., and Eke, A. (2019). Multifractal and entropy analysis of resting-state electroencephalography reveals spatial organization in local dynamic functional connectivity. *Sci. Rep.* 9:13474. doi: 10.1038/s41598-019-49726-5

Racz, F. S., Stylianou, O., Mukli, P., and Eke, A. (2020). Multifractal and entropy-based analysis of delta band neural activity reveals altered functional connectivity dynamics in schizophrenia. *Front. Syst. Neurosci.* 14:49. doi: 10.3389/fnsys.2020.00049

Raichle, M. E., MacLeod, A. M., Snyder, A. Z., Powers, W. J., Gusnard, D. A., and Shulman, G. L. (2001). A default mode of brain function. *Proc. Natl. Acad. Sci. U. S. A.* 98, 676–682. doi: 10.1073/pnas.98.2.676

Rak, R., and Grech, D. (2018). Quantitative approach to multifractality induced by correlations and broad distribution of data. *Physica A* 508, 48–66. doi: 10.1016/j.physa.2018.05.059

Rong-Yi, Y., and Zhong, C. (2005). Blind source separation of multichannel electroencephalogram based on wavelet transform and ICA. *Chin. Phys.* 14, 2176–2180. doi: 10.1088/1009-1963/14/11/006

Rubinov, M., and Sporns, O. (2010). Complex network measures of brain connectivity: uses and interpretations. *Neuroimage* 52, 1059–1069. doi: 10.1016/j.neuroimage.2009.10.003

Skroumpelou, K., Mavros, P., and Smith, A. H. (2015). Are we there yet? Exploring distance perception in urban environments with mobile electroencephalography. *GIS Res.*

Stam, C. J., and de Bruin, E. A. (2004). Scale-free dynamics of global functional connectivity in the human brain. *Hum. Brain Mapp.* 22, 97–109. doi: 10.1002/hbm.20016

Stylianou, O., Racz, F. S., Eke, A., and Mukli, P. (2021). Scale-free coupled dynamics in brain networks captured by bivariate focus-based multifractal analysis. *Front. Physiol.* 11:615961. doi: 10.3389/fphys.2020.615961

Tel, T. (1988). Fractals, multifractals, and thermodynamics. *Z. Für Nat. A* 1174, 1154–1174. doi: 10.1515/zna-1988-1221

Van Hoesen, G. W. (1993). The modern concept of association cortex. *Curr. Opin. Neurobiol.* 3, 150–154. doi: 10.1016/0959-4388(93)90202-A

Wang, J., and Zhao, D.-Q. (2012). Detrended cross-correlation analysis of electroencephalogram. *Chin. Phys. B* 21:028703. doi: 10.1088/1674-1056/21/2/028703

Werner, G. (2010). Fractals in the nervous system: conceptual implications for theoretical neuroscience. *Front. Physiol.* 1:15. doi: 10.3389/fphys.2010.00015

Yang, Y., Qiu, Y., and Schouten, A. C. (2015). Dynamic Functional brain connectivity for face perception. *Front. Hum. Neurosci.* 9:662. doi: 10.3389/fnhum.2015.00662

Yilmaz, G., Budan, A. S., Ungan, P., Topkara, B., and Türker, K. S. (2019). Facial muscle activity contaminates EEG signal at rest: evidence from frontalis and temporalis motor units. *J. Neural Eng.* 16:066029. doi: 10.1088/1741-2552/ab3235

Yu, H., and Winkler, S. (2013). "Image complexity and spatial information," in *Proceedings of the In 2013 5th International Workshop on Quality of Multimedia Experience (QoMEX)* (Klagenfurt: IEEE), 12–17. doi: 10.1109/QoMEX.2013.6603194

Zhang, C., Dougherty, C. C., Baum, S. A., White, T., and Michael, A. M. (2018). Functional connectivity predicts gender: evidence for gender differences in resting brain connectivity. *Hum. Brain Mapp.* 39, 1765–1776. doi: 10.1002/hbm.23950

Conflict of Interest: The authors declare that the research was conducted in the absence of any commercial or financial relationships that could be construed as a potential conflict of interest.

frontiers in Human Neuroscience

ORIGINAL RESEARCH
published: 10 January 2022
doi: 10.3389/fnhum.2021.757128

Resting-State Functional Connectivity in the Dorsal Attention Network Relates to Behavioral Performance in Spatial Attention Tasks and May Show Task-Related Adaptation

Björn Machner[1,2], Lara Braun[1], Jonathan Imholz[1], Philipp J. Koch[1,2], Thomas F. Münte[1,2], Christoph Helmchen[1,2] and Andreas Sprenger[1,2,3]*

[1] Department of Neurology, University Hospital Schleswig-Holstein, Campus Lübeck, Lübeck, Germany, [2] Center of Brain, Behavior and Metabolism, University of Lübeck, Lübeck, Germany, [3] Department of Psychology II, University of Lübeck, Lübeck, Germany

OPEN ACCESS

Edited by:
Stephen José Hanson, Rutgers, The State University of New Jersey, United States

Reviewed by:
Amanda Elton, University of North Carolina at Chapel Hill, United States
Abraham Z. Snyder, Washington University in St. Louis, United States

***Correspondence:**
Björn Machner
Bjoern.Machner@neuro.uni-luebeck.de
orcid.org/0000-0001-7981-2906

Specialty section:
This article was submitted to Cognitive Neuroscience, a section of the journal Frontiers in Human Neuroscience

Received: *11 August 2021*
Accepted: *10 December 2021*
Published: *10 January 2022*

Citation:
Machner B, Braun L, Imholz J, Koch PJ, Münte TF, Helmchen C and Sprenger A (2022) Resting-State Functional Connectivity in the Dorsal Attention Network Relates to Behavioral Performance in Spatial Attention Tasks and May Show Task-Related Adaptation. Front. Hum. Neurosci. 15:757128. doi: 10.3389/fnhum.2021.757128

Between-subject variability in cognitive performance has been related to inter-individual differences in functional brain networks. Targeting the dorsal attention network (DAN) we questioned (i) whether resting-state functional connectivity (FC) within the DAN can predict individual performance in spatial attention tasks and (ii) whether there is short-term adaptation of DAN-FC in response to task engagement. Twenty-seven participants first underwent resting-state fMRI (PRE run), they subsequently performed different tasks of spatial attention [including visual search (VS)] and immediately afterwards received another rs-fMRI (POST run). Intra- and inter-hemispheric FC between core hubs of the DAN, bilateral intraparietal sulcus (IPS) and frontal eye field (FEF), was analyzed and compared between PRE and POST. Furthermore, we investigated rs-fMRI-behavior correlations between the DAN-FC in PRE/POST and task performance parameters. The absolute DAN-FC did not change from PRE to POST. However, different significant rs-fMRI-behavior correlations were revealed for intra-/inter-hemispheric connections in the PRE and POST run. The stronger the FC between left FEF and IPS before task engagement, the better was the learning effect (improvement of reaction times) in VS (r = 0.521, p = 0.024). And the faster the VS (mean RT), the stronger was the FC between right FEF and IPS after task engagement (r = −0.502, p = 0.032). To conclude, DAN-FC relates to the individual performance in spatial attention tasks supporting the view of functional brain networks as priors for cognitive ability. Despite a high inter- and intra-individual stability of DAN-FC, the change of FC-behavior correlations after task performance possibly indicates task-related adaptation of the DAN, underlining that behavioral experiences may shape intrinsic brain activity. However, spontaneous state fluctuations of the DAN-FC over time cannot be fully ruled out as an alternative explanation.

Keywords: functional connectivity, spatial attention, resting-state fMRI, attention network, behavior

INTRODUCTION

Inter-individual differences in cognitive abilities have been related to inter-individual differences in functional brain networks (Baldassarre et al., 2012; Harmelech and Malach, 2013; Finn et al., 2015). These functional networks are considered to be shaped by lifelong learning experiences providing an indispensable memory system for upcoming cognitive challenges (Harmelech and Malach, 2013; Sadaghiani and Kleinschmidt, 2013). They can be assessed by analyzing spontaneous low-frequency fluctuations of the blood-oxygen level dependent (BOLD) signal in functional MRI, usually while the brain is at rest (Biswal et al., 1995). Remote brain regions of temporally coherent oscillations are regarded as functionally connected within one resting-state network (RSN) (Lowe et al., 1998; Fox and Raichle, 2007). RSNs comprise different functional domains, e.g., motor action, visual perception or attention, and the regions belonging to one RSN are also activated together when the brain is actively engaged in a related task (Smith et al., 2009).

While RSNs are reproducible across different subjects (Damoiseaux et al., 2006), their specific functional connectivity (FC) pattern appears to be unique and very stable in the individual subject, almost acting as an individual "fingerprint" (Finn et al., 2015; Osher et al., 2019). As it was first shown for the sensorimotor network, the strength of the FC largely accounts for the variability in behavioral responses, indicating the RSNs' relevance for behavior (Fox et al., 2007). Moreover, the individual FC within (or between) RSNs has been shown to predict individual performance (or improvement/learning) in different cognitive tasks such as visual search (VS) (Chou et al., 2013; Bueicheku et al., 2020), audio-/visual perception (Hipp et al., 2011; Baldassarre et al., 2012; Sadaghiani et al., 2015; Berry et al., 2017) or mirror drawing (Manuel et al., 2018).

Despite the stability of RSNs, within- and between-network FCs can immediately change when a task is performed, i.e., when the brain changes its state from rest ("idling") to action (Szczepanski et al., 2013; Spadone et al., 2015). Moreover, repetitive training or only one session of a novel task can induce persisting reorganization of RSNs, as it has been shown for different cognitive domains, including visual perception (Lewis et al., 2009; Urner et al., 2013; Guidotti et al., 2015; Sarabi et al., 2018), VS (Bueicheku et al., 2019), memory (Dresler et al., 2017), language (Waites et al., 2005), and visuo-motor skills (Manuel et al., 2018).

The current study focused on the dorsal attention network (DAN) as one of the RSNs (Fox et al., 2006; Hacker et al., 2013). The DAN is centered on bilateral regions in the frontal and parietal cortex, including the frontal eye field (FEF) and the intraparietal sulcus (IPS) (Fox et al., 2006; Corbetta and Shulman, 2011). These regions are recruited when attention is voluntarily shifted to spatial locations (Corbetta and Shulman, 2002) or task-relevant salient objects (Shulman et al., 2009) as well as during intentional visual exploration using eye movements (Corbetta et al., 1998). Experimental tasks that typically activate DAN regions include the Posner paradigm assessing covert orienting and reorienting (Posner and Petersen, 1990; Vossel et al., 2006; Doricchi et al., 2010), the Landmark task requiring spatial judgments (Milner et al., 1993; Fink et al., 2000; Revill et al., 2011) and VS paradigms (Corbetta et al., 1998; Nobre et al., 2003).

Pursuing the hypothesis that RSNs represent individual traits/priors of cognitive ability (Harmelech and Malach, 2013; Sadaghiani and Kleinschmidt, 2013; Spadone et al., 2015), the current study investigated whether pre-task resting-state FC in the DAN can predict individual behavioral performance in spatial attention tasks. Furthermore, as RSN's are assumed to be malleable over short (to long) temporal scales in order to allow lifelong learning (Sadaghiani and Kleinschmidt, 2013), we questioned whether the DAN's FC or FC-behavior relationship can already be changed by one training session of spatial attention tasks.

MATERIALS AND METHODS

Participants

We recruited 29 healthy adult participants, most of whom were students at the University of Lübeck. The inclusion criteria encompassed right-handedness as tested by the Edinburgh Handedness Inventory (Oldfield, 1971), a normal or corrected-to-normal visual acuity and intact color vision as tested by the Ishihara's Test (Kanehara & Co., Ltd., Tokyo, Japan). Exclusion criteria were a known neurological, psychiatric, or ophthalmological disease.

Before participation, written informed consent according to the Declaration of Helsinki and its later amendments was obtained from each participant. The study was approved by the local Ethics Committee of the University of Lübeck (14-189).

Two of the participants had to be excluded due to excessive head motion in the MRI scanner (see section "Materials and Methods" on quality control of rs-fMRI data), leaving 27 subjects [female: $n = 16$ (59%); mean age: 24.2 $\pm$ 0.8 years, range: 19–38 years] for final analysis.

Stimuli and Tasks

Participants viewed the stimuli on a screen (NNL LCD monitor, NordicNeuroLab, Bergen, Norway; active TFT, 69.8 $\times$ 39.3 cm visual area), positioned on the front end of the MRI scanner, *via* a mirror that was attached to the head coil (eye-to-screen distance: 130 cm, i.e., visual area 30.1° $\times$ 17.2°). A keypad with buttons for the manual responses was fixed at the participant's right thigh using hook-and-loop tape.

Three different tasks were presented, each addressing a specific subcomponent of spatial attention. The (I) Posner task tests covert reflexive shifts of attention (orienting and re-orienting) (Posner et al., 1984), the (II) Landmark task visuospatial judgments (Milner et al., 1993) and the (III) VS task (Machner et al., 2018) overt shifts of attention by exploratory eye movements. All these tasks are known to activate the bilateral FEF and IPS as core regions of the DAN (Corbetta et al., 1998; Fink et al., 2000; Doricchi et al., 2010).

For our experiment, the original *Posner* paradigm was adapted to the scanner environment in analogy to a previous study (Thiel et al., 2004). The basic display showed a dark-gray background with a light-gray diamond at the center and two light-gray square

frames (size 2°), positioned on the horizontal meridian at either side with an eccentricity of 12° from the center. As an attentional cue, one side of the central diamond briefly (200 ms) lighted up. After a delay of either 150 or 400 ms (stimulus onset asynchrony), the target (a light gray asterisk) appeared for 100 ms within one of the two peripheral frames. The inter-trial interval varied between 1650 and 1900 ms. The participant was instructed to press the left button on the keypad with the index finger as quick as possible upon target appearance. One run of the Posner task included 48 valid (cue and target on the same side) and 12 invalid (target on the opposite side as indicated by the preceding cue) trials, corresponding to a cue validity of 80%, which allows assessment of endogenous attention shifting (Chica et al., 2011).

The *Landmark task* represents a "perceptive version" of the established line bisection task (Schenkenberg et al., 1980) but is better suited for the scanner environment (Fink et al., 2000). A white line (20° or 24° of visual angle) appeared on a dark-gray background. It was pre-bisected with a vertical dash either directly in the middle, i.e., with both parts of the line having the same length, or with a leftward or rightward shift of either 0.25° or 0.5°. The vertical dash bisecting the horizontal line was always aligned with the screen's center so that the absolute spatial position of the bisection mark on the screen could not be used as a cue for the final spatial judgment of the line length (Ellison et al., 2004). The participants were asked to judge which half of the line was longer or whether both were equal in length. If the left part of the line was estimated to be longer, they should press the left button on a keypad with their right index finger. In case of a longer segment on the right, they should press a button with their fourth finger and in case of equal lengths of both halves of the line they used their middle finger. The line was presented for 300 ms and participants had a maximum time of 2000 ms to give their response by pressing the respective button. One run of the Landmark task consisted of 80 trials, 32 of which showed a correctly bisected line with both halves having the same length ("equal"), 24 trials with a longer left segment and 24 trials with a longer right segment.

In the *VS task* a computerized but naturalistic image of a desk scene was presented, in which participants were asked to find a paperclip (target) among different other everyday objects (e.g., a pen, coin, key, etc.) that served as distractors (Machner et al., 2018, 2020a). Each VS trial started with a central fixation cross presented on a black background, followed by the appearance of a desk image containing 30 different objects (see **Figure 1** for an example). Participants were instructed to press a response button on a keypad as soon as they found the target. If there was no paperclip to be found, participants were asked to press a different button. A trial ended upon the button press or after a maximum time of 5000 ms. One run of the VS task included 30 trials of different desk images, 80% of which contained a paperclip ("target trials").

Experimental Design

The experimental design is depicted in **Figure 1**. Before entering the MRI scanner, subjects were briefly familiarized with the three tasks outside the MRI scanner. In the MRI scanner, subjects first received a structural MRI scan of the brain. Then, the PRE resting-state fMRI run was conducted. Next, there was the task block (total duration 24 min), in which participants performed three runs of each task in a predefined order (see **Figure 1**). Afterwards, the session was completed with a second rs-fMRI (POST) run.

To control for adherence to the tasks as well as for wakefulness during the rs-fMRI runs (eyes open), we continuously recorded and monitored eye movements of the participants using an MRI-compatible, remote eye tracker with a sampling rate at 1000 Hz (Eyelink 1000 Plus, SR Research, Ottawa, ON, Canada). This monitoring could exclude that participants fall asleep during the rs-fMRI sessions, also proven by offline analyses of eye position signals that showed only a small number of lacking eye signals in the PRE ($14 \pm 2\%$) and POST ($18 \pm 3\%$) rs-fMRI run, which were largely due to transient lid closure and artifacts.

Behavioral Analysis

From the Posner task, we analyzed the mean reaction time ("RT mean") of the responses in all the valid and invalid trials. Furthermore, we calculated the difference in RT between the invalid and valid trials ("RT invalid-valid") as a more specific indicator for attentional reorienting (Rengachary et al., 2011). From the VS task, we analyzed the mean RT for trials, in which a target was present and the response button was correctly pressed. The performance in the Landmark task was assessed by calculating the "error rate (ER)." Therefore, the number of trials incorrectly judged was divided by the total number of trials presented $\times 100$.

For each task, we additionally assessed the individual improvement by calculating the difference in the subject's RT (ER, respectively) between the first and the last (third) run.

Structural and Functional Magnetic Resonance Imaging

Acquisition of Imaging Data

Structural and functional MR imaging was performed at the CBBM Core Facility Magnetic Resonance Imaging using a 3-T Siemens Magnetom Skyra scanner equipped with a 64-channel head-coil. First, structural images of the whole brain using a 3D T1-weighted MP-RAGE sequence were acquired (TR = 2300 ms; TE = 2.43 ms; TI = 1100 ms; flip angle 8°; 0.85 mm × 0.75 mm × 0.75 mm resolution; 185 mm × 240 mm × 240 mm field of view; acquisition time: 8 min).

The resting-state functional image recordings were acquired by applying a single-shot gradient-recalled echo-planar imaging (GRE-EPI) sequence sensitive to blood oxygen level dependent (BOLD) contrast (480 volumes, TR = 1000 ms; TE = 30 ms; flip angle = 60°; in-plane resolution 3 mm × 3 mm; 204 mm × 204 mm field of view; 56 axial slices; 3 mm slice thickness, no interslice gap; simultaneous multi-slice factor 4; acquisition time: 8 min).

Lights were switched off during recordings. Subjects were asked to keep their eyes open and to foveate a small red dot on a black background. In order to minimize noise, ear plugs were

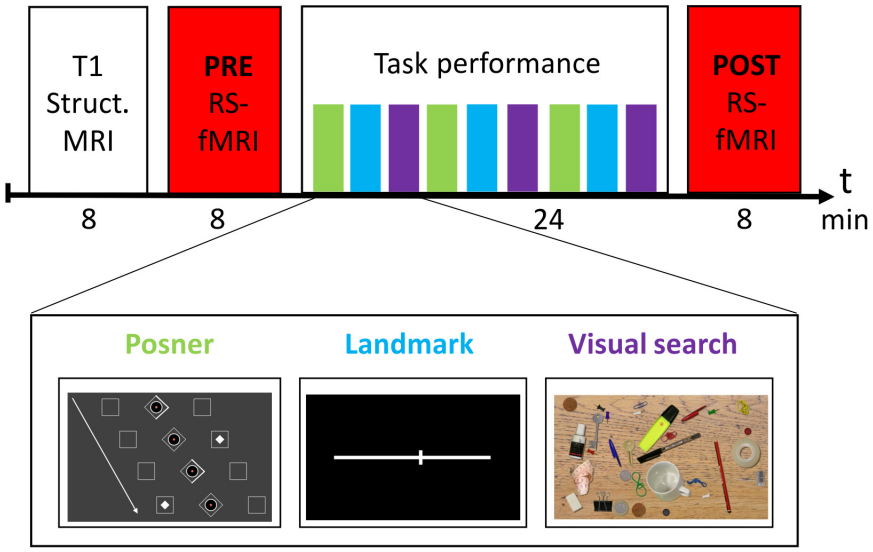

FIGURE 1 | Experimental design.

used. Head movements were reduced by using ear pads (Multipad Ear, Pearltec Technology AG, Schlieren/CH).

Preprocessing of Resting-State fMRI Data

Preprocessing was performed using the DPARSFA toolbox (data processing assistant for resting-state fMRI, version 4.4[1]; Yan et al., 2016), while slice timing correction and further statistical analysis was performed with the SPM12 software[2] (Wellcome Trust Centre for Neuroimaging, London, United Kingdom), both implemented in Matlab® 2018B (MathWorks®, Natick, MA, United States).

First, the first 10 time points of each data set were discarded to allow for magnetization equilibrium and for subjects to adjust to the environment. The next steps included: (i) correction for differences in the image acquisition time between slices; (ii) a six parameter rigid body spatial transformation to correct for head motion during data acquisition; (iii) co-registration of the structural image to the mean functional image; (iv) gray and white matter segmentation, bias correction and spatial normalization of the structural image to a standard template (Montreal Neurological Institute, MNI); (v) regression of nuisance variables from the data (including white matter and ventricular signals, the six motion parameters determined in the realignment procedure as well as their first derivatives, the constant and linear trend); (vi) spatial normalization of the functional images using the DARTEL (Diffeomorphic Anatomical Registration Through Exponentiated Lie) method and resampling to 3-mm isotropic voxels; (vii) spatial smoothing with a 6 mm full-width at half-maximum Gaussian kernel. (viii) Before the FC analyses a temporal bandpass filter was applied to all voxel time series retaining only the low frequency spectrum (0.01–0.08 Hz).

[1]https://www.nitrc.org/projects/dparsf
[2]http://www.fil.ion.ucl.ac.uk/spm

Quality Control of Resting-State fMRI Data and Exclusion Due to Head Motion

The six realignment parameters, i.e., three displacements and three elementary rotations with respect to the first image in the EPI series, were used as an estimator for head motion. The maximum displacements were required to be smaller than 3.0 mm and individual rotations smaller than 3.0°. Because instantaneous motion below this threshold can still have a major confounding effect on rs-fMRI measures (Power et al., 2012; Van Dijk et al., 2012), we enabled DPARSFA to scrub the data by identifying and cutting out single motion contaminated frames ("bad" time points). The method is based on calculating the frame-to-frame displacement as described by Power et al. (2012), defining a "bad" time point when the framewise displacement threshold of >0.5 mm was exceeded and deleting the current time point (EPI volume), the previous one and the following two. The reduction of EPI volumes due to this cutting was required to be less than 38% in order to leave at least 5 min of rs-fMRI data for final analysis. Two subjects, who exceeded the cut-offs mentioned above, were excluded from final analysis. The remaining subjects had in the PRE rs-fMRI session on average a maximal head motion of 0.7 mm [standard deviation (SD): 0.4 mm], a mean framewise displacement of 0.2 mm (SD 0.1 mm), and for final analysis a mean reduction of 5.5% (SD 9.0%) EPI volumes due to the predefined cut-off of 0.5 mm framewise displacement. In the POST rs-fMRI session, their maximal head motion was on average 1.0 mm (SD 0.9 mm), the mean framewise displacement was of 0.2 mm (SD 0.1 mm), and the cut-off defined reduction of EPI volumes in the final analysis was 6.8% (SD 8.7%).

Definition of Regions of Interest

We defined the following regions of interest (ROIs) previously shown to be the most relevant hubs of the DAN (Fox et al., 2006; Corbetta and Shulman, 2011): the bilateral FEF and IPS. The

center coordinates for the ROIs were taken from the literature, based on previous resting-state and/or task-related fMRI studies investigating the DAN (He et al., 2007; Hacker et al., 2013; Machner et al., 2020b): right FEF (23, −8, 55; *x*, *y*, *z* in MNI space], left FEF (−19, −8, 57) right IPS (27, −63, 54), and left IPS (−24, −60, 54). A 6 mm radius sphere was centered on the respective ROI coordinate, resulting in a ROI volume of ∼0.9 cm^3 each.

Functional Connectivity Analyses

For the *seed-based (ROI-to-voxel) FC analyses*, the time courses of all voxels within a sphere ROI were averaged and then correlated to the time course of all the other voxels in the brain. The resulting connectivity maps of each participant were Fisher's r-to-z transformed to obtain normally distributed measures for the subsequent statistical analyses. Next, group-wise ROI-to-voxel FC maps for each ROI and each rs-fMRI run were generated by calculating one-sample *t*-test contrasts that were corrected for multiple comparisons by applying the family-wise error (FWE) rate at the voxel level (corrected $p < 0.05$). Differences in ROI-to-voxel FC between the two rs-fMRI runs were assessed by calculating two-sample paired *t*-test contrasts (POST > PRE) for each ROI with the cluster-defining threshold set at $p < 0.001$ (uncorrected), followed by a $p < 0.05$ FWE correction at cluster level.

For the *pairwise (ROI-to-ROI) FC analyses*, the time courses of all voxels within a sphere ROI were averaged and correlated to the mean time course of voxels in the other sphere ROI. The resulting Pearson correlation coefficients of the four predefined intra-/interhemispheric ROI pairs (FEF_L–FEF_R, IPS_L–IPS_R, FEF_L–IPS_L, and FEF_R–IPS_R) were Fisher-z-transformed before entering further analyses.

For each participant, we also calculated one mean FC value for the whole DAN network ("DAN-FC") in the PRE and the POST session by summing up the individual FC values of the predefined ROI pairs and dividing it by their number ($n = 4$).

Statistics

Statistical analyses, apart from the fMRI analyses described above, were performed using the SPSS software package (version 22.0.0.2; IBM Corp., Somer, NY, United States).

Unless otherwise reported, data in the manuscript are presented as mean ± standard error of the mean (SEM). Differences in the ROI-to-ROI FC values between the PRE and the POST rs-fMRI run were assessed using paired *t*-tests. Correlation analyses between rs-fMRI (ROI-to-ROI FC) and behavioral (RT and ER, respectively) parameters were performed using the non-parametric Spearman's rho correlation coefficient. The results of the rs-fMRI-behavior analyses, which tested whether behavioral performance was correlated to the DAN-FC in a hypothesis-driven set of four predefined ROI pairs, were corrected for multiple comparisons by applying the Bonferroni–Holm correction (*p*-value × 4). Furthermore, significant FC-behavior correlations in one rs-fMRI session (e.g., PRE) were tested for a significant difference to the corresponding rs-fMRI session (e.g., POST). Therefore we assessed the interaction FC × behavior by weighting the individual FC value with the linear regression coefficient from the FC-behavior correlation and subsequently performed a paired *t*-test on the weighted FC between PRE and POST. Regression coefficients were calculated using "robustfit" function within Matlab (DuMouchel and O'Brian, 1989). This function uses iteratively reweighted least squares to compute the coefficients, which makes it robust against extreme values and outliers. The level of significance was set at $p < 0.05$.

RESULTS

Behavioral Task Performance

The participants' mean RT in the Posner task was 435 ± 11 ms and there was significant improvement from the first to the last run ($d = -32 \pm 6$, $p < 0.001$). The validity effect, i.e., the difference in RT between invalid and valid trials, was on average 32 ms ± 6. The mean RT in the VS task was 1500 ± 54 ms, again with significant improvement over time ($d = -270 \pm 49$, $p < 0.001$). The mean ER in the Landmark task was 39 ± 1%. In this task, the participants revealed no improvement between the first and the last run ($d = -1 \pm 1\%$, $p = 0.522$).

Resting-State fMRI Results

Figure 2 depicts the statistical maps showing the results of the seed-based (ROI-to-voxel) FC analysis of the four predefined DAN-ROIs, separately for the PRE and POST rs-fMRI run.

For each of the four seeds, we consistently observed functional connections to the (bilateral) FEF, IPS, middle frontal gyrus (MFG), and MT+ (middle temporal complex) as well as to the basal ganglia and the thalamus.

Statistical comparison of the different seed-based FC maps between the PRE and the POST run did not reveal supra-threshold voxels. Hence, FC of the predefined ROIs to whole brain did not change significantly from PRE to POST.

Table 1 depicts the group-mean of Fisher's z-transformed ROI-to-ROI FC results of the different intra- and inter-hemispheric ROI pairs, separately for the PRE and POST rs-fMRI run. Pairwise comparisons did not reveal significant differences between the PRE and POST rs-fMRI run (p always > 0.104).

Correlation of Behavioral and fMRI Parameters

Correlation analyses were performed between behavioral results (mean RT and RT improvement in the Posner and VS task, ER in the Landmark task) and ROI pairs' FC results in the PRE and the POST run (**Table 2**).

The following significant rs-fMRI-behavior correlations were revealed for the PRE run (**Figure 3**): The intra-hemispheric FC between left FEF and IPS correlated with the RT improvement in the VS task ($r = 0.521$, $p = 0.024$) as well as with the RT improvement in the Posner task ($r = 0.496$, $p = 0.052$, statistical trend). Thus, the stronger the participant's FC between left FEF and IPS, the better was the individual learning effect in both tasks. Furthermore, the FC between right and left FEF was correlated with the mean RT in VS ($r = 0.527$, $p = 0.020$), i.e., participants

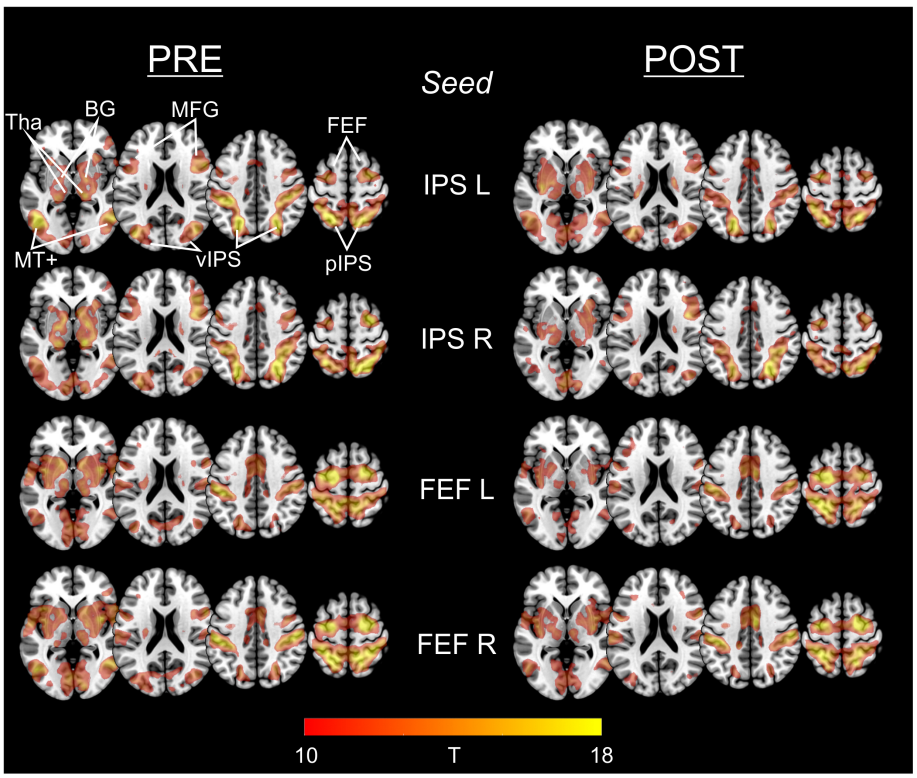

FIGURE 2 | Functional connectivity of IPS and FEF seed regions in PRE and POST run. For each of the predefined DAN-ROIs (bilateral IPS and FEF) and separately for the rs-fMRI run before (PRE) and after (POST) task performance, group statistical FC maps were obtained using one-sample *t*-tests on the individual Fisher's z-transformed correlation maps, corrected for multiple comparisons applying a false family-wise error (FWE) at $p < 0.05$. Results are presented at a threshold of $T > 9.86$ (equals FWE-corrected $p < 0.00001$), depicted on axial slices (*z*: 0, 30, and 60) of a MNI brain template. The predefined seed-ROIs almost uniformly show functional connections to other DAN regions including ventral/posterior IPS and FEF, middle frontal gyrus (MFG), middle temporal complex (MT+) as well as to the basal ganglia (BG) and thalamus (Tha).

with stronger interhemispheric FEF-FC needed on average more time to detect the target in the VS task.

In the POST run (**Figure 3**), the FC between right FEF and IPS was found to be inversely correlated with the mean RT in VS ($r = -0.502$, $p = 0.032$). Thus, participants with faster VS revealed stronger intrahemispheric FC in the right DAN after task performance. Moreover, the POST run FC between right FEF and IPS was negatively correlated with the RT improvement in the Posner task (-0.676, $p < 0.001$) and also the average DAN-FC was negatively correlated with the RT improvement in the Posner task (-0.581, $p = 0.001$). Hence, participants with greater improvement in the Posner task subsequently revealed more decreased intrahemispheric FC in the DAN.

When comparing these correlation results between PRE and POST, the interaction FC*behavior became significantly different in four ($p < 0.001$) and showed a statistical trend ($p < 0.01$) in one of the comparisons (**Figure 3**).

Finally, the individual difference in FC between the POST and PRE run was correlated to the different behavioral parameters (**Table 2**, POST-PRE lines). This yielded significant inverse correlations with the RT improvement in the Posner task for the two ROI pairs FEF_L–FEF_R and FEF_L–IPS_L as well as for the DAN-FC (**Table 2**, corrected *p* always < 0.05).

TABLE 1 | Intra- and interhemispheric ROI-to-ROI functional connectivity in the DAN before (PRE) and after (POST) task performance.

ROI pairs	z-FC in PRE	z-FC in POST	Statistics
Inter-hemispheric			
FEF_L–FEF_R	1.00 (0.05)	0.98 (0.05)	n.s.
IPS_L–IPS_R	0.61 (0.05)	0.52 (0.06)	n.s.
Intra-hemispheric			
FEF_L–IPS_L	0.38 (0.04)	0.40 (0.05)	n.s.
FEF_R–IPS_R	0.69 (0.04)	0.69 (0.06)	n.s.
Whole network			
DAN	0.67 (0.03)	0.65 (0.04)	n.s.

Data are Fisher-z-transformed FC value (SEM).
Statistical comparison between rs-fMRI runs were performed using paired t-tests; n.s., not significant (p > 0.05).

DISCUSSION

Using rs-fMRI, we investigated the FC of and between core regions of the DAN (FEF and IPS) *before* (PRE) and immediately

TABLE 2 | Overview of all FC–behavior correlations.

ROI-to-ROI FC		FEF_L–FEF_R		FEF_L–IPS_L		FEF_R–IPS_R		IPS_R–IPS_L		DAN-FC	
Task performance	***Session***	***r***	***p***	***r***	***p***	***r***	***p***	***r***	***p***	***r***	***p***
Posner RT mean	*Pre*	0.114	0.573	0.043	0.832	0.108	0.592	−0.200	0.318	0.051	0.802
	Post	0.389	0.045	0.263	0.185	0.098	0.628	0.073	0.716	0.225	0.260
	Post–Pre	0.208	0.297	0.176	0.380	0.137	0.496	0.364	0.062	0.246	0.216
Posner RT change Run 1–3	*Pre*	**0.469**	**0.013**	0.354	0.070	−0.353	0.070	0.060	0.765	0.275	0.165
	Post	−0.299	0.130	−0.224	0.261	**−0.676**	**0.000**	−0.440	0.022	**−0.581**	**0.001**
	Post–Pre	**−0.635**	**0.000**	**−0.563**	**0.002**	−0.394	0.042	−0.379	0.051	**−0.651**	**0.000**
Posner RT invalid–valid	*Pre*	0.288	0.145	−0.123	0.542	−0.235	0.238	−0.325	0.098	−0.214	0.285
	Post	0.287	0.147	−0.210	0.293	−0.371	0.057	−0.370	0.058	−0.238	0.232
	Post–Pre	0.072	0.721	0.030	0.882	−0.256	0.197	−0.125	0.534	−0.059	0.769
Posner RT invalid–valid	*Pre*	−0.116	0.565	0.121	0.548	0.355	0.069	−0.090	0.654	−0.023	0.909
change Run 1–3	*Post*	0.026	0.897	0.335	0.087	0.189	0.344	−0.106	0.598	0.079	0.694
	Post–Pre	0.090	0.656	0.294	0.137	0.058	0.774	0.031	0.877	0.164	0.413
Visual Search RT mean	*Pre*	**0.527**	**0.005**	0.085	0.672	−0.364	0.062	−0.021	0.916	0.137	0.496
	Post	−0.017	0.933	−0.276	0.164	**−0.502**	**0.008**	−0.366	0.060	−0.415	0.031
	Post–Pre	−0.367	0.060	−0.393	0.042	−0.274	0.166	−0.358	0.066	−0.454	0.017
Visual search RT	*Pre*	0.288	0.146	**0.521**	**0.005**	−0.077	0.703	0.266	0.180	0.412	0.033
change Run 1–3	*Post*	0.070	0.730	0.139	0.491	−0.204	0.308	−0.185	0.356	−0.127	0.528
	Post–Pre	−0.101	0.617	−0.151	0.453	−0.119	0.554	−0.412	0.033	−0.281	0.155
Landmark ER mean	*Pre*	0.329	0.094	−0.002	0.992	0.401	0.038	−0.034	0.865	0.292	0.139
	Post	0.360	0.065	0.311	0.115	0.119	0.554	0.274	0.164	0.329	0.094
	Post–Pre	0.026	0.896	0.323	0.100	−0.281	0.156	0.238	0.233	0.094	0.640
Landmark ER change Run 1–3	*Pre*	0.140	0.485	0.036	0.859	−0.091	0.650	−0.031	0.880	0.023	0.911
	Post	0.047	0.814	0.159	0.428	−0.122	0.546	−0.080	0.690	−0.007	0.973
	Post–Pre	−0.131	0.514	0.046	0.820	−0.053	0.795	0.012	0.952	−0.051	0.800

RT, reaction time; ER, error rate; "RT invalid-valid" difference in RT between invalid and valid trials; "change Run 1–3" difference between the first and third task run; DAN-FC, mean FC of all four ROI pairs.

p-Values are uncorrected. Bold values are significant at $p < 0.05$ after correction for multiple comparisons (see main text for details).

after (POST) engagement in a set of spatial attention tasks (Posner, VS, Landmark). Beside the PRE-POST comparisons, we analyzed FC-behavior relationships for each rs-fMRI run, i.e., the respective correlation of ROI-to-ROI DAN-FC and behavioral measures of task performance. Based on the hypothesis that intrinsic functional networks determine individual cognitive abilities we expected that (i) DAN-FC strength could predict individual behavioral performance in spatial attention tasks. Furthermore, following the assumption that experiences shape functional brain networks, we expected (ii) DAN-FC to change from PRE to POST as well as the FC-behavior relationship to differ between PRE and POST.

Dorsal Attention Network -Functional Connectivity Relates to Behavioral Performance in Spatial Attention Tasks

The strength of FC in several DAN-ROI pairs was found to be related to the behavioral performance in different tasks of spatial attention. For example, an increased FC between left-hemisphere DAN regions (left FEF and IPS) was associated with better learning (improvement of RTs over time) in the VS task. Furthermore, stronger inter-hemispheric DAN-FC (bilateral FEF) predicted better learning (RT improvement) in the Posner task but counterintuitively it was also correlated with slower (not faster) RTs in the VS task. There was no significant correlation between DAN-FC and behavioral performance in the Landmark task. However, this task appeared to be too demanding with high ERs (about 40% on average) and without significant improvement (learning) over the runs. Thus, this behavioral parameter might not have been an optimal candidate for FC-behavior correlations.

As mentioned above, the correlations between PRE-task DAN-FC and behavioral parameters in VS and Posner were not unidirectional (same accounted for the POST task FC results), i.e., stronger DAN-FC was often – but not always – associated with better performance (faster mean RT or greater improvement over the runs). One reason may be that the FC between brain regions indicates a functional connection but the direction/type of influence cannot directly be inferred (Friston, 2011), being either beneficial (excitatory) or disturbing (inhibitory). Hence, an increase of FC between two connected brain areas, in which one region functionally inhibits the other, may result in worse behavioral output, whereas the FC increase between functionally synergistic regions can lead to better performance.

Despite some dissociations, our findings principally support the previous proposal of RSNs representing individual traits that may determine the personal cognitive ability of humans

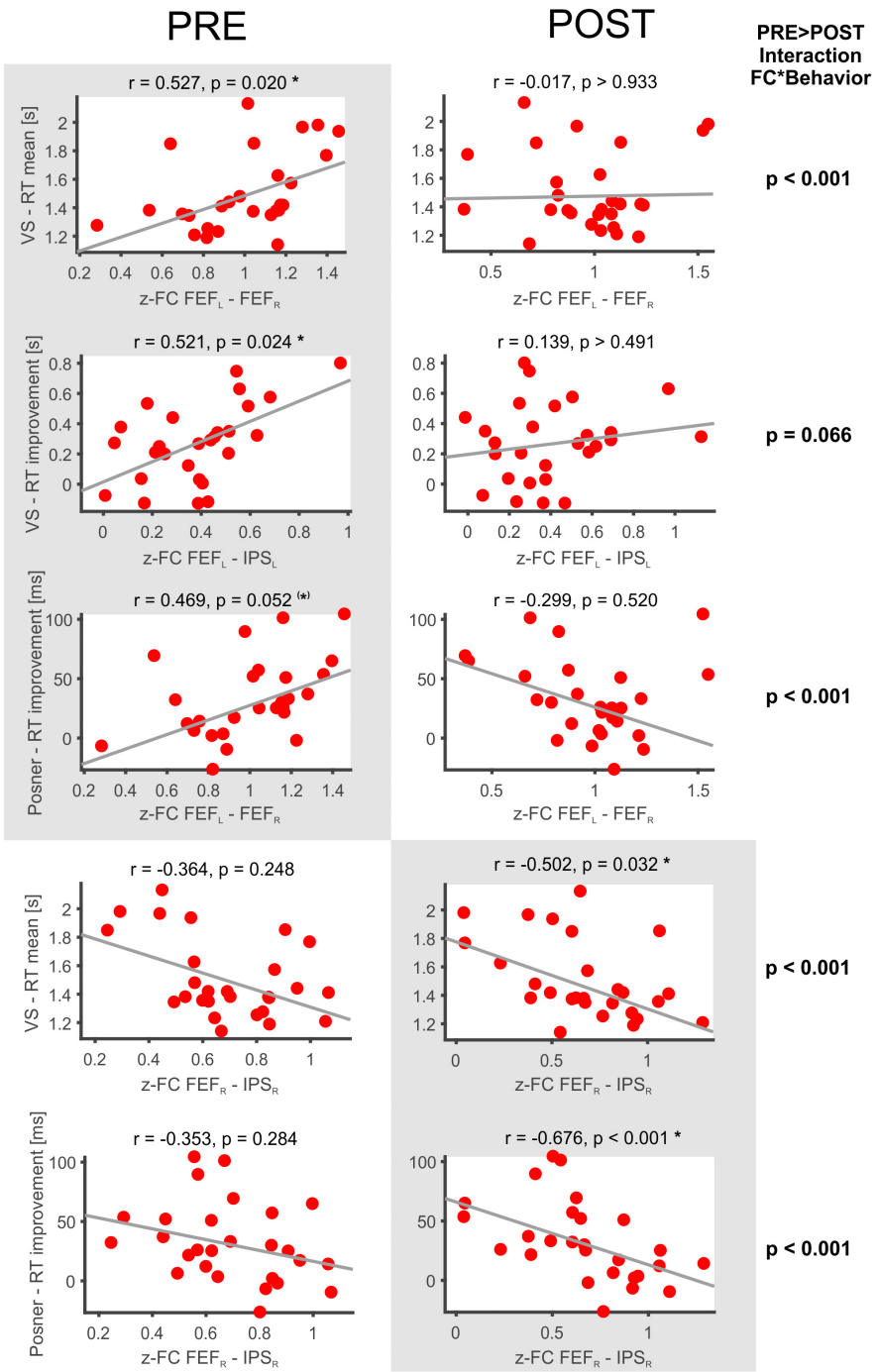

FIGURE 3 | Significant FC-behavior correlations in the PRE and POST rs-fMRI session. The z-transformed FC of several DAN-ROI pairs is correlated with measures of behavioral performance in spatial attentions tasks (mean RT, RT improvement). For each correlation, the Spearman's rank correlation coefficient (*r*) and a robust fit (gray line) is provided as well as the respective *p*-value (corrected for multiple comparisons applying Bonferroni–Holm). Significant correlations are highlighted on a gray background and marked with * (corrected $p < 0.05$) or (*) for a statistical trend ($p < 0.1$), while the non-significant counterparts in the PRE or POST condition are shown beside on a white background.

(Harmelech and Malach, 2013; Sadaghiani and Kleinschmidt, 2013). Our results underline that such a relation is also found for the DAN, which is recruited during behavioral engagement in the related functional domain (visuospatial attention). Different previous studies on the relation of pre-task FC and attentional performance stressed the importance of *between-networks* FC, specifically the functional interaction of prefrontal DAN areas and visual cortices (Baldassarre et al., 2012), of right parietal DAN

regions and dorsal anterior cingulate cortex belonging to the default mode network (Bueicheku et al., 2020) or between parietal DAN regions and remote subcortical/medial-temporal/orbito-frontal regions belonging to several different RSNs (Chou et al., 2013). In our study, the *within-network* FC of the DAN was shown to be predictive of the individual behavioral performance in spatial attention tasks. This confirms previous findings where performance in a visual signal detection task was related to pre-task FC between parietal and dorsolateral prefrontal DAN regions (Berry et al., 2017) and that attentional performance of children between 4 and 7 years was correlated to the individual FC in fronto-parietal DAN regions (Rohr et al., 2017). Studies assessing FC by use of electroencephalography (EEG-FC) also revealed the behavioral relevance of pre-task EEG-FC in DAN regions for attentional tasks involving audio-visual stimuli (Hipp et al., 2011) or visuo-motor performance (learning of mirror drawing skills) (Manuel et al., 2018). That the ongoing "spontaneous" activity in the RSNs may even be a prerequisite for the learning of skills is supported by a recent study using magnetoencephalography during engagement in a motor task. It showed that performance improvement relied on micro-offline gains acquired during the phases of rest interspersed between bouts of motor practice (Bönstrup et al., 2019).

In summary, our findings together with those of previous studies underline the predictive value of both within- and between-network FC of the DAN for the individual ability in visuo-spatial attention.

Within-Network Functional Connectivity of the Dorsal Attention Network Is Stable – And Still It Seems to Adapt Following Task Performance

As revealed by ROI-to-whole brain FC analyses, the predefined DAN core regions (bilateral IPS and FEF) were functionally connected with each other as well as with the bilateral MFG and MT+, regions that are usually considered to build the DAN (Fox et al., 2006; He et al., 2007; Hacker et al., 2013). These brain regions are also recruited during active engagement in tasks that require shifts of spatial attention (Corbetta and Shulman, 2002). The ROI-to-whole brain FC as well as the ROI-to-ROI FC did not change from the PRE- to the POST-task recording. These findings are in line with previous studies reporting the DAN to be an inter-individually reproducible (Fox et al., 2006) and intra-individually highly stable RSN (Choe et al., 2015; Finn et al., 2015). The within-network FC of the DAN remains even stable when its state changes from rest to action, as previously shown in a study that compared resting-state FC to intra-task FC while participants performed a visuospatial attention task (Spadone et al., 2015).

That there was no significant change of absolute FC values from PRE to POST in our study does not mean that the DAN is not malleable or influenceable by experience. Of note, there was a certain change in the DAN-FC from PRE to POST in that several significant FC-behavior relations were only present in the PRE but not the POST rs-fMRI session and vice versa.

Hence, there must have been some kind of reorganization of the DAN's FC between PRE and POST, either (I) in direct response to the task performance or (II) spontaneously in terms of state fluctuations. As an example, the FC-behavior relation of right FEF-IPS FC and the mean RT in the VS task was significant only in the POST session after task engagement, because only then (but not before) a faster search was associated with stronger intra-hemispheric connectivity in the right DAN. Following hypothesis I, this may indicate an early and specific adaptation of the DAN to the task demands. That a behavioral intervention (i.e., one session of task performance or a several-day cognitive training) can in principle change RSNs was previously shown for different cognitive domains. For instance, one session of a new language task was able to change the FC in the language network immediately after the task (Waites et al., 2005). A 6-weeks mnemonic training in naïve subjects induced persistent FC changes in and between the medial temporal network, DMN, and other RSNs, finally resembling those of memory athletes (Dresler et al., 2017). Regarding the DAN and visuo-spatial attention, an intense training over several days on a shape-identification task led to changes in FC between visual cortex and frontal-parietal DAN areas, which were correlated with learning effects (Lewis et al., 2009). Engaging in a visual classification task (faces or scenes) caused differential coupling between ventral frontal cortex and category-preferential visual cortex regions in subsequent periods of rest (Stevens et al., 2010). Furthermore, one session of a VS task was shown to increase the FC between the right posterior parietal cortex and the dorsolateral prefrontal cortex (Bueicheku et al., 2019). A visuo-perceptional task training (motion coherence discrimination) was shown to increase the FC of MT+ as the cortical region responsible for the processing of moving visual stimuli (Sarabi et al., 2018) but also the FC of the hippocampus as a region involved in the consolidation of early learning (Urner et al., 2013).

In the light of these studies, our findings of different FC-behavior relations in the DAN before and after performance of spatial attention tasks could be interpreted in support of task-induced DAN-FC changes. This would underline the hypothesis that the DAN – although intra-individually very stable – can be shaped by learning experiences and that RSNs may serve as a flexible, continuously updated "memory system" that helps the individual to be better prepared for upcoming cognitive challenges (Sadaghiani and Kleinschmidt, 2013; Manuel et al., 2018). It is also in line with the hypothesis that RSNs may – at least partly – be the result of learning, i.e., repetitions of task-related co-activations of different brain regions (Miall and Robertson, 2006; Harmelech and Malach, 2013; Guerra-Carrillo et al., 2014), and that this rather flexible system plays on the rigid backbone of structural connections in the brain (Sadaghiani and Kleinschmidt, 2013).

However, following hypothesis II, there is also an alternative explanation for the observed differences between the two rs-fMRI sessions (PRE/POST) regarding different FC-behavior correlations in our study: spontaneous state fluctuations over time. Previous studies accordingly emphasized the "intrinsic activity," "ongoing dynamics," or "time-varying FC" of RSNs fluctuating over seconds and minutes independent from specific inputs or outputs (Raichle, 2015; Sadaghiani et al., 2015; Kucyi et al., 2018). Ongoing intrinsic fluctuations over large-scale

networks were also shown to determine different attentional states, such as in sustained attention and task-unrelated mind wandering (Yamashita et al., 2021; Zuberer et al., 2021). The extent of these fluctuations can still influence the upcoming behavioral performance in a cognitive task explaining inter-trial (and indirectly also inter-subject) variability (Coste et al., 2011). Interestingly, when correlating the change in FC from PRE to POST with behavioral performance parameters in our cohort, smaller DAN-FC changes were associated with larger improvement in the Posner task. Hence, one could speculate that participants with a very stable "less fluctuating" DAN had better learning in this specific task. This assumption is also supported by a previous study, which showed that task-related reduction of FC variability was associated with improved behavioral performance in a letter recognition task (Elton and Gao, 2015).

Due to the design of our study, we cannot exclude that small spontaneous fluctuations of DAN-FC over time finally led to different FC-behavior correlations in the POST than in the PRE rs-fMRI session. Task-independent spontaneous state changes could even resolve some of the discrepancies in our FC-behavior correlations, for instance, that stronger post-task FC between right FEF and IPS was related to shorter RTs in VS and at the same time to smaller RT improvement in the Posner task.

Limitations

To thoroughly disentangle task-induced changes from time-varying spontaneous fluctuations of the RSN one would have required a control rs-fMRI experiment without an interleaved task performance, which was not part of this study. The modest sample size of this study might have prevented to detect smaller effects of PRE/POST FC changes due to a lack of statistical power. Furthermore, significant FC-behavior correlations in a rather small sample may be statistically inflated and may not be replicated in larger (>2000) brain-wide association studies (Marek et al., 2020). This also casts some doubt on the general assumption that rs-fMRI FC strongly indexes inter-individual differences in cognitive ability, as long as it is not replicated in larger brain-wide association studies.

CONCLUSION

In our study, the DAN was confirmed to be an intra- and inter-individually stable RSN. The significant association between the DAN's within-network FC and individual behavioral performance in spatial attention tasks underlines its functional relevance and gives rise to the importance of RSNs for individual cognitive ability. Although time-varying spontaneous fluctuations of DAN-FC cannot be fully ruled out as a confounder, the change of the relation between DAN-FC and behavioral performance measures following task performance support the concept of RSNs as a flexible internal memory system continuously shaped by learning experiences, helping individuals to meet upcoming cognitive challenges with improved performance.

DATA AVAILABILITY STATEMENT

The raw data supporting the conclusions of this article will be made available by the authors upon reasonable request.

ETHICS STATEMENT

This study was reviewed and approved by the Ethics Committee of the University of Lübeck (14-189). All subjects provided their written informed consent to participate in this study.

AUTHOR CONTRIBUTIONS

BM: conceptualization, methodology, data analysis, visualization, and writing – original draft. LB and JI: investigation and project administration. PK: visualization and software. TM: conceptualization, resources, and writing – review and editing. CH: writing – review and editing and supervision. AS: conceptualization, methodology, visualization, software, data analysis, and writing – review and editing. All authors contributed to the article and approved the submitted version.

FUNDING

This work was supported by the German Research Council (Deutsche Forschungsgemeinschaft, grant MA5332/3-1 to BM).

REFERENCES

Baldassarre, A., Lewis, C. M., Committeri, G., Snyder, A. Z., Romani, G. L., and Corbetta, M. (2012). Individual variability in functional connectivity predicts performance of a perceptual task. *Proc. Natl. Acad. Sci. U.S.A.* 109, 3516–3521. doi: 10.1073/pnas.1113148109

Berry, A. S., Sarter, M., and Lustig, C. (2017). Distinct frontoparietal networks underlying attentional effort and cognitive control. *J. Cogn. Neurosci.* 29, 1212–1225. doi: 10.1162/jocn_a_01112

Biswal, B., Yetkin, F. Z., Haughton, V. M., and Hyde, J. S. (1995). Functional connectivity in the motor cortex of resting human brain using echo-planar MRI. *Magn. Reson. Med.* 34, 537–541. doi: 10.1002/mrm.1910340409

Bönstrup, M., Iturrate, I., Thompson, R., Cruciani, G., Censor, N., and Cohen, L. G. (2019). A rapid form of offline consolidation in skill learning. *Curr. Biol.* 29, 1346–1351.e4. doi: 10.1016/j.cub.2019.02.049

Bueicheku, E., Miro-Padilla, A., and Avila, C. (2019). Resting-state fMRI detects the effects of learning in short term: a visual search training study. *Hum. Brain Mapp.* 40, 2787–2799. doi: 10.1002/hbm.24560

Bueicheku, E., Miro-Padilla, A., and Avila, C. (2020). Functional connectivity at rest captures individual differences in visual search. *Brain Struct. Funct.* 225, 537–549. doi: 10.1007/s00429-019-02008-2

Chica, A. B., Bartolomeo, P., and Valero-Cabre, A. (2011). Dorsal and ventral parietal contributions to spatial orienting in the human brain. *J. Neurosci.* 31, 8143–8149. doi: 10.1523/JNEUROSCI.5463-10.2010

Choe, A. S., Jones, C. K., Joel, S. E., Muschelli, J., Belegu, V., Caffo, B. S., et al. (2015). Reproducibility and temporal structure in weekly resting-state fMRI over a period of 3.5 years. *PLoS One* 10:e0140134. doi: 10.1371/journal.pone.0140134

Chou, Y. H., Chen, N. K., and Madden, D. J. (2013). Functional brain connectivity and cognition: effects of adult age and task demands. *Neurobiol. Aging* 34, 1925–1934. doi: 10.1016/j.neurobiolaging.2013.02.012

Corbetta, M., Akbudak, E., Conturo, T. E., Snyder, A. Z., Ollinger, J. M., Drury, H. A., et al. (1998). A common network of functional areas for attention and eye movements. *Neuron* 21, 761–773. doi: 10.1016/s0896-6273(00)80593-0

Corbetta, M., and Shulman, G. L. (2002). Control of goal-directed and stimulus-driven attention in the brain. *Nat. Rev. Neurosci.* 3, 201–215. doi: 10.1038/nrn755

Corbetta, M., and Shulman, G. L. (2011). Spatial neglect and attention networks. *Annu. Rev. Neurosci.* 34, 569–599. doi: 10.1146/annurev-neuro-061010-113731

Coste, C. P., Sadaghiani, S., Friston, K. J., and Kleinschmidt, A. (2011). Ongoing brain activity fluctuations directly account for intertrial and indirectly for intersubject variability in Stroop task performance. *Cereb. Cortex* 21, 2612–2619. doi: 10.1093/cercor/bhr050

Damoiseaux, J. S., Rombouts, S. A., Barkhof, F., Scheltens, P., Stam, C. J., Smith, S. M., et al. (2006). Consistent resting-state networks across healthy subjects. *Proc. Natl. Acad. Sci. U.S.A.* 103, 13848–13853. doi: 10.1073/pnas.0601417103

Doricchi, F., Macci, E., Silvetti, M., and Macaluso, E. (2010). Neural correlates of the spatial and expectancy components of endogenous and stimulus-driven orienting of attention in the Posner task. *Cereb. Cortex* 20, 1574–1585. doi: 10.1093/cercor/bhp215

Dresler, M., Shirer, W. R., Konrad, B. N., Muller, N. C. J., Wagner, I. C., Fernandez, G., et al. (2017). Mnemonic training reshapes brain networks to support superior memory. *Neuron* 93, 1227–1235.e6. doi: 10.1016/j.neuron.2017.02.003

DuMouchel, W. H., and O'Brian, F. L. (1989). "Integrating a robust option into a multiple regression computing environment," in *Proceedings of the 21st Symposium on the Interface. Computer Science and Statistics* (Alexandria, VA: American Statistical Association).

Ellison, A., Schindler, I., Pattison, L. L., and Milner, A. D. (2004). An exploration of the role of the superior temporal gyrus in visual search and spatial perception using TMS. *Brain* 127, 2307–2315. doi: 10.1093/brain/awh244

Elton, A., and Gao, W. (2015). Task-related modulation of functional connectivity variability and its behavioral correlations. *Hum. Brain Mapp.* 36, 3260–3272. doi: 10.1002/hbm.22847

Fink, G. R., Marshall, J. C., Shah, N. J., Weiss, P. H., Halligan, P. W., Grosse-Ruyken, M., et al. (2000). Line bisection judgments implicate right parietal cortex and cerebellum as assessed by fMRI. *Neurology* 54, 1324–1331. doi: 10.1212/wnl.54.6.1324

Finn, E. S., Shen, X., Scheinost, D., Rosenberg, M. D., Huang, J., Chun, M. M., et al. (2015). Functional connectome fingerprinting: identifying individuals using patterns of brain connectivity. *Nat. Neurosci.* 18, 1664–1671. doi: 10.1038/nn.4135

Fox, M. D., Corbetta, M., Snyder, A. Z., Vincent, J. L., and Raichle, M. E. (2006). Spontaneous neuronal activity distinguishes human dorsal and ventral attention systems. *Proc. Natl. Acad. Sci. U.S.A* 103, 10046–10051. doi: 10.1073/pnas.0604187103

Fox, M. D., and Raichle, M. E. (2007). Spontaneous fluctuations in brain activity observed with functional magnetic resonance imaging. *Nat. Rev. Neurosci.* 8, 700–711. doi: 10.1038/nrn2201

Fox, M. D., Snyder, A. Z., Vincent, J. L., and Raichle, M. E. (2007). Intrinsic fluctuations within cortical systems account for intertrial variability in human behavior. *Neuron* 56, 171–184. doi: 10.1016/j.neuron.2007.08.023

Friston, K. J. (2011). Functional and effective connectivity: a review. *Brain Connect.* 1, 13–36. doi: 10.1089/brain.2011.0008

Guerra-Carrillo, B., Mackey, A. P., and Bunge, S. A. (2014). Resting-state fMRI: a window into human brain plasticity. *Neuroscientist* 20, 522–533. doi: 10.1177/1073858414524442

Guidotti, R., Del Gratta, C., Baldassarre, A., Romani, G. L., and Corbetta, M. (2015). Visual learning induces changes in resting-state fMRI multivariate pattern of information. *J. Neurosci.* 35, 9786–9798. doi: 10.1523/JNEUROSCI.3920-14.2015

Hacker, C. D., Laumann, T. O., Szrama, N. P., Baldassarre, A., Snyder, A. Z., Leuthardt, E. C., et al. (2013). Resting state network estimation in individual subjects. *Neuroimage* 82, 616–633. doi: 10.1016/j.neuroimage.2013.05.108

Harmelech, T., and Malach, R. (2013). Neurocognitive biases and the patterns of spontaneous correlations in the human cortex. *Trends Cogn. Sci.* 17, 606–615. doi: 10.1016/j.tics.2013.09.014

He, B. J., Snyder, A. Z., Vincent, J. L., Epstein, A., Shulman, G. L., and Corbetta, M. (2007). Breakdown of functional connectivity in frontoparietal networks underlies behavioral deficits in spatial neglect. *Neuron* 53, 905–918. doi: 10.1016/j.neuron.2007.02.013

Hipp, J. F., Engel, A. K., and Siegel, M. (2011). Oscillatory synchronization in large-scale cortical networks predicts perception. *Neuron* 69, 387–396. doi: 10.1016/j.neuron.2010.12.027

Kucyi, A., Tambini, A., Sadaghiani, S., Keilholz, S., and Cohen, J. R. (2018). Spontaneous cognitive processes and the behavioral validation of time-varying brain connectivity. *Netw. Neurosci.* 2, 397–417. doi: 10.1162/netn_a_00037

Lewis, C. M., Baldassarre, A., Committeri, G., Romani, G. L., and Corbetta, M. (2009). Learning sculpts the spontaneous activity of the resting human brain. *Proc. Natl. Acad. Sci. U.S.A.* 106, 17558–17563. doi: 10.1073/pnas.0902455106

Lowe, M. J., Mock, B. J., and Sorenson, J. A. (1998). Functional connectivity in single and multislice echoplanar imaging using resting-state fluctuations. *Neuroimage* 7, 119–132. doi: 10.1006/nimg.1997.0315

Machner, B., Könemund, I., Von Der Gablentz, J., Bays, P. M., and Sprenger, A. (2018). The ipsilesional attention bias in right-hemisphere stroke patients as revealed by a realistic visual search task: neuroanatomical correlates and functional relevance. *Neuropsychology* 32, 850–865. doi: 10.1037/neu0000493

Machner, B., Lencer, M. C., Moller, L., Von Der Gablentz, J., Heide, W., Helmchen, C., et al. (2020a). Unbalancing the attentional priority map via gaze-contingent displays induces neglect-like visual exploration. *Front. Hum. Neurosci.* 14:41. doi: 10.3389/fnhum.2020.00041

Machner, B., Von Der Gablentz, J., Gottlich, M., Heide, W., Helmchen, C., Sprenger, A., et al. (2020b). Behavioral deficits in left hemispatial neglect are related to a reduction of spontaneous neuronal activity in the right superior parietal lobule. *Neuropsychologia* 138:107356. doi: 10.1016/j.neuropsychologia.2020.107356

Manuel, A. L., Guggisberg, A. G., Theze, R., Turri, F., and Schnider, A. (2018). Resting-state connectivity predicts visuo-motor skill learning. *Neuroimage* 176, 446–453.

Marek, S., Tervo-Clemmens, B., Calabro, F., Montez, D., Kay, B., Hatoum, A., et al. (2020). Towards reproducible brain-wide association studies. *bioRxiv* [Preprint] doi: 10.1101/2020.08.21.257758

Miall, R. C., and Robertson, E. M. (2006). Functional imaging: is the resting brain resting? *Curr. Biol.* 16, R998–R1000. doi: 10.1016/j.cub.2006.10.041

Milner, A. D., Harvey, M., Roberts, R. C., and Forster, S. V. (1993). Line bisection errors in visual neglect: misguided action or size distortion? *Neuropsychologia* 31, 39–49. doi: 10.1016/0028-3932(93)90079-f

Nobre, A. C., Coull, J. T., Walsh, V., and Frith, C. D. (2003). Brain activations during visual search: contributions of search efficiency versus feature binding. *Neuroimage* 18, 91–103. doi: 10.1006/nimg.2002.1329

Oldfield, R. C. (1971). The assessment and analysis of handedness: the Edinburgh inventory. *Neuropsychologia* 9, 97–113. doi: 10.1016/0028-3932(71)90067-4

Osher, D. E., Brissenden, J. A., and Somers, D. C. (2019). Predicting an individual's dorsal attention network activity from functional connectivity fingerprints. *J. Neurophysiol.* 122, 232–240. doi: 10.1152/jn.00174.2019

Posner, M. I., and Petersen, S. E. (1990). The attention system of the human brain. *Annu. Rev. Neurosci.* 13, 25–42.

Posner, M. I., Walker, J. A., Friedrich, F. J., and Rafal, R. D. (1984). Effects of parietal injury on covert orienting of attention. *J. Neurosci.* 4, 1863–1874. doi: 10.1523/jneurosci.04-07-01863.1984

Power, J. D., Barnes, K. A., Snyder, A. Z., Schlaggar, B. L., and Petersen, S. E. (2012). Spurious but systematic correlations in functional connectivity MRI networks arise from subject motion. *Neuroimage* 59, 2142–2154. doi: 10.1016/j.neuroimage.2011.10.018

Raichle, M. E. (2015). The restless brain: how intrinsic activity organizes brain function. *Philos. Trans. R. Soc. Lond. B Biol. Sci.* 370:20140172. doi: 10.1098/rstb.2014.0172

Rengachary, J., He, B. J., Shulman, G. L., and Corbetta, M. (2011). A behavioral analysis of spatial neglect and its recovery after stroke. *Front. Hum. Neurosci.* 5:29. doi: 10.3389/fnhum.2011.00029

Revill, K. P., Karnath, H. O., and Rorden, C. (2011). Distinct anatomy for visual search and bisection: a neuroimaging study. *Neuroimage* 57, 476–481. doi: 10.1016/j.neuroimage.2011.04.066

Rohr, C. S., Vinette, S. A., Parsons, K. A. L., Cho, I. Y. K., Dimond, D., Benischek, A., et al. (2017). Functional connectivity of the dorsal attention network predicts selective attention in 4-7 year-old girls. *Cereb. Cortex* 27, 4350–4360. doi: 10.1093/cercor/bhw236

Sadaghiani, S., and Kleinschmidt, A. (2013). Functional interactions between intrinsic brain activity and behavior. *Neuroimage* 80, 379–386. doi: 10.1016/j.neuroimage.2013.04.100

Sadaghiani, S., Poline, J. B., Kleinschmidt, A., and D'esposito, M. (2015). Ongoing dynamics in large-scale functional connectivity predict perception. *Proc. Natl. Acad. Sci. U.S.A.* 112, 8463–8468. doi: 10.1073/pnas.1420687112

Sarabi, M. T., Aoki, R., Tsumura, K., Keerativittayayut, R., Jimura, K., and Nakahara, K. (2018). Visual perceptual training reconfigures post-task resting-state functional connectivity with a feature-representation region. *PLoS One* 13:e0196866. doi: 10.1371/journal.pone.0196866

Schenkenberg, T., Bradford, D. C., and Ajax, E. T. (1980). Line bisection and unilateral visual neglect in patients with neurologic impairment. *Neurology* 30, 509–517. doi: 10.1212/wnl.30.5.509

Shulman, G. L., Astafiev, S. V., Franke, D., Pope, D. L., Snyder, A. Z., Mcavoy, M. P., et al. (2009). Interaction of stimulus-driven reorienting and expectation in ventral and dorsal frontoparietal and basal ganglia-cortical networks. *J. Neurosci.* 29, 4392–4407. doi: 10.1523/JNEUROSCI.5609-08.2009

Smith, S. M., Fox, P. T., Miller, K. L., Glahn, D. C., Fox, P. M., Mackay, C. E., et al. (2009). Correspondence of the brain's functional architecture during activation and rest. *Proc. Natl. Acad. Sci. U.S.A.* 106, 13040–13045. doi: 10.1073/pnas.0905267106

Spadone, S., Della Penna, S., Sestieri, C., Betti, V., Tosoni, A., Perrucci, M. G., et al. (2015). Dynamic reorganization of human resting-state networks during visuospatial attention. *Proc. Natl. Acad. Sci U.S.A.* 112, 8112–8117. doi: 10.1073/pnas.1415439112

Stevens, W. D., Buckner, R. L., and Schacter, D. L. (2010). Correlated low-frequency BOLD fluctuations in the resting human brain are modulated by recent experience in category-preferential visual regions. *Cereb. Cortex* 20, 1997–2006. doi: 10.1093/cercor/bhp270

Szczepanski, S. M., Pinsk, M. A., Douglas, M. M., Kastner, S., and Saalmann, Y. B. (2013). Functional and structural architecture of the human dorsal frontoparietal attention network. *Proc. Natl. Acad. Sci. U.S.A.* 110, 15806–15811. doi: 10.1073/pnas.1313903110

Thiel, C. M., Zilles, K., and Fink, G. R. (2004). Cerebral correlates of alerting, orienting and reorienting of visuospatial attention: an event-related fMRI study. *Neuroimage* 21, 318–328. doi: 10.1016/j.neuroimage.2003.08.044

Urner, M., Schwarzkopf, D. S., Friston, K., and Rees, G. (2013). Early visual learning induces long-lasting connectivity changes during rest in the human brain. *Neuroimage* 77, 148–156. doi: 10.1016/j.neuroimage.2013.03.050

Van Dijk, K. R., Sabuncu, M. R., and Buckner, R. L. (2012). The influence of head motion on intrinsic functional connectivity MRI. *Neuroimage* 59, 431–438. doi: 10.1016/j.neuroimage.2011.07.044

Vossel, S., Thiel, C. M., and Fink, G. R. (2006). Cue validity modulates the neural correlates of covert endogenous orienting of attention in parietal and frontal cortex. *Neuroimage* 32, 1257–1264. doi: 10.1016/j.neuroimage.2006.05.019

Waites, A. B., Stanislavsky, A., Abbott, D. F., and Jackson, G. D. (2005). Effect of prior cognitive state on resting state networks measured with functional connectivity. *Hum. Brain Mapp.* 24, 59–68. doi: 10.1002/hbm.20069

Yamashita, A., Rothlein, D., Kucyi, A., Valera, E. M., and Esterman, M. (2021). Brain state-based detection of attentional fluctuations and their modulation. *Neuroimage* 236:118072. doi: 10.1016/j.neuroimage.2021.118072

Yan, C. G., Wang, X. D., Zuo, X. N., and Zang, Y. F. (2016). DPABI: data processing & analysis for (resting-state) brain imaging. *Neuroinformatics* 14, 339–351.

Zuberer, A., Kucyi, A., Yamashita, A., Wu, C. M., Walter, M., Valera, E. M., et al. (2021). Integration and segregation across large-scale intrinsic brain networks as a marker of sustained attention and task-unrelated thought. *Neuroimage* 229:117610. doi: 10.1016/j.neuroimage.2020.117610

Conflict of Interest: The authors declare that the research was conducted in the absence of any commercial or financial relationships that could be construed as a potential conflict of interest.

Publisher's Note: All claims expressed in this article are solely those of the authors and do not necessarily represent those of their affiliated organizations, or those of the publisher, the editors and the reviewers. Any product that may be evaluated in this article, or claim that may be made by its manufacturer, is not guaranteed or endorsed by the publisher.

frontiers in Human Neuroscience

ORIGINAL RESEARCH
published: 21 February 2022
doi: 10.3389/fnhum.2022.749767

The Relationship Between Default Mode and Dorsal Attention Networks Is Associated With Depressive Disorder Diagnosis and the Strength of Memory Representations Acquired Prior to the Resting State Scan

*Skye Satz[1], Yaroslav O. Halchenko[2], Rachel Ragozzino[1], Mora M. Lucero[1], Mary L. Phillips[1], Holly A. Swartz[1] and Anna Manelis[1]**

[1] Department of Psychiatry, Western Psychiatric Institute and Clinic, University of Pittsburgh Medical Center, University of Pittsburgh, Pittsburgh, PA, United States, [2] Department of Psychological and Brain Sciences, Dartmouth College, Hanover, NH, United States

OPEN ACCESS

Edited by:
Ruben Sanchez-Romero, Rutgers University, United States

Reviewed by:
Ruiyang Ge, University of British Columbia, Canada
Kristen Ellard, Massachusetts General Hospital and Harvard Medical School, United States

***Correspondence:**
Anna Manelis
anna.manelis@gmail.com

Specialty section:
This article was submitted to Cognitive Neuroscience, a section of the journal Frontiers in Human Neuroscience

Received: *29 July 2021*
Accepted: *01 February 2022*
Published: *21 February 2022*

Citation:
Satz S, Halchenko YO, Ragozzino R, Lucero MM, Phillips ML, Swartz HA and Manelis A (2022) The Relationship Between Default Mode and Dorsal Attention Networks Is Associated With Depressive Disorder Diagnosis and the Strength of Memory Representations Acquired Prior to the Resting State Scan. Front. Hum. Neurosci. 16:749767. doi: 10.3389/fnhum.2022.749767

Previous research indicates that individuals with depressive disorders (DD) have aberrant resting state functional connectivity and may experience memory dysfunction. While resting state functional connectivity may be affected by experiences preceding the resting state scan, little is known about this relationship in individuals with DD. Our study examined this question in the context of object memory. 52 individuals with DD and 45 healthy controls (HC) completed clinical interviews, and a memory encoding task followed by a forced-choice recognition test. A 5-min resting state fMRI scan was administered immediately after the forced-choice task. Resting state networks were identified using group Independent Component Analysis across all participants. A network modeling analysis conducted on 22 networks using FSLNets examined the interaction effect of diagnostic status and memory accuracy on the between-network connectivity. We found that this interaction significantly affected the relationship between the network comprised of the medial prefrontal cortex, posterior cingulate cortex, and hippocampal formation and the network comprised of the inferior temporal, parietal, and prefrontal cortices. A stronger positive correlation between these two networks was observed in individuals with DD who showed higher memory accuracy, while a stronger negative correlation (i.e., anticorrelation) was observed in individuals with DD who showed lower memory accuracy prior to resting state. No such effect was observed for HC. The former network cross-correlated with the default mode network (DMN), and the latter cross-correlated with the dorsal attention network (DAN). Considering that the DMN and DAN typically anticorrelate, we hypothesize that our findings indicate aberrant reactivation and consolidation processes that occur after the task is completed. Such aberrant processes may lead to continuous "replay" of previously learned, but currently irrelevant, information and underlie rumination in depression.

Keywords: resting state, fMRI, functional connectivity, depression, memory, default mode network, dorsal attention network

INTRODUCTION

Resting state neuroimaging techniques examine brain activation and functional connectivity in the absence of stimuli or tasks. Previous studies characterized a set of networks in which brain regions co-activate during resting state (Beckmann et al., 2005; Damoiseaux et al., 2006; De Luca et al., 2006; Smith et al., 2009; Biswal et al., 2010; van den Heuvel and Hulshoff Pol, 2010; Yeo et al., 2011; Lv et al., 2018). Resting state functional connectivity may be related to sustained information processing (Gusnard and Raichle, 2001) as well as environment monitoring and internal thought processes (Buckner et al., 2008) that can dynamically change based on the experiences preceding the resting state scan (Daselaar et al., 2010; Sami et al., 2014; Cecchetto et al., 2019) as well as predict task performance that follows the resting state scan (Tambini et al., 2010; Sala-Llonch et al., 2012; López Zunini et al., 2013; Reineberg et al., 2015).

Resting state functional connectivity is altered in a variety of psychiatric illnesses (Greicius, 2008; Zhang and Raichle, 2010) including depressive disorders (Greicius et al., 2007; Woodward and Cascio, 2015; Zhang et al., 2021). Depressive disorders (DD) (e.g., major depressive and persistent depressive disorders) are characterized by feelings of sadness, loss of interest and motivation, fatigue, anhedonia, feelings of hopelessness, worthlessness and guilt, as well as changes in sleeping, eating, and overall cognitive and psychosocial functioning (First et al., 2015). In addition, individuals with DD may experience memory dysfunction (Burt et al., 1995; Williams et al., 2007; Hamilton and Gotlib, 2008; Vasic et al., 2009; Gotlib and Joormann, 2010; Dillon and Pizzagalli, 2018; Ge et al., 2019). Previous neuroimaging studies found elevated connectivity within the default mode network (DMN) as well as between the DMN and non-DMN regions, including the dorsal attention network (DAN), insula, thalamus, and subgenual cingulate in individuals with DD relative to healthy controls (HC) (Sheline et al., 2010; Scalabrini et al., 2020). Clinical features of depression, such as symptom severity, illness duration, medication status and, most notably, ruminative and self-referential thought, have been linked to disruption of the cognitive control, salience, and default mode networks (Greicius et al., 2007; Bluhm et al., 2009; Sheline et al., 2010; Zeng et al., 2012; Brakowski et al., 2017; Scalabrini et al., 2020).

Mind wandering (Kucyi and Davis, 2014; Chou et al., 2017) and experiencing self-referential thoughts (Sheline et al., 2009) and spontaneous rumination (Rosenbaum et al., 2017) might be related to intentional or unintentional reactivation of memory representations that participants encountered prior to the resting state scan and memory consolidation (Sami et al., 2014). During memory consolidation, recently formed memories change into stable memory representations through reorganization and transitioning of hippocampal-dependent to neocortex supported memories (Squire et al., 2015). Memory representations can be reactivated during stimulus re-study (Vilberg and Davachi, 2013), memory tests (Manelis et al., 2011), or spontaneously during rest following stimuli encoding (Deuker et al., 2013; Wittkuhn and Schuck, 2021). The latter is particularly relevant for the study of psychiatric disorders as it might explain such phenomena as depressive rumination, obsessive thoughts, and other aberrant forms of cognition. Given that the majority of previous studies focused on healthy individuals and administered the resting state scan following stimulus encoding and prior to a memory test (Tambini et al., 2010; Tambini and Davachi, 2013; Schlichting and Prestona, 2014; Tompary et al., 2015; Murty et al., 2017), little is known about how the accuracy of memories acquired prior to the resting state scan is related to functional connectivity within and between resting state networks in individuals with DD, compared to HC.

Our study examined whether the relationship between memory retrieval accuracy for recently encoded stimuli and resting state functional connectivity was moderated by diagnostic status. The experimental paradigm consisted of the encoding phase, during which participants encountered pictures of objects and tried to memorize them, the forced-choice recognition task, and the subsequent resting state scan in which the memorized stimuli were no longer relevant. Memory encoding, retrieval, and consolidation involve the hippocampus (Nadel and Moscovitch, 1997; Squire et al., 2015). Considering that the hippocampus is a part of the DMN (Buckner et al., 2008; Andrews-Hanna et al., 2010b) that has aberrant functional connectivity in individuals with DD (Sheline et al., 2009; Marchetti et al., 2012; Scalabrini et al., 2020) and that individuals with DD have difficulty disengaging from previously learned information (Xia and Evans, 2020), we hypothesized that memory accuracy in individuals with DD would be associated with aberrant DMN connectivity relative to HC.

MATERIALS AND METHODS

Participants

This study was approved by the University of Pittsburgh Institutional Review Board. Participants were recruited from the community, universities, and counseling and medical centers through referrals and advertisements. Written informed consent was obtained from all participants. Participants were right-handed, fluent in English, and matched on age, sex, and IQ. HC had no personal or family history of psychiatric disorders. Symptomatic participants met DSM-5 criteria for a depressive disorder (DD) such as major depressive disorder (MDD) or persistent depressive disorder (PDD).

Neuroimaging data were collected from 114 participants (53 HC and 61 DD). A total of 17 participants were excluded from the analyses due to excessive motion (>2 mm translation; 7 HC and 5 DD), poor data quality due to scanner noise (1 DD) or falling asleep during the resting state scan (1 HC and 3 DD). The final sample included 45 HC and 52 DD for a total of 97 participants. Of the 52 individuals with DD, 35 were diagnosed with MDD and 17 were diagnosed with PDD. MDD and PDD differ in some characteristics, such as symptom duration and severity, yet display substantial overlap in symptomatology (First et al., 2015). Of the 17 individuals with PDD, 13 had intermittent major depressive episodes, a clinical feature making the

symptom profiles of MDD and PDD difficult to differentiate (Schramm et al., 2020).

Clinical Assessment

All diagnoses were made by a trained clinician and confirmed by a psychiatrist according to DSM-5 criteria using the SCID-5 clinical interview (First et al., 2015). We also collected information about current depression symptoms using the Hamilton Depression Rating Scale (HDRS-25) (Hamilton, 1960) and lifetime dimensional symptoms of depression using the MOODS-SR (Dell'Osso et al., 2002). A total psychotropic medication load was calculated for each participant, with greater numbers and doses of medications corresponding to a greater medication load (Hassel et al., 2008; Manelis et al., 2016). Exclusion criteria included a history of head injury, metal in the body, pregnancy, claustrophobia, neurodevelopmental disorders, systemic medical illness, premorbid IQ < 85 per the National Adult Reading Test (Nelson, 1982), current alcohol/drug abuse, the YMRS (Young et al., 1978) scores >10 at scan, and meeting criteria for any psychotic-spectrum disorder. **Table 1** reports group statistics for participants' demographic and clinical characteristics.

Memory Encoding and Retrieval

The experimental paradigm is depicted on **Figure 1**. During encoding, participants were presented with 48 pictures of common objects and food items (Blechert et al., 2014). To ensure deep information processing, they were instructed to rate each stimulus as pleasant or unpleasant (Richardson-Klavehn, 2010; Schott et al., 2013), and to memorize the presented stimuli. Approximately 25 min after encoding, participants performed the forced-choice object recognition task in which they were presented with pictures of an old (seen previously) and a novel (not seen previously) stimulus side-by-side and were required to select the old stimulus by pressing a corresponding button. The task consisted of 48 trials. The set of the novel stimuli was obtained from the same database as the set of the old stimuli (Blechert et al., 2014) and consisted of the items that categorically matched and visually resembled old stimuli (i.e., were from subordinate categories of old items). The pairings of novel and old stimuli were assigned randomly so that the old stimulus could be paired with a similar novel stimulus (e.g., blue chair and yellow chair), or a novel stimulus from a different category (e.g., bread and tomatoes). Each old stimulus had a closely resembling novel stimulus; therefore, participants had to have a detailed memory representation of an old stimulus to correctly identify it as old. The memory accuracy was calculated as a percent of correct responses relative to a total number of responses. While participants were scanned during both the encoding and forced-choice tasks, the neuroimaging results of these tasks will be described in separate reports.

The scans administered between encoding and forced choice object recognition tasks included spin-echo field maps in the posterior-to-anterior and anterior-to-posterior phase encoding directions (30 s each), a 7-min T1w anatomical scan, a 6.5-min T2w anatomical scan, and a forced-choice recognition task for face stimuli (approximately 10 min) that were encoded before the objects in the separate task.

Resting State Scan

Immediately following the forced-choice recognition task, participants completed a 5-min resting state scan in which they were asked to look at the fixation star presented in the center of the screen and to stay awake. We used an eye-tracking camera system to monitor the participants' wakefulness during the scan and made a note if a participant fell asleep or kept their eyes closed for more than 20 s. Participants also self-reported their wakefulness after the resting state scan.

Neuroimaging Data Acquisition

The neuroimaging data were collected at the University of Pittsburgh/UPMC Magnetic Resonance Research Center (MRRC) using a 3T Siemens Prisma scanner with a 64-channel head coil. The acquisition series were named according to the ReproIn naming convention (Visconti di Oleggio Castello et al., 2020). The EPI data were collected in the anterior-to-posterior direction using a multi-band sequence (factor = 8, TR = 800 ms, resolution = 2 × 2 × 2 mm, FOV = 210 mm, TE = 30 ms, flip angle = 52°, 72 slices, 375 volumes). High-resolution T1w images were collected using the MPRAGE sequence (TR = 2,400 ms, resolution = 0.8 × 0.8 × 0.8 mm, 208 slices, FOV = 256 mm, TE = 2.22 ms, flip angle = 8°). Field maps were collected in the AP and PA directions using the spin echo sequence (TR = 8,000 ms, resolution = 2 × 2 × 2 mm, FOV = 210 mm, TE = 66 ms, flip angle = 90°, 72 slices).

Data Analyses

Demographic and Clinical Data Analysis

The demographic and clinical characteristics were compared between DD and HC groups using *t*- and chi-square tests.

Memory Retrieval Analysis

We used *t*-tests to compare recognition accuracy and response time (RT) in DD vs. HC groups. RT was calculated across trials with correct responses only.

Neuroimaging Data Analysis

Preprocessing

The DICOM images were converted to BIDS standard using *heudiconv version 0.5.4* (Halchenko et al., 2019; RRID:SCR_017427) After that, the images were preprocessed using *fMRIPrep version 20.1.2* (Esteban et al., 2019; RRID:SCR_016216). First, a reference volume and its skull-stripped version were generated using a custom methodology of *fMRIPrep*. Head-motion parameters with respect to the BOLD reference (transformation matrices, and six corresponding rotation and translation parameters) are estimated before any spatiotemporal filtering using mcflirt (FSL 5.0.9, (Jenkinson et al., 2002; RRID:SCR_002823). BOLD runs were slice-time corrected using *3dTshift* (Cox and Hyde, 1997), (AFNI 20160207; RRID:SCR_005927). A B0-non-uniformity map (or fieldmap) was estimated based on two echo-planar imaging (EPI) references with opposing phase-encoding directions, with

TABLE 1 | Demographic and clinical characteristics.

	HC	UD	Statistics HC vs. UD
Number of participants	45	52	
Gender composition (number females)	33	42	$chi^2 = 0.40$, $p = 0.53$
UD diagnoses (MDD/PDD)	na	35/17	na
Age (years)	29.02 (1.00)	28.20 (0.93)	$t(95) = 0.60$, $p = 0.55$
BMI	26.12 (0.69)	25.25 (0.54)	$t(95) = 1.01$, $p = 0.31$
IQ (NART)	106.79 (0.81)	109.40 (1.01)	$t(95) = -1.97$, $p = 0.052$
Current depression severity (HDRS-25)	1.69 (0.31)	12.81 (0.98)	$t(95) = -10.18$, $p < 0.001$
Current mania severity (YMRS)	0.267 (0.12)	1.17 (0.20)	$t(95) = -3.69$, $p < 0.001$
Lifetime depression (MOODS-SR)	2.09 (0.34)	18.65 (0.57)	$t(95) = -24.05$, $p < 0.001$
Illness Onset (year of age)	na	14.90 (0.50)	na
Number of participants taking Antidepressants	na	34	na
Number of participants taking Mood stabilizers	na	2	na
Number of participants taking Antipsychotics	na	1	na
Number of participants taking Benzodiazepines	na	7	na
Number of participants taking Stimulants	na	4	na
A mean number of psychotropic medications	na	1.10 (0.14)	na
A mean total medication load	na	1.40 (0.19)	na
Number of participants with comorbid diagnoses	na	34	na

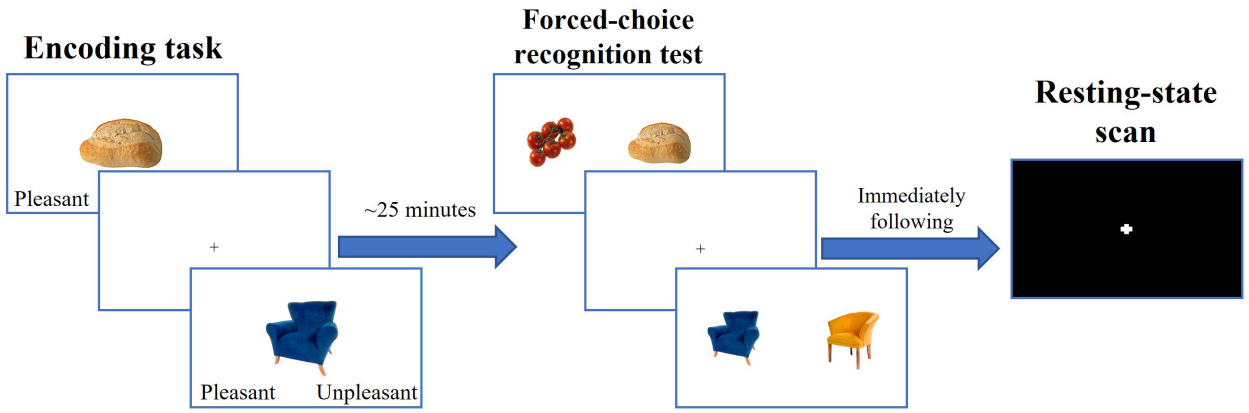

FIGURE 1 | Experimental paradigm.

3dQwarp (Cox and Hyde, 1997) (AFNI 20160207). Based on the estimated susceptibility distortion, a corrected EPI (echo-planar imaging) reference was calculated for a more accurate co-registration with the anatomical reference. The BOLD reference was then co-registered to the T1w reference using *bbregister* (FreeSurfer) (Dale et al., 1999; RRID:SCR_001847) which implements boundary-based registration (Greve and Fischl, 2009). Co-registration was configured with six degrees of freedom. The BOLD time-series were resampled onto the following surfaces (FreeSurfer reconstruction nomenclature): *fsaverage*. The BOLD time-series (including slice-timing correction) were resampled onto their original, native space by applying a single, composite transform to correct for head-motion and susceptibility distortions. These resampled BOLD time-series will be referred to as preprocessed BOLD in original space, or just preprocessed BOLD. The BOLD time-series were resampled into standard space, generating a preprocessed BOLD run in MNI152NLin2009cAsym space. Automatic removal of motion artifacts using independent component analysis (ICA-AROMA) (Pruim et al., 2015) was performed on the preprocessed BOLD on MNI space time-series after removal of non-steady state volumes and spatial smoothing with an isotropic, Gaussian kernel of 6 mm full-width half-maximum (FWHM). Corresponding "non-aggressively" denoised runs were produced after such smoothing. Additionally, the aggressive noise-regressors were collected and placed in the corresponding confounds file. All resamplings were performed with a single interpolation step by composing all the pertinent transformations (i.e., head-motion transform matrices, susceptibility distortion correction when available, and co-registrations to anatomical and output spaces). Gridded (volumetric) resamplings were performed using *antsApplyTransforms* (ANTs), configured with Lanczos interpolation to minimize the smoothing effects of other kernels

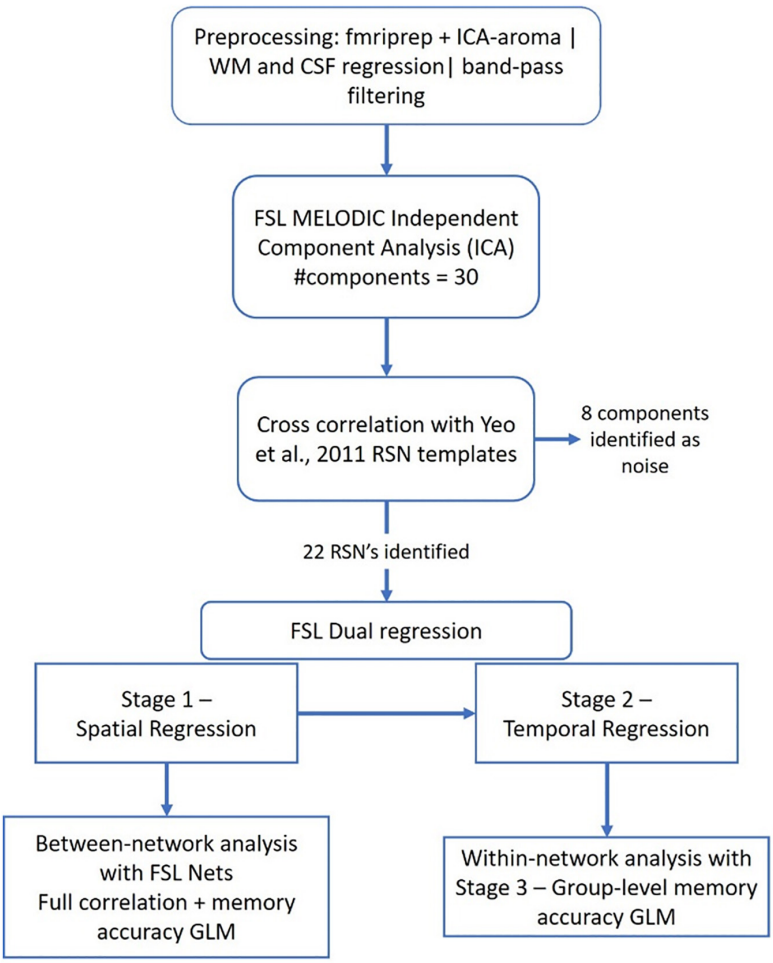

FIGURE 2 | Processing pipeline for the resting state data analysis.

(Lanczos, 1964). Non-gridded (surface) resamplings were performed using mri_vol2surf (FreeSurfer).

While *fMRIPrep* automatically extracts the three global signals within the CSF, the WM, and the whole-brain masks, they are extracted prior to removal of motion artifacts using ICA-AROMA (Pruim et al., 2015). Therefore, instead of using the automatically generated values, we extracted these signals after running the ICA-AROMA (from the files with the suffix "space-MNI152NLin6Asym_desc-smoothAROMAnonaggr_bold") and regressed the CSF and WM from preprocessed resting state data. After that, the data were band-pass temporal filtered (0.01–0.1 Hz). The processing pipeline is depicted in **Figure 2**.

Group-Level Independent Component Analysis

The preprocessed, registered-to-MNI-space and band-pass filtered BOLD images described above served as input files to MELODIC group-ICA (Beckmann et al., 2005). We limited the number of components discovered by MELODIC to 30 to obtain large-scale networks. MELODIC uses a mixture model and the loss function to estimate the probability for a voxel to belong to the "active" or to the "background noise" classes. We implemented a default threshold of 0.5 that "places an equal loss on false positives and false negatives" (Beckmann and Smith, 2004) to obtain thresholded group-ICA components. Prior to performing any between-group statistical analyses, these thresholded group-ICA components (3D spatial maps) were cross-correlated with Yeo's 7-network solution maps (Yeo et al., 2011) using *fslcc*, a tool that estimates spatial similarities between ICA outputs and/or other volumetric data. The group-ICA components whose cross-correlation values exceeded 0.2 were retained for the further analyses. The remaining components were visually examined for usability. The components that followed WM tracts, or resembled physiological noise were removed from the analyses.

Within- and Between-Network Analysis

All analyses were conducted on thresholded independent component maps. Within-network connectivity was assessed with a *dual regression* which generated both subject-specific component time courses and subject-specific spatial maps as output. Dual regression automatically utilizes *randomize* [with 5000 permutations and threshold free cluster enhancement

(TFCE) to correct for multiple comparisons] for non-parametric permutation testing (Winkler et al., 2014) to perform a diagnostic status-by-memory accuracy interaction analysis in this study.

The time courses generated by dual regression were fed into *FSLNets* (v0.6) to estimate between-network connectivity (Smith et al., 2013). *FSLNets* was run using aggressive component denoising and a full correlation. *FSLNets* uses network modeling in which each variable (in our case, each ICA component) is a node in the model and each connection between any two nodes is an edge. FSLNets produces a node × node matrix of correlation coefficients that represent the strength of connections (edge strength) between any two selected nodes. The effect of the diagnostic status-by-memory accuracy interaction on edge strength was tested using *randomize* with 5000 permutations and TFCE to correct for multiple comparisons corrected-$p < 0.05$. To correct for the number of estimated contrasts ($n = 2$), we used a Bonferroni corrected $p < 0.025$.

Exploratory Analysis

Because the effects identified in the analyses described above could be related to severity of current or lifetime depression symptoms as well as the use of medications, we conducted exploratory analyses to examine the associations between severity of current (HDRS-25) and lifetime depression (MOODS-SR depression scale), as well as the age of depressive disorder onset, illness duration, current mood episode duration, and a total medication load with all significant effects identified in the resting state analyses. The exploratory analyses were conducted only in the DD group.

To further examine the heterogeneity of our patient population, we compared clinical, behavioral, and neuroimaging characteristics in individuals with DD who are diagnosed with MDD vs. those diagnosed with PDD, as well as in individuals with DD with and without comorbid diagnoses.

Finally, since we administered the forced-choice recognition test for faces prior to the recognition test for objects, we conducted an exploratory analysis to examine the relationship between accuracy on the facial recognition task with accuracy on the object recognition task and on the overall functional connectivity model.

RESULTS

Demographic and Clinical Data Analysis

The two groups did not significantly differ in age, sex, or IQ (**Table 1**). Individuals with DD, compared to HC, had significantly higher scores of current depression severity measured by HDRS-25, lifetime depression measured by MOODS-SR, and current mania symptoms measured by YMRS ($p < 0.001$).

Memory Retrieval Analysis

The two groups did not significantly differ in recognition accuracy [HC = 76.3 (1.8); UD 76.9 (1.9), $t(95) = -0.22$, $p = 0.8$] and recognition RT [HC = 968 (25) msec; UD = 1010 (21) msec, $t(95) = -1.36$, $p = 0.18$].

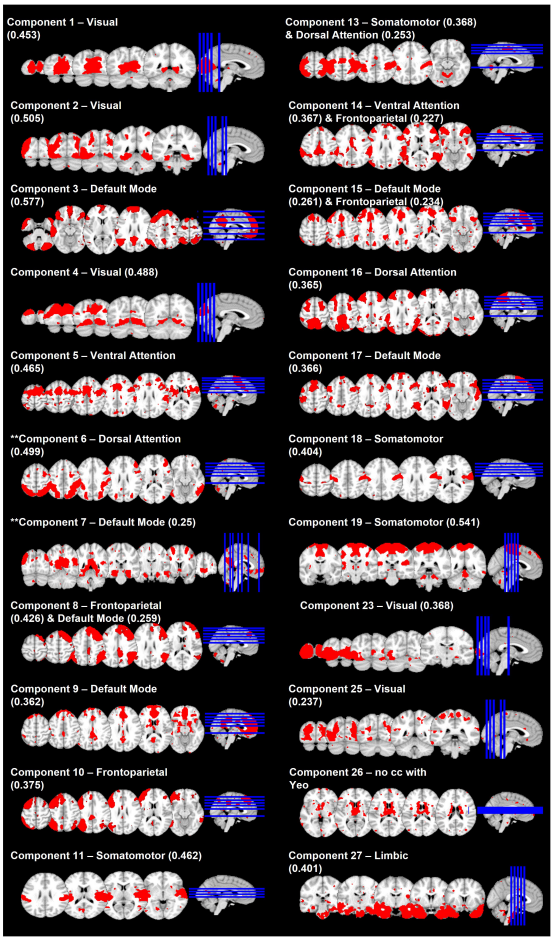

FIGURE 3 | Spatial maps of 22 selected network components. Network labels are based on cross-correlation with Yeo et al. (2011) and values in parentheses indicate the cross-correlation coefficient. ** denotes the two components whose connectivity was related to diagnostic status-by-memory accuracy interaction.

Resting State Data Analysis

Of the 30 independent components, 21 cross-correlated with Yeo's 7-network solution (Yeo et al., 2011) with at least 0.2 (**Figure 3**). During further visual examination, we identified a component that was comprised of regions in the basal ganglia. Even though this component did not correlate with any of Yeo's networks, we retained it for the further analyses. The remaining eight components followed white matter pathways, represented the cerebellum, or followed patterns of physiological noise and, therefore, were excluded from the further analyses.

Dual regression did not reveal any significant effects of diagnosis-by-memory accuracy interaction on functional connectivity in any of 22 independent components.

FSLNets revealed that the strength of connectivity between the independent component (IC) 7 that cross-correlated with

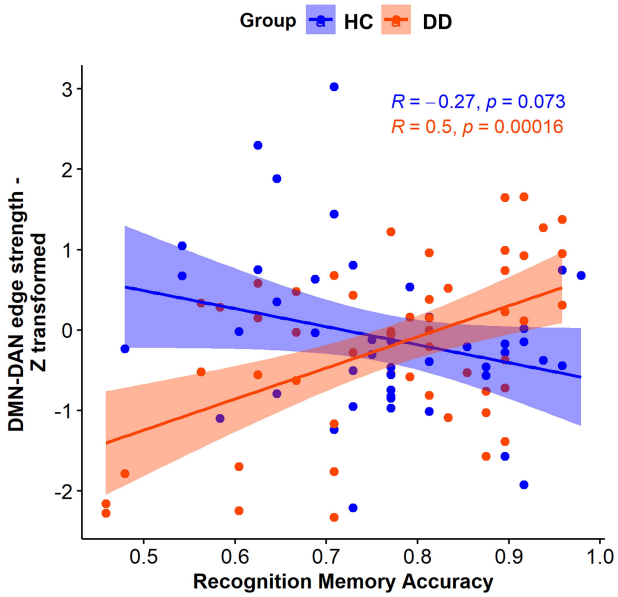

FIGURE 4 | The diagnosis-by-memory accuracy interaction effect on the edge strength between the DMN and DAN in individuals with DD and HC.

the DMN and the IC6 that cross-correlated with the DAN (**Figure 4**) was significantly associated with the interaction between diagnostic status and memory accuracy (p = 0.0156). A *post hoc* analysis showed that this effect was driven by the positive correlation between the connectivity strength and memory accuracy in individuals with DD (t = 4.1, p = 0.00016). Specifically, the individuals with DD who had more accurate memory for objects had a positive relationship between the DMN and DAN connectivity. However, those with less accurate memory had a negative relationship (anticorrelation) between the DMN and DAN. In HC, the DMN-DAN relationship was not significantly associated with memory accuracy ($t = -1.8$, $p = 0.07$) and, on average, was not different from 0 [one-sample t-test: $t(44) = -0.66$, $p = 0.5$].

Exploratory Analyses

Exploratory analyses investigated whether recognition accuracy and the connection strength between the DMN and DAN were associated with clinical variables in individuals with DD. Neither accuracy nor connection strength between the DMN and DAN were related to current or lifetime depressive symptom severity, age of DD onset, medication load, or duration of current mood episode (all p-values > 0.05).

Analyses investigating difference between MDD and PDD revealed that the two groups did not significantly differ in their current or lifetime depressive symptom severity, age of illness onset, or medication load (all p-values > 0.05; **Table 2**). Further, the two disorders did not significantly differ in recognition accuracy [MDD: 77.3 (2.2)%; PDD: 76.2 (13.8)%, $t(50) = 0.26$, $p = 0.8$] and recognition RT [MDD: 1010 (22) msec; PDD: 1019 (48) msec, $t(50) = -0.2$, $p = 0.84$]. Importantly, the linear regression analysis that predicted the DMN-DAN connectivity strength from memory accuracy yielded significant results in the MDD only sample [$F(1,33) = 4.5$, $p = 0.04$], as well as in the PDD only sample [$F(1,15) = 13.6$, $p = 0.002$], which paralleled the findings for the whole DD sample.

Individuals with DD with comorbid disorders had significantly higher lifetime depression severity than those without comorbid disorders based on the MOODS (Dell'Osso et al., 2002) assessment [$t(50) = 3.3$, $p < 0.005$]. Other clinical, behavioral, and connectivity measures were not related to the presence of comorbid disorders.

Finally, although the memory accuracy for faces significantly correlated with memory for objects across all participants ($r = 0.52$, $p < 0.001$), it was significantly lower than the memory accuracy for objects [$t(96) = -9.6$, $p < 0.001$]. Memory accuracy for faces was not associated with the presence of DD diagnosis. Importantly, the connectivity values were not related to the interaction between diagnostic status and memory accuracy for faces [$F(1,93) = 1.64$, $p = 0.2$].

DISCUSSION

In this study, we investigated the interaction effect of diagnostic status (DD vs. HC) and the strength of memory representations acquired prior to the resting state scan on within- and between-network resting state connectivity. The results indicated that diagnostic status moderated the relationship between memory accuracy and the DMN-DAN connectivity strength. Specifically, the DMN and DAN anticorrelated in the individuals with DD who had lower recognition memory accuracy, but positively correlated in those with DD who had higher recognition memory accuracy. In contrast, the DMN and DAN connectivity was not associated with memory accuracy in HC. We hypothesize that the distinct relationship between memory accuracy and the DMN-DAN connectivity in individuals with DD could indicate aberrant memory reactivation and consolidation processes in depressive disorders because the resting state scan was acquired immediately after the stimulus recognition and was conducted within a timeframe of continued memory consolidation, the results were correlated with memory performance, and one of the networks included bilateral hippocampus.

The DMN increases in activation during rest (Buckner et al., 2008; Smith et al., 2009; Raichle, 2015) and supports perception-independent (Smallwood et al., 2013) and internally oriented cognition, such as autobiographical memory (Andrews-Hanna et al., 2010a), abstract representation of task details in ongoing thought processes (Sormaz et al., 2018), future-oriented thought (Xu et al., 2016), and spontaneous cognition (Buckner et al., 2008; Andrews-Hanna et al., 2010a). In contrast, the DAN increases in activation during cognitive task performance and is implicated in top-down control of attention (Corbetta and Shulman, 2002; Vossel et al., 2014). While the DMN typically anticorrelates with the DAN (Fox et al., 2005; Buckner et al., 2008; Hampson et al., 2010), the degree of such anticorrelation may vary across cognitive states (Dixon et al., 2017) and environmental factors (Qian et al., 2020). For example, one study reported that the regions in these networks co-activated during task preparation

TABLE 2 | Demographic and clinical characteristics of individuals diagnosed with major depressive (MDD) and persistent depressive (PDD) disorders.

	MDD	PDD	Statistics MDD vs. PDD
Number of participants	35	17	
Gender composition (number females)	29	13	$chi^2 = 0.03$, $p = 0.86$
Age (years)	27.32 (0.89)	30.02 (2.14)	$t(50) = -1.38$, $p = 0.18$
BMI	25.18 (0.67)	25.4 (0.92)	$t(50) = -0.19$, $p = 0.85$
IQ (NART)	109.12 (1.3)	109.95 (1.55)	$t(50) = -0.38$, $p = 0.7$
Current depression severity (HDRS-25)	11.57 (1.17)	15.35 (1.67)	$t(50) = -1.85$, $p = 0.07$
Current mania severity (YMRS)	1.31 (0.27)	0.88 (0.27)	$t(50) = 0.99$, $p = 0.33$
Lifetime depression (MOODS-SR)	18.51 (0.76)	18.94 (0.81)	$t(50) = -0.35$, $p = 0.73$
Illness Onset (year of age)	14.69 (0.51)	15.35 (1.11)	$t(50) = -0.63$, $p = 0.53$
Number of participants taking Antidepressants	22	7	na
Number of participants taking Mood stabilizers	0	2	na
Number of participants taking Antipsychotics	1	0	na
Number of participants taking Benzodiazepines	4	3	na
Number of participants taking Stimulants	4	0	na
A mean number of psychotropic medications	1.00 (0.14)	1.29 (0.31)	$t(50) = -1.02$, $p = 0.31$
A mean total medication load	1.29 (0.19)	1.65 (0.43)	$t(50) = -0.9$, $p = 0.37$
Number of participants with comorbid diagnoses	20	14	na

but "anti-correlated" during task performance (Koshino et al., 2014). Another study found that the DMN and working memory network (that included the regions comprising the DAN in our study) co-activated during encoding and retrieval phases of a working memory task but anticorrelated during the maintenance phase of this task (Piccoli et al., 2015). Our study contributes to this line of research by showing that the relationship between the DMN and DAN is associated with psychopathology and memory accuracy in the task immediately preceding the resting state scan.

Resting state functional connectivity may reflect experiences acquired prior to the resting state scan (Daselaar et al., 2010; Sami et al., 2014; Cecchetto et al., 2019). Specifically, one study has demonstrated that the patterns of activation observed during encoding can spontaneously reactivate during a subsequent resting state scan (Deuker et al., 2013). Consistent with the memory consolidation theories (McClelland et al., 1995; Squire et al., 2015), consolidation starts in the hippocampus and continues in the neocortex, including the PFC. Given that more accurate memory in individuals with DD, but not HC, was associated with a stronger positive relationship between the DMN (that included the bilateral hippocampus) and DAN (that included the PFC and parietal regions) during the subsequent resting state scan, we hypothesize that these findings indicate aberrant spontaneous memory reactivation and consolidation in these individuals. This pattern of results may indicate that HC disengaged from the task when the task was over, while the individuals with DD who accurately memorized the stimuli in the task were not able to do so. The latter individuals might experience spontaneous reactivation and "replay" of memories even in the absence of direct stimulation. Individuals with more accurate memories might reactivate those memories more than individuals with less accurate memories. Future studies should directly test the spontaneous memory reactivation and consolidation hypothesis because these memory processes could be a neurobiological basis for depressive rumination, which is a repetitive internal thinking pattern focusing on negative experiences and affect (Holtzheimer and Mayberg, 2011). While we did not directly examine memory reactivation at rest or ruminative processes, the previous literature on rumination supports this idea and suggests a relationship between rumination, resting state functional connectivity, and depression. For example, in depressed individuals, this phenomenon was positively associated with functional connectivity in the anterior DMN (Zhu et al., 2012; Lois and Wessa, 2016), negatively associated with functional connectivity in the cortical DMN regions (Rosenbaum et al., 2017), and was associated with more variable functional connectivity between medial prefrontal cortex and insula (Kaiser et al., 2016). Future studies are needed to clarify and test the hypothesized relationship between rumination and memory reactivation and consolidation processes proposed here.

The findings from exploratory analyses in the individuals with DD revealed that the memory accuracy and DMN-DAN correlation were not significantly related to current or lifetime depressive symptom severity, the use of psychiatric medications, age of illness onset, comorbid diagnoses, or diagnosis of MDD vs. PDD in the individuals with DD. While these findings are indicative of general reorganization of connectivity between brain networks in individuals with DD, future studies need to examine other factors affecting the DMN-DAN connectivity in affected individuals.

One limitation of this study is the relatively short duration of the resting state scan. A longer scan time is preferable because it provides more reliable estimates of functional connectivity (Birn et al., 2013). However, longer scan times also increase the likelihood of a participant falling asleep during the scan, which would affect resting state functional connectivity (Soehner et al., 2019). Sleep disturbance is one of the clinical symptoms of DD; therefore, staying awake during a longer resting state scan may be especially challenging for individuals with DD.

Another limitation of this study is the lack of a baseline resting state scan performed prior to stimulus encoding or between encoding and memory retrieval. Many studies that examined the relationship between resting state functional connectivity and task performance included an additional resting state scan prior to task performance to capture baseline functional connectivity to better distinguish "trait-like" from "task-related" changes. However, determining the baseline in individuals with mood disorders might be challenging because there is no way to eliminate bias or interference from previous experiences and thus, baseline resting state data may still be affected by rumination or thoughts about previous experiences. Although we hypothesized that our findings might be related to aberrant reactivation and consolidation processes in the individuals with DD, our study was not designed to directly measure consolidation processes. Future studies should modify the existing experimental paradigm by adding a baseline resting state scan between encoding and memory retrieval as well as the second memory test after the resting state scan to test the consolidation hypothesis. Future studies should also incorporate rumination surveys and inquire about the specific thought content that participants experience during rest to discern how ruminative or other thinking patterns are related to basic memory consolidation processes in depression. In this study, we used the pictures of neutral everyday objects. However, the notion of "neutral" stimuli should be interpreted with caution in mood disorders research because affected individuals tend to misinterpret neutral stimuli as emotional (Manelis et al., 2019). Future studies should specifically examine the relationship between resting state functional connectivity and memory for positive vs. negative information immediately preceding the resting state scan.

In summary, we have demonstrated that connectivity strength between the DMN and DAN during resting state was significantly associated with the interaction between participants' diagnostic status (DD or HC) and memory accuracy in the task preceding the resting state scan. We hypothesize that these differences may relate to aberrant memory consolidation in depression, which may in turn be a basis for depressive rumination and an inability to disengage from thoughts and feelings associated with previous experiences. Understanding the relationship between resting state connectivity and previous experiences may inform the development of interventions strategies alleviating repetitive and intrusive thoughts in depression. However, future studies are needed to clarify the relationship between post-encoding and retrieval DMN-DAN resting state functional connectivity, memory consolidation, and rumination.

DATA AVAILABILITY STATEMENT

The raw data supporting the conclusions of this article will be made available by the authors, without undue reservation.

ETHICS STATEMENT

This study was approved by the University of Pittsburgh Institutional Review Board. The patients/participants provided their written informed consent to participate in this study.

AUTHOR CONTRIBUTIONS

SS acquired the data, evaluated data quality, analyzed and interpreted the data, and drafted and critically evaluated the manuscript. YH curated the data organization and analyses and drafted and critically evaluated the manuscript. RR and ML acquired the data, evaluated data quality, and critically evaluated the manuscript. MP curated the study development, interpreted the data, and critically evaluated the manuscript. HS curated the study development, participants' recruitment, and evaluation, and critically evaluated the manuscript. AM obtained funding, designed the study, acquired the data, evaluated data quality, analyzed and interpreted the data, and drafted and critically evaluated the manuscript. All authors have read and approved the final version of the manuscript and agreed to be accountable for all aspects of this work.

FUNDING

This work was supported by grants from the National Institutes of Health R01MH114870 to AM.

ACKNOWLEDGMENTS

We thank participants for taking part in this research study.

REFERENCES

Andrews-Hanna, J. R., Reidler, J. S., Huang, C., and Buckner, R. L. (2010a). Evidence for the default network's role in spontaneous cognition. *J. Neurophysiol.* 104, 322–335. doi: 10.1152/jn.00830.2009

Andrews-Hanna, J. R., Reidler, J. S., Sepulcre, J., Poulin, R., and Buckner, R. L. (2010b). Functional-anatomic fractionation of the brain's default network. *Neuron* 65, 550–562. doi: 10.1016/j.neuron.2010.02.005

Beckmann, C. F., DeLuca, M., Devlin, J. T., and Smith, S. M. (2005). Investigations into resting-state connectivity using independent component analysis. *Philos. Trans. R. Soc. B Biol. Sci.* 2005:1634. doi: 10.1098/rstb.2005.1634

Beckmann, C. F., and Smith, S. M. (2004). Probabilistic independent component analysis for functional magnetic resonance imaging. *IEEE Trans. Med. Imag.* 23, 137–152. doi: 10.1109/TMI.2003.822821

Birn, R. M., Molloy, E. K., Patriat, R., Parker, T., Meier, T. B., Kirk, G. R., et al. (2013). The effect of scan length on the reliability of resting-state fMRI connectivity estimates. *Neuroimage* 83, 550–558. doi: 10.1016/j.neuroimage.2013.05.099

Biswal, B. B., Mennes, M., Zuo, X.-N., Gohel, S., Kelly, C., Smith, S. M., et al. (2010). Toward discovery science of human brain function. *Proc. Natl. Acad. Sci. USA* 107, 4734–4739. doi: 10.1073/pnas.0911855107

Blechert, J., Meule, A., Busch, N. A., and Ohla, K. (2014). Food-pics: An image database for experimental research on eating and appetite. *Front. Psychol.* 2014:617. doi: 10.3389/fpsyg.2014.00617

Bluhm, R., Williamson, P., Lanius, R., Théberge, J., Densmore, M., Bartha, R., et al. (2009). Resting state default-mode network connectivity in early depression using a seed region-of-interest analysis: Decreased connectivity with caudate nucleus. *Psychiatry Clin. Neurosci.* 63, 754–761. doi: 10.1111/j.1440-1819.2009.02030.x

Brakowski, J., Spinelli, S., Dörig, N., Bosch, O. G., Manoliu, A., Holtforth, M. G., et al. (2017). Resting state brain network function in major depression – Depression symptomatology, antidepressant treatment effects, future research. *J. Psychiatr. Res.* 2017:7. doi: 10.1016/j.jpsychires.2017.04.007

Buckner, R. L., Andrews-Hanna, J. R., and Schacter, D. L. (2008). The brain's default network: anatomy, function, and relevance to disease. *Ann. NY Acad. Sci.* 1124, 1–38. doi: 10.1196/annals.1440.011

Burt, D. B., Zembar, M. J., and Niederehe, G. (1995). Depression and memory impairment: a meta-analysis of the association, its pattern, and specificity. *Psychol. Bull.* 117, 285. doi: 10.1037/0033-2909.117.2.285

Cecchetto, C., Fischmeister, F. P. S., Reichert, J. L., Bagga, D., and Schöpf, V. (2019). When to collect resting-state data: The influence of odor on post-task resting-state connectivity. *Neuroimage* 191, 361–366. doi: 10.1016/j.neuroimage.2019.02.050

Chou, Y. H., Sundman, M., Whitson, H. E., Gaur, P., Chu, M. L., Weingarten, C. P., et al. (2017). Maintenance and representation of mind wandering during resting-state fMRI. *Sci. Rep.* 7:722. doi: 10.1038/srep40722

Corbetta, M., and Shulman, G. L. (2002). Control of goal-directed and stimulus-driven attention in the brain. *Nat. Rev. Neurosci.* 3, 201–215. doi: 10.1038/nrn755

Cox, R. W., and Hyde, J. S. (1997). Software tools for analysis and visualization of fMRI data. *NMR Biomed.* 10, 171–178. doi: 10.1002/(SICI)1099-1492

Dale, A. M., Fischl, B., and Sereno, M. I. (1999). Cortical surface-based analysis: I. Segmentation and surface reconstruction. *Neuroimage* 9, 179–194. doi: 10.1006/nimg.1998.0395

Damoiseaux, J. S., Rombouts, S. A. R. B., Barkhof, F., Scheltens, P., Stam, C. J., Smith, S. M., et al. (2006). Consistent resting-state networks across healthy subjects. *Proc. Natl. Acad. Sci. USA* 103, 13848–13853. doi: 10.1073/pnas.0601417103

Daselaar, S. M., Huijbers, W., de Jonge, M., Goltstein, P. M., and Pennartz, C. M. A. (2010). Experience-dependent alterations in conscious resting state activity following perceptuomotor learning. *Neurobiol. Learn. Mem.* 93, 422–427. doi: 10.1016/j.nlm.2009.12.009

De Luca, M., Beckmann, C. F., De Stefano, N., Matthews, P. M., and Smith, S. M. (2006). fMRI resting state networks define distinct modes of long-distance interactions in the human brain. *Neuroimage* 29, 1359–1367. doi: 10.1016/j.neuroimage.2005.08.035

Dell'Osso, L., Armani, A., Rucci, P., Frank, E., Fagiolini, A., Corretti, G., et al. (2002). Measuring mood spectrum: Comparison of interview (SCI-MOODS) and self-report (MOODS-SR) instruments. *Compr. Psychiatry* 2002:29852. doi: 10.1053/comp.2002.29852

Deuker, L., Olligs, J., Fell, J., Kranz, T. A., Mormann, F., Montag, C., et al. (2013). Memory consolidation by replay of stimulus-specific neural activity. *J. Neurosci.* 33, 19373–19383. doi: 10.1523/JNEUROSCI.0414-13.2013

Dillon, D. G., and Pizzagalli, D. A. (2018). Mechanisms of memory disruption in depression. *Trends Neurosci.* 2018:6. doi: 10.1016/j.tins.2017.12.006

Dixon, M. L., Andrews-Hanna, J. R., Spreng, R. N., Irving, Z. C., Mills, C., Girn, M., et al. (2017). Interactions between the default network and dorsal attention network vary across default subsystems, time, and cognitive states. *Neuroimage* 147, 632–649. doi: 10.1016/j.neuroimage.2016.12.073

Esteban, O., Markiewicz, C. J., Blair, R. W., Moodie, C. A., Isik, A. I., Erramuzpe, A., et al. (2019). fMRIPrep: a robust preprocessing pipeline for functional MRI. *Nat. Methods* 2019:2354. doi: 10.1038/s41592-018-0235-4

First, M. B., Williams, J. B. W., Karg, R. S., and Spitzer, R. L. (2015). *Structured clinical interview for DSM-5—Research version (SCID-5 for DSM-5, research version; SCID-5-RV)*. Washingt. D.C: American Psychiatric Association.

Fox, M. D., Snyder, A. Z., Vincent, J. L., Corbetta, M., Van Essen, D. C., and Raichle, M. E. (2005). The human brain is intrinsically organized into dynamic, anticorrelated functional networks. *Proc. Natl. Acad. Sci. USA* 2005:102. doi: 10.1073/pnas.0504136102

Ge, R., Torres, I., Brown, J. J., Gregory, E., McLellan, E., Downar, J. H., et al. (2019). Functional disconnectivity of the hippocampal network and neural correlates of memory impairment in treatment-resistant depression. *J. Affect. Disord.* 253, 248–256. doi: 10.1016/j.jad.2019.04.096

Gotlib, I. H., and Joormann, J. (2010). Cognition and depression: Current status and future directions. *Annu. Rev. Clin. Psychol* 2010:305. doi: 10.1146/annurev.clinpsy.121208.131305

Greicius, M. (2008). Resting-state functional connectivity in neuropsychiatric disorders. *Curr. Opin. Neurol.* 2008:5. doi: 10.1097/wco.0b013e328306f2c5

Greicius, M. D., Flores, B. H., Menon, V., Glover, G. H., Solvason, H. B., Kenna, H., et al. (2007). Resting-state functional connectivity in major depression: abnormally increased contributions from subgenual cingulate cortex and thalamus. *Biol. Psychiatry* 62, 429–437. doi: 10.1016/j.biopsych.2006.09.020

Greve, D. N., and Fischl, B. (2009). Accurate and robust brain image alignment using boundary-based registration. *Neuroimage* 48, 63–72. doi: 10.1016/j.neuroimage.2009.06.060

Gusnard, D. A., and Raichle, M. E. (2001). Searching for a baseline: Functional imaging and the resting human brain. *Nat. Rev. Neurosci.* 2, 685–694. doi: 10.1038/35094500

Halchenko, Y., Goncalves, M., Castello, M. V., Ghosh, S., Hanke, M., DaeAmlien, I., et al. (2019). *nipy/heudiconv: v0.5.4 [0.5.4]*. San Francisco: GitHub. doi: 10.5281/ZENODO.2653784

Hamilton, J. P., and Gotlib, I. H. (2008). Neural substrates of increased memory sensitivity for negative stimuli in major depression. *Biol. Psychiatry* 63, 1155–1162. doi: 10.1016/j.biopsych.2007.12.015

Hamilton, M. (1960). A rating scale for depression. *J. Neurol. Neurosurg. Psychiatry* 23, 56–62. doi: 10.1136/jnnp.23.1.56

Hampson, M., Driesen, N., Roth, J. K., Gore, J. C., and Constable, R. T. (2010). Functional connectivity between task-positive and task-negative brain areas and its relation to working memory performance. *Magn. Reson. Imag.* 28, 1051–1057. doi: 10.1016/j.mri.2010.03.021

Hassel, S., Almeida, J. R., Kerr, N., Nau, S., Ladouceur, C. D., Fissell, K., et al. (2008). Elevated striatal and decreased dorsolateral prefrontal cortical activity in response to emotional stimuli in euthymic bipolar disorder: no associations with psychotropic medication load. *Bipolar. Disord.* 10, 916–927. doi: 10.1111/j.1399-5618.2008.00641.x

Holtzheimer, P. E., and Mayberg, H. S. (2011). Stuck in a rut: Rethinking depression and its treatment. *Trends Neurosci.* 2011:4. doi: 10.1016/j.tins.2010.10.004

Jenkinson, M., Bannister, P., Brady, M., and Smith, S. (2002). Improved optimization for the robust and accurate linear registration and motion correction of brain images. *Neuroimage* 17, 825–841. doi: 10.1016/S1053-8119(02)91132-8

Kaiser, R. H., Whitfield-Gabrieli, S., Dillon, D. G., Goer, F., Beltzer, M., Minkel, J., et al. (2016). Dynamic resting-state functional connectivity in major depression. *Neuropsychopharmacology* 41, 1822–1830. doi: 10.1038/npp.2015.352

Koshino, H., Minamoto, T., Yaoi, K., Osaka, M., and Osaka, N. (2014). Coactivation of the default mode network regions and working memory network regions during task preparation. *Sci. Rep.* 4:5954. doi: 10.1038/srep05954

Kucyi, A., and Davis, K. D. (2014). Dynamic functional connectivity of the default mode network tracks daydreaming. *Neuroimage* 100, 471–480. doi: 10.1016/j.neuroimage.2014.06.044

Lanczos, C. (1964). Evaluation of noisy data. *J. Soc. Ind. Appl. Math. Ser. B Numer. Anal.* 1, 76–85. doi: 10.1137/0701007

Lois, G., and Wessa, M. (2016). Differential association of default mode network connectivity and rumination in healthy individuals and remitted MDD patients. *Soc. Cogn. Affect. Neurosci.* 11:85. doi: 10.1093/scan/nsw085

López Zunini, R. A., Thivierge, J. P., Kousaie, S., Sheppard, C., and Taler, V. (2013). Alterations in resting-state activity relate to performance in a verbal recognition task. *PLoS One* 2013:8. doi: 10.1371/journal.pone.0065608

Lv, H., Wang, Z., Tong, E., Williams, L. M., Zaharchuk, G., Zeineh, M., et al. (2018). Resting-state functional MRI: Everything that nonexperts have always wanted to know. *Am. J. Neuroradiol.* 39, 1390–1399. doi: 10.3174/ajnr.A5527

Manelis, A., Almeida, J. R. C., Stiffler, R., Lockovich, J. C., Aslam, H. A., and Phillips, M. L. (2016). Anticipation-related brain connectivity in bipolar and unipolar depression: A graph theory approach. *Brain* 139, 2554–2566. doi: 10.1093/brain/aww157

Manelis, A., Hanson, C., and Hanson, S. J. (2011). Implicit memory for object locations depends on reactivation of encoding-related brain regions. *Hum. Brain Mapp.* 32, 32–50. doi: 10.1002/hbm.20992

Manelis, A., Huppert, T. J., Rodgers, E., Swartz, H. A., and Phillips, M. L. (2019). The role of the right prefrontal cortex in recognition of facial emotional expressions in depressed individuals: fNIRS study. *J. Affect. Disord.* 2019:6. doi: 10.1016/j.jad.2019.08.006

Marchetti, I., Koster, E. H. W., Sonuga-Barke, E. J., and De Raedt, R. (2012). The Default Mode Network and recurrent depression: A neurobiological model of cognitive risk factors. *Neuropsychol. Rev.* 22, 229–251. doi: 10.1007/s11065-012-9199-9

McClelland, J. L., McNaughton, B. L., and O'Reilly, R. C. (1995). Why there are complementary learning systems in the hippocampus and neocortex: Insights from the successes and failures of connectionist models of learning and memory. *Psychol. Rev.* 102, 419–457. doi: 10.1037/0033-295X.102.3.419

Murty, V. P., Tompary, A., Adcock, R. A., and Davachi, L. (2017). Selectivity in postencoding connectivity with high-level visual cortex is associated with reward-motivated memory. *J. Neurosci.* 37, 537–545. doi: 10.1523/JNEUROSCI.4032-15.2016

Nadel, L., and Moscovitch, M. (1997). Memory consolidation, retrograde amnesia and the hippocampal complex. *Curr. Opin. Neurobiol.* 7, 217–227. doi: 10.1016/S0959-4388(97)80010-4

Nelson, H. E. (1982). *National Adult Reading Test (NART): Test manual*. Florida: Academica.

Piccoli, T., Valente, G., Linden, D. E. J., Re, M., Esposito, F., Sack, A. T., et al. (2015). The default mode network and the working memory network are not anti-correlated during all phases of a working memory task. *PLoS One* 10:123354. doi: 10.1371/journal.pone.0123354

Pruim, R. H. R., Mennes, M., van Rooij, D., Llera, A., Buitelaar, J. K., and Beckmann, C. F. (2015). ICA-AROMA: A robust ICA-based strategy for removing motion artifacts from fMRI data. *Neuroimage* 2015:64. doi: 10.1016/j.neuroimage.2015.02.064

Qian, S., Zhang, J., Yan, S., Shi, Z., Wang, Z., and Zhou, Y. (2020). Disrupted anti-correlation between the default and dorsal attention networks during hyperthermia exposure: an fMRI Study. *Front. Hum. Neurosci* 14:564271. doi: 10.3389/fnhum.2020.564272

Raichle, M. E. (2015). The brain's default mode network. *Annu. Rev. Neurosci* 2015:14030. doi: 10.1146/annurev-neuro-071013-014030

Reineberg, A. E., Andrews-Hanna, J. R., Depue, B. E., Friedman, N. P., and Banich, M. T. (2015). Resting-state networks predict individual differences in common and specific aspects of executive function. *Neuroimage* 104, 69–78. doi: 10.1016/j.neuroimage.2014.09.045

Richardson-Klavehn, A. (2010). Priming, automatic recollection, and control of retrieval: toward an integrative retrieval architecture, in: the act of remembering: toward an understanding of how we recall the past. 2010:202. doi: 10.1002/9781444328202.ch7

Rosenbaum, D., Haipt, A., Fuhr, K., Haeussinger, F. B., Metzger, F. G., Nuerk, H. C., et al. (2017). Aberrant functional connectivity in depression as an index of state and trait rumination. *Sci. Rep.* 7:2211. doi: 10.1038/s41598-017-02277-z

Sala-Llonch, R., Pena-Gomez, C., Arenaza-Urquijo, E. M., Vidal-Pineiro, D., Bargallo, N., Junque, C., et al. (2012). Brain connectivity during resting state and subsequent working memory task predicts behavioural performance. *Cortex* 48, 1187–1196. doi: 10.1016/j.cortex.2011.07.006

Sami, S., Robertson, E. M., and Chris Miall, R. (2014). The time course of task-specific memory consolidation effects in resting state networks. *J. Neurosci.* 34, 3982–3992. doi: 10.1523/JNEUROSCI.4341-13.2014

Scalabrini, A., Vai, B., Poletti, S., Damiani, S., Mucci, C., Colombo, C., et al. (2020). All roads lead to the default-mode network—global source of DMN abnormalities in major depressive disorder. *Neuropsychopharmacology* 45, 2058–2069. doi: 10.1038/s41386-020-0785-x

Schlichting, M. L., and Prestona, A. R. (2014). Memory reactivation during rest supports upcoming earning of related content. *Proc. Natl. Acad. Sci. USA* 111, 15845–15850. doi: 10.1073/pnas.1404396111

Schott, B. H., Wüstenberg, T., Wimber, M., Fenker, D. B., Zierhut, K. C., Seidenbecher, C. I., et al. (2013). The relationship between level of processing and hippocampal-cortical functional connectivity during episodic memory formation in humans. *Hum. Brain Mapp.* 2013:21435. doi: 10.1002/hbm.21435

Schramm, E., Klein, D. N., Elsaesser, M., Furukawa, T. A., and Domschke, K. (2020). Review of dysthymia and persistent depressive disorder: history, correlates, and clinical implications. *Lancet Psychiatry* 2020:997. doi: 10.1016/S2215-0366(20)30099-7

Sheline, Y. I., Barch, D. M., Price, J. L., Rundle, M. M., Vaishnavi, S. N., Snyder, A. Z., et al. (2009). The default mode network and self-referential processes in depression. *Proc. Natl. Acad. Sci. USA* 106, 1942–1947. doi: 10.1073/pnas.0812686106

Sheline, Y. I., Price, J. L., Yan, Z., and Mintun, M. A. (2010). Resting-state functional MRI in depression unmasks increased connectivity between networks via the dorsal nexus. *Proc. Natl. Acad. Sci. USA* 107, 11020–11025. doi: 10.1073/pnas.1000446107

Smallwood, J., Tipper, C., Brown, K., Baird, B., Engen, H., Michaels, J. R., et al. (2013). Escaping the here and now: Evidence for a role of the default mode network in perceptually decoupled thought. *Neuroimage* 69, 120–125. doi: 10.1016/j.neuroimage.2012.12.012

Smith, S. M., Fox, P. T., Miller, K. L., Glahn, D. C., Fox, P. M., Mackay, C. E., et al. (2009). Correspondence of the brain's functional architecture during activation and rest. *Proc. Natl. Acad. Sci. USA* 106, 13040–13045. doi: 10.1073/pnas.0905267106

Smith, S. M., Vidaurre, D., Beckmann, C. F., Glasser, M. F., Jenkinson, M., Miller, K. L., et al. (2013). Functional connectomics from resting-state fMRI. *Trends Cogn. Sci.* 2013:16. doi: 10.1016/j.tics.2013.09.016

Soehner, A. M., Chase, H. W., Bertocci, M. A., Greenberg, T., Stiffler, R., Lockovich, J. C., et al. (2019). Unstable wakefulness during resting-state fMRI and its associations with network connectivity and affective psychopathology in young adults. *J. Affect. Disord.* 2019:66. doi: 10.1016/j.jad.2019.07.066

Sormaz, M., Murphy, C., Wang, H., Hymers, M., Karapanagiotidis, T., Poerio, G., et al. (2018). Correction: Default mode network can support the level of detail in experience during active task. *Proc. Natl. Acad. Sci. USA* 115, E11198. doi: 10.1073/pnas.1817966115

Squire, L. R., Genzel, L., Wixted, J. T., and Morris, R. G. (2015). Memory consolidation. *Cold Spring Harb. Perspect. Biol.* 7:21766. doi: 10.1101/cshperspect.a021766

Tambini, A., and Davachi, L. (2013). Persistence of hippocampal multivoxel patterns into postencoding rest is related to memory. *Proc. Natl. Acad. Sci. USA* 110, 19591–19596. doi: 10.1073/pnas.1308499110

Tambini, A., Ketz, N., and Davachi, L. (2010). Enhanced brain correlations during rest are related to memory for recent experiences. *Neuron* 65, 280–290. doi: 10.1016/j.neuron.2010.01.001

Tompary, A., Duncan, K., and Davachi, L. (2015). Consolidation of associative and item memory is related to post-encoding functional connectivity between the ventral tegmental area and different medial temporal lobe subregions during an unrelated task. *J. Neurosci.* 35, 7326–7331. doi: 10.1523/JNEUROSCI.4816-14.2015

van den Heuvel, M. P., and Hulshoff Pol, H. E. (2010). Exploring the brain network: A review on resting-state fMRI functional connectivity. *Eur. Neuropsychopharmacol.* 2020:8. doi: 10.1016/j.euroneuro.2010.03.008

Vasic, N., Walter, H., Sambataro, F., and Wolf, R. C. (2009). Aberrant functional connectivity of dorsolateral prefrontal and cingulate networks in patients with major depression during working memory processing. *Psychol. Med.* 39, 977–987. doi: 10.1017/S0033291708004443

Vilberg, K. L., and Davachi, L. (2013). Perirhinal-hippocampal connectivity during reactivation is a marker for object-based memory consolidation. *Neuron* 79, 1232–1242. doi: 10.1016/j.neuron.2013.07.013

Visconti di Oleggio Castello, M., Dobson, J. E., Sackett, T., Kodiweera, C., Haxby, J. V., Goncalves, M., et al. (2020). *ReproNim/reproin 0.6.0*. San Francisco: GitHub. doi: 10.5281/ZENODO.3625000

Vossel, S., Geng, J. J., and Fink, G. R. (2014). Dorsal and ventral attention systems: Distinct neural circuits but collaborative roles. *Neuroscientist* 20, 150–159. doi: 10.1177/1073858413494269

Williams, J. M. G., Barnhofer, T., Crane, C., Hermans, D., Raes, F., Watkins, E., et al. (2007). Autobiographical memory specificity and emotional disorder. *Psychol. Bull.* 2007:122. doi: 10.1037/0033-2909.133.1.122

Winkler, A. M., Ridgway, G. R., Webster, M. A., Smith, S. M., and Nichols, T. E. (2014). Permutation inference for the general linear model. *Neuroimage* 2014:60. doi: 10.1016/j.neuroimage.2014.01.060

Wittkuhn, L., and Schuck, N. W. (2021). Dynamics of fMRI patterns reflect sub-second activation sequences and reveal replay in human visual cortex. *Nat. Commun* 12:2. doi: 10.1038/s41467-021-21970-2

Woodward, N. D., and Cascio, C. J. (2015). Resting-state functional connectivity in psychiatric disorders. *JAMA Psychiatry* 2015:484. doi: 10.1001/jamapsychiatry.2015.0484

Xia, J., and Evans, L. H. (2020). Neural evidence that disengaging memory retrieval is modulated by stimulus valence and rumination. *Sci. Rep.* 101, 1–11. doi: 10.1038/s41598-020-64404-7

Xu, X., Yuan, H., and Lei, X. (2016). Activation and connectivity within the default mode network contribute independently to future-oriented thought. *Sci. Rep.* 2016:21001. doi: 10.1038/srep21001

Yeo, B. T., Krienen, F. M., Sepulcre, J., Sabuncu, M. R., Lashkari, D., Hollinshead, M., et al. (2011). The organization of the human cerebral cortex estimated by intrinsic functional connectivity. *J. Neurophysiol.* 106, 1125–1165. doi: 10.1152/jn.00338.2011

Young, R. C., Biggs, J. T., Ziegler, V. E., and Meyer, D. A. (1978). A rating scale for mania: reliability, validity and sensitivity. *Br. J. Psychiatry* 133, 429–435. doi: 10.1192/bjp.133.5.429

Zeng, L. L., Shen, H., Liu, L., Wang, L., Li, B., Fang, P., et al. (2012). Identifying major depression using whole-brain functional connectivity: A multivariate pattern analysis. *Brain* 135, 1498–1507. doi: 10.1093/brain/aws059

Zhang, D., and Raichle, M. E. (2010). Disease and the brain's dark energy. *Nat. Rev. Neurol.* 2010:198. doi: 10.1038/nrneurol.2009.198

Zhang, Y., Wu, W., Toll, R. T., Naparstek, S., Maron-Katz, A., Watts, M., et al. (2021). Identification of psychiatric disorder subtypes from functional connectivity patterns in resting-state electroencephalography. *Nat. Biomed. Eng.* 5, 309–323. doi: 10.1038/s41551-020-00614-8

Zhu, X., Wang, X., Xiao, J., Liao, J., Zhong, M., Wang, W., et al. (2012). Evidence of a dissociation pattern in resting-state default mode network connectivity in first-episode, treatment-naive major depression patients. *Biol. Psychiatry* 71, 611–617. doi: 10.1016/j.biopsych.2011.10.035

Conflict of Interest: HS receives royalties from Wolters Kluwer, royalties and an editorial stipend from APA Press, and served as a consultant for Intracellular Therapeutics and Medscape/WebMD.

The remaining authors declare that the research was conducted in the absence of any commercial or financial relationships that could be construed as a potential conflict of interest.

Publisher's Note: All claims expressed in this article are solely those of the authors and do not necessarily represent those of their affiliated organizations, or those of the publisher, the editors and the reviewers. Any product that may be evaluated in this article, or claim that may be made by its manufacturer, is not guaranteed or endorsed by the publisher.

frontiers in Computational Neuroscience

ORIGINAL RESEARCH
published: 03 March 2022
doi: 10.3389/fncom.2022.729556

Quantification of Kuramoto Coupling Between Intrinsic Brain Networks Applied to fMRI Data in Major Depressive Disorder

*Lena G. Bauer[1], Fabian Hirsch[2,3], Corey Jones[2,3], Matthew Hollander[2,3], Philipp Grohs[1,4], Amit Anand[5], Claudia Plant[1,6] and Afra Wohlschläger[2,3]**

[1] Research Network Data Science, University of Vienna, Vienna, Austria, [2] Departement of Neuroradiology, Klinikum Rechts der Isar, Technical University of Munich, Munich, Germany, [3] TUMNIC, Klinikum Rechts der Isar, Technical University of Munich, Munich, Germany, [4] Faculty of Mathematics, University of Vienna, Vienna, Austria, [5] Center for Behavioral Health, Cleveland Clinic, Cleveland, OH, United States, [6] Faculty of Computer Science, University of Vienna, Vienna, Austria

Organized patterns of system-wide neural activity adapt fluently within the brain to adjust behavioral performance to environmental demands. In major depressive disorder (MD), markedly different co-activation patterns across the brain emerge from a rather similar structural substrate. Despite the application of advanced methods to describe the functional architecture, e.g., between intrinsic brain networks (IBNs), the underlying mechanisms mediating these differences remain elusive. Here we propose a novel complementary approach for quantifying the functional relations between IBNs based on the Kuramoto model. We directly estimate the Kuramoto coupling parameters (*K*) from IBN time courses derived from empirical fMRI data in 24 MD patients and 24 healthy controls. We find a large pattern with a significant number of *K*s depending on the disease severity score Hamilton D, as assessed by permutation testing. We successfully reproduced the dependency in an independent test data set of 44 MD patients and 37 healthy controls. Comparing the results to functional connectivity from partial correlations (*FC*), to phase synchrony (*PS*) as well as to first order auto-regressive measures (*AR*) between the same IBNs did not show similar correlations. In subsequent validation experiments with artificial data we find that a ground truth of parametric dependencies on artificial regressors can be recovered. The results indicate that the calculation of *K*s can be a useful addition to standard methods of quantifying the brain's functional architecture.

Keywords: Kuramoto model, functional connectivity, synchronization, fMRI, major depressive disorder (MDD)

OPEN ACCESS

Edited by:
Ruben Sanchez-Romero, Rutgers University, United States

Reviewed by:
Adrián A. P. A. Ponce-Alvarez, Pompeu Fabra University, Spain
Sebastiano Stramaglia, University of Bari Aldo Moro, Italy

****Correspondence:***
Afra Wohlschläger
afra.wohlschlaeger@tum.de

Received: *23 June 2021*
Accepted: *28 January 2022*
Published: *03 March 2022*

Citation:
Bauer LG, Hirsch F, Jones C, Hollander M, Grohs P, Anand A, Plant C and Wohlschläger A (2022) Quantification of Kuramoto Coupling Between Intrinsic Brain Networks Applied to fMRI Data in Major Depressive Disorder. Front. Comput. Neurosci. 16:729556. doi: 10.3389/fncom.2022.729556

1. INTRODUCTION

The human brain is a complex adaptive system in which a stable neuronal substrate of gray and white matter architecture allows for a vast array of cognitive sets. At any moment integrative overall network interaction defines attainable cognitive sets as well as the degree of flexibility to react to outer stimuli (Sporns et al., 2004; Deco et al., 2008; Breakspear, 2017). Empirically, on the one hand a structural connectome can be described (Sporns et al., 2005), and complementary to that functional imaging allows for assessing the functional architecture which is in parts defined by processes of chemical connectivity depending on the status of the various transmitter systems of the

brain (Shine et al., 2019). Different measures have been proposed to quantify the complex interplay of brain areas measured with functional magnetic resonance imaging (fMRI) including statistical measures of coherence (functional connectivity; Friston, 2011), phase coherence (Glerean et al., 2012; Deco and Kringelbach, 2016; Cabral et al., 2017), and models of first order auto-regressive representation (Liégeois et al., 2017, 2019). Still a full understanding of how a brain state arises from neuronal underpinnings of structural and chemical connectivity remains elusive. Alternative approaches might help to fill into this gap. **Table 1** contains all abbreviations used in this paper.

The Kuramoto model of coupled oscillators (Okuda and Kuramoto, 1991) has been introduced to neuroscience as one potential generative model governing fluctuating oscillations in large-scale cortical circuits (Breakspear et al., 2010; Cocchi et al., 2016). The model poses that the differences in time course phases between any two oscillators are causal to phase readjustments at both ends (Okuda and Kuramoto, 1991).

While classical functional connectivity analyses look for first order statistical associations, the application of the Kuramoto model to fMRI data employs a more specific, yet simple, biophysiological model, i.e., it addresses the issue of a slow BOLD response to fast neuronal processes. As depicted in **Figure 1A** an event of fast neuronal firing in one region would cause an attraction of the phase of the fMRI signal in a second region receiving excitatory neuronal projections from the first one. Conversely, repetitive inhibitory impact from one region onto the other on a fast time scale would cause phase repulsion on the fMRI time scale. In this broader conceptualization, the Kuramoto coupling strengths can serve as empirical measures even without the assumption that the brain regions are perfect oscillators.

The overall energy landscape, which determines the likelihood of any pattern of simultaneously active brain regions (Okuda and Kuramoto, 1991; Shine, 2020), depends on the individual coupling strengths (see **Figure 1B**). Minor, but widespread modifications in the coupling strengths result in changes of this landscape and thereby in a notably different spectrum of co-activations. These ultimately have to be understood as different brain processes, i.e., alterations in thought and behavior. The idea is illustrated in a conceptual sketch in **Figure 1C**. In this view Kuramoto coupling between brain areas could for instance be changed by underlying changes in the transmitter system status which impacts on the amount of fast firing. The model, therefore, might offer a distinct complementary approach to other existing ones based on an appealing generative model.

Major depressive disorder (MD) is associated with experiences of depressed mood, with impaired cognition, energy loss, vegetative symptoms, and suicidal thoughts (American Psychiatric Association, 2013). This spectrum of diverse symptoms suggests a likely involvement of several distinct neural circuits in creating an aberrant brain state (Northoff, 2016). MD is not associated with a major focal brain lesion, but is frequently associated with alterations in synaptic, chemical rather than structural connectivity, in particular with monoamine dysfunction, which has been investigated in detail in animal and human models of depression (Cooper et al., 1991; Delgado et al., 1994; Hamon and Blier, 2013). Most antidepressants act on monoamine re-uptake mechanisms or monoamine post-synaptic receptors (Anand and Charney, 1997). Monoamine transmitter systems are mainly centrally controlled by brainstem nuclei, which exert wide spread influence via broad projections to nearly all cortico-limbic regions (Goldman-Rakic et al., 1989; Robbins and Arnsten, 2009; Jacob and Nienborg, 2018). Although they may be central to the generative mechanisms determining pathological alterations of the brain's energy landscape their direct impact on fMRI measures is difficult to establish. Therefore, a method investigating moderate but wide spread changes in the brain's functional architecture focussing on causal impact of brain regions onto each other might be of use.

In the present study we present a novel approach which consists of the direct estimation of Kuramoto coupling parameters (K) from empirical data (section 2.2). Statistical analysis is designed (section 2.4) to assess significance based not on individual coupling parameters, but on whole sets of couplings, which is in line with the underlying assumptions. The focus, therefore, shifts away from spatial localization toward modifications of the dynamics of the brain as a system. We use an exploratory data set to detect dependencies of K on clinical severity. These specific hypotheses are then tested in an entirely independent larger test data set, which underwent identical preprocessing. Specifically, within the initial exploratory analysis, we apply this method to intrinsic brain networks (IBNs) in a collective of patients with major depressive disorder (MD) and matched healthy controls, and compare it to three other measures (section 2.3): (i) functional connectivity via partial correlations (FC), (ii) phase synchrony (PS), and (iii) parameters of a first order auto-regressive model (AR). We

TABLE 1 | Abbreviations.

Section	Abbreviation	Meaning
Connectivity Measures	*K*	Kuramoto coupling parameters
	FC	Functional connectivity from partial correlations
	(I)PS	(Instantaneous) phase synchrony
	AR	First order auto-regressive measures
Neuroscience	fMRI	Functional magnetic resonance imaging
	MD	Major depressive disorder
	MDE	Major depressive episode
	HC	Healthy controls
	IBN	Intrinsic brain network
	BG	Basal ganglia network
	Ham-D	Hamilton Rating Scale for Depression
Methods	ICA	Independent component analysis
	KM	Kuramoto model
	ODE	Ordinary differential equation
	LES	Linear equation system
Simulation	IC	Inside correlation pattern coefficients
	BC	Bridging coefficients
	RC	Reference coefficients

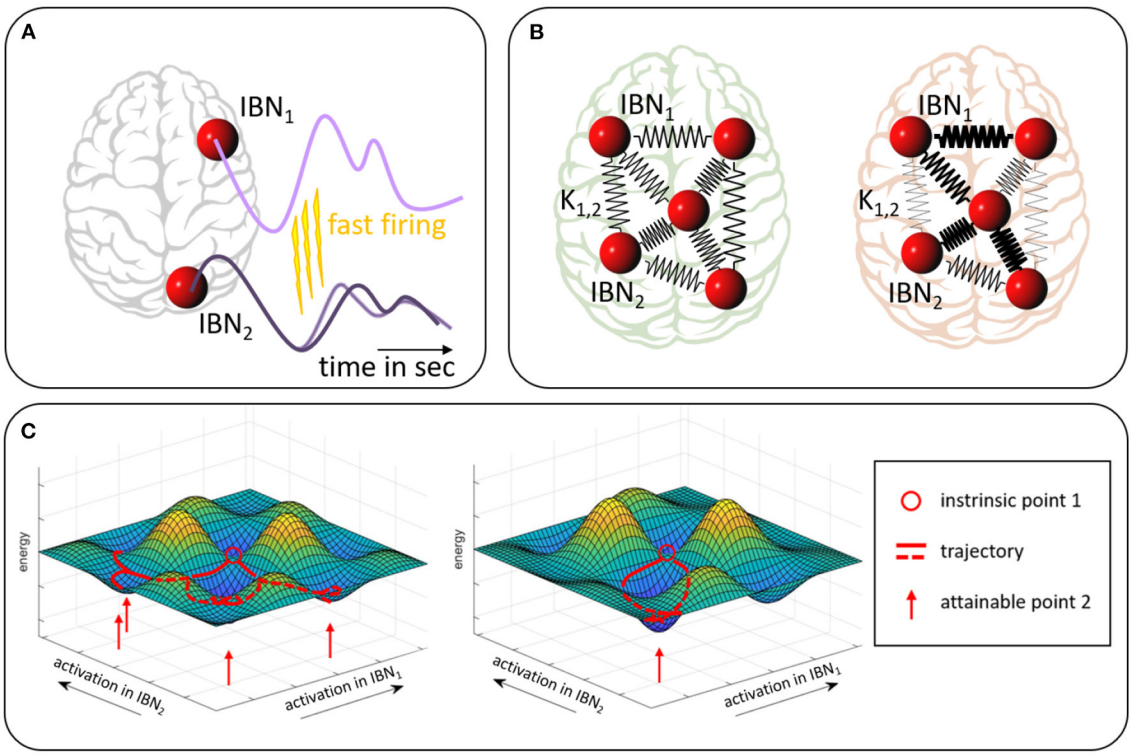

FIGURE 1 | Sketch of the model assumption. **(A)** Excitatory neuronal firing from IBN_1 on a fast time scale leads to an earlier signal rise in IBN_2 which effectively means a phase readjustment in the slow BOLD time course of the targeted IBN. Conversely, inhibitory firing would lead to a phase adjustment in the form of phase repulsion. **(B)** Pair-wise Kuramoto phase couplings of IBNs, symbolized by spring constants (here undirected), determine network-wide dynamics and are altered in pathology (compare red vs. green). **(C)** Energy landscape on a very reduced subspace of only two IBNs. Different activation constellations of the two IBNs (x- and y-axis) are associated with different energy levels (z-axis). Intrinsic information flow between the IBNs favors selective co-activations and penalizes others. The red circle indicates an arbitrary intrinsic state (i.e., co-activation constellation between IBNs), red lines indicate trajectories from this state which are favored by the landscape, red arrows indicate a set of states likely to be attained under the prevailing structural and synaptic conditions. The landscape is based on the underlying neuronal and synaptic connectivity. Minor adjustments to an overall stable energy landscape (compare left and right) may impact on fast firing intensity and thereby on Kuramoto coupling parameters $K_{i,j}$. This might allow for or subdue more versatile co-activation patterns. Widely projecting transmitter systems bear the potential of widespread moderate adjustments to the energy landscape.

then test if significant findings on K can be recovered in the independent test data set. We hypothesize that Ks show wide spread alterations with severity of pathology. By a set of simulations (section 4, **Appendix A**) we test the ability of our method to recover parametric dependencies and delineate scenarios in which parametric dependencies of Ks on external variables are accessible to the methodology.

2. MATERIALS AND METHODS

2.1. Empirical Data of Resting State fMRI in Patients With Major Depressive Disorder and Healthy Controls

2.1.1. Participants

2.1.1.1. Exploratory Data Set

Data was acquired in 25 patients with recurrent MD and 25 age matched control subjects. One patient and one control had to be excluded due to image artifacts, resulting in 24 subjects per group. Mean age in the MD group was 48y [min/max: 23y/79y, 13 female], and 44y [min/max: 26y/68y, 14 female] in the control group. All patients received medication at the time of scanning. **Supplementary Table 1** provides details on demographic and clinical characteristics. Participant data have been used in several previous studies (Manoliu et al., 2014; Meng et al., 2014; Ries et al., 2018, 2019). To render results of the IBN determination more robust 25 young healthy control (HC) participants (age 19–32, right handed) were included into the independent component analysis described below. All participants gave informed consent in accordance with the in-house ethics committee of the Klinikum rechts der Isar, TU Munich. Patients were recruited at the psychiatry department of the Klinikum rechts der Isar, TU Munich. Clinical assessment, including DSM IV (American Psychiatric Association, 2000) and Hamilton Rating Scale for Depression (Ham-D, Hamilton, 1960), was performed by two experienced psychiatrists [Structured Clinical Interview for DSM-IV (SCID) inter-rater reliability of 95%]. HCs were recruited by word-of-mouth advertising. MD was the primary diagnosis for all patients, with all of them meeting criteria for a current major depressive episode (MDE)

with an average current episode length of 16 weeks (SD = 7), an average Ham-D score of 21.8 (SD = 7.1). The mean duration of MD was 16.72 years (SD = 10.20), the mean number of episodes 6 (SD = 3). Exclusion criteria for patients were psychotic symptoms, schizophrenia, schizo-affective disorder, bipolar disorder, and substance abuse. Exclusion criteria for all participants were pregnancy, neurological or severe internal systemic diseases, and general contraindications for MRI. All patients were medicated (for details see Meng et al., 2014) except for one patient who was free of any psychotropic medication during MRI assessment.

All participants underwent 10 min of rs-fMRI with the instruction to keep their eyes closed and not to fall asleep.

2.1.1.2. Test Data Set

All subjects were included in the study after signing an informed consent form approved by the Investigational Review Board (IRB) at Indiana University School of Medicine and at the Cleveland Clinic Foundation.

One hundred seven medication-free MD subjects and 51 HCs were recruited as part of a study of young adult MD subjects at high and low risk for bipolar disorder. Out of the 107 MD subjects 28 subjects were excluded due to excessive motion, falling asleep during scanning, incomplete or lacking data, and poor data quality. Thirty-five further subjects were excluded from the statistical analysis due to inconsistent imaging parameters, and mild symptoms of mania as assessed by a score of more than 1 on the Young Mania Rating Scale (YMRS). Out of the 51 HCs 10 subjects were excluded due to excessive motion, falling asleep during scanning, incomplete or lacking data, and poor data quality or family history of psychiatric illness. Four further subjects were excluded from statistical analysis due to inconsistent scanning parameters. Data of the extended patient data set without restrictions on YMRS and inconsistent imaging parameters were processed and included into the independent component analysis described below.

Finally, 44 patients (age: mean [min/max] 24y [18y/30y], 33 females) and 37 healthy controls (age: mean [min/max] 24y [18y/30y], 22 females) were included into the statistical analysis. See **Supplementary Table 1** for a detailed presentation of demographic and clinical characteristics. A subgroup of the collective was part of a previous investigation (Wohlschläger et al., 2018). Both patients and HCs were paid $25 for screening and $75 for MRI scan. All subjects underwent a detailed structured diagnostic interview—Mini Neuropsychiatric Interview (MINI) that generated a DSM-IV diagnosis (Sheehan et al., 1997). Inclusion criteria for MD were: (1) between 15 and 30 years and able to give voluntary informed consent; (2) satisfy DSM-IV-TR criteria for MD using a structured interview; (3) never met criteria for mania or hypomania; (4) 17-item Ham-D > 18 and < 25; (5) Young Mania Rating Scale (YMRS) (Young et al., 1978) score < 10; (6) satisfy safety criteria to undergo an MRI scan; (7) able to be managed as outpatients during the study, ascertained by the following—(i) Clinical Global Severity Scale < 5 i.e., moderately ill, (ii) no significant suicidal or homicidal ideation or grossly disabled.

All participants underwent 6:16 min of rs-fMRI with the instruction to keep their eyes open and to look at a fixation cross.

2.1.2. MRI Data Acquisition

2.1.2.1. Exploratory Data Set

All measurements were performed on a 3T MR scanner (Achieva, Philips, Netherland) using an 8-channel phased-array head coil. T1-weighted anatomical images were obtained from a magnetization-prepared rapid acquisition gradient echo (MPRAGE) sequence (FoV = 240 × 240 mm^2, 170 slices). FMRI data were obtained from a gradient echo planar imaging (EPI) sequence (TR/TE = 2,000/35 ms, 32 slices, slice thickness = 4 mm, 300 volumes). For the additional data set of young subjects respective parameters were: T1 (FoV = 480 × 480 mm^2, 340 slices), fMRI (TR/TE = 2,007/30 ms, 36 slices, slice thickness = 3 mm; 300 volumes).

2.1.2.2. Test Data Set

Measurements were acquired at Cleveland Clinic Main Campus using 3T Siemens Prisma MR Scanner. T1-weighted anatomical images were obtained from a MPRAGE sequence (FoV = 240 × 256 mm^2, 160 slices). FMRI data were obtained from an EPI sequence (TR/TE =2,800/29 ms, 39 slices, slice thickness = 3.5 mm, 132 volumes). To limit the head motion scans at Cleveland Clinic were acquired with subjects fitted with a bite bar.

2.1.3. Preprocessing

During preprocessing particular care was taken to address physiological as well as movement artifacts. Effects of heart beat and breathing were quantified from the data using Physiologic Estimation by Temporal ICA (PESTICA) (Beall and Lowe, 2007), and a physiologic noise removal tool, RETROICOR (Glover et al., 2000). During this step instantaneous effects of heart beat and respiration are corrected for. Estimates of the cardiac and respiratory rates can be retrieved. There were no significant group differences in both measures. Because it has been shown that magnitude of cardiac and respiratory rate can have delayed effects within the BOLD signal (Birn et al., 2008; Chang et al., 2009) respective regressors were calculated and accounted for within the subsequent procedures (see below). Movement correction was optimized with slice-based realignment using slice-oriented motion correction (SLOMOCO) (Beall and Lowe, 2014). No significant group differences in volume-wise or slice-wise mean motion were detected (see **Supplementary Table 1**). Further preprocessing steps included coregistration to the T1 image, slice time correction, spatial normalization, and spatial smoothing with the full width at half maximum (FWHM) of the Gaussian filter 8 × 8 × 8 mm^3 (SPM12, https://www.fil.ion.ucl.ac.uk/spm/).

2.1.4. IBN Time Course Preparation

Exploratory and test data sets of the preprocessed data were each entered into independent component analyses (ICA) and each separated into 75 spatially independent components (Calhoun et al., 2001) based on the Infomax-algorithm and implemented in the fMRI Toolbox (GIFT, http://www.icat.sourceforge.net) which was run 20 times through ICASSO to ensure stability

of the estimated components. For both data sets group average components were back-projected on the single-subject data. Via multiple spatial regression 20 of the 75 independent components in the exploratory data set and 28 of the 75 independent components in the test data set were identified as neuronally meaningful IBNs with correlation coefficients above 0.15 to the spatial templates of the IBNs as described in Allen et al. (2011). The IBNs are presented in the **Supplementary Figures 1, 2**. Time courses from these IBNs for each subject were corrected for effects of white matter signal, and signal from the cerebrospinal fluid, and additionally for effects of the respiratory (Birn et al., 2008), and the cardiac (Chang et al., 2009) response functions, by regression. The latter two functions compensate for delayed effects of variations in respiratory and breathing rates on the BOLD signal. In order to select a frequency band affected by dynamical changes in the patient group, metastability was calculated for a range of frequency bins (Ries et al., 2019) as described in the **Supplementary Material** (section 1.3) (**Figure 3**). Frequency bin 3 displayed significant reduction in metastability in the patients. Based on this finding, time courses were bandpass filtered to a narrow frequency band of 0.05–0.075 Hz in preparation for a subsequent Hilbert transformation (Córdova-Palomera et al., 2017) using a Butterworth filter of order 7. The *FC* and *AR* measures are not based on phase analysis, therefore, the frequency range does not have to be that strongly reduced. Here the less stringent, commonly used frequency band of 0.01–0.1 Hz (Zang et al., 2007) was chosen as band pass filter.

2.2. Calculation of Kuramoto Coupling Coefficients

This section describes the methodological concepts which we will use to analyze the coupling behavior in our data sets. **Table 2** gives an overview of the most important notation used in the following sections.

TABLE 2 | Notation.

Notation	Meaning
$\mathbf{X}$	Bold capital letters indicate matrices
$\mathbf{x}$	bold small letters indicate vectors
X,x	Non bold capital or small letters indicate real numbers
$\mathbb{X}$	Three dimensional matrix
$\mathbf{x}_i$	i−th row of a matrix $\mathbf{X}$
$X_{i,j}$	(i,j)−th entry of a matrix $\mathbf{X}$
x_i	i−th entry of a vector $\mathbf{x}$
s	Number of subjects
r	Number of IBNs per subject
T	Number of measure points in the recording
K	Notation for the measure "Kuramoto coupling parameters" for empirical data analysis
$\mathbb{K}^{o}$, $\mathbf{K}^{o}$, $K^{o}_{i,j}$	Original random coefficient matrices/matrix/matrix entry for the simulations
$\mathbb{K}^{c}$, $\mathbf{K}^{c}$, $K^{c}_{i,j}$	Manipulated coefficient matrices/matrix/matrix entry with induced correlations on *score*
$\mathbb{K}^{res}$, $\mathbf{K}^{res}$, $K^{res}_{i,j}$	Resulting Kuramoto coefficient matrices/matrix/matrix entry calculated with our model
ω_i	Eigenfrequency of the i−th oscillator/IBN
d	Overall coupling parameter
n	Noise level weight
$\mathbf{N}$, $\mathbf{N}_s$, $\mathbf{N}_{as}$	Correlation patterns
$\mathbf{M}$, $\mathbf{M}_{in/out}$	Individual coefficient weight matrix ("mask matrix")

2.2.1. Kuramoto Model

First, we consider the Kuramoto model (KM) (Kuramoto, 1975; Acebrón et al., 2005). This is a system of ordinary differential equations (ODEs) describing the temporal change of the phases $\varphi_1, \ldots, \varphi_r$ of r oscillators, which are coupled by the sine of their phase differences:

$$\dot{\varphi}_i(t) = \frac{\partial \varphi_i(t)}{\partial t} = \omega_i + \frac{C}{r} \sum_{j=1}^{r} K_{i,j} \sin(\varphi_j(t) - \varphi_i(t)) = f(t, \varphi_i(t))$$
$$i = 1, \ldots, r. \quad (1)$$

Here, $\varphi_i(t)$ is the phase angle of the i–th oscillator at time point t and ω_i is the eigenfrequency of the i-th oscillator. The only parameters in this model are the coupling coefficients $K_{i,j}$ describing the connection between oscillator i and j. In this model couplings between each and every oscillator are considered, which matches our assumption of wide-spread effects and simultaneous involvement of all IBNs. The coupling strength C can be set to 1 since it is an equal scaling for the $K_{i,j}$ parameters. Note, that the model can attain different forms. The choice of this form is discussed in the **Supplementary Material** (section 2.1).

Each subject in our data set has r time courses $x(t)$ representing the activity in r IBNs. The use of this model for our time series data $x(t)$ first requires the extraction of the instantaneous phases $\varphi(t)$ for each time course.

2.2.2. Hilbert Transform

The Hilbert transform (Hahn, 1996) denoted by $H\{x(t)\}$ returns a version of the original time series shifted by $\frac{\pi}{2}$. Considering the analytical signal $x_a(t)=x(t)+i\cdot H\{x(t)\}$, we can then represent the time series in an amplitude-phase representation.

$$x(t) = a(t) \cdot \cos(\varphi(t)) \quad (2)$$

with the instantaneous amplitude $a(t)=|x_a(t)|$ and the instantaneous phase $\varphi(t)=\angle x_a(t)$.

2.2.3. Numerical Solution Method

The usual way of utilizing an ODE model such as the KM, is to set the model parameters (in this case the $K_{i,j}$) suitable for the domain application and subsequently calculate a solution that fulfills the model equations (i.e., the functions $\varphi_1, \ldots, \varphi_r$) with a numerical solver. This has been done previously in Neuroscience (Stramaglia et al., 2017)—also for the Kuramoto model (Schmidt et al., 2015). There exist many numerical approximation methods. One of the most basic approaches is Euler's method (Epperson, 2013). The approximation of the

solution is calculated step-wise according to the following rule

$$\varphi_i(s+1) = \varphi_i(s) + f(s, \varphi_i(s)). \tag{3}$$

with the iteration steps s and $s+1$ and a step size h chosen as 1. Discussion about this choice and also the choice of the Euler method as a numerical solution method can be found in the **Supplementary Material** (section 2.2).

In this work, we are already given phase courses from the recordings (i.e., the functions $\varphi_1, \ldots, \varphi_r$). The time courses in our experiments are filtered to a very narrow frequency band. Therefore, we can model the eigen-frequencies ω_i as the mean frequency $\bar{\omega}$ of the respective frequency band. Another option would be to estimate each eigen-frequency from the largest peak in the frequency profile of each time course via fast Fourier transform (FFT). Our codes provide both options. Unless mentioned otherwise, all our experiments were conducted using a fixed mean eigen-frequency. Given all phase and eigen-frequency values, we are able to choose a reverse engineering approach. We assume that the KM can describe synchronization or coupling respectively of our given data and utilize formula (3) to calculate the KM parameters $K_{i,j}$ which optimally fit our data.

2.2.4. Goal

Our goal is the estimation of the coupling coefficients $K_{i,j}$ of model (1) considering the given phase courses $(\varphi_1(t), \ldots, \varphi_r(t)$, t=1, ... $T)$ and eigen-frequencies (ω_i) of the IBN time series. The coefficients may be interpreted as the coupling strengths between the time series and, therefore, between the IBNs of a subject. We proceed as follows.

2.2.5. Linear Equation System

By transforming the time series $x_i(t)$ of each IBN of a participant using the Hilbert transformation, we get an amplitude-phase representation of each time series

$$x_i(t) = a_i(t) \cdot \cos(\varphi_i(t)) \quad t = 0, \ldots, T-1. \tag{4}$$

This way we obtain the actual time course of the phases $\varphi_i(t)$ of the time series $x_i(t)$, i=1, ..., r. So instead of simulating the synchronization of initial phase values of a subject's time series, we assume that synchronization of the phases is explainable by the above Kuramoto model (1). Considering the phase values $\varphi_i(t)$, t=0, ..., $T-1$ of a single time course of a single subject and plugging in those phase values into Equation (3) leads to linear equations of the form

$$\varphi_i(s+1) = \varphi_i(s) + \omega_i + \frac{1}{r}\sum_{j=1}^{r} K_{i,j} \sin(\varphi_j(s) - \varphi_i(s)),$$
$$s = 0, \ldots, T-2. \tag{5}$$

In our exploratory data set, we have $T = 300$ measure points in the recording and each of the $s = 24$ subjects per group has recordings for $r = 20$ IBNs. Thus, we obtain 299 (# time steps) equations for 20 (# IBNs) unknown variables $K_{i,j}$, j=1, ..., 20 for each IBN of each subject. This results in total in 400 coefficients $K_{i,j}$, i, j=1, ..., 20 for one subject. Note again, that time steps are labeled as s=0, 1, 2, ..., 299 corresponding to iterations while the values correspond to time points t=0, 2, 4, ..., 598 in seconds. The equations can be rearranged to the form of a linear equation system (LES)

$$\mathbf{S}_i \cdot \mathbf{k}_i = \mathbf{b}_i, \tag{6}$$

with $\mathbf{S}_i \in \mathbb{R}^{299\times 20}$, $\mathbf{k}_i \in \mathbb{R}^{20}$, and $\mathbf{b}_i \in \mathbb{R}^{299}$. The system matrix $\mathbf{S}_i$ will, however, have one zero column, which corresponds to the coefficient $K_{i,i}$. We have to eliminate this column in order to obtain a system matrix with full rank. Accordingly, we reduce the number of unknowns by not solving for $K_{i,i}$, but determining it instead. As it represents the coupling between an IBN to itself, we simple set the value to 1 (any constant would suffice). Thus, we will determine 380 coefficients per subject. Details about the entries of $\mathbf{S}_i$ and $\mathbf{b}_i$ as well as the derivation of the entries can be found in the **Supplementary Material** (section 2.3).

2.2.6. Solving the LES

Since the LES (6) is over-determined, i.e., the number of equations is larger than the number of variables, we can not simply invert the non-squared system matrix $\mathbf{S}_i$. We solve the over-determined LES optimal with respect to the ℓ_2 norm by building the *normal equations* (Gauß, 1809; Abdulle and Wanner, 2002).

$$\underbrace{\mathbf{S}_i^{\mathrm{T}}\mathbf{S}_i}_{\hat{\mathbf{S}}_i} \cdot \hat{\mathbf{k}}_i = \underbrace{\mathbf{S}_i^{\mathrm{T}} \cdot \mathbf{b}_i}_{\hat{\mathbf{b}}_i}. \tag{7}$$

The symmetric matrix $\hat{\mathbf{S}}_i \in \mathbb{R}^{19\times 19}$ is regular and can, therefore, be inverted to obtain a unique solution $\hat{\mathbf{k}}_i \in \mathbb{R}^{19}$, where it holds

$$||\mathbf{S}_i \cdot \hat{\mathbf{k}}_i - \mathbf{b}_i||_{\ell_2}^2 = \min_{\mathbf{x}\in\mathbb{R}^{19}} ||\mathbf{S}_i \cdot \mathbf{x} - \mathbf{b}_i||_{\ell_2}^2 \tag{8}$$

Derivations of the normal equations to yield the optimal solution in the sense of Equation (8) are given in the **Supplementary Material** (section 2.4). In order to solve the equations simultaneously for all IBNs of one subject, we build a block diagonal equation matrix, and append the inhomogeneity terms resulting in

$$\mathbf{S} = \begin{pmatrix} \mathbf{S}_1 & \mathbf{0} & \cdots & \mathbf{0} \\ \mathbf{0} & \mathbf{S}_2 & \cdots & \mathbf{0} \\ \vdots & \vdots & \ddots & \vdots \\ \mathbf{0} & \mathbf{0} & \cdots & \mathbf{S}_{20} \end{pmatrix} \tag{9}$$

$$\mathbf{b} = \begin{pmatrix} \mathbf{b}_1 \\ \mathbf{b}_2 \\ \vdots \\ \mathbf{b}_{20} \end{pmatrix} \tag{10}$$

We calculate the solution $\hat{\mathbf{k}} \in \mathbb{R}^{380}$ of the LES

$$\mathbf{S}^{\mathrm{T}} \cdot \mathbf{S} \cdot \hat{\mathbf{k}} = \mathbf{S}^{\mathrm{T}} \cdot \mathbf{b} \tag{11}$$

by a simple matrix inversion

$$\hat{\mathbf{k}} = (\mathbf{S}^{\mathrm{T}} \cdot \mathbf{S})^{-1} \cdot \mathbf{S}^{\mathrm{T}} \cdot \mathbf{b} \tag{12}$$

Finally, we set the resulting Kuramoto coupling coefficients for one subject $\mathbf{k}^{\mathrm{res}} := \hat{\mathbf{k}}$. We perform these steps for each subject which provides us with 380 coefficients $K^{\mathrm{res}}_{i,j}$, i,j=1, . . . , 20, $i \neq j$ per individual. The vector $\mathbf{k}^{\mathrm{res}}$ can be reshaped to a Kuramoto coupling matrix $\mathbf{K}^{\mathrm{res}}$ of size 20 × 20 by putting the coefficient estimating the coupling between IBN i to IBN j in the $(i,j)-$th entry and filling up the diagonal with ones. This can nicely be visualized by a heat map (see **Supplementary Figure 4** for an example visualization). Gathering all Kuramoto coupling coefficient for all subjects in a group results in a three dimensional matrix object of size $s \times r \times r$, which we term $\mathbb{K}^{\mathrm{res}}$. This object contains the calculated Kuramoto coupling coefficient, which are given the marker name K in Introduction (section 1), Results (section 3.1) and Discussion (section 5) in the context of the empirical data sets.

All calculations were implemented in Matlab R2018a[1]. Scripts are available via the following link: https://doi.org/10.6084/m9.figshare.13352399.

2.3. Calculation of Reference Coupling Measures

2.3.1. Partial Correlations (*FC*)

Time course data were filtered to a frequency band of 0.01–0.1 Hz (Zang et al., 2007). Partial correlations between each and any of the IBNs were calculated from the time courses of all IBNs using Matlab.

2.3.2. Phase Synchrony (*PS*)

Time course data were filtered to a frequency band of 0.05–0.075 Hz (as in the calculation of K) in preparation for the subsequently conducted Hilbert transformation (Córdova-Palomera et al., 2017). *PS* were calculated pairwise from the phase time courses between each and any of the IBNs according to

$$PS_{i,j} = \mathrm{med}(IPS_{i,j}(t)) = \mathrm{med}(\cos(\varphi_j(t) - \varphi_i(t))) \tag{13}$$

Here, med$(\cdot)$ is the median function across time applied to the instantaneous phase synchrony $IPS(t)$ (Zarghami et al., 2020) and $\varphi_i(t)$ is the phase angle of the i–th oscillator at time point t given in rad.

2.3.3. Coefficients of a First Order Auto-Regressive Model (*AR*)

Time course data were filtered to a frequency band of 0.01–0.1 Hz (Zang et al., 2007). Calculation of the auto-regressive coefficients, including auto-regression within one and the same time course, were performed using the scripts available from Liégeois et al. (2019) according to their Equation (1):

$$x(t) = AR \times x(t-1) + \epsilon(t) \tag{14}$$

[1]https://www.mathworks.com/.

2.4. Statistical Analysis

2.4.1. Set-Level Statistics

We were particularly interested in wide spread changes of Ks and the control measures across the whole brain. We therefore tested whether the number of individual correlations depending on a regressor (Ham-D) were likely to occur by chance. To this, we compared the sizes of sets containing couplings with statistically significant dependencies on the regressor against the distribution of set sizes derived from random permutations of K-values.

In detail, we assessed the significance of sets of $K_{i,j}s$ showing moderate associations to a parametric regressor per group via the number of these association. We calculated Spearman correlations per individual coupling to a given regressor, and counted the number of significant correlation at a threshold of $P_u < 0.05$, uncorrected for multiple comparisons. Subsequently, all couplings were permuted within each subject of the group and we repeated the correlation procedure yielding a number of chance correlations and, therefore, chance set sizes at the threshold of $P_u < 0.05$. By repeating this procedure we produced a distribution of the number of chance set sizes, to which we compared the actual set size (see **Figure 2**). We generated a P-value from the percentage of chance set sizes larger than the actual set size. The script accounts for the fact, that matrices can be symmetric (*FC*, *PS*) or non-symmetric (K, *AR*). A number of 500 permutations yielded stable results for the P-values.

We performed similar tests on the set-level for finding sets of significant couplings versus zero and sets of significant couplings showing group differences, by replacing the correlation procedure with Wilcoxon signed rank and Wilcoxon rank sum test, respectively.

Data deviating more than two standard deviations from the mean were regarded as outliers. All procedures were implemented in Matlab including parts of the script *sig_permtest.m* (http://commdetect.weebly.com/).

Corrections for multiple comparisons was necessary, because we performed correlations on two regressors (Ham-D, Age) in three versions (bi-directional, positive, negative) in the patient group, amounting to a Bonferroni factor of 6. In the control group we only analyzed the age regressor in the three versions, amounting to a Bonferroni factor of 3. In all other tests of couplings versus zero or between groups we corrected the threshold for significance by a Bonferroni factor of 3 for the three directions of the test always performed. P-values reported for the test data set are not corrected for multiple comparisons.

In the exploratory data set, dependencies of coupling sets with age were found for *PS* in patients as well as healthy controls [MD: bi-directional (*i*): P_u=0.004, positive (*ii*): P_u=0.022, negative (*iii*): P_u=0.008; HC: bi-directional (*i*): P_u=0.036, positive (*ii*): P_u=0.046, negative (*iii*): P_u=0.092, uncorrected for multiple comparisons]. No such sets were found for K and *AR*. Therefore, all set-level statistics for *FC* and *PS* were corrected for age by regressing out age from each individual coupling. There was no significant dependence on sex for any coupling measure.

We investigated correlations of K with mean head motion and cardiac rate. In the patient group of the exploratory data set we detected a correlation of head motion with sets of Ks. This is discussed detail in **Supplementary Material** (section 4.1). There

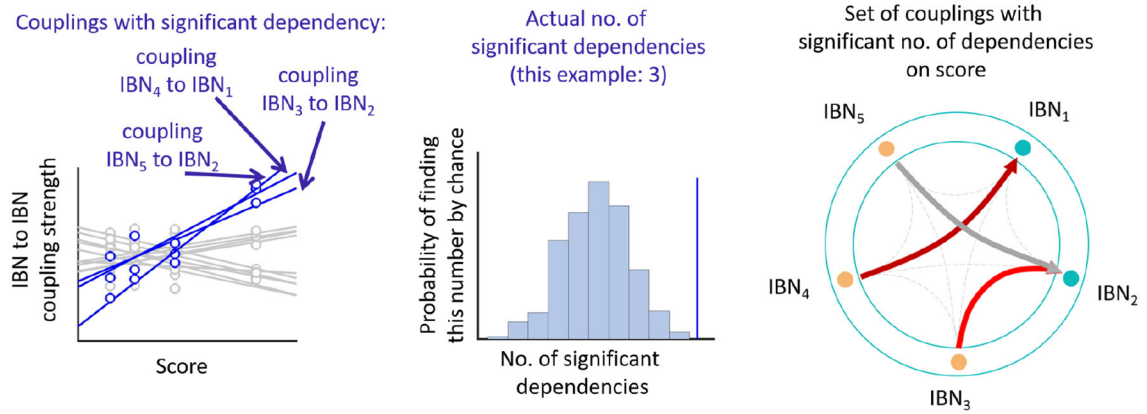

FIGURE 2 | Analysis pipeline on empirical data. **(Left)** From correlations of all individual coupling parameters to a parametric score across subjects, moderately significant correlations (blue) vs. non-significant correlations (gray) are detected. **(Middle)** The number of these correlating couplings ("set size") is compared to the distribution of the set sizes derived from permutations of the couplings. **(Right)** Sets of couplings reaching significance are displayed.

were no other significant correlations of K with movement or cardiac rate.

2.4.2. Phase Randomized Surrogates

Significant dependence of the coupling measures K and PS on regressors was additionally assessed by using phase randomized surrogates to eliminate any estimation bias. Time course phases were randomized while preserving their power spectra by the following steps (Ponce-Alvarez et al., 2015): (i) each time course underwent Fourier transformation, (ii) the phase values were replaced by values from a random uniform distribution between $-\pi$ and π, and (iii) in order to return to the time domain an inverse Fourier transform was applied. K and PS calculation was applied to the phase randomized data sets. Significance of set-level correlation was tested against 500 phase randomizations.

3. RESULTS

3.1. Results on Empirical fMRI Data in Patients With Major Depression and Healthy Controls

3.1.1. Sets of *K*s Show Particular Dependence on Disease Severity

We wanted to see if there were sets of specific Ks exhibiting group differences or parametric dependencies in the exploratory data set. We used a permutation approach to estimate the probability of the number of couplings showing moderate dependence on either group or a parametric regressor occurring by chance (see **Figure 2**). This approach allows for detecting parametric dependencies with opposite signs in different couplings. The tests were, therefore, performed separately (i) irrespective of the direction of associations between couplings and parametric regressor or group, (ii) for positive associations, or (iii) negative associations.

With regards to group differences, none could be detected from the Ks. FC provided a set of couplings being at trend (P_c=0.063) in the contrast of type (*ii*), i.e., they displayed higher values in the patient group than in controls (see **Supplementary Figure 8**, section 4.2). No other significant or trending sets were found.

Contrasting to the lack of overall group difference, Ks yielded sets of couplings displaying significant parametric dependence on the regressor of interest in the patient group.

Sets of Ks were significantly depending on the Ham-D score in the patient group (see **Figures 3A,B** and **Table 3**, showing the uncorrected P-values). The dependence was mainly driven by a positive correlation of type (*ii*) (P_c=0.012), meaning that Ks increased with higher disease severity, but a set including both ways of dependence, i.e., of type (*i*) was also significant (P_c=0.006). The set with negative dependence on Ham-D of type (*iii*) was not significant (P_c=0.096). We checked for set-level significance of the dependence on the Ham-D score when the eigenfrequencies in equation (1) are calculated from the data. This method yielded very similar results (*i*) P_c=0.012, (*ii*) P_c=0.036, (*iii*) P_c=0.11.

All other analyses of FC, PS, and AR in patients and controls yielded no significant results in the dependence on Ham-D.

A significant negative correlation was found between the coupling K from the salience network onto the basal ganglia network (P_c=0.002) to Ham-D after rigorous Bonferroni correction for 380 multiple comparisons. This coupling was the only one showing a significant dependence on a score under investigation.

The re-assessment of set dependence on Ham-D in the test data set shows that the association of K to this external regressor can be recovered in the test data set.

4. VALIDATION

The K couplings did not significantly differ from zero. Nevertheless, on a set level, dependencies to clinical severity scores could be detected in two independent empirical data sets. As an additional validation of the capabilities of our novel method, we conducted experiments with synthetically generated

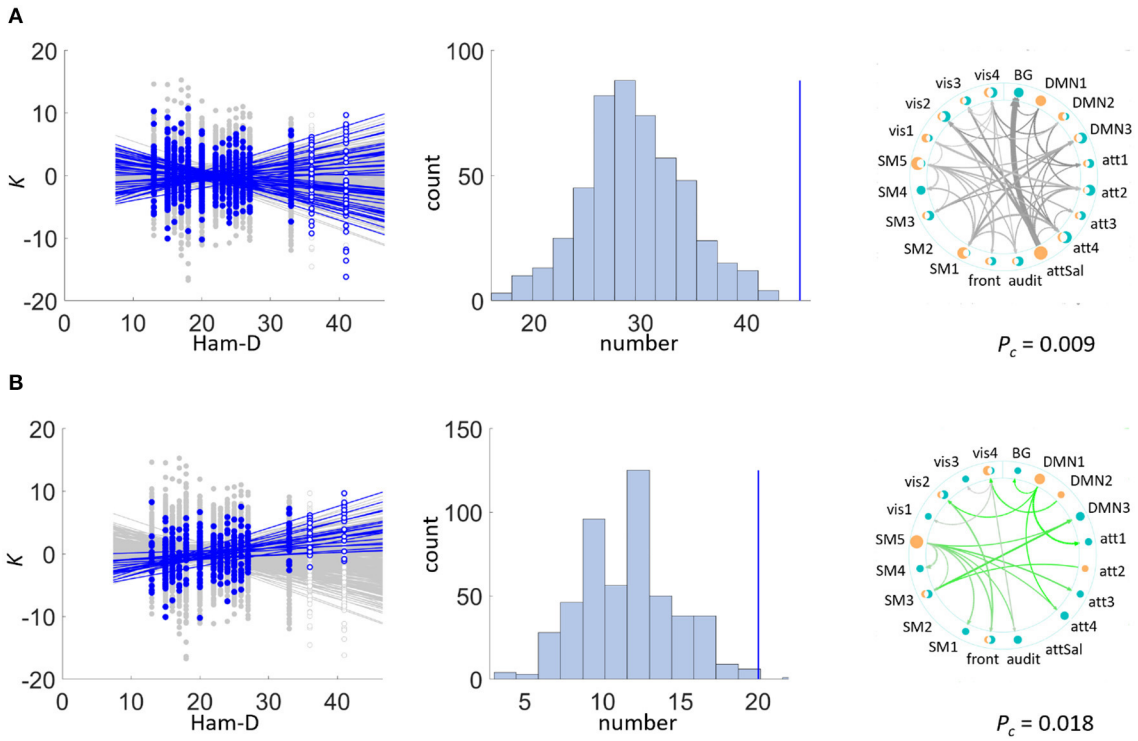

FIGURE 3 | Set-level results. Sets of couplings of statistically significant size were detected in the exploratory data set within the patient group: *K* significantly depended on Ham-D in **(A)** the bi-directional test, mainly driven by **(B)** positive correlations. Left side plots depict the individual significant correlations of couplings on the regressor in blue and in gray otherwise. Note that indicated regressions in this figure were fitted to data excluding outliers (non filled markers). Middle plots depict the chance distribution on set sizes, with the actual data indicated by the blue vertical line. The right plot displays those connections constituting the significant set. Color varies with direction of correlation: bi-directional (grey), positive (green), line width scales with correlation coefficient ρ. Dots marking the IBNs are two-fold for outbound (orange) and inbound (teal) couplings, scaling in size with overall coupling strength toward all other IBNs. **(A)** Patient group: *K* vs. Ham-D. **(B)** Patient group: *K* vs. Ham-D (positive dependence).

data. More specifically, we simulated phase courses, where we induce a dependence in the data generating coupling parameters on an independent score. Our hypothesis is, that our model should be able to detect these dependencies in the generated data. The purpose of these experiments is not to prove our method superior in comparison to other methods, but they should serve as a proof of concept, that induced dependencies can be recovered by our method.

4.1. The Simulation Model

We generate a synthetic data set for s subjects with r IBNs and T measure points each. We utilize the Kuramoto model to simulate the data, but we alter model (1) in various aspects to fit our purpose of generating phase courses. The simulated phase courses for one subject are the solution functions of the following Kuramoto model:

$$\dot{\varphi}_i(t) = \frac{\partial \varphi_i(t)}{\partial t} = \omega_i + \frac{d}{r}\sum_{j=1}^{r} K_{i,j} \cdot M_{i,j} \cdot \sin(\varphi_j(t) - \varphi_i(t)) + n \cdot \varepsilon_i(t)$$

$$i = 1, \ldots, r. \tag{15}$$

As shown several parameters are included in the model now. First, we include eigen-frequencies ω_i for the oscillators. These are the driving forces hindering synchronization. The coupling coefficients $K_{i,j}$ are the second forces determining synchronization behavior between each two oscillators i and j, i.e., $\mathbf{K} \in \mathbb{R}^{r\times r}$. The parameter d is a positive weight for the coupling coefficients, which acts equally on all coefficients and can be seen as an overall coupling strength. The additional weight $M_{i,j}$ acts individually on each single coefficient, i.e., $\mathbf{M} \in \mathbb{R}^{r\times r}$. Furthermore, we include noise $\varepsilon_i(t)$ in our model which is also weighted with an intensity level n.

To obtain simulated phase courses, we have to solve the system of ODEs. As the numerical solver of the ODE system, we choose not to work with the same as when calculating the coefficients (i.e., Euler's method). This prevents to simply get out what we put in. The solver used for the simulations is the classical Runge-Kutta algorithm (Schwarz and Köckler, 2011) also called RK-4. Providing initial values $\varphi_i(0)$, i=1, . . . , r, the Runge Kutta method iteratively yields the phase courses. A detailed formulation of the RK-4 method is given in the **Supplementary Material** (section 3.1).

TABLE 3 | Set level statistics.

	MD		HC	
EXPL.	**Ham-D**	**Age**	**Age**	
	All (pos.neg.)	**All (pos.neg.)**	**All (pos.neg.)**	
K	**0.001** (**0.002**/0.016)	n.s. (n.s./n.s.)	n.s. (n.s./n.s.)	
	<0.001 (**0.004**/**<0.001**)	n.s. (n.s./n.s.)	n.s. (n.s./n.s.)	†
FC	n.s. (n.s./n.s.)	n.s. (n.s./0.080)	**<0.001** (**0.003**/**0.005**)	
PS	n.s. (n.s./n.s.)	**0.004** (0.022/0.008)	0.036 (0.046/0.092)	
	n.s. (n.s./n.s.)	**<0.001** (0.018/**<0.001**)	0.046 (0.022/n.s.)	†
AR	n.s. (n.s./n.s.)	n.s. (n.s./n.s.)	n.s. (n.s./n.s.)	
TEST				
K	0.006 (0.002/0.12)			
	0.022 (0.032/0.19)			†

P-values, not corrected for multiple comparisons, from permutation testing indicating the significance of the size of a set appearing by chance, for bi-directional test ("all"), or including only positive ("pos.") or only negative ("neg.") correlations. For the exploratory data sets P-values surviving multiple comparisons correction, with Bonferroni factors 3 and 6 for HC and MD, respectively, are indicated in bold print. FC and PS were corrected for age in all tests, except for vs. age itself. For the test data set the table provides the P-values derived from re-assessing the significant or close to significant dependencies from the exploratory data set in the test data set. †Statistical testing was performed against measures calculated from phase randomized surrogates. n.s., not significant.

4.2. Simulation Procedure

For best possible comparability, we generate 20 time courses with 300 time points for 24 subjects. Therefore, we have to provide our data generating pipeline with the parameters as explained above. This includes matrices $\Omega \in \mathbb{R}^{20\times24}$ and $\Phi_{\mathbf{0}} \in \mathbb{R}^{20\times24}$ containing the 20 eigenfrequencies and initial phase values for each subject—which are both randomly initialized—, the weight matrix $\mathbf{M} \in \mathbb{R}^{20\times20}$, and the weights $d \in \mathbb{R}^{+}$ and $n \in \mathbb{R}^{+}$ for the coefficients and noise. We randomly initialize coupling coefficient matrices $\mathbf{K} \in \mathbb{R}^{20\times20}$ and an independent score value $s \in \mathbb{R}$ (representing the Ham-D) for each subject. Across subjects, the coefficients will not be significantly correlated with this independent score, but we can manipulate each subjects coefficient matrix, such that a certain portion of the coefficients shows very high positive or negative correlation (see **Figure 4A**). By inserting dependencies on **s** for specific coefficients, this results in a correlation pattern, as can be seen in **Figure 4B**, where coefficients between regions from 1 to 13 show distinct correlations compared to others. The resulting manipulated coefficient matrices for all subjects $\mathbb{K}^{c} \in \mathbb{R}^{24\times20\times20}$ are then also provided for the data generating procedure. An example of a generated phase course can be seen in **Supplementary Figure 5**.

For the $24 \times 20 \times 300$ generated phase course data a Kuramoto coupling coefficient matrix is calculated for each subject with our Kuramoto coupling estimation model, which results in 24 matrices of size 20×20 ($\mathbb{K}^{res}$). To account for the randomness in the initialization of Ω and $\Phi_{\mathbf{0}}$, we repeat the simulation pipeline for six different random phase and eigenvalue initializations and perform evaluations in account of these six runs, i.e., medians of *P*-values. We equidistantly set *d* and *n* within a limited value ranges and make calculations with all combinations of theses two parameters while keeping the other parameters fixed. The simulation process is quite run time intensive, therefore, we choose the number of runs to stay within a moderate run time but at the same time account to a certain degree for the randomness of the initialization. For the cluster permutation test on the resulting $\mathbb{K}^{res}$, bi-directional correlations were considered with a number of 100 permutations.

4.3. Exemplary Result on Simulated Data

One result can be seen in **Figure 4D**. Each cell of the heatmap shows the median *P*-value of the cluster permutation test over the six runs for one combination of (n, d). The correlation pattern of the data generating coupling coefficients corresponds to **Figures 4A,B**, respectively. The weights in **M** are chosen as shown in **Figure 4C**, i.e., couplings are only considered in the data generation, if they show a significant correlation. As we can observe, the induced dependence on the independent score **s** can indeed be recovered, when the relation of noise to coupling is in a certain range.

In **Appendix A**, the full simulation design, parameter choices, pipeline, and results are explained in detail. Additional results are also given in the **Supplementary Material**.

5. DISCUSSION

In the present study we showed that Kuramoto coupling parameters estimated from empirical data relate to a clinical scores indicating disease severity in patients with major depressive disorder. The findings acquired from the *K*-values differ qualitatively from findings with other methods for quantification of functional connectivity and, therefore, rather provide complementary information. While the variability within single *K*-values is minor, significantly larger sets of *K*s relate to external scores. The findings are in line with the initial hypothesis which puts wide-spread coupling changes into context with chemical connectivity alterations at the synapses. The data provide an initial indication that parametric changes of the *K*-values can be discussed in context of pathological alterations of brain function in major depressive disorder (MD). By analyzing artificial data with a ground truth of parametric dependence in the couplings, we prove the ability of our analysis pipeline to recover this dependence within a reasonable parameter space of the model.

A number of recent studies highlight the explanatory power of following the trajectories of fMRI co-activation patterns from time point to time point via analysis of inter-regional connectivity measures (Gu et al., 2015; Braun et al., 2018; Liégeois et al., 2019). Gu et al. (2015) analyze how activity spread along a known structural connectome in a step-wise re-iterated way favors easy to reach states of co-activation patterns over hard to reach states. While this analysis excludes variability due to the impact of chemical transmission in activity flow, it demonstrates that co-activation states observed from fMRI can, in principle, be tracked back to the magnitude of activity flow among the whole set of brain areas from one iteration step to the next. Relating to the latter concept, Liégeois et al. (2019) show in a recent study that

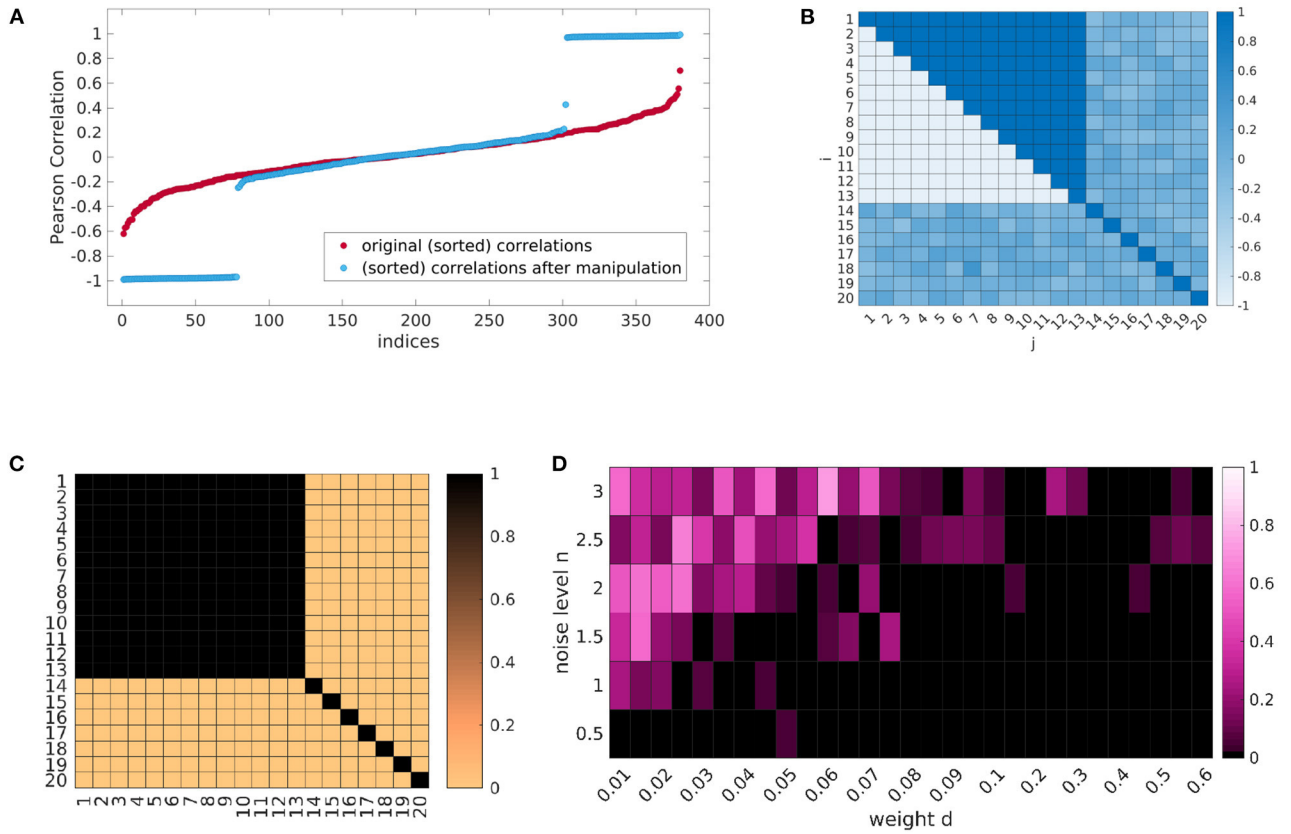

FIGURE 4 | One exemplary result of the simulation procedure. By inserting dependencies on the data generating coupling coefficients **(A)** we can generate a certain correlation pattern **(B)**. Emphasizing the influence of the significant couplings in the data generating process **(C)** allows to retrieve the dependencies with our method **(D)**, when the noise to data ratio is in a certain range. **(A)** Correlations in ascending order for the random initial coefficients and after explicit insertion of parametric dependence. **(B)** Correlation pattern. **(C)** Weight matrix M. **(D)** Median *P*-values over the six runs for all (n, d) combinations. ($P < 0.05$ black).

parameters estimated for the first order auto-regressive model from fMRI data possess a much higher capacity of explaining variance in behavioral data than a static model. For this, they used a large data set of resting state fMRI data and behavioral scores from the Human Connectome Project. Similarly in dementia, analysis of dynamic fluctuations yields more specific results than analysis of static functional connectivity (Moguilner et al., 2021). Following an alternative approach, parameters of the Ising model can be estimated from empirical data (Nguyen et al., 2017) in an application which is particularly apt for processes on the neuronal level based on binary processes of firing vs. no firing or brain states under anesthesia which involve cortical up- and down-states.

Within the present study we modified the step-wise strategy for analyzing trajectories by replacing actual activity percolation between brain regions over a time scale of seconds by a different model of spring-like attraction/repulsion between time courses of different brain regions by estimating the respective (directed) spring constants as Kuramoto coupling parameters. By this, we attempt to capture effects of fast neuronal firing on slow fMRI signal. The Kuramoto model has been used in many fields of research to investigate synchronization behavior as it is the most popular and most studied model for this phenomenon. The model can take on many different forms by adding or leaving out parameters. We decided to choose Euler's method for the following reasons: for once, it is the simplest method. Furthermore, we only consider a very short time span (T=300) alleviating stability issues, but foremost, we do not use the model for solution generation/simulation but for coefficient estimation. Therefore, the method is appropriate. For future work, however, other methods like the trapezoid method, implicit Euler's method or Runge-Kutta methods could be considered as well. When solving the linear equation system, the solution does not exist a-priori, since the number of equations will in general not be equal to the number of unknown variables. Ill-posedness in the sense that we have less equations than unknown variables will hardly occur, since this would mean that we have less measure points from the recordings than we have IBNs (In our case this meant, that we have <20 measure points, which further meant that our recording was less than about 40 s long). For the over-determined case, however, we need a strategy to find a unique solution that is optimal in a certain sense. The common approach is to solve such problems by finding the best solution in a least-squared error sense. The problem could be proposed in a more general manner, such that different norms than the ℓ_2-norm are possible. However, interpretability is more difficult in other spaces and

distances than Euclidean spaces. Therefore, we solve our problem with the normal equations optimizing the ℓ_2-norm, although other approaches could also be considered in the future.

We show a correlation of the Ham-D score, assessing clinical disease severity, to K, which can very clearly be confirmed in the test data set. The nature of the correlation in exploratory as well as test data set is bipartite with a positive and a negative contribution. Positive correlation indicates that the amplitudes in a set of K values increase with increasing disease severity and vice versa. All IBNs included into the analysis contribute to the dependence on Ham-D (except for one in the exploratory data set) indicating a broad change within the inter-regional communication in clinically severe states. In the exploratory data set the directed coupling from the salience network onto the basal ganglia network shows a strong negative correlation to Ham-D. A tendency of a reduced input from the salience network into the basal ganglia matches well with hypotheses of compromised reward processing and anhedonia which is discussed in combination with the dopamine dysregulation hypothesis (Szczypiński and Gola, 2018; Whitton et al., 2020). The correlation of this particular coupling to Ham-D though is not reproduced in the test data set. Our results indicated that clinical severity of MD is associated to a mild change of cross-regional IBN interactions across the whole cortex and sub-cortex.

All our analyses aimed at wide-spread changes. We were able to retrieve global patterns of dependence. The sensitivity of the approach to localized focal changes would need to be addressed with a different appropriate data set.

Using a simulation experiment we provide a proof of principle that our method is able to recover a ground truth, in which a large number of $K_{i,j}$s depend on an artificial external regressor. Notably, this parametric dependence is not associated to a systematic deviation of the $K_{i,j}$s from zero. The simulations indicated that increased overall Kuramoto coupling facilitates the re-discovery of the coupling from the data. Conversely, an increasing noise level decreases the ability of our method to recover the ground truth (**Supplementary Figure 3**). A stronger directional bias in the couplings as well as a strong contrast in coupling dependence on the external regressor between an intrinsically coupled cluster versus the outside of the cluster, also benefit the detection of the parametric dependence. Notably, we only investigated one type of ground truth, although the artificial data simulation leaves a lot of options for design choices. The size of the generated data set was chosen to allow for comparability to the empirical exploratory data set. Also the choices for the eigenfrequencies and the magnitude of the coupling coefficients for the simulation was guided by the empirical data. The magnitude of the coefficients has subordinate impact, as this can—to a certain degree—later be scaled with the appropriate weight d.

The most interesting design choices concern the correlation pattern shape $\mathbf{N}$. The possibilities here are highly diverse. First, the shape itself can be varied, i.e., which IBNs are involved and in which constellation. Additionally, the number of IBNs within the network, the intensity, pattern, and trend ("gradual progression" vs. "plateau" as for our experiments) of the correlations might be altered. Also the mask matrices used in our synthetic data experiments are only a choice of many more possible variations.

The power of our analysis pipeline for recovering the ground truth of actually parametrically manipulated couplings was limited in the considered simulation settings. Most positives were found in the "boundary" group of couplings, which crossed from one IBN, affected by parametrically dependent coupling to other regions, to another IBN, not affected by any parametrically dependent coupling to other regions. For the analysis of empirical data sets this implies that the reliability of recovering the exact couplings is low, which are actually parametrically dependent on the regressor under concern. More reliable information can be retrieved from the IBNs involved in the set themselves rather than the couplings. We would like to emphasize, that the proposed simulation pipeline and the presented results should be seen as a proof of concept, that it is possible to retrieve parametric dependencies, rather than a validation procedure, since it is impossible to have access to the ground truth of a real world data set. It is important to note, that we did find the induced dependencies in certain scenarios despite the large amount of possible parameter combinations, which supports that we did not find this by chance.

Our approach allows for an estimate of Kuramoto coupling parameters from empirical data and therefore contrasts with other studies which apply generative models in order to simulate and study arising activity dynamics, which are subsequently put in relation to empirical data. This kind of approaches has, e.g., been followed employing the Kuramoto model (Breakspear et al., 2010; Sadilek and Thurner, 2015; Schmidt et al., 2015), the Ising model (Stramaglia et al., 2017), and other spin glass models (Hudetz et al., 2014).

6. CONCLUSION

In summary, we present a novel method for analyzing functional connectivity from fMRI resting state data. Our initial analysis on empirical data indicates that the method provides novel results, which are complementary to other methods established in the field. The focus of the presented analysis pipeline lies on assessing wide spread connectivity changes relating to the brain state and might be useful in the analysis of the relation to slow changing chemical connectivity. The results proved to be robust to a re-test in an entirely independent data set. We further support the validity of our empirical findings by using simulated data, containing a ground truth, in that we show the ability of the method to retrieve this ground truth. Future studies are needed to extend and validate our findings.

DATA AVAILABILITY STATEMENT

The original contributions presented in the study are publicly available. This data can be found here: https://doi.org/10.6084/m9.figshare.13352399.

ETHICS STATEMENT

The studies involving human participants were reviewed and approved by the in-house Ethics Committee of the Klinikum rechts der Isar, TU Munich for the exploratory data set and by the Investigational Review Board (IRB) at Indiana University School of Medicine and at the Cleveland Clinic Foundation for the test data set. The patients/participants provided their written informed consent to participate in this study.

AUTHOR CONTRIBUTIONS

LB: methodology, software, data curation, writing, and visualization. FH, CJ, and MH: validation, investigation, and data curation. PG: supervision. AA: resources and supervision. CP: writing—review and editing and supervision. AW: conceptualization, methodology, software, formal analysis, resources, data curation, writing, and visualization. All authors contributed to the article and approved the submitted version.

ACKNOWLEDGMENTS

Amit Anand was supported by grant number R01MH093420. We thank Dr. Mario Archila Melendez for his helpful suggestions.

SUPPLEMENTARY MATERIAL

The Supplementary Material for this article can be found online at: https://www.frontiersin.org/articles/10.3389/fncom.2022.729556/full#supplementary-material

REFERENCES

Abdulle, A., and Wanner, G. (2002). 200 years of least squares method. *Elemen. Math*. 57, 45–60. doi: 10.1007/PL00000559

Acebrón, J. A., Bonilla, L. L., Pérez Vicente, C. J., Ritort, F., and Spigler, R. (2005). The Kuramoto model: a simple paradigm for synchronization phenomena. *Rev. Mod. Phys*. 77, 137–185. doi: 10.1103/RevModPhys.77.137

Allen, E. A., Erhardt, E. B., Damaraju, E., Gruner, W., Segall, J. M., Silva, R. F., et al. (2011). A baseline for the multivariate comparison of resting-state networks. *Front. Syst. Neurosci*. 5, 2. doi: 10.3389/fnsys.2011.00002

American Psychiatric Association (2000). *Diagnostic and Statistical Manual of Mental Disorders*. Washington, DC: Am Psychiatric Association.

American Psychiatric Association (2013). *Diagnostic and Statistical Manual of Mental Disorders*. Washington, DC: Am Psychiatric Association. doi: 10.1176/appi.books.9780890425596

Anand, A., and Charney, D. (1997). *Depression: Neurobiological, Psychopathological and Therapeutic Advances*. London: John Wiley & Sons Ltd.

Beall, E. B., and Lowe, M. J. (2007). Isolating physiologic noise sources with independently determined spatial measures. *NeuroImage* 37, 1286–1300. doi: 10.1016/j.neuroimage.2007.07.004

Beall, E. B., and Lowe, M. J. (2014). SimPACE: Generating simulated motion corrupted BOLD data with synthetic-navigated acquisition for the development and evaluation of SLOMOCO: a new, highly effective slicewise motion correction. *NeuroImage* 101, 21–34. doi: 10.1016/j.neuroimage.2014.06.038

Birn, R. M., Smith, M. A., Jones, T. B., and Bandettini, P. A. (2008). The respiration response function: the temporal dynamics of fMRI signal fluctuations related to changes in respiration. *NeuroImage* 40, 644–654. doi: 10.1016/j.neuroimage.2007.11.059

Braun, U., Schaefer, A., Betzel, R. F., Tost, H., Meyer-Lindenberg, A., and Bassett, D. S. (2018). From maps to multi-dimensional network mechanisms of mental disorders. *Neuron* 97, 14–31. doi: 10.1016/j.neuron.2017.11.007

Breakspear, M. (2017). Dynamic models of large-scale brain activity. *Nat. Neurosci*. 20, 340–352. doi: 10.1038/nn.4497

Breakspear, M., Heitmann, S., and Daffertshofer, A. (2010). Generative models of cortical oscillations: neurobiological implications of the Kuramoto model. *Front. Hum. Neurosci*. 4, 190. doi: 10.3389/fnhum.2010.00190

Cabral, J., Vidaurre, D., Marques, P., Magalh aes, R., Silva Moreira, P., Miguel Soares, J., et al. (2017). Cognitive performance in healthy older adults relates to spontaneous switching between states of functional connectivity during rest. *Sci. Rep*. 7, 1–13. doi: 10.1038/s41598-017-05425-7

Calhoun, V. D., Pearlson, G. D., and Pekar, J. J. (2001). Spatial and temporal independent component analysis of functional MRI data containing a pair of task-related waveforms. *Hum. Brain Mapp*. 13, 43–53. doi: 10.1002/hbm.1024

Chang, C., Cunningham, J. P., and Glover, G. H. (2009). Influence of heart rate on the BOLD signal: the cardiac response function. *NeuroImage* 44, 857–869. doi: 10.1016/j.neuroimage.2008.09.029

Cocchi, L., Sale, M. V., Gollo, L. L., Bell, P. T., Nguyen, V. T., Zalesky, A., et al. (2016). A hierarchy of timescales explains distinct effects of local inhibition of primary visual cortex and frontal eye fields. *eLife* 5, e73456. doi: 10.7554/eLife.15252.024

Cooper, J., Bloom, F., and Roth, R. (1991). *The Biochemical Basis of Neuropharmacology*. New York, NY: Oxford University Press.

Córdova-Palomera, A., Kaufmann, T., Persson, K., Alnæs, D., Doan, N. T., Moberget, T., et al. (2017). Disrupted global metastability and static and dynamic brain connectivity across individuals in the Alzheimer's disease continuum. *Sci. Rep*. 7, 40268. doi: 10.1038/srep40268

Deco, G., Jirsa, V. K., Robinson, P. A., Breakspear, M., and Friston, K. (2008). The dynamic brain: from spiking neurons to neural masses and cortical fields. *PLoS Comput. Biol*. 4:e1000092. doi: 10.1371/journal.pcbi.1000092

Deco, G., and Kringelbach, M. L. (2016). Metastability and coherence: extending the communication through coherence hypothesis using a whole-brain computational perspective. *Trends Neurosci*. 39, 125–135. doi: 10.1016/j.tins.2016.01.001

Delgado, P. L., Price, L. H., Miller, H. L., Salomon, R. M., Aghajanian, G. K., Heninger, G. R., et al. (1994). Serotonin and the neurobiology of depression: effects of tryptophan depletion in drug-free depressed patients. *Arch. Gen. Psychiatry* 51, 865–874. doi: 10.1001/archpsyc.1994.03950110025005

Epperson, J. F. (2013). *An Introduction to Numerical Methods and Analysis*. Hoboken, NJ: John Wiley and Sons.

Friston, K. J. (2011). Functional and effective connectivity: a review. *Brain Connect*. 1, 13–36. doi: 10.1089/brain.2011.0008

Gauß, C. F. (1809). Theoria motus corporum coelestium. *Rev. Mod. Phys*. 7, 1–288.

Glerean, E., Salmi, J., Lahnakoski, J. M., Jääskeläinen, I. P., and Sams, M. (2012). Functional magnetic resonance imaging phase synchronization as a measure of dynamic functional connectivity. *Brain Connect*. 2, 91–101. doi: 10.1089/brain.2011.0068

Glover, G. H., Li, T., and Ress, D. (2000). Image-based method for retrospective correction of physiological motion effects in fMRI: RETROICOR. *Magn. Reson. Med*. 44, 162–167. doi: 10.1002/1522-2594(200007)44:1<162::AID-MRM23>3.0.CO;2-E

Goldman-Rakic, P. S., Leranth, C., Williams, S. M., Mons, N., and Geffard, M. (1989). Dopamine synaptic complex with pyramidal neurons in primate cerebral cortex. *Proc. Natl. Acad. Sci. U.S.A*. 86, 9015–9019. doi: 10.1073/pnas.86.22.9015

Gu, S., Pasqualetti, F., Cieslak, M., Telesford, Q. K., Yu, A. B., Kahn, A. E., et al. (2015). Controllability of structural brain networks. *Nat. Commun*. 6, 1–10. doi: 10.1038/ncomms9414

Hahn, S. L. (1996). "Hilbert transforms in signal processing," in *Artech House Signal Processing Library* (Boston, MA: Artech House).

Hamilton, M. (1960). A rating scale for depression. *J. Neurol. Neurosurg. Psychiatry* 23, 56–62. doi: 10.1136/jnnp.23.1.56

Hamon, M., and Blier, P. (2013). Monoamine neurocircuitry in depression and strategies for new treatments. *Prog. Neuro-Psychopharmacol. Biol. Psychiatry* 45, 54–63. doi: 10.1016/j.pnpbp.2013.04.009

Hudetz, A. G., Humphries, C. J., and Binder, J. R. (2014). Spin-glass model predicts metastable brain states that diminish in anesthesia. *Front. Syst. Neurosci.* 8, 234. doi: 10.3389/fnsys.2014.00234

Jacob, S. N. and Nienborg, H. (2018). Monoaminergic neuromodulation of sensory processing. *Front. Neural Circuits* 12, 51. doi: 10.3389/fncir.2018.00051

Kuramoto, Y. (1975). "Self-entrainment of a population of coupled non-linear oscillators," in *International Symposium on Mathematical Problems in Theoretical Physics*, ed H. Araki (Berlin; Heidelberg: Springer), 420–422. doi: 10.1007/BFb0013365

Liégeois, R., Laumann, T. O., Snyder, A. Z., Zhou, J., and Yeo, B. T. (2017). Interpreting temporal fluctuations in resting-state functional connectivity MRI. *NeuroImage* 163, 437–455. doi: 10.1016/j.neuroimage.2017.09.012

Liégeois, R., Li, J., Kong, R., Orban, C., Van De Ville, D., Ge, T., et al. (2019). Resting brain dynamics at different timescales capture distinct aspects of human behavior. *Nat. Commun.* 10, 2317. doi: 10.1038/s41467-019-10317-7

Manoliu, A., Meng, C., Brandl, F., Doll, A., Tahmasian, M., Scherr, M., et al. (2014). Insular dysfunction within the salience network is associated with severity of symptoms and aberrant inter-network connectivity in major depressive disorder. *Front. Hum. Neurosci.* 7, 930. doi: 10.3389/fnhum.2013.00930

Meng, C., Brandl, F., Tahmasian, M., Shao, J., Manoliu, A., Scherr, M., et al. (2014). Aberrant topology of striatum's connectivity is associated with the number of episodes in depression. *Brain* 137(Pt 2), 598–609. doi: 10.1093/brain/awt290

Moguilner, S., García, A. M., Perl, Y. S., Tagliazucchi, E., Piguet, O., Kumfor, F., et al. (2021). Dynamic brain fluctuations outperform connectivity measures and mirror pathophysiological profiles across dementia subtypes: a multicenter study. *NeuroImage* 225, 117522. doi: 10.1016/j.neuroimage.2020.117522

Nguyen, H. C., Zecchina, R., and Berg, J. (2017). Inverse statistical problems: from the inverse ising problem to data science. *Adv. Phys.* 66, 197–261. doi: 10.1080/00018732.2017.1341604

Northoff, G. (2016). Spatiotemporal psychopathology I: no rest for the brain's resting state activity in depression? spatiotemporal psychopathology of depressive symptoms. *J. Affect. Disord.* 190, 854–866. doi: 10.1016/j.jad.2015.05.007

Okuda, K., and Kuramoto, Y. (1991). Mutual entrainment between populations of coupled oscillators. *Prog. Theor. Phys.* 86, 1159–1176. doi: 10.1143/ptp/86.6.1159

Ponce-Alvarez, A., Deco, G., Hagmann, P., Romani, G. L., Mantini, D., and Corbetta, M. (2015). Resting-state temporal synchronization networks emerge from connectivity topology and heterogeneity. *PLoS Comput. Biol.* 11, e1004100. doi: 10.1371/journal.pcbi.1004100

Ries, A., Chang, C., Glim, S., Meng, C., Sorg, C., and Wohlschläger, A. (2018). Grading of frequency spectral centroid across resting-state networks. *Front. Hum. Neurosci.* 12, 436. doi: 10.3389/fnhum.2018.00436

Ries, A., Hollander, M., Glim, S., Meng, C., Sorg, C., and Wohlschläger, A. (2019). Frequency-dependent spatial distribution of functional hubs in the human brain and alterations in major depressive disorder. *Front. Hum. Neurosci.* 13, 146. doi: 10.3389/fnhum.2019.00146

Robbins, T. W., and Arnsten, A. F. (2009). The neuropsychopharmacology of fronto-executive function: monoaminergic modulation. *Annu. Rev. Neurosci.* 32, 267–287. doi: 10.1146/annurev.neuro.051508.135535

Sadilek, M., and Thurner, S. (2015). Physiologically motivated multiplex Kuramoto model describes phase diagram of cortical activity. *Sci. Rep.* 5, 1–8. doi: 10.1038/srep10015

Schmidt, R., LaFleur, K., de Reus, M., van den Berg, L. H., and van den Heuvel, M. P. (2015). Kuramoto model simulation of neural hubs and dynamic synchrony in the human cerebral connectome. *BMC Neurosci.* 16, 54. doi: 10.1186/s12868-015-0193-z

Schwarz, H. R., and Köckler, N. (2011). *Numerische Mathematik,s Vol. 6*. Washington, DC: Vieweg+Teubner Verlag. doi: 10.1007/978-3-8348-8166-3

Sheehan, D. V., Lecrubier, Y., Sheehan, K. H., Janavs, J., Weiller, E., Keskiner, A., et al. (1997). The validity of the Mini International Neuropsychiatric Interview (MINI) according to the SCID-P and its reliability. *Eur. Psychiatry* 12, 232–241. doi: 10.1016/S0924-9338(97)83297-X

Shine, J. M. (2020). The thalamus integrates the macrosystems of the brain to facilitate complex, adaptive brain network dynamics. *Prog. Neurobiol.* 199, 101951. doi: 10.1016/j.pneurobio.2020.101951

Shine, J. M., Breakspear, M., Bell, P. T., Martens, K. E., Shine, R., Koyejo, O., et al. (2019). Human cognition involves the dynamic integration of neural activity and neuromodulatory systems. *Nat. Neurosci.* 22, 289–296. doi: 10.1038/s41593-018-0312-0

Sporns, O., Chialvo, D. R., Kaiser, M., and Hilgetag, C. C. (2004). Organization, development and function of complex brain networks. *Trends Cogn. Sci.* 8, 418–425. doi: 10.1016/j.tics.2004.07.008

Sporns, O., Tononi, G., and Kötter, R. (2005). The human connectome: a structural description of the human brain. *PLoS Comput. Biol.* 1:e42. doi: 10.1371/journal.pcbi.0010042

Stramaglia, S., Pellicoro, M., Angelini, L., Amico, E., Aerts, H., Cortés, J. M., et al. (2017). Ising model with conserved magnetization on the human connectome: implications on the relation structure-function in wakefulness and anesthesia. *Chaos* 27, 047407. doi: 10.1063/1.4978999

Szczypiński, J. J., and Gola, M. (2018). Dopamine dysregulation hypothesis: the common basis for motivational anhedonia in major depressive disorder and schizophrenia? *Rev. Neurosci.* 29, 727–744. doi: 10.1515/revneuro-2017-0091

Whitton, A. E., Reinen, J. M., Slifstein, M., Ang, Y. S., McGrath, P. J., Iosifescu, D. V., et al. (2020). Baseline reward processing and ventrostriatal dopamine function are associated with pramipexole response in depression. *Brain* 143, 701–710. doi: 10.1093/brain/awaa002

Wohlschläger, A., Karne, H., Jordan, D., Lowe, M., Jones, S., and Anand, A. (2018). Spectral dynamics of resting state fMRI within the ventral tegmental area and dorsal raphe nuclei in medication-free major depressive disorder in young adults. *Front. Psychiatry* 9, 163. doi: 10.3389/fpsyt.2018.00163

Young, R. C., Biggs, J. T., Ziegler, V. E., and Meyer, D. A. (1978). A rating scale for mania: reliability, validity and sensitivity. *Br. J. Psychiatry* 133, 429–435. doi: 10.1192/bjp.133.5.429

Zang, Y. F., Yong, H., Chao-Zhe, Z., Qing-Jiu, C., Man-Qiu, S., Meng, L., et al. (2007). Altered baseline brain activity in children with ADHD revealed by resting-state functional MRI. *Brain Dev.* 29, 83–91. doi: 10.1016/j.braindev.2006.07.002

Zarghami, T. S., Hossein-Zadeh, G. A., and Bahrami, F. (2020). Deep temporal organization of fMRI phase synchrony modes promotes large-scale disconnection in schizophrenia. *Front. Neurosci.* 14, s214. doi: 10.3389/fnins.2020.00214

Conflict of Interest: The authors declare that the research was conducted in the absence of any commercial or financial relationships that could be construed as a potential conflict of interest.

frontiers | Frontiers in Computational Neuroscience

ORIGINAL RESEARCH
published: 06 June 2022
doi: 10.3389/fncom.2022.877912

Functional Connectivity and Complexity in the Phenomenological Model of Mild Cognitive-Impaired Alzheimer's Disease

*Surya Das and Subha D. Puthankattil**

Department of Electrical Engineering, National Institute of Technology, Calicut, India

Background: Functional connectivity and complexity analysis has been discretely studied to understand intricate brain dynamics. The current study investigates the interplay between functional connectivity and complexity using the Kuramoto mean-field model.

Method: Functional connectivity matrices are estimated using the weighted phase lag index and complexity measures through popularly used complexity estimators such as Lempel-Ziv complexity (LZC), Higuchi's fractal dimension (HFD), and fluctuation-based dispersion entropy (FDispEn). Complexity measures are estimated on real and simulated electroencephalogram (EEG) signals of patients with mild cognitive-impaired Alzheimer's disease (MCI-AD) and controls. Complexity measures are further applied to simulated signals generated from lesion-induced connectivity matrix and studied its impact. It is a novel attempt to study the relation between functional connectivity and complexity using a neurocomputational model.

Results: Real EEG signals from patients with MCI-AD exhibited reduced functional connectivity and complexity in anterior and central regions. A simulation study has also displayed significantly reduced regional complexity in the patient group with respect to control. A similar reduction in complexity was further evident in simulation studies with lesion-induced control groups compared with non-lesion-induced control groups.

Conclusion: Taken together, simulation studies demonstrate a positive influence of reduced connectivity in the model imparting a reduced complexity in the EEG signal. The study revealed the presence of a direct relation between functional connectivity and complexity with reduced connectivity, yielding a decreased EEG complexity.

Keywords: functional connectivity, complexity, Kuramoto model, MCI-AD, EEG

OPEN ACCESS

Edited by:
Pedro Antonio Valdes-Sosa, University of Electronic Science and Technology of China, China

Reviewed by:
Ernesto Estevez Rams, University of Havana, Cuba
Fabio Baselice, University of Naples Parthenope, Italy

***Correspondence:**
Subha D. Puthankattil
subhadp@nitc.ac.in

Received: *17 February 2022*
Accepted: *26 April 2022*
Published: *06 June 2022*

Citation:
Das S and Puthankattil SD (2022) Functional Connectivity and Complexity in the Phenomenological Model of Mild Cognitive-Impaired Alzheimer's Disease. Front. Comput. Neurosci. 16:877912. doi: 10.3389/fncom.2022.877912

INTRODUCTION

Alzheimer's disease (AD) is one of the most common neurodegenerative diseases affecting the elderly population (Jeong, 2004). Electroencephalogram (EEG) studies, especially non-linear dynamics, are gaining popularity as a potential tool for the early detection of AD. An early diagnosis of the disease could aid in early interventions against the disease, subsequently increasing the quality of life. The three hallmark features from the non-linear/linear analysis of EEG signals of

patients with AD are the slowing of EEG signals and reduction of functional connectivity and complexity (Dauwels and Cichocki, 2011). Recent studies with EEG signals have revealed the presence of reduced functional connectivity (Das and Puthankattil, 2020) and reduced complexity in the early stages of AD [mild cognitive-impaired AD (MCI-AD)] (Nimmy John et al., 2018).

Functional connectivity represents the correlation of neural activity among different brain regions through statistical interdependence measures. It provides the indices for functional integration between segregated cortical regions and has been correlated with aging (Varangis et al., 2019), learning (Veroude et al., 2010), and neurological disorders (Orekhova et al., 2014; Engels et al., 2015; Sargolzaei et al., 2015). The concept of complexity could be interpreted in different ways. Commonly used EEG complexity measures explain the complexity as a measure of the degree of randomness or degree of freedom associated with the system. However, complex behavior in a non-linear system could be exhibited with fewer degrees of freedom (Wackerbauer et al., 1994). Generally, a high and low entropy (i.e., random and regular order) system would have lower complexity, and an intermediate system would have higher complexity (Wackerbauer et al., 1994; Tononi et al., 1998).

A reduction in connectivity and complexity in MCI-AD/AD could be attributed to atypical non-linear neurodynamics in the brain (Jeong, 2004). Atypical non-linear dynamics in MCI-AD/AD brain could arise from pathophysiological changes due to the presence of tangles, alteration in synaptic couplings, and neuronal death (Nestor et al., 2004; Hornero et al., 2009). The AD brain has shown the presence of modest degrees of lesions with medial temporal lobe atrophy as a significant indicator in multiple studies (Visser et al., 2002; Clerx et al., 2013; Dhikav et al., 2014). Structural and functional connectivity studies in AD have revealed a reduction in the connectivity between different regions of the brain, converging into a network disconnection hypothesis (Delbeuck et al., 2003; Brier et al., 2014; Kundu et al., 2019). The disconnection hypothesis explains a neurodegenerative model with edges in the network model displaying a reducing trend of connectivity strength (Brier et al., 2014). Several research studies have related the reduction in the complexity measures to the decreased cortical connectivity, resulting in the diminished flexibility of the neural system to reach different information processing states (Babiloni et al., 2004; Al-nuaimi et al., 2018; Nobukawa et al., 2019). However, studies exploring the relation between complexity and functional connectivity are limited. This article attempts to explore the relation between functional connectivity and complexity using the Kuramoto mean-field model in the MCI-AD condition. The study also utilizes a lesion model to examine its impact on the network dynamics.

The Kuramoto model is a popularly used neurocomputational model based on weakly coupled limit-cycle oscillators. Nodes of the networks are defined by differential equations and edges by the cortical connectivity. The dynamics of the model could simulate data that have physiological properties similar to macroscopic features found in neurophysiological signals like EEG (Breakspear et al., 2010). One of the major advantages of the neurocomputational model based on Kuramoto would be the direct utilization of the connectivity matrix. One of the common applications of the Kuramoto model is in analyzing the structural–functional correlation of the brain to understand cortical dynamics (Finger et al., 2016; Lee and Frangou, 2017). The Kuramoto model has also been applied to studies on anesthesia (Schartner et al., 2015), consciousness (Ibáñez-molina et al., 2018; Lee et al., 2019), mind wandering (Ibáñez-molina et al., 2016), lesion (František et al., 2015; Jos et al., 2018), and complexity (Escudero et al., 2015). The studies generally used diffusion tensor tractography data for the connectivity pattern in the Kuramoto model (Escudero et al., 2015; Jos et al., 2018; Lee et al., 2019). The current study proposes to utilize functional connectivity data instead of structural connectivity data in the Kuramoto model to study the relationship between functional connectivity and complexity. Previous studies have utilized the Kuramoto model to study the relation between structural connectivity and complexity (Jos et al., 2018). We have used the Kuramoto model to validate the reduction of functional integration caused by the pathological process in MCI-AD, which would result in the reduction of the complexity score. The computational study also uses a lesion model in which edges originating from one specific region of the cortex are set to the lowest value. Lesions preferentially in the central part of a network could be a possible network lesion model in developing a neurocomputational model of AD (Aerts et al., 2016). The lesion model is exploited to study the impact of reduced connectivity with the complexity parameter.

Electroencephalogram studies reveal a gradual reduction in connectivity and complexity with the progression of the disease. This study analyzes the occurrence of the possible relation between connectivity and complexity in the context of the EEG signal simulation. It could be elucidated that reduction of connectivity could result in relatively isolated neural activities in the cortex that could influence the complexity of the system. This study explores the relation between connectivity and complexity through simulated EEG signals generated from the functional connectivity matrix of patients and controls. Complexity metrics were applied to real and simulated EEG signals to study the variation. The study also simulated EEG signals from the connectivity matrix with an induced lesion to study its characteristics. The steps followed in the study are represented in the form of a flowchart in **Figure 1**. The functional connectivity matrix from EEG signals was estimated using the weighted phase lag index (WPLI) (Vinck et al., 2011). WPLI is an efficient connectivity measure that indices the phase relation between brain regions with minimal interference through volume conduction. The complexity analysis was performed using Lempel-Ziv complexity (LZC), Higuchi's fractal dimension (HFD), and fluctuation-based dispersion entropy (FDispEn), where LZC and HFD are commonly used EEG complexity measures. FDispEn is a recent approach to measure dynamic variability in the fluctuation of EEG signals.

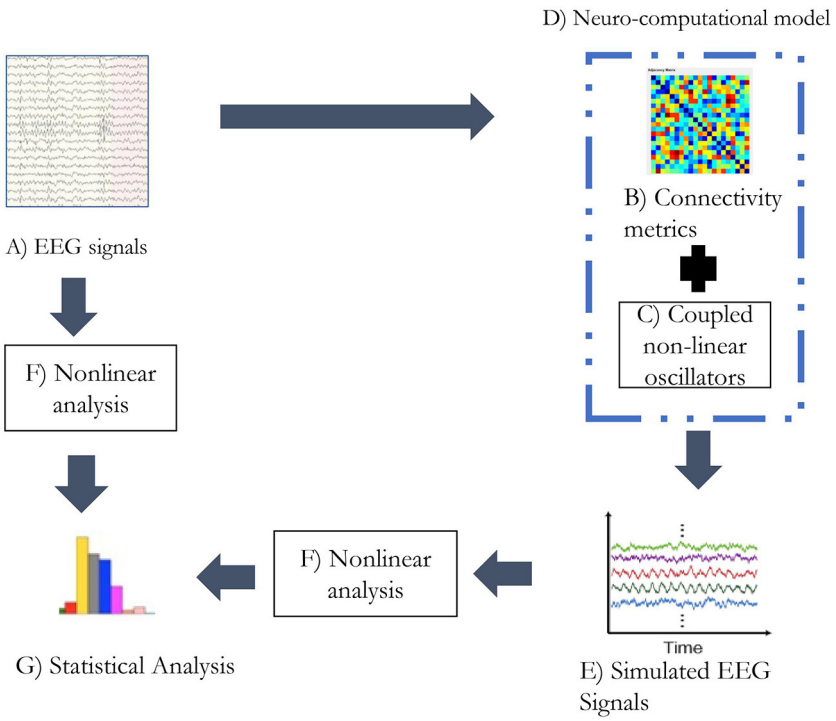

FIGURE 1 | The analytic plan followed in the study. **(A)** The alpha band of the EEG signals was extracted through wavelet transform. **(B)** The connectivity matrix was generated from the alpha band of EEG signal utilizing weighted PLI. **(C)** Kuramoto's mean-field model was simulated with 21 oscillators. **(D)** Functional connectivity matrix and coupled non-linear oscillators form the neurocomputational model used in the study. **(E)** Simulated EEG signals being generated from the neurocomputational model. **(F)** Non-linear analysis was performed with metrics: LZC, HFD, and FDispEn. **(G)** Statistical analysis was performed on the estimates of non-linear analysis on real and simulated EEG signals separately.

METHODOLOGY

Data Collection

Electroencephalogram data for the analysis were collected from 15 healthy controls and 13 subjects with MCI-AD. The sample population consists of participants from both genders in the age group of 57–75 years. Clinical dementia rating (CDR), Mini-Mental Scale Examination (MMSE), and Addenbrooke's cognitive examination (ACE) were used to rate dementia in MCI-AD. Patients with MCI-AD with the CDR score ≤ 1 were selected for the study. The mean and standard deviation of the various parameters of the sample population along with a significant difference between the groups considered in the study are provided in **Table 1**. Data acquisition was carried out at Sree Chithra Tirunal Institute of Medical Sciences and Technology, Trivandrum, Kerala, India. Ethical committee sanction was accorded for the study. Written and informed consent from patients and controls were obtained for the study.

Electroencephalogram data were acquired through a 32-channel digital acquisition system (NicVue, Nicolet-Viking, USA). EEG data from 21 electrode locations (Fp1, Fp2, F3, F4, C3, C4, P3, P4, O1, O2, T1, T2, F7, F8, T3, T4, T5, T6, Fz, Cz, and Pz) were preprocessed using simultaneous low-pass filtering and total variation denoising (LPF/TVD) algorithm (Selesnick et al., 2014). The signals were recorded with a sampling frequency of 400 Hz. EEG data were recorded for a duration of 5 min in the eyes open resting state. For the targeted lesion study, EEG data channels were clustered into three groups, namely, anterior (i.e., Fp1, Fp2, F7, F3, Fz, F4, and F8), central (i.e., T3, C3, Cz, C4, and T4), and posterior (i.e., T5, P3, Pz, P4, T6, O1, and O2). The alpha band of the EEG signals was extracted using wavelet transform. Wavelet transform is a multi-resolution decomposition method. The technique requires the selection of an appropriate wavelet function for the signal to be decomposed into different frequency scales. Wavelet "db10" was used in this study as it has given a good correlation coefficient with most of the signals acquired from the sample population. The functional connectivity analysis is performed through WPLI as a connectivity measure. The connectivity matrix thus generated

TABLE 1 | Mean and standard deviation of parameters in control and patient with mild cognitive-impaired Alzheimer's disease (MCI-AD).

	Sample size (*n*)	Age (years)	Sex	MMSE	ACE
Control	15	65.18 ± 3.15	7 males, 8 females	29.31 ± 1.03	92.47 ± 4.76
Patient	13	67.78 ± 6.10	7 males, 6 females	23.92 ± 4.15	63.85 ± 8.45
Significant difference	–	$p = 0.09$	–	$p = 0.0001$	$p = 0.0002$

was then fed into the Kuramoto model for generating simulated EEG signals. Complexity measures of LZC, HFD, and FDispEn were applied in real EEG signals and simulated EEG signals to study the variation.

Functional Connectivity

Weighted phase lag index (Vinck et al., 2011) is the weighted version of PLI. PLI is a measure to quantify phase synchronization and indexes, the asymmetry of the distribution of relative phase around zero. It is motivated by the fact that non-zero phase difference occurs only through the result of true interaction. Thus, the measure is invulnerable to volume conduction and depends only on the phase difference. To increase the sensitivity to small signals and to mitigate the effect of noise, Vinck et al. have proposed some adjustments in PLI, yielding WPLI. In WPLI connectivity measure, phase leads or lags are weighted by the magnitude of the imaginary part of the complex cross-spectrum.

$$WPLI_{xy} = \frac{\frac{1}{n}\sum_{t=1}^{n}\left|imag\left(S_{xyt}\right)\right| sgn(imag(S_{xyt}))}{\frac{1}{n}\sum_{t=1}^{n}\left|imag(S_{xyt})\right|} \quad (1)$$

In this equation, S_{xy} indicates the cross-spectral density between x and y time series data at time point t in the complex plane xy. Sgn is the sign function (-1, $+1$, or 0).

Kuramoto Model

The Kuramoto model is used to mimic the dynamics of synchronization of activity between brain regions of MCI-AD and control. The model consists of a set of coupled differential equations. The model defines the dynamics of N identical oscillators.

$$\frac{d\theta_i}{dt} = \omega_i + k\sum_{j=1}^{N} a_{ij}\sin(\theta_j - \theta_i) \quad (2)$$

where N is the number of oscillators (nodes) in the model. Each node is equated to different electrode locations in the brain. θ_i is the phase of i^{th} oscillator on its limit cycle. In this study, $(\frac{d\theta_i}{dt})$ represents the rate of change of the phase of i^{th} oscillator. The variables ω and k denote the natural frequency and coupling strength of the oscillator network, respectively. The behavior of the system is strongly determined by the parameter k. When the system has $k > k_{critical}$value, the system reaches a state of global synchrony. Similarly, when $k < k_{critical}$ value, the system exhibits a low value of global synchrony. Thus, $k_{critical}$ defines the bifurcation in the system dynamics. When k is poised near the $k_{critical}$value, the system displays complex behavior. The variable a_{ij} denotes the connectivity matrix.

The degree of synchrony in the coupled oscillators can be measured through an order parameter $r(t)$.

$$r(t)\, e^{-i\psi(t)} = \frac{1}{N}\sum_{j=1}^{N} e^{-i\theta_j(t)} \quad (3)$$

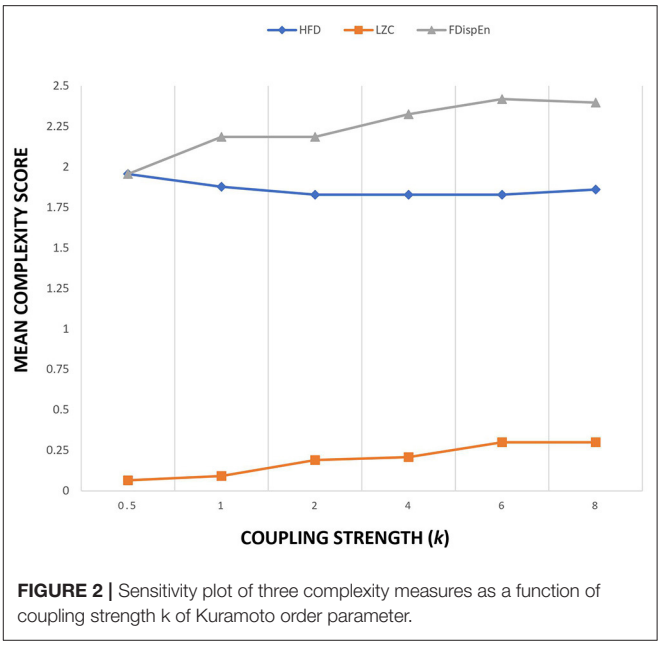

FIGURE 2 | Sensitivity plot of three complexity measures as a function of coupling strength k of Kuramoto order parameter.

The order parameter takes the value from 0 to 1 and measures the phase coherence of N oscillators. The order parameter of 1 represents perfectly synchronized oscillators and 0 represents perfectly unsynchronized oscillators. The symbol ψ represents the average phase of collective oscillators.

EEG Simulation

The Kuramoto model implemented in this study uses 21 oscillators to simulate 21-channel electrode locations. The connectivity matrix obtained from WPLI measure on 21 channel EEG signals is used as the connection strength a_{ij}. WPLI measure was extracted from the alpha band of patients and controls during the eyes open protocol. WPLI operates on phase space and estimates maximally weighting $\pm 90^{\circ}$ phase difference between different EEG channels. It essentially detects phase lag interactions from a complex coupled system like the brain. Since the connection strength matrix a_{ij} is the connectivity strength estimated from the functional connectivity data instead of the structural connectivity data, the value of coupling strength k is kept constant at 1. **Figure 2** provides the sensitivity plot between the mean complexity measure and coupling strength. A variation in the coupling value of k in the Kuramoto model alters the global connectivity strength. Complexity measures used are LZC, HFD, and FDispEn. From the sensitivity plot, the complexity estimates were nominally altered by the change in the coupling parameter. To ensure uniformity among the simulation studies for conducting a comparative analysis, the coupling strength was maintained at a constant value of 1. Since the Kuramoto model utilized in the study uses functional connectivity data, the data matrix is also inclusive of the bias from time delay, the weighted contribution from different sources, and the weighted reduction while passing through different layers of the brain.

The simulation model uses a frequency range (ω) that matches the frequency of the alpha band. The alpha band was specifically

chosen in this study as this band was significantly affected in multiple functional connectivity studies conducted in AD/MCI-AD (Miraglia et al., 2016; Afshari and Jalili, 2017; Das and Puthankattil, 2020; Duan et al., 2020). The natural frequency of the coupled oscillators ($f_i = \frac{\omega_i}{2\pi}$) is randomly assigned with the distribution of mean and standard deviation of 10 Hz and 2 Hz, respectively.

$$x_i(t) = \sum_{i=1}^{N=21} \sin\theta_i(t) \quad (4)$$

In this study, $x_i(t)$ is the simulated EEG signal. The model was simulated to produce 15,000 sample points with Euler's integration scheme of h to be 0.1. Initial 1,000 sample points were discarded as the initial condition. The simulation is repeated 15 times with connectivity matrices of patients with MCI-AD, healthy controls, and lesion-induced controls. The connectivity matrices were averaged across patients with MCI-AD, healthy controls, and lesion-induced controls.

Lesion Model

The popular hypothesis explaining AD pathology is the network disconnection model (Brier et al., 2014). For progressive neurodegenerative diseases such as Alzheimer's, the hub regions are preferentially vulnerable to lesions (Aerts et al., 2016). Hubs in the topologically central regions were likely to be more vulnerable to a pathological process like AD. In this study, the lesion in the topologically central region of the network is simulated by the reduction of connectivity strength. Thus, the lesion simulates a transformed network with limited edge strength, specifically in the topological central region. Edges originating in the central region of the brain (i.e., T3, C3, Cz, C4, and T4) were replaced with constant edge strength of 0.1 to simulate the effect of a lesion. The introduction of the lesion could significantly alter the functional dynamics, possibly influencing the complexity score of the system. The constant edge strength of 0.1 was specifically chosen as it is the lowest non-zero connectivity strength in the averaged connectivity matrix over the patient population. The connectivity strength in the averaged patient matrix varied between 0.1 and 0.6. The selection of 0.1 edge strength could accentuate the difference between the matrices. This resulted in the reduction of the mean connectivity strength of the control matrix from 0.5575 to 0.2454. The study generated lesioned network from the connectivity matrix generated from the controls.

Complexity measures were estimated from the real EEG signals of patients and controls and simulated EEG signals of patients, controls, and lesion-induced control signals.

Complexity Measures

Electroencephalogram complexity has been studied in the context of different neurological disorders and in healthy controls to gain insights into the dynamical property of the brain. LZC, HFD, and FDispEn had provided reliable conclusions in studies related to neurological diseases. LZC estimates the compressibility of EEG data and HFD measures fractal characteristics in EEG data. FDispEn estimates the uncertainty of the signal through the difference between the adjacent elements of the dispersion pattern.

Lempel-Ziv Complexity

Lempel-Ziv complexity is derived from the compressibility of the binary data (Lempel and Ziv, 1976). This measure could reveal the regularity and randomness in high-dimensional non-linear systems and is widely used in biomedical applications (Aboy et al., 2006). EEG signals are binarized using a threshold level and then analyzed for LZC. The median value in the EEG data sample is selected as the threshold level. Data sample above the threshold is equated to 1 and below the threshold level to 0. The resulting binary segment is scanned for different patterns. The counter $c(n)$ is increased by one unit when a new pattern is encountered in the scanning process (Zhang et al., 2001).

$$lim_{n\to\infty} c(n) = b(n) = \frac{n}{\log_2 n} \quad (5)$$

In this equation, n is the length of the binary sequence and $b(n)$ provides the upper bound of $c(n)$. $c(n)$ is normalized as follows:

$$C(n) = \frac{c(n)}{b(n)} \quad (6)$$

After normalization, the complexity measure ($C(n)$) reflects the rate of occurrences of new patterns with an increase in time.

Higuchi's Fractal Dimension

Higuchi's fractal dimension measures the self-similarity (scale-free behavior) of a system. In a time-series data, FD could range from 1 to 2, with a higher value indicating higher signal complexity. EEG data show fractal properties with statistical similarity at different time scales. In this study, the fractal dimension algorithm has been selected as it provides a good approximation of fractal dimension in EEG signals. The algorithm uses a small number of data points to approximate the mean length of the curve. HFD had been successfully utilized by Gómez et al. (2009) and Smits et al. (2016) in order to analyze EEG.

An EEG signal $[y(1), y(2), \ldots\ldots y(N)]$ with a sample length of N can be divided into k length sub-data as

$$y_k^m : y(m), y(m+k), y(m+2k), \ldots\ldots y\left(m+\text{int}\left[\frac{N-m}{k}\right]k\right) \quad (7)$$

In this equation, k is constant, and $m = 1, 2, \ldots . k$. The [ ] is the Gauss' notation and length $L_m(k)$ of each curve y_k^m is calculated as follows:

$$L_m(k) = \frac{1}{k}\left[\frac{N-1}{\text{int}\left[\frac{N-m}{k}\right]k}\left(\sum_{i=1}^{\text{int}\left[\frac{N-m}{k}\right]} |y(m+ik) - y(m+(i-1)k)|\right)\right] \quad (8)$$

The mean of $L_m(k)$ is computed to estimate HFD.

$$HFD = \frac{1}{k}\sum_{m=1}^{k} L_m(k) \tag{9}$$

For the HFD calculation, k involved in the estimation was optimized at 18 and 6 for real and simulated EEG signals, respectively.

Fluctuation-Based Dispersion Entropy

Fluctuation-based dispersion entropy is a recent approach based on Shannon entropy and symbolic dynamics (Azami and Escudero, 2018). It is an efficient method to measure dynamic variability in real-time neurological data. The measure is relatively faster, insensitive to noise, and detects simultaneous amplitude and phase variations. Dispersion entropy (DispEn) uses a mapping function that transforms the EEG data to a new time series data of symbolic sequences with fewer elements (Azami and Escudero, 2018; Nieto-Del-amor et al., 2021). It estimates the regularity of the patterns with similar dispersion patterns. FDispEn captures the difference between adjacent elements of the dispersion pattern.

Algorithm for the FDispEn calculation for a given univariate data sample $y_j\left(j = 1 \ldots\ldots N\right)$ of length N is as follows:

1. The time series y_j is mapped with a mapping function to c classes. The classes are labeled as 1–c. A number of linear and non-linear mapping functions can be utilized for this process. Each sample is grouped to its nearest class based on its amplitude. A classified signal $u_j\left(j = 1 \ldots\ldots N\right)$ is thus obtained.
2. With an embedding dimension (m), and time delay (d) multiple time series, of length m, $u_i^{m,c} = \left\{u_i^c, u_{i+d}^c, \ldots\ldots u_{i+(m-1)d}^c\right\}$ for each $i = 1, 2, \ldots..N-(m-1)d$ are generated. Each $u_i^{m,c}$ is mapped to its dispersion pattern (Azami and Escudero, 2018). The number of possible dispersion patterns for each $u_i^{m,c}$ is c^m.
3. FDispEn calculates the difference between adjacent dispersion patterns. For a vector length of $m-1$, each element changes from $-c+1$ to $c-1$. Thus, the number of fluctuation-based dispersion patterns for each $u_i^{m,c}$ is $(2c-1)^{m-1}$.
4. The relative frequency of each $(2c-1)^{m-1}$ dispersion patterns is calculated. It is used for the calculation of the FDispEn value of the input time series based on Shannon's entropy.

The study used $m = 3$ and $c = 3$ as the embedding dimension and number of classes, respectively, for the estimation of FDispEn (Azami and Escudero, 2018).

STATISTICS

The Student's t-test has been used to investigate the significant difference between the patient and the control group. Normality in the data was ensured using the Shapiro-Wilk test. As the results from simulation experiments did not meet parametric assumptions, the Wilcoxon rank-sum (Mann-Whitney) test, a non-parametric test, has been used for simulated EEG signals. A false discovery rate (FDR) correction was applied across multiple comparison studies.

RESULTS

In this study, the complexity analysis was carried out in real and simulated EEG signals to explore the relation between functional connectivity and complexity in the context of MCI-AD under resting eyes open conditions. The mean connectivity strength of control, patient, and lesion-induced connectivity matrices was 0.5575, 0.4945, and 0.2454, respectively. The study performed three statistical investigations, namely, (1) comparison between real EEG signals of MCI-AD and healthy controls, 2) comparison between simulated EEG signals of patients with MCI-AD and healthy controls, and 3) comparison between simulated EEG signals from control and lesion-induced control. Results from these analyses are described in the following subsections. The ANOVA test conducted between real and simulated EEG signals displayed a significant difference of $p = 0.0001$.

Comparison Between Real EEG Signals of Patients With MCI-AD and Healthy Controls

The complexity measures of LZC, HFD, and FDispEn were used to analyze EEG signals of patients with MCI-AD and healthy controls. It was observed from the analysis of all the three complexity measures that the patients with MCI-AD have reduced complexity with respect to the control group. Reduction in complexity was displayed in anterior ($p = 0.001$), posterior ($p = 0.005$), and central ($p = 0.001$) regions for the LZC measure. However, significantly reduced complexity was observed only in the central region ($p = 0.05$), employing the HFD metric. Lower values of the FDispEn value were obtained for the anterior ($p = 0.05$) and central ($p = 0.05$) regions. Bar chart plots for the values computed for LZC, HFD, and FDispEn for patients with MCI-AD and controls across the three regions are displayed in **Figures 3–5**, respectively. It is observed from the plots that the MCI-AD condition is accompanied by a reduction in EEG complexity. Additionally, the central region of the MCI-AD brain has displayed reduced complexity for all the EEG complexity measures employed.

Comparison Between Simulated EEG Signals of Patients With MCI-AD and Healthy Controls

Complexity measures are calculated from simulated EEG signals generated from the Kuramoto mean-field model utilizing connectivity network of patients and controls. The analysis has revealed a reduction in complexity estimates in simulated EEG signals of patients with respect to that of the simulated EEG signals from controls. A bar chart plot of mean values of LZC complexity measured across three regions, anterior, central, and posterior, is shown in **Figure 6**. A significant reduction

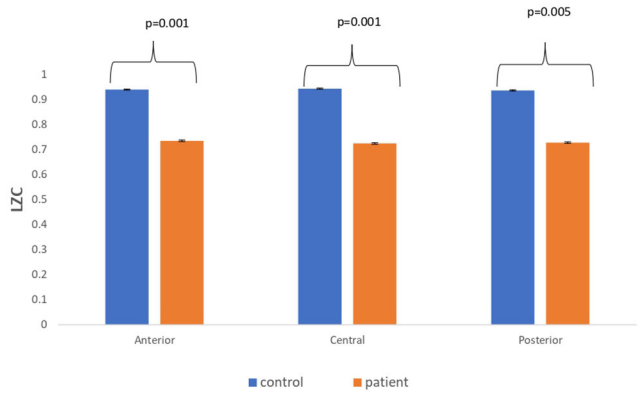

FIGURE 3 | A bar chart plot of mean LZC values of real EEG signals of patients with MCI-AD and controls computed for anterior, central, and posterior regions.

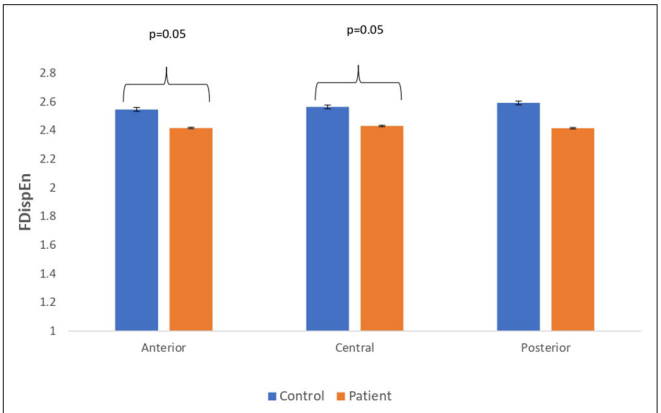

FIGURE 5 | A bar chart plot of mean FDispEn values of real EEG signals of patients with MCI-AD and controls computed for anterior, central, and posterior regions.

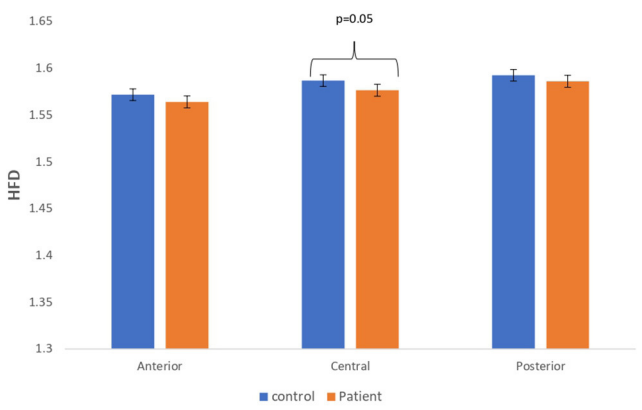

FIGURE 4 | A bar chart plot of mean HFD values of real EEG signals of patients with MCI-AD and controls computed for anterior, central, and posterior regions.

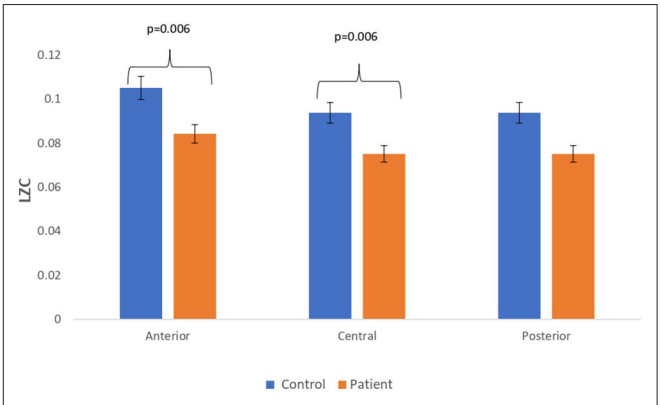

FIGURE 6 | Mean LZC values calculated from simulated EEG data channels of patient and control group across anterior, central, and posterior regions.

in the complexity score was observed for the anterior (p = 0.006) and central (p = 0.006) regions. However, a significant difference was not visible for HFD and FDispEn measures. The reduction in complexity measure on simulated patient EEG channels indicated that the signals have become more regular and less complex than the simulated control EEG signals. This study indicated that lesser functional connectivity registered in patient matrix leads to a reduced patient EEG complexity estimate with respect to control. The results thus imply that connectivity between the limit cycle oscillator in the Kuramoto model has a direct effect on complexity values in the subsequently generated signal.

Comparison Study Between Simulated EEG Signals of Controls and Lesion-Induced Control Signals

Lesion-induced connectivity patterns were generated by replacing the connectivity score of the edges joining the central region by a value of 0.1. This would result in a transformed connectivity pattern with lowered connectivity score. A comparative study was conducted between simulated EEG signals generated from control and lesion-induced control signals. The results revealed a reduction in complexity values in the simulated EEG signals obtained from the lesion-induced control connectivity matrix in comparison with the simulated EEG signals generated from the connectivity matrix of the controls. Bar chart plots of mean complexity values of LZC, HFD, and FDispEn measures from control and lesion-induced control signals are shown in **Figures 7–9**, respectively. A significant difference was observed for LZC values in anterior (p = 0.001) and central (p = 0.005) regions. Reduced values of HFD were obtained for the central region (p = 0.006) with no significant statistical difference in the anterior and posterior regions. FDispEn has revealed differences in the central (p = 0.06) and posterior (p = 0.09) regions. From the analysis, it is apparent that the introduced lesion has induced a significant reduction in complexity values.

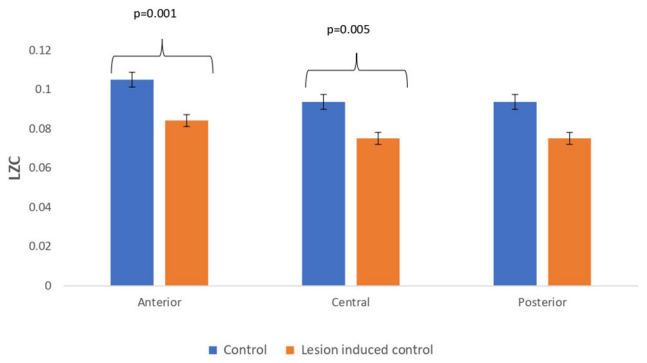

FIGURE 7 | Mean LZC values calculated from simulated EEG data channels of control and lesion-induced control signals across anterior, central, and posterior regions.

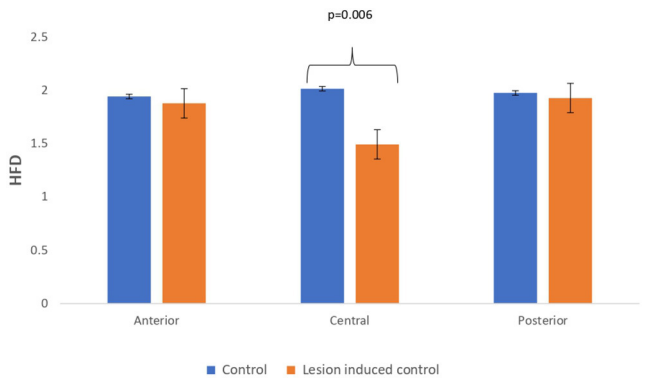

FIGURE 8 | Mean HFD values calculated from simulated EEG data channels of control and lesion-induced control signals across anterior, central, and posterior regions.

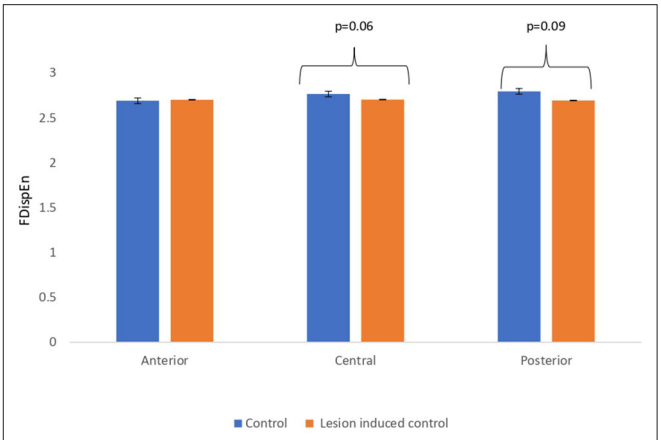

FIGURE 9 | Mean FDispEn values calculated from simulated EEG data channels of control and lesion-induced control signals across anterior, central, and posterior regions.

The EEG complexity analysis carried out on the signals from patients with MCI-AD and controls revealed a reduction in complexity in the patient group with respect to the controls. Results from the comparative study between simulated EEG signals of patients with MCI-AD and healthy controls and between simulated EEG signals from control and lesion-induced control, ascertain a positive relation between reduced EEG complexity to reduced connectivity pattern.

DISCUSSION

In this study, the relation between two prominent features, namely, functional connectivity and complexity of MCI-AD, are explored. The study investigates the influence of brain connectivity on EEG complexity by employing a phenomenological model of MCI-AD. The study employed functional connectivity matrix of patients with MCI-AD and the control group to generate simulated EEG signals using the Kuramoto mean-field model. Complexity measures are calculated from real and simulated EEG signals. The study also explored the effect of an induced lesion in the connectivity pattern and its resultant effect on complexity values. The functional connectivity matrix is calculated using WPLI. Popularly used complexity measures in EEG signal analysis such as LZC and HFD together with the novel entropy measure of fluctuation-based dispersion were used for EEG signal analysis.

Complexity analysis is performed to understand the amount of uncertainty or irregularity in data. The complexity aspect of neurological data has been explored with the hypothesis that complexity in the data indicates the adaptability of the system to function in varying environments. It further hypothesizes that the effect of a pathological process could hamper adaptability and would be reflected in the complexity estimates. The brain may exhibit increased or reduced complexity as a result of underlying pathology. Deviation in the mean complexity score observed in the patient group in comparison to a healthy control population could be the result of the detrimental effects of the underlying condition. Complexity studies conducted in the brain have shown this deviation with an increase in the complexity in the case of schizophrenia (Takahashi et al., 2010; Fernández et al., 2013; Ibáñez-molina et al., 2018), in normal aging (Anokhin et al., 1996) and a decrease in the complexity with MCI-AD in this study. In this study, the complexity scores of the patient were compared with that of the control group to study the deviation. The study reveals that alternations in the complexity estimates have their onset in the early phases of AD. All the three complexity measures of LZC, HFD, and FDispEn revealed a reduction in complexity in the EEG signals in patients with MCI-AD in comparison to the control group.

The reduction of EEG complexity estimates in patients is an indication of the EEG waveforms becoming more regular and less complex. It is suggestive of the possible effect of the MCI-AD-related pathological process, disintegrating the functional coupling and enabling neuronal bodies to behave more independently generating simple predictable waveforms (Jeong, 2004; Dauwels and Cichocki, 2011). The study has further revealed that the reduction in complexity estimates was significant in the anterior and central regions of the MCI-AD brain. The result is in agreement with previous studies conducted in AD (Dauwels and Cichocki, 2011; Smits et al., 2016; Al-nuaimi

et al., 2018; Nesma et al., 2018; Nobukawa et al., 2019) and in limited studies conducted in early AD (Labate et al., 2013; Zhu et al., 2017). Histopathological studies in early AD and AD have shown the presence of atrophy in the medial temporal lobe and the association cortices (Chetelata and Baron, 2003; Teipel et al., 2006). The evidence of change revealed in this study in the anterior and central regions is inclusive of frontal and temporal lobes that account for the memory and non-memory impairment observed in the prodromal phase of AD (Chetelata and Baron, 2003; Teipel et al., 2006; Dauwels and Cichocki, 2011).

Along with the reduction of complexity, reduction in functional connectivity is a hallmark feature of the EEG analysis in AD (Dauwels and Cichocki, 2011). The functional connectivity analysis in this study is carried out using the WPLI. The connectivity analysis based on WPLI revealed a reduction in mean connectivity strength in the patient group. Several electrophysiological studies have extensively explored AD-related changes revealing a reduction in connectivity (Babiloni et al., 2004; Engels et al., 2015; Afshari and Jalili, 2017; Triggiani et al., 2017) and complexity (Dauwels and Cichocki, 2011; Labate et al., 2013; Smits et al., 2016; Al-nuaimi et al., 2018; Nesma et al., 2018) discretely, without analyzing the influence of one over the other. The results from the current study disclose a positive influence between the two features of functional connectivity and complexity accomplished through the study of the Kuramoto model. A reduction in values of complexity estimates was observed for the simulated EEG signal from the patients with MCI-AD when matched with the controls. In addition, results from the simulated EEG analysis from lesion-induced controls and controls provide a similar inference. From the simulated EEG signals analysis, it was observed that reduced complexity has been consecutively associated with the group having a reduced connectivity score. Simulated EEG signal from lesion-induced control is an attempt to simulate the effect of the discontinuous network in MCI-AD. The Kuramoto model could generate a more disconnected set of EEG signals by reducing the connectivity strength from the edges originating from the central region of the connectivity matrix. Thus, from the comparative studies, it is evident that the functional connectivity matrix holds intricate relation with the signal complexity estimated.

The relation between connectivity and complexity could be understood with the help of the meta-stability concept. The meta-stability concept in the brain provides the theoretical foundation to explain how complex features emerge and are capable of information processing, data transmission, and storage. The Kuramoto model essentially describes a phase model that can exhibit spontaneous translations from random incoherent phases to collective synchrony as the coupling parameter passes through a critical threshold value. The coupling parameter in the metastable region allows the model to simulate data that resemble brain data with features of spontaneous transition between multiple transient states. The reduction in the connectivity/coupling in the coupled system of oscillators could have enabled the individual oscillators to behave more incoherently, thus reducing the "meaningful structural richness" (Costa et al., 2005) of the simulated signal. Accordingly, the reduction in the complexity could be related to the decline in the capability of the system to visit a wide repertoire of possible states, thus affecting the adaptability of the brain to varying environmental conditions.

Several complexity measures have been applied to study EEG signals over the years. The distinction between meaningful structural richness and randomness in the system remains unclear as both systems are capable of generating unpredictable and irregular signals. Complexity is defined as an intermediate stage between randomness and order. Complexity measures used in this study, LZC, HFD, and FdispEn, capture different aspects of the system dynamics. LZC and FDispEn measure the regularity index of a dynamical system through the amount of the uncertainty element. FDispEn is based on Shannon entropy and estimates dynamical variability through dispersion patterns. LZC estimates are based on scanning the symbolic representation of time series data for new patterns. It is a useful means to estimate the bandwidth of random process and harmonic variability in a quasi-periodic signal (Aboy et al., 2006). HFD captures the signal at different scales and investigates the self-similarity in the time series data. HFD is insensitive to stereotypical or repetitive signals. Therefore, it is possible to have a signal with a low LZC value with high HFD if the signal is a disordered signal composed of similar patterns (Jos et al., 2018). The complexity measures LZC, HFD, and FDispEn are capable of measuring certain aspects of "structural richness" in the signal. From the results of simulation studies, it is discerned that the regional complexity score is influenced by the introduction of lesion in the connectivity matrix. Thus, the reduction in coordination with multiple coupling strength in the simulation of EEG signal could have resulted in reduction in "meaningful structural richness" or complexity.

Mixed patterns of both positive (Nobukawa et al., 2020) and negative correlation (Mcdonough and Nashiro, 2014; Jos et al., 2018) between connectivity and complexity have been reported in few studies conducted on neurophysiological and simulated data. A recent study observed a positive correlation between connectivity and complexity in AD (Nobukawa et al., 2020). The current study supports this result with an abstract modeling approach to the MCI-AD condition. However, it should be noted that it is yet to be fully understood whether the reduction of connectivity and complexity could be the result of a direct association or is the by-product of diverse neurological activities in the MCI-AD brain. One of the major limitations of the study is that the Kuramoto model used in the study is a fairly simple model and would not be able to reconstruct all the characteristic features of the EEG signal. Furthermore, this model used a limited number of oscillators to simulate the signal. Despite this, the comparison analysis by using the complexity analysis showed that the model could fairly simulate EEG signals at a similar level of complexity as a real EEG signal. This study suggests that the reduction of functional integration between brain regions caused by the loss of connectivity could be one of the possible reasons for the reduction of richness or complexity in the EEG signals. Future studies could use the results from this study to understand the neurodynamics behind the electrophysiological observation in EEG under MCI-AD conditions.

CONCLUSION

The study attempted to analyze the relation between functional connectivity and complexity by modeling the MCI-AD condition with the help of the Kuramoto model. EEG signals from the MCI-AD condition have shown altered neurodynamics, displaying a reduction in the estimates of connectivity and complexity. From the studies using the Kuramato model, it was found that the connectivity of the coupled oscillators has a direct influence on the complexity of the generated signal. A significant observation from the results of the study is the possible direct influence of reduced connectivity between brain regions in lowering the complexity score of the EEG signal.

DATA AVAILABILITY STATEMENT

The datasets presented in this article are not readily available because the data is protected by a copyright that restricts sharing. Requests to access the datasets should be directed to SP, subhadp@nitc.ac.in.

ETHICS STATEMENT

The studies involving human participants were reviewed and approved by the research and ethical committee of Sree Chithra Tirunal Institute of Medical Sciences and Technology, Trivandrum, Kerala, India. The patients/participants provided their written informed consent to participate in this study.

AUTHOR CONTRIBUTIONS

All authors listed have made a substantial, direct, and intellectual contribution to the work and approved it for publication.

ACKNOWLEDGMENTS

We thank Dr. Ramshekhar N. Menon, consultant neurologist, SCTIMST Trivandrum, Kerala. He was instrumental in acquiring EEG data.

REFERENCES

Aboy, M., Hornero, R., Abasolo, D., and Alvarez, D. (2006). Interpretation of the lempel-ziv complexity measure in the context of biomedical signal analysis. *IEEE Transact. Biomed. Eng.* 53, 2282–2288. doi: 10.1109/TBME.2006.883696

Aerts, H., Fias, W., Caeyenberghs, K., and Marinazzo, D. (2016). Brain networks under attack: robustness properties and the impact of lesions. *Brain* 139, 3063–3083. doi: 10.1093/brain/aww194

Afshari, S., and Jalili, M. (2017). Directed functional networks in alzheimer's disease: disruption of global and local connectivity measures. *IEEE J. Biomed. Health Inform.* 21, 949–955. doi: 10.1109/JBHI.2016.2578954

Al-nuaimi, A. H. H., Jammeh, E., Sun, L., and Ifeachor, E. (2018). Complexity measures for quantifying changes in electroencephalogram in alzheimer's disease. *Complexity* 2018, 22–24. doi: 10.1155/2018/8915079

Anokhin, A. P., Birbaumer, N., Lutzenberger, W., Nikolaev, A., and Vogel, F. (1996). Age increases brain complexity. Electroencephal. *Clin. Neurophysiol.* 99, 63–68. doi: 10.1016/0921-884x(96)95573-3

Azami, H., and Escudero, J. (2018). Amplitude- and fluctuation-based dispersion entropy. *Entropy* 20, 1–21. doi: 10.3390/e20030210

Babiloni, C., Ferri, R., Moretti, D. V., Strambi, A., Binetti, G., Dal Forno, G., et al. (2004). Abnormal fronto-parietal coupling of brain rhythms in mild Alzheimer's disease: a multicentric EEG study. *Eur. J. Neurosci.* 19, 2583–2590. doi: 10.1111/j.0953-816X.2004.03333.x

Breakspear, M., Heitmann, S., and Daffertshofer, A. (2010). Generative models of cortical oscillations : neurobiological implications of the Kuramoto model. *Front. Hum. Neurosci.* 4, 1–14. doi: 10.3389/fnhum.2010.00190

Brier, M. R., Thomas, J. B., and Ances, B. M. (2014). Network dysfunction in alzheimer's disease: refining the disconnection hypothesis. *Brain Connectiv.* 4, 299–311. doi: 10.1089/brain.2014.0236

Chetelata, G., and Baron, J. (2003). Early diagnosis of Alzheimer's disease : contribution of structural neuroimaging. *NeuroImage* 18, 525–541. doi: 10.1016/S1053-8119(02)00026-5

Clerx, L., van Rossum, I. A., Burns, L., Knol, D. L., Scheltens, P., Verhey, F., et al. (2013). Measurements of medial temporal lobe atrophy for prediction of Alzheimer's disease in subjects with mild cognitive impairment. *Neurobiol. Aging* 34, 2003–2013. doi: 10.1016/j.neurobiolaging.2013.02.002

Costa, M., Goldberger, A. L., and Peng, C. K. (2005). Multiscale entropy analysis of biological signals. *Physic. Rev. E – Statistic. Nonlin. Soft Matter Physic.* 71, 1–18. doi: 10.1103/PhysRevE.71.021906

Das, S., and Puthankattil, S. D. (2020). Complex network analysis of MCI-AD EEG signals under cognitive and resting state. *Brain Res.* 20, 1735. doi: 10.1016/j.brainres.2020.146743

Dauwels, J., and Cichocki, A. (2011). Diagnosis of Alzheimer's Disease from EEG Signals : where are we standing? *Current Alzheimer Res.* 7, 487–505. doi: 10.2174/156720510792231720

Delbeuck, X., der Linden, M., and Collette, F. (2003). Alzheimer' disease as a disconnection syndrome? *Neuropsychol. Rev.* 13, 79–92. doi: 10.1023/A:1023832305702

Dhikav, V., Sethi, M., and Anand, K. S. (2014). Medial temporal lobe atrophy in Alzheimer's disease/mild cognitive impairment with depression. *Br. J. Radiol.* 87, 5–7. doi: 10.1259/bjr.20140150

Duan, F., Huang, Z., Sun, Z., Zhang, Y., Zhao, Q., Cichocki, A., et al. (2020). Topological Network analysis of early alzheimer's disease based on resting-state eeg. *IEEE Transact. Neural Syst. Rehabil. Eng.* 28, 2164–2172. doi: 10.1109/TNSRE.2020.3014951

Engels, M. M. A., Stam, C. J., van der Flier, W. M., Scheltens, P., de Waal, H., and van Straaten, E. C. W. (2015). Declining functional connectivity and changing hub locations in Alzheimer's disease: an EEG study. *BMC Neurol.* 15, 1–8. doi: 10.1186/s12883-015-0400-7

Escudero, J., Ibáñez-molina, A., and Iglesias-parro, S. (2015). "Effect of the average delay and mean connectivity of the kuramoto model on the complexity of the output electroencephalograms," in *37th Annual International Conference of the IEEE Engineering in Medicine and Biology Society (EMBC)*, pp. 7873–7876.

Fernández, A., Gomez, C., Hornero, R., and Lopez-Ibor, J. J. (2013). Complexity and schizophrenia. *Prog. Neuropsychopharmacol. Biol. Psychiatry* 45, 267–276. doi: 10.1016/j.pnpbp.2012.03.015

Finger, H., Bönstrup, M., Cheng, B., and Mess,é, A. (2016). Modeling of large-scale functional brain networks based on structural connectivity from DTI: comparison with EEG derived phase coupling networks and evaluation of alternative methods along the modeling path. *PLoS Computat. Biol.* 16, 1–28. doi: 10.1371/journal.pcbi.1005025

František, V., Shanahan, M., Hellyer, P. J., Scott, G., Cabral, J., and Leech, R. (2015). Effects of lesions on synchrony and metastability in cortical networks. *NeuroImage* 118, 456–467. doi: 10.1016/j.neuroimage.2015.05.042

Gómez, C., Mediavilla, Á., Hornero, R., Abásolo, D., Fernández, A., Gómez, C. (2009). Use of the Higuchi's fractal dimension for the analysis of MEG recordings from Alzheimer's disease patients. *Med. Eng. Physics* 9, 1−26. doi: 10.1016/j.medengphy.2008.06.010

Hornero, R., Abásolo, D., Escudero, J., and Gómez, C. (2009). Non-linear analysis of EEG and MEG in patients with Alzheimer's disease. *Royal Soc. Philos. T R Soc. A* 367, 317–336. doi: 10.1098/rsta.2008.0197

Ibáñez-molina, A., Iglesias, J., Parro, S. (2016). Neurocomputational Model of EEG complexity during mind wandering. *Front. Comput. Neurosci.* 10, 1–10. doi: 10.3389/fncom.2016.00020

Ibáñez-molina, A., Iglesias, J., Parro, S. (2018). A Comparison between theoretical and experimental measures of consciousness as integrated information in an anatomically based network of coupled oscillators. *Complexity* 8, 586. doi: 10.1155/2018/6101586

Jeong, J. (2004). EEG dynamics in patients with Alzheimer's disease. *Clinical Neurophysiol.* 115, 1490–1505. doi: 10.1016/j.clinph.2004.01.001

Jos, A., Iglesias-parro, S., and Escudero, J. (2018). Differential effects of simulated cortical network lesions on synchrony and EEG. *Complexity*. 28, 1–17. doi: 10.1142/S0129065718500247

Kundu, S., Lukemire, J., Wang, Y., Guo, Y., Weiner, M. W., Schuff, N., et al. (2019). A novel joint brain network analysis using longitudinal alzheimer's disease data. *Scientific Rep.* 9, 1–18. doi: 10.1038/s41598-019-55818-z

Labate, D., Foresta, F. L., Morabito, G., Palamara, I., and Morabito, F. C. (2013). Entropic Measures of EEG complexity in Alzheimer's disease through a multivariate multiscale approach. *IEEE Sensors J.* 13, 3284–3292. doi: 10.1109/JSEN.2013.2271735

Lee, H., Golkowski, D., Jordan, D., Berger, S., Ilg, R., Lee, J., et al. (2019). Relationship of critical dynamics, functional connectivity, and states of consciousness in large-scale human brain networks. *NeuroImage.* 188, 228–238. doi: 10.1016/j.neuroimage.2018.12.011

Lee, W. H., and Frangou, S. (2017). Linking functional connectivity and dynamic properties of resting-state networks. *Scientific Rep.* 9, 1–10. doi: 10.1038/s41598-017-16789-1

Lempel, A., and Ziv, J. (1976). On the complexity of finite sequences. *IEEE Transact. Inform. Theory* 22, 75–81. doi: 10.1109/TIT.1976.1055501

Mcdonough, I. M., and Nashiro, K. (2014). Network complexity as a measure of information processing across resting-state networks: evidence from the Human Connectome Project. *Front. Human Neurosci.* 8, 1–16. doi: 10.3389/fnhum.2014.00409

Miraglia, F., Vecchio, F., Bramanti, P., and Rossini, P. M. (2016). EEG characteristics in "eyes-open" versus "eyes-closed" conditions: small-world network architecture in healthy aging and age-related brain degeneration. *Clinic. Neurophysiol.* 127, 1261–1268. doi: 10.1016/j.clinph.2015.07.040

Nesma, H., Vialatte, F., Gallego-Jutgl,à4, E., Dreyfus, G., Nguyen-Michel, V.-H., and Jean Mariani, K. K. (2018). Diagnosis of Alzheimer's disease with Electroencephalography in a differential framework. *PLoS Comput. Biol.* 18, 1—19. doi: 10.1371/journal.pone.0193607

Nestor, P. J., Scheltens, P., and Hodges, J. R. (2004). Advances in the early detection of Alzheimer's disease. *Nature Med.* 10, S34–41. doi: 10.1038/nrn1433

Nieto-Del-amor, F., Beskhani, R., Ye-Lin, Y., Garcia-Casado, J., Diaz-Martinez, A., Monfort-Ortiz, R., et al. (2021). Assessment of dispersion and bubble entropy measures for enhancing preterm birth prediction based on electrohysterographic signals. *Sensors* 21, 6071. doi: 10.3390/s21186071

Nimmy John, T., D., Puthankattil, S., and Menon, R. (2018). Analysis of long range dependence in the EEG signals of Alzheimer patients. *Cognitive Neurodynam.s* 12, 183–199. doi: 10.1007/s11571-017-9467-8

Nobukawa, S., Yamanishi, T., Kasakawa, S., and Nishimura, H. (2020). Classi fi cation methods based on complexity and synchronization of electroencephalography signals in Alzheimer's disease. *Front. Psychiatry*11, 1–12. doi: 10.3389/fpsyt.2020.00255

Nobukawa, S., Yamanishi, T., Nishimura, H., Wada, Y., Kikuchi, M., and Takahashi, T. (2019). Atypical temporal-scale-specific fractal changes in Alzheimer's disease EEG and their relevance to cognitive decline. *Cogn. Neurodynam.* 13, 1–11. doi: 10.1007/s11571-018-9509-x

Orekhova, E. V., Elsabbagh, M., Jones, E. J., Dawson, G., Charman, T., and Johnson, M. H. (2014). EEG hyper-connectivity in high-risk infants is associated with later autism. *Journal of Neurodevelopment. Disord.* 6, 1–11. doi,: 10.1186/1866-1955-6-40

Sargolzaei, S., Cabrerizo, M., Sargolzaei, A., Noei, S., Eddin, A. S., Rajaei, H., et al. (2015). A probabilistic approach for pediatric epilepsy diagnosis using brain functional connectivity networks. *BMC Bioinform.* 16, 1–11. doi: 10.1186/1471-2105-16-S7-S9

Schartner, M., Seth, A., Noirhomme, Q., Boly, M., Bruno, A., Laureys, S., et al. (2015). Complexity of multi-dimensional spontaneous EEG decreases during propofol induced general anaesthesia. *PLoS ONE* 15, 1–21. doi: 10.1371/journal.pone.0133532

Selesnick, I. W., Graber, H. L., Pfeil, D. S., and Barbour, R. L. (2014). Simultaneous low-pass filtering and total variation denoising. *IEEE Transact. Signal Process.* 62, 1109–1124. doi: 10.1109/TSP.2014.2298836

Smits, F. M., Porcaro, C., Cottone, C., and Cancelli, A. (2016). electroencephalographic fractal dimension in healthy ageing and Alzheimer's electroencephalographic fractal dimension in healthy ageing and Alzheimer's Disease. *PLoS ONE.* 16, 587. doi: 10.1371/journal.pone.0149587

Takahashi, T., Cho, R. Y., Mizuno, T., Kikuchi, M., Murata, T., Takahashi, T., et al. (2010) Antipsychotics reverse abnormal EEG complexity in drug-naive schizophrenia: A multiscale entropy analysis. *NeuroImage* 51, 173–182. doi: 10.1016/j.neuroimage.2010.02.009

Teipel, S. J., Pruessner, J. C., Faltraco, F., Born, C., Rocha-Unold, M., Evans, A., et al. (2006). Comprehensive dissection of the medial temporal lobe in AD: measurement of hippocampus, amygdala, entorhinal, perirhinal and parahippocampal cortices using MRI. *J. Neurol.* 253, 794–800. doi: 10.1007/s00415-006-0120-4

Tononi, G., Edelman, G. M., and Sporns, O. (1998). Complexity and coherency: integrating information in the brain. *Trends Cogn. Sci.* 6613, 474–484. doi: 10.1016/S1364-6613(98)01259-5

Triggiani, A. I., Bevilacqua, V., Brunetti, A., Lizio, R., Tattoli, G., Cassano, F., et al. (2017). Classification of healthy subjects and Alzheimer's disease patients with dementia from cortical sources of resting state EEG rhythms: a study using artificial neural networks. *Front. Neurosci.* 10, 1–13. doi: 10.3389/fnins.2016.00604

Varangis, E., Habeck, C. G., Razlighi, Q. R., and Stern, Y. (2019). The effect of aging on resting state connectivity of predefined networks in the brain. *Front. Aging Neurosci.* 19, 6613. doi: 10.3389/fnagi.2019.00234

Veroude, K., Norris, D. G., Shumskaya, E., Gullberg, M., and Indefrey, P. (2010). Functional connectivity between brain regions involved in learning words of a new language brain and language functional connectivity between brain regions involved in learning words of a new language. *Brain Lang.* 113, 21–27. doi: 10.1016/j.bandl.2009.12.005

Vinck, M., Oostenveld, R., Van Wingerden, M., Battaglia, F., and Pennartz, C. M. A. (2011). An improved index of phase-synchronization for electrophysiological data in the presence of volume-conduction, noise and sample-size bias. *NeuroImage* 55, 1548–1565. doi: 10.1016/j.neuroimage.2011.01.055

Visser, P. J., Verhey, F. R. J., Hofman, P. A. M., Scheltens, P., and Jolles, J. (2002). Medial temporal lobe atrophy predicts Alzheimer's disease in patients with minor cognitive impairment. *J. Neurol. Neurosurg. Psychiatry* 72, 491–497. doi: 10.1136/jnnp.72.4.491

Wackerbauer, R., Witt, A., Atmanspacher, J., and Kurths, H. S. (1994). A comparative classification of complexity measures. *Chaos Solitons Fract.* 4, 133–173. doi: 10.1016/0960-0779(94)90023-X

Zhang, X. -S., Roy, R. J., and Jensen, E. W. (2001). EEG complexity as a measure of depth of anesthesia for patients. *IEEE. Trans. Biomed. Eng.* 48, 1424–1433. doi: 10.1109/10.966601

Zhu, B., Chai, C., Gao, S., Ren, H., Cao, L., Dong, Z., et al. (2017). Analysis of EEG complexity in patients with mild cognitive impairment. *J. Neurologic. Disord.* 05, 354. doi: 10.4172/2329-6895.1000354

Conflict of Interest: The authors declare that the research was conducted in the absence of any commercial or financial relationships that could be construed as a potential conflict of interest.

Publisher's Note: All claims expressed in this article are solely those of the authors and do not necessarily represent those of their affiliated organizations, or those of the publisher, the editors and the reviewers. Any product that may be evaluated in this article, or claim that may be made by its manufacturer, is not guaranteed or endorsed by the publisher.

frontiers | Frontiers in Human Neuroscience

TYPE Original Research
PUBLISHED 15 September 2022
DOI 10.3389/fnhum.2022.982905

OPEN ACCESS

EDITED BY
Ruben Sanchez-Romero,
Rutgers University, United States

REVIEWED BY
Juha M. Lahnakoski,
Julich Research Center (HZ), Germany
Xiuyuan Wang,
Cornell University, United States

*CORRESPONDENCE
Guosheng Ding
dinggsh@bnu.edu.cn
Lanfang Liu
liulanfang21@bnu.edu.cn

SPECIALTY SECTION
This article was submitted to Cognitive Neuroscience, a section of the journal Frontiers in Human Neuroscience

RECEIVED 30 June 2022
ACCEPTED 18 August 2022
PUBLISHED 15 September 2022

CITATION
Zhang J, Zhuang L, Jiang J, Yang M, Li S, Tang X, Ma Y, Liu L and Ding G (2022) Brain fingerprints along the language hierarchy. *Front. Hum. Neurosci.* 16:982905. doi: 10.3389/fnhum.2022.982905

Brain fingerprints along the language hierarchy

Juan Zhang[1], Liping Zhuang[2], Jiahao Jiang[3], Menghan Yang[1], Shijie Li[1], Xiangrong Tang[1], Yingbo Ma[3], Lanfang Liu[2,4]* and Guosheng Ding[1]*

[1]State Key Laboratory of Cognitive Neuroscience and Learning, IDG/McGovern Institute for Brain Research, Beijing Normal University, Beijing, China, [2]Department of Psychology, School of Arts and Sciences, Beijing Normal University, Zhuhai, China, [3]School of Psychology, Beijing Normal University, Beijing, China, [4]State Key Laboratory of Cognitive Neuroscience and Learning, Center for Cognition and Neuroergonomics, Beijing Normal University, Zhuhai, China

Recent studies have shown that the brain functional connectome constitutes a unique fingerprint that allows the identification of individuals from a group. However, what information encoded in the brain that makes us unique remains elusive. Here, we addressed this issue by examining how individual identifiability changed along the language hierarchy. Subjects underwent fMRI scanning during rest and when listening to short stories played backward, scrambled at the sentence level, and played forward. Identification for individuals was performed between two scan sessions for each task as well as between the rest and task sessions. We found that individual identifiability tends to increase along the language hierarchy: the more complex the task is, the better subjects can be distinguished from each other based on their whole-brain functional connectivity profiles. A similar principle is found at the functional network level: compared to the low-order network (the auditory network), the high-order network is more individualized (the frontoparietal network). Moreover, in both cases, the increase in individual identifiability is accompanied by the increase in inter-subject variability of functional connectivities. These findings advance the understanding of the source of brain individualization and have potential implications for developing robust connectivity-based biomarkers.

KEYWORDS

brain fingerprint, functional connectivity, language hierarchy, fMRI, individual identification

Introduction

For a long time, neuroimaging studies on human brains have been primarily concerned with the generic principles of brain function that are shared across people, with relatively little attention paid to inter-subject variability. In the seminal work conducted by Finn et al., individual variability in brain functional organization was found to be both robust and reliable (Finn et al., 2015). It is possible to identify a target subject from a sample database by computing the spatial similarity of the target subject's

brain functional connectivity (FC) profile against the FCs' of the database ones, similar to a "fingerprint." Following this work, further studies have detected various brain features that may act as a "fingerprint" (Liu et al., 2018, 2020; Sareen et al., 2021), proposed novel methods to improve the accuracy of individual identification (Amico and Goni, 2018; Cai et al., 2021), and related the brain fingerprinting features to behavioral traits (Kaufmann et al., 2017).

Yet, what makes our brains unique remains poorly understood. Understanding the source of brain individualization is important for several reasons. First, it will provide critical information for improving the accuracy of individual identification. Second, it will help establish the link between individual differences in brain function and individual differences in cognition and behavior, which in turn may have important implications in precision medicine. Finally, it can provide valuable information for evaluating to what extent the group-level results about brain function can be applied to unknown individuals.

Currently, only a few studies have explored factors that potentially influence individual identifiability, including: (i) the temporal window used to compute FC profiles. It has been reported that the greater identifiability occurred at longer time scales (Van De Ville et al., 2021); (ii) the anatomical loci. Across the whole brain, the connectivity profiles of the frontoparietal network and medial frontal networks were most distinctive for individuals (Amico and Goni, 2018); and (iii) factors affecting fMRI data which might be unique to individuals and stable enough across time, including global signals (Chen and Hu, 2018), head motion and brain anatomy (Finn et al., 2015).

The above work has been mainly focused on the physiological or structural aspects of the brain. Few studies have examined the roles of the functional aspects of the brain in individual identification. In particular, are the high-order functions (such as those supporting story comprehensions) or the low-order functions (such as those supporting auditory perception) of the brain more critical for individual identifiability? There are at least two possibilities: on the one hand, an individual's brain involved in low-order functions may show a high degree of stability across time, therefore facilitating individual identification; on the other hand, brains involved in high-order functions may vary greatly among people, thus making individual discrimination easier.

A further question is, how important are those task-evoked neural processes compared to task-independent intrinsic processes in distinguishing individuals? Several studies have performed individual identifications across resting states and obtained a high accuracy of above 90% (Finn et al., 2015; Horien et al., 2019). In comparison, identifications made across the resting state and a set of tasks typically produced lower accuracies ranging from about 60% to 85% (Kaufmann et al., 2017; Amico and Goni, 2018). Among the many factors (such as the characteristics of head motion and data length) potentially accounting for the differences in identification accuracy, one possibility is that, under resting states, subjects are actually engaged in a set of active mental processes, including unconstrained verbally mediated thoughts, monitoring, and episodic and autobiographical retrieval processes (Binder, 2012). Therefore, the results of identification across resting states might come from a combination of contributions from both state-independent and state-specific neural processes. Instead, the results of rest-task identification may better capture the contribution of state-independent processes to brain individualization. Yet, no study has systematically investigated the contribution of state-independent, low-order and high-order processes to brain fingerprints.

This study addresses the above two questions by tapping into the hierarchical nature of language. In our experiment, each subject underwent a resting-state fMRI scan, then listened to stories played backward, stories scrambled at the sentence level, and stories played forward during fMRI scanning. For each of the three tasks, brain imaging data were acquired from two separate scan sessions. The three tasks were assumed to involve increasingly complex cognitive processes, while the resting state was used to create a baseline condition. For the backward-played speech, which would appear as meaningless audio streams, subjects should be mainly engaged in low-level acoustic analysis. For the sentence-scrambled story, subjects would need to additionally recognize single words and combine words into sentences (termed as "middle-level linguistic/semantic operations"). For the intact story, in addition to the perceptual and linguistic/semantic computations, subjects would need to combine single sentences into coherent mental models that allow for inferences and conceptual associations. We termed these processes recruited specifically by story comprehension as "high-level conceptual processes."

To investigate the contribution of low-order and high-order functions of the brain to individual identification, we predicted subjects' identities across two scan sessions corresponding to the same task, and then compared the success rates (SRs) among the three task conditions. The state-independent neural process (the baseline) is assumed to play a role in both resting and task states. To assess its contribution, we conducted identifications between the resting session and each task session. Finally, to understand why individual identifiability may differ along the language hierarchy, we compared the degree of within-subject stability and inter-subject variability of FCs among the four conditions (including the three task conditions and condition of rest-task pairs).

We first performed individual identification based on the whole-brain functional connectomes. To establish a closer relationship between task-evoked brain functions and individual identifiability, we further conducted individual identification using FC profiles of single functional networks. Three networks known to be critically involved in speech processing were investigated, including a primary auditory network, a

perisylvian language network and a frontoparietal network (Price, 2010). In addition, the default mode networks (DMN) which have been suggested to be actively engaged in resting states and a set of high-order functions are also examined (Yeshurun et al., 2021).

Materials and methods

Subjects

A total of 30 college students (females, aged between 18 to 35 years) who were native Chinese speakers and proficient in English participated in this study. The criterion applied to screen participants included: (i) having passed the Test for English Majors-Band 8; (ii) scoring above 7 on the International English Language Testing System (IELTS); or (iii) scoring above 95 on the Test of English as a Foreign Language (TOEFL). The data of three subjects were excluded from further analyses due to excessive head movements (more than 3 mm or 3 degrees) during one or more sessions of the fMRI scanning. All subjects were right-handed and had no history of neurological, psychiatric or language disorders.

Experimental procedure

Stimuli for the experiment were generated from a set of cartoon stories (each lasting ~60 s) told by two female Chinese speakers during fMRI scanning. Each story was told in both Chinese and English. A noise-canceling microphone (FOMRI-III, Optoacoustics Ltd., Or-Yehuda, Israel) was used to record the speech. The recordings were further de-noised offline using Adobe Audition CS6 (Adobe Systems Inc., United States). Three types of audio clips (lasting 60–62 s) were created from those recordings. The first type of audio clip was the raw stories played forward (intact). The second type (sentence-scrambled) was created by randomly shuffling the sentences of the first half of a story and keeping the second half intact. The third type (backward) was created by presenting the first half of a story waveform-reversed in time and keeping the second half intact. For the latter two conditions, the intact parts of the stories were not included in the analyses. A more detailed description of the stimuli presentation is provided in the **Supplementary material** (**Supplementary Figures 1**, **2**).

Each subject underwent five fMRI scan sessions over 2 days. On the first day, following an 8-min resting-state scan session, subjects listened to backward-played stories and sentence-scrambled stories (presented in separate blocks) during two successive scan sessions. On the second day, subjects listened to intact stories during two successive scan sessions (**Figure 1**). The contents of stories differed between successive sessions.

Half of the subjects were exposed to the Chinese version of audio clips and the other half were exposed to the English version. As bilingualism is not the focus of the current study, we pooled the two subgroups of data together. This study was undertaken with the understanding and written consent of each subject and was approved by the Institutional Reviewer Board of Beijing Normal University.

MRI acquisition

Imaging data were collected with a 3T Siemens Trio scanner in the MRI Center of the Beijing Normal University in China. For the functional scan, a gradient echo-planar imaging sequence was applied with the following parameters: repetition time = 2,000 ms, echo time = 30 ms, flip angle = 90°, field of view = 220 mm^2, 33 interleaved slice, voxel size = 3.125 mm^3 × 3.125 mm^3 × 4 mm^3. Additionally, high-resolution T1 structural images were acquired using an MPRAGE sequence. The parameters were: repetition time = 2,530 ms, echo time = 3.39 ms, flip angle = 7°, FOV = 256 mm^2, and voxel size = 1.0 mm^3 × 1.0 mm^3 × 1.33 mm^3.

Imaging data preprocessing

The fMRI imaging data were preprocessed using DPARSF (Yan and Zang, 2010),[1] which integrates the preprocessing modules of Statistical Parametric Mapping (SPM12).[2] The steps of preprocessing included slice timing adjustment and realignment for head-motion correction, spatial normalization to the Montreal Neurological Institute (MNI) space, resampling into a voxel size of 3 mm^3 × 3 mm^3 × 3 mm^3, and smoothing with an isotropic Gaussian kernel (FWHW = 7 mm). The preprocessed images were further detrended, nuisance variable regressed, and high-pass filtered (1/128 Hz). The nuisance variables included the five principal components of signals in the white matter and cerebrospinal fluid masks (Behzadi et al., 2007) and Friston's 24 motion parameters (including each of the six motion parameters of the current and preceding volume, plus each of these values squared) (Friston et al., 1996).

Data analysis

Functional connectivity estimation

Identification for individual subjects was made based on their brain FC profiles and performed across two sessions of the same task and across the rest and each of the task sessions. For each task session, the time series corresponding to the task blocks were extracted. Before the data extraction,

1 http://rfmri.org/dpabi

2 http://www.fil.ion.ucl.ac.uk/spm

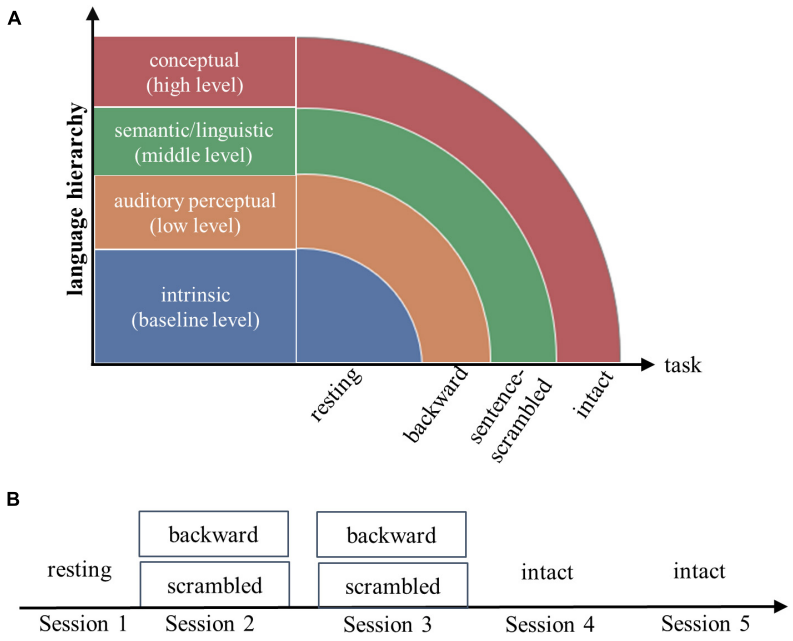

FIGURE 1
Experimental design **(A)** and fMRI scanning scheme **(B)**. Each subject underwent a resting-state fMRI scanning, then followed by three tasks: listening to short stories presented waveform-reversed in time (backward), stories scrambled at the sentence level, and stories played forward (intact). The resting state and three tasks were assumed to engage increasingly complex processes along the language hierarchy. For each of the three tasks, the brain imaging data were collected from two successive scan sessions.

the time series of each brain subregion were normalized in time using z-score. The data were shifted back in time by 4 s to account for the hemodynamic lag of blood-oxygen-level-dependent (BOLD) signals. As previous studies have shown that data length can influence the accuracy of identification (Van De Ville et al., 2021), we extracted an equal number of time points (N = 32) from each session. This number was determined by the maximum data length of the backward and the scrambled conditions.

To estimate FC, we partitioned the whole brain into 368 subregions using the Shen-368 Atlas (Salehi et al., 2020; Luo and Constable, 2022). This was a fine-grained atlas obtained by integrating the parcellation of cortex from Shen et al. (2013), subcortex from the anatomical Yale Brodmann Atlas (Lacadie et al., 2008), and cerebellum from Yeo et al. (2011). Pearson correlation coefficients between each possible pair of subregions were computed, resulting in a 368 by 368 connectivity matrix (**Figure 2A**). This was done for each subject and each condition, such that each subject had a total of seven connectivity matrices representing connectivity patterns during resting and the three tasks (two matrices for each task).

Identification using whole-brain functional connectivities

To detect the contribution of the four types of information to brain individualization, we conducted identification for individuals across time using the pairing scheme illustrated in **Figure 2B**. Specifically, to detect the task-independent intrinsic processes (the baseline level), identification was conducted across the resting state session and each of the six task sessions. To detect the auditory perceptual processes (the low level), identification was conducted across the two sessions of the backward condition. To detect the linguistic/semantic processes (the middle level), identification was performed across the two sessions of the sentence-scrambled condition. Finally, to detect the conceptual processes (the high level), identification was performed across the two sessions of the intact condition. For each level, the FCs derived from one scanning session served as the database and another session served as the target. The two sessions then changed the roles (**Figure 2B**).

To predict subjects' identities, an identifiability matrix was defined as Pearson's correlations between the database and the target (Amico and Goni, 2018). The main diagonal elements of the matrix represent the FC similarity of the same subjects across sessions, referred to as I_self. The off-diagonal elements of the matrix, averaged by columns, represent the FC similarity of subjects (from the database session) with other subjects (from the target session). This was referred to as I_other. The result of I_self minus I_other was referred to as I_diff, which reflects the identifiability of individual subjects for a given fold of identification (**Figure 2C**).

In addition to the I_diff which served as a continuous variable to quantify the identifiability of individual subjects, we also calculated the group-level SR of identification. For a given

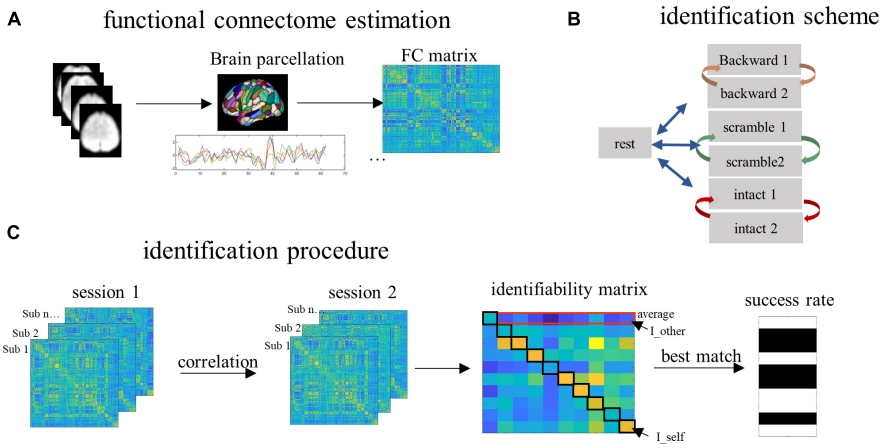

FIGURE 2
The procedure of data analysis. **(A)** The whole brain was partitioned into 368 parcels. Time series corresponding to the task blocks were extracted and concatenated to compute the functional connectivity (FC). **(B)** To detect the contribution of task-independent brain processes, we paired the resting scan with each of the six task scans for the identification. To detect the contribution of low- and high-order brain processes, for each task condition, we paired the two successive scan sessions corresponding to the same task. **(C)** To predict subjects' identities, the FCs from a database set were correlated with the FCs from the target set, resulting in an identifiability matrix. Based on this matrix, we obtained the within-subject FC similarity (quantified by the I_self), between-subject FC similarity (quantified by the I_other), individual identifiability (quantified by the I_diff, which is computed by I_self minus I_other), and the group-level success rate of identification.

subject, if the I_self was larger than every other element on the same row in the identifiability matrix, the identification was successful, otherwise it failed. In other words, if a subject's FCs in the database showed greater similarity with his/her own FCs than with any other subjects in the target set, the identification succeeded. This procedure was iterated over all subjects. The accuracy of identification was measured as the percentage of subjects whose identities were correctly predicted out of the total number of subjects in the group (Finn et al., 2015).

We first evaluated the identifiability index (I_diff) and SR for each pair separately and then averaged the results of corresponding pairs into one.

Statistical analysis

Non-parametric permutation tests were performed to assess whether the obtained identification accuracy was significantly above chance. In the permutation, the subjects' identities of the target set were randomly assigned and then the identification was performed. This procedure was repeated 1,000 times to create a null distribution for each session pair. Then for each condition, the null distributions of identification pairs were combined and the maximum SR from the null distributions was extracted as the threshold for the given condition. In addition, Chi-squared tests were applied to compare the SR of identification among the four conditions.

Comparison of within- and between-subject similarity

The success of individual identification mainly depends on how similar was the connectome patterns of a given subject with his/her own FCs (quantified by the I_self) and with the FCs of other subjects (quantified by the I_other). To gain insights into the potential differences in individual identification along the language hierarchy, we compared the two variables among the four conditions using paired *t*-tests. Multiple comparisons were corrected using a false discovery rate (FDR) at $Q = 0.05$.

Identification based on single functional networks

In the above analyses, the whole-brain connectome may encode not only task-related information, but also multiple task-unrelated neurophysiological processes as well as task-free intrinsic processes. To establish a closer relationship between task-related processes and individual identifiability, we further performed the identification based on the FC profiles of single functional networks. Currently, most brain functional networks reported in the literature are created from resting-state fMRI data. To more accurately detect those functional networks closely involved in the language task, we conducted brain network parcellation using an independent data set involving 61 subjects listening to a 10-min real-life story while undergoing fMRI scanning. Applying a recently-developed technique (Ji et al., 2019; Barnett et al., 2021), a group-mean 368 by 368 FC matrix was clustered into 15 networks. Details of network partition are presented in the **Supplementary material**. The four networks of interest, including the auditory, language, DMN and frontoparietal networks were selected via visual inspection and validated by comparing with

corresponding templates on Neurosynth[3] in terms of spatial overlap.

Tests for the robustness of results

Functional connectivities assessed with a different brain atlas

To test the robustness of the major findings, we re-analyzed the data by assessing the functional connectomes using the Schaefer atlas which partitioned the brain into 400 areas (Schaefer et al., 2018). Then we assessed individual identifiability along the language hierarchy based on 400 by 400 FC matrices.

Identification using a different strategy of condition pair and longer data length

To validate the main results, we adopted a different strategy of condition pair to assess individual identifiability, which allowed us to use more time points to compute FCs. Given the hierarchical nature of language, it is reasonable to assume that, in addition to the state-independent intrinsic activities, those state-specific processes engaged in the low-level task (e.g., listening to the backward-played story) are also engaged in the high-level task (e.g., listening to the intact story) (as illustrated in **Figure 1A**). Thus, the degree of similarity of subjects' FCs between the low- and the high-level tasks should mainly depend on the low-level task, which in turn would largely determine whether a subject can be identified between the conditions. Nevertheless, we noted that while the shared components of low- and high-level tasks can improve the accuracy through shared state-specific contribution, differences between state-specific activities could reduce the performance. In this way, changes in identification accuracy between conditions may underestimate the contribution of the targeted processes (the shared state-specific processes).

Following the above logic, we combined one dataset of the intact condition with the dataset of the rest, the backward, the sentence-scrambled, and the second intact conditions separately. Then identification was conducted between the two datasets for each of the four pairs. We predicted that the identifications of the rest-intact, backward-intact, scrambled-intact and intact-intact conditions should follow a similar pattern as the identification of the rest-task, backward-backward, scrambled-scrambled and intact-intact sessions.

For each condition, a total of 64 time points were extracted to compute FCs. For the backward and sentence-scrambled conditions, this was done by concatenating the corresponding time series from two scan sessions. For the intact condition, this was done by concatenating the corresponding time series from two blocks. For the resting state, the first 64 time points were extracted. Time series were normalized within a session before the concatenation.

3 https://www.neurosynth.org

Results

Individual identifiability along the language hierarchy based on whole-brain functional connectivities

Based on the whole-brain FC patterns, we predicted subjects' identities across the rest and each of the six task sessions with a mean accuracy of 62.9% (the baseline, ranging from 44.44 to 85.19% across pairs), which was much higher than the best performance (22.2%) from the permutation test (**Figures 3A,B**). Across the two sessions for the backward condition, which was presumed to involve low-level acoustic processing, the mean SR of identification was 85.2% (ranging from 81.48 to 88.89%). Across the two sessions for the sentence-scrambled condition, which was presumed to involve additionally middle-level linguistic and semantic processing, the mean SR of identification dropped slightly to 83.3% (ranging from 81.48 to 85.19%). The greatest SR was achieved across the two sessions for the intact condition (mean = 90.74%, ranging from 88.89 to 92.59%), which was presumed to involve further high-level conceptual processing.

For all three task conditions, the SR of individual identification across two sessions was significantly higher than that of the baseline ($p < 0.005$, by Chi-squared test). Nevertheless, the differences in SR among the three task conditions were not statistically significant ($p > 0.25$).

The analysis of the I_diff revealed a similar pattern: the individual identifiability increased along the language hierarchy, and the I_diff for all three tasks was greater than that of the baseline, but had no statistically significant differences among the three tasks (**Figure 3C**).

Changes in within- and between-subject similarity along the language hierarchy

To gain insights into why the individual identifiability varied along the language hierarchy, we compared the degree of within- and between-subject similarity (quantified by the I_self and I_other, respectively) in FC patterns across corresponding sessions. The within-subject similarity (or stability) in whole-brain FC profiles was the greatest across the two sessions for the sentence-scrambled condition, next for the backward condition, and the weakest for the intact condition (**Figure 3D**). This pattern was partially consistent with our prediction that the functional brains involved in the low-order tasks varied less across time than the brains involved in high-order tasks. The FC profiles within subjects were the least stable across the rest-task sessions (the baseline condition), which was significantly lower than that of all three task conditions ($p < 10^{-4}$, by paired t-test).

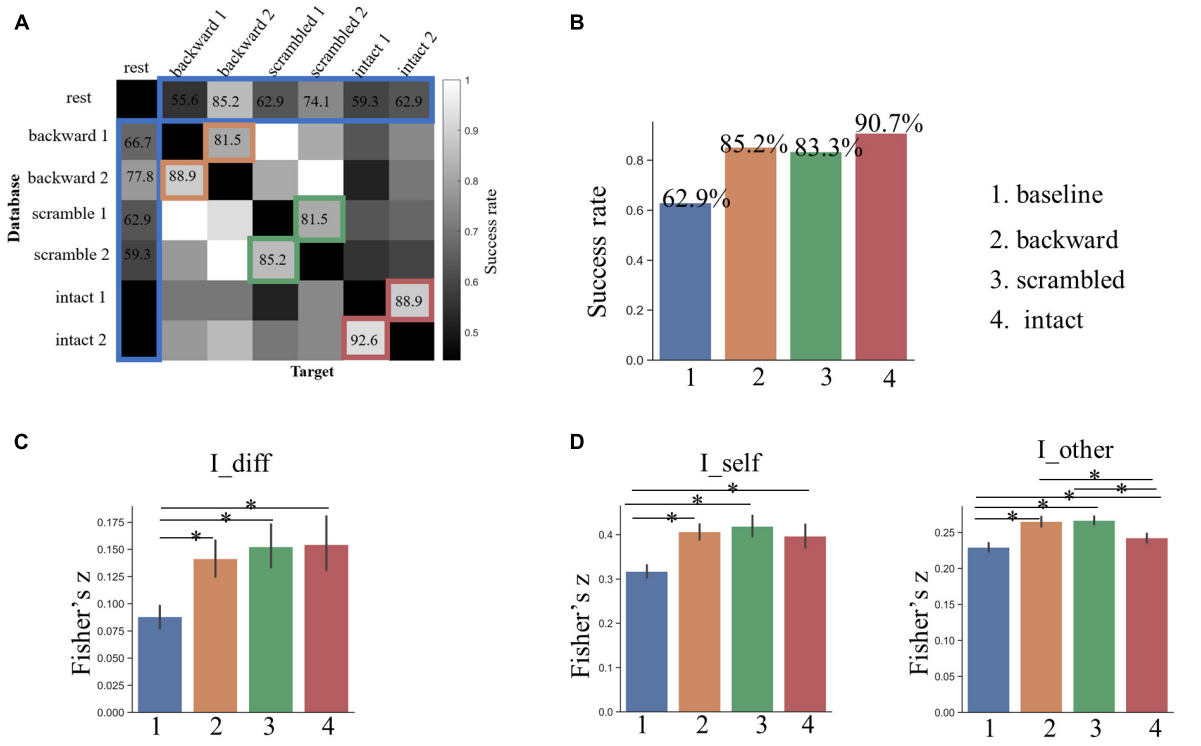

FIGURE 3
(A) The result of individual identification along the language hierarchy based on whole-brain FCs. **(B)** The success rate of identification across all possible pairs of sessions. Grids marked by colors are the interests of this study. The bar plot shows the group-level success rates averaged across corresponding pairs for the four conditions. **(C)** Individual identifiability quantified by I_diff. **(D)** Within- and between-subject similarity across sessions quantified by I_self and I_other, respectively. The asterisk indicates a significant difference between two conditions at $p < 0.05$ after FDR correction. The error bars denote the standard deviation of means.

The distribution of between-subject similarity resembled that of within-subject similarity. That is, compared to the higher-level intact condition, subjects were more similar to each other in their brain FCs under the lower-level backward and the sentence-scrambled conditions ($p < 10^{-3}$) (Figure 3D). This pattern was consistent with our prediction that the functional brain involved in higher-order functions is more variable across people. Still, compared to three task conditions, the brain FCs varied more between subjects across the rest and task states ($p < 10^{-3}$).

Together, those results suggest that the greater individual identifiability across the task sessions than that across the rest and task sessions might be related to the more stable brain FCs across the task sessions. The greater individual identifiability under the high-order condition than that under the low-order conditions might be related to the larger between-subject variability.

Network-based identification

The whole-brain FCs during tasks may be shaped by both task-related and task-unrelated processes, such as intrinsic activities or physiological noises. To gain more insights into the task-related information that potentially makes our brains distinguishable, we performed the identification using the FCs of functional networks.

Among the four examined networks, the auditory network achieved the lowest identification accuracies (ranging between 14.8 and 48.1%) under all four conditions. Further analyses showed the within-subject similarity in network FC profiles was the largest in the auditory network, especially under the backward condition. At the same time, the between-subject similarity in FC profiles was also the largest in this network. In other words, different subjects seemed to have similar FCs in the auditory network across sessions, potentially leading to the low SR in identification. The language network achieved SRs ranging from 32.1 to 59.2%, which also tended to increase along the hierarchy: the performance was lowest for the baseline, better for subjects under the backward condition, and the best for subjects under the sentence-scrambled condition, which then dropped down slightly for subjects under the intact condition. The DMN achieved SR ranging from 43.5 to 74.1%. The best performance obtained by this network was for subjects under the backward condition. The frontoparietal network performed the best (ranging from 61.1 to 92.6%) in

distinguishing individuals under most conditions. Consistent with the performance of the language network and the whole-brain connectome, the frontoparietal network also distinguished individuals with increasing accuracies along the hierarchy (**Figures 4A,B**).

When averaging the results over networks, the individual identifiability of the four conditions was ordered as baseline < backward < scrambled < intact. This pattern was in line with the results obtained from the whole-brain connectome (**Figure 4C**). When averaging the results over conditions, the SR of networks was ordered as auditory network < language network < DMN < frontoparietal. Further analyses showed, compared with the other three networks, there was significantly lower between-subject similarity (or higher inter-subject variability) in the FCs profiles of the frontoparietal network (**Figure 4D**).

The results of validations

Reproduce the findings with a different brain atlas

Applying the Schaefer atlas to assess the brain connectivities, we obtained a similar pattern of individual identifiability as the main analyses. The SR of identification increased along the language hierarchy: 56.17% for the baseline, 81.48% for the backward condition, 85.19% for the sentence-scrambled condition, and 87.04% for the intact condition.

Identification using a different strategy to pair conditions

The analyses using a different strategy to pair conditions for identification yielded a similar picture as the main analyses. The SR in identifying individuals between the rest and intact conditions was the lowest (70.37%), which increased to 84.26% between the backward and intact conditions. It then dropped slightly to 83.3% between the sentence-scrambled and the intact conditions and rose to 100% between the two sessions of the intact condition. We note that the overall SRs were higher than those of the main analyses, likely due to the use of more data points to compute the FCs.

Discussion

Establishing the link between individual differences in the brain with the differences in cognition, behavior, and dysfunctions is a major goal of cognitive neuroscience. To fulfill this goal, the neuroscientific community, which has been mainly focused on the generic patterns of brain activities shared across the population, is now moving forward to characterize brain patterns that are robust and unique to individuals. Existing studies have discovered a set of brain features that can be used to distinguish individuals from each other and may serve as "brain fingerprints." However, what is the information encoded in the brain that makes us unique remains elusive.

To understand the source of functional brain individualization, we explored the degree of individual identifiability along the language hierarchy. Subjects were scanned with fMRI during a resting state and when listening to backward-played, sentence-scrambled, and intact stories. For each task, the imaging data were collected from two scan sessions. Extracting the whole-brain FC profiles as features, we found that the individual identifiability tends to increase along the language hierarchy. The identification between the resting state and each of the task states achieved an average SR of 62.9% (the baseline). The mean SR across the two sessions for the backward condition (the low level) increased to 85.2%, which decreased slightly for the scrambled condition (83.3%) (the middle level), and then rose to 90.7% for the intact condition (the high level). This pattern was also observed when using the FCs of single networks (the language network and the frontoparietal network) to characterize individuals. In addition, we obtained a similar pattern by employing a different brain atlas to compute the brain connectome and by applying a different strategy of condition pairing for the identification.

Increased individual identifiability along the language hierarchy

Using whole-brain FCs as features, we identified individuals across the resting and task sessions with an average SR greater than 60%. This performance is close to the results of previous studies which examined the individual identifiability across resting states and a set of tasks involving emotion, motor, memory, and language processing (Finn et al., 2015; Kaufmann et al., 2017). Together with previous studies, our work suggests that the state-independent, intrinsic processes are the major contributor to brain fingerprints.

Compared to the baseline, the SR in identifying subjects under the backward condition (the low-level) improved significantly by about 22%. One possibility is that this improvement reflected the *direct* contribution of low-order acoustic processing to brain fingerprints. However, when looking into single functional networks, the auditory network only obtained an identification accuracy of 44% for this condition, which was the worst among the four networks. Instead, it was the DMN that showed the highest SR (74%) in identifying individuals under the backward condition. These results seem to argue against the possibility of a direct contribution, suggesting that the low-order auditory perceptual process *per se* may not provide critical information in characterizing individuals. Alternatively, we propose that the presence of audio streams may constrain the activities of the auditory network as well as other brain networks (especially

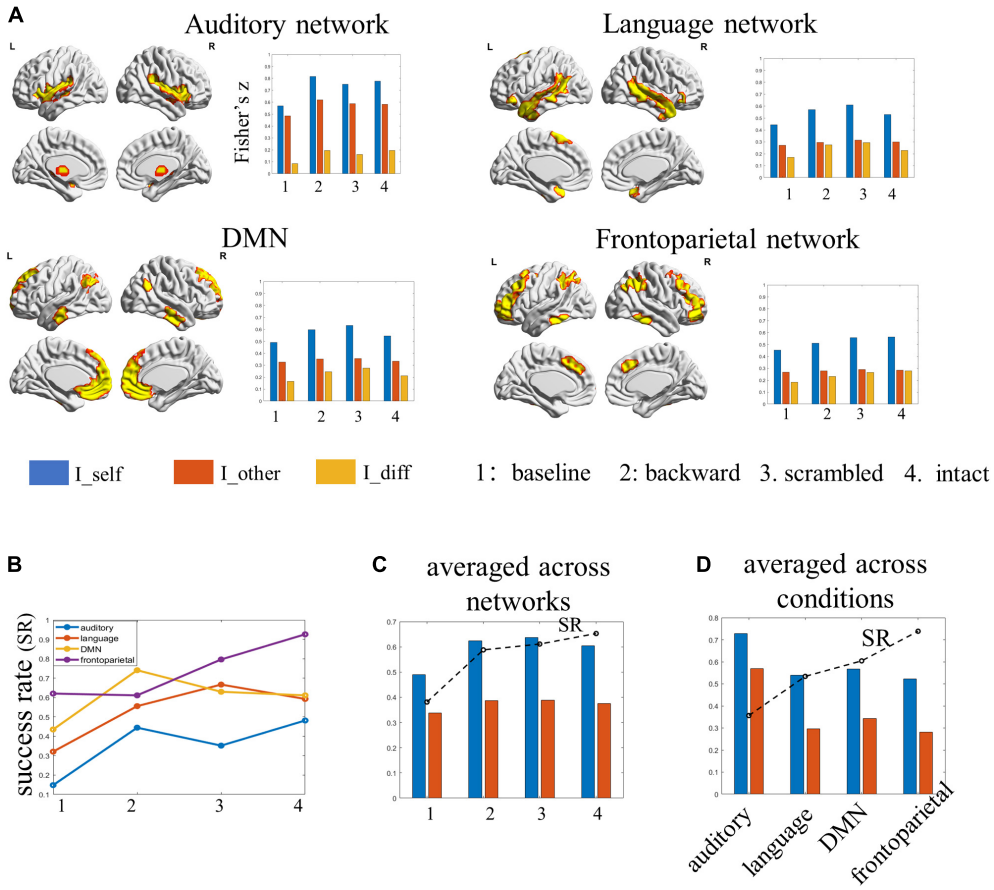

FIGURE 4
The results of individual identification based on single functional networks. **(A)** The spatial map of the selected functional networks and the individual identifiability, within- and between-subject similarity in the FC profiles of each network. **(B)** The success rate of each network in identifying individuals under each condition. **(C)** The success rate and the within- and between-subject similarity for each condition, averaged by networks. **(D)** The success rate and the within- and between-subject similarities for each network, averaged by conditions.

the DMN) as a whole, leading to a high degree of within-subject stability in brain connectivities across sessions (as can be seen in **Figures 4A,C**). This may explain the significant improvement in identifying individuals based on the whole-brain FCs.

Compared to the low-level condition, the SR in identifying individuals under the sentence-scrambled condition (the middle level) based on whole-brain FCs decreased slightly by about 2%. However, when taking the FCs of single functional networks as features, both the language network and the frontoparietal network performed better in identifying individuals under the scrambled condition than that under the backward condition. This pattern was also found in the averaged performance across the four networks. The increase in identifiability was accompanied by the increase in within-subject stability and a slight drop in inter-subject variability. These results suggest that, compared to listening to the meaningless backward-played story, comprehending sentences may help to blur irrelevant features (background noises), therefore enhancing those key individual features meanwhile making subjects' FCs more similar to one another.

The greatest SR was obtained for the identification of individual subjects under the intact condition (the high level). Compared to the other two task conditions, there was greater inter-subject variability and slightly lower within-subject stability in brain FCs under the intact condition. The increased individual identifiability may be related to the fact that comprehending stories requires the integration of information over a longer time scale than did the two lower-level tasks. This is consistent with previous findings that the best identification emerges at longer time scales (Van De Ville et al., 2021).

The differences among networks in distinguishing individuals

Among the four networks, the auditory networks consistently showed the lowest SR in discriminating subjects

under all four conditions. Further analyses revealed that, while the within-subject FC similarity was the greatest, the inter-subject FC variability was the least in the auditory network among the four networks. The low inter-subject variability (or high inter-subject similarity) in the auditory network across the language hierarchy is consistent with previous findings (Lerner et al., 2011), which likely explains the comparatively poor performance of this network in distinguishing individuals.

The condition-averaged SR derived from the language network was higher than that derived from the auditory network but lower than that derived from the DMN. In comparison with the auditory network, both the language network and the DMN were characterized by greater inter-subject variability but lower within-subject stability.

The frontoparietal network consistently showed the best performance in identification under all conditions except for the backward condition. Under the intact condition, identification using the FCs of the frontoparietal network alone performed even better than that using the whole-brain FCs. Moreover, similar to the whole-brain FC profiles, the SR obtained using the FC profiles of the frontoparietal network also increased along the language hierarchy. Still, this increase was accompanied by the increase in inter-subject variability rather than within-subject stability of FCs. These findings are consistent with previous reports about a high degree of individualization (Finn et al., 2015; Amico and Goni, 2018; Horien et al., 2019) and inter-subject variability in the frontoparietal network (Mueller et al., 2013). Our study extends previous work by suggesting that the special role of the frontoparietal network in individual identification is likely owing to its function rather than its anatomical features.

Limitations and implications

One limitation of the current study is the small sample of subjects and the short data length used to compute the FC. Despite that we have validated the main results with the analysis using a different data length (32 versus 64 time points), future studies based on a larger sample size are required to replicate our findings and evaluate the effect of data length (stimuli duration). Besides, all the subjects recruited in this study are females. Whether the results can be extended to males remains to be tested. Finally, while we observed that the more complex cognitive task and the network associated with higher-level cognitive functions tended to better distinguish individuals, most of the changes in identification accuracy did not reach statistical significance. Although this trend was reproducible across the analyses with different brain atlas and different strategies of condition pair, more work is needed to establish that this trend is meaningful rather than arbitrary.

Despite the above limitations, the current study may provide useful implications for future research. First, we demonstrated that, during the high-order story comprehension task, the brain functional connectivities are quite different across subjects but stable enough across time within the same subjects. Meanwhile, on the low-order perceptual task, the brain connectivities were quite stable across time and similar across individuals. These results imply that, for low-order functions, conclusions about the brain obtained from a relatively small pool of subjects can be generalized to larger groups. However, for high-order functions, averaged brain patterns obtained from a small sample may not well represent the general principles of brain function. However, if properly exploited, individual differences in brain activities on high-order tasks can provide useful information that is beyond what can be captured by those group-mean focused approaches (Liu et al., 2020).

Second, in line with previous work (Mueller et al., 2013; Finn et al., 2015; Amico and Goni, 2018), this study highlights the special role of the frontoparietal network in characterizing individuals. In addition, we found that the individual distinguishing ability of the frontoparietal network increased with the complexity of tasks. Based on these findings, we speculate that executive processes, which are the typical function of the frontoparietal network and demands for it usually increase with the complexity of tasks, might be the core factor underlying inter-individual differences in the brain and behavior. Future studies aiming to manipulate brain states to maximize individual differences may give priority to tasks involving executive processes.

Conclusion

This study demonstrated that individual identifiability tended to increase along the language hierarchy: the more complex the task was, the better subjects were distinguished from each other based on their functional brain data. A similar principle was also found at the functional network level: compared to the low-order network (the auditory network), the high-order network was more individualized (the DMN and frontoparietal networks). Moreover, in both cases, the increase in individual identifiability was accompanied by the increase in inter-subject variability of the FC profiles. The two folds of results together suggest that, compared to the low-order functions, the high-order functions of the brain are more important in making us unique. At the same time, task-independent neural processes seem to contribute more than task-evoked neural processes to brain individualization. What is exactly encoded in the task-independent brain activities and its function in cognition and behavior remain an open question.

Data availability statement

The data that supports the findings of this study are available from the corresponding authors, upon reasonable request.

Ethics statement

The studies involving human participants were reviewed and approved by Beijing Normal University. The patients/participants provided their written informed consent to participate in this study.

Author contributions

JZ: conceptualization, investigation, methodology, and writing. LZ: conceptualization, methodology, and writing. JJ: writing—review and editing. MY, SL, and XT: investigation and project administration. YM: writing—review and editing. LL and GD: conceptualization, methodology, writing—review and editing, and supervision. All authors contributed to the article and approved the submitted version.

Funding

This work was supported by grants from the National Natural Science Foundation of China (NSFC: 31971036, 31900802, and 31971039).

Conflict of interest

The authors declare that the research was conducted in the absence of any commercial or financial relationships that could be construed as a potential conflict of interest.

Publisher's note

All claims expressed in this article are solely those of the authors and do not necessarily represent those of their affiliated organizations, or those of the publisher, the editors and the reviewers. Any product that may be evaluated in this article, or claim that may be made by its manufacturer, is not guaranteed or endorsed by the publisher.

Supplementary material

The Supplementary Material for this article can be found online at: https://www.frontiersin.org/articles/10.3389/fnhum.2022.982905/full#supplementary-material

References

Amico, E., and Goni, J. (2018). The quest for identifiability in human functional connectomes. *Sci. Rep.* 8:8254. doi: 10.1038/s41598-018-25089-1

Barnett, A. J., Reilly, W., Dimsdale-Zucker, H. R., Mizrak, E., Reagh, Z., and Ranganath, C. (2021). Intrinsic connectivity reveals functionally distinct cortico-hippocampal networks in the human brain. *PLoS Biol.* 19:e3001275. doi: 10.1371/journal.pbio.3001275

Behzadi, Y., Restom, K., Liau, J., and Liu, T. T. (2007). A component based noise correction method (CompCor) for BOLD and perfusion based fMRI. *Neuroimage* 37, 90–101. doi: 10.1016/j.neuroimage.2007.04.042

Binder, J. R. (2012). Task-induced deactivation and the "resting" state. *Neuroimage* 62, 1086–1091. doi: 10.1016/j.neuroimage.2011.09.026

Cai, B., Zhang, G., Zhang, A., Xiao, L., Hu, W., Stephen, J. M., et al. (2021). Functional connectome fingerprinting: identifying individuals and predicting cognitive functions via autoencoder. *Hum. Brain. Mapp.* 42, 2691–2705. doi: 10.1002/hbm.25394

Chen, S., and Hu, X. (2018). Individual identification using the functional brain fingerprint detected by the recurrent neural network. *Brain Connect.* 8, 197–204. doi: 10.1089/brain.2017.0561

Finn, E. S., Shen, X., Scheinost, D., Rosenberg, M. D., Huang, J., Chun, M. M., et al. (2015). Functional connectome fingerprinting: identifying individuals using patterns of brain connectivity. *Nat. Neurosci.* 18, 1664–1671. doi: 10.1038/nn.4135

Friston, K. J., Williams, S., Howard, R., Frackowiak, R. S., and Turner, R. (1996). Movement-related effects in fMRI time-series. *Magn. Reson. Med.* 35, 346–355. doi: 10.1002/mrm.1910350312

Horien, C., Shen, X., Scheinost, D., and Constable, R. T. (2019). The individual functional connectome is unique and stable over months to years. *Neuroimage* 189, 676–687. doi: 10.1016/j.neuroimage.2019.02.002

Ji, J. L., Spronk, M., Kulkarni, K., Repovs, G., Anticevic, A., and Cole, M. W. (2019). Mapping the human brain's cortical-subcortical functional network organization. *Neuroimage* 185, 35–57. doi: 10.1016/j.neuroimage.2018.10.006

Kaufmann, T., Alnaes, D., Doan, N. T., Brandt, C. L., Andreassen, O. A., and Westlye, L. T. (2017). Delayed stabilization and individualization in connectome development are related to psychiatric disorders. *Nat. Neurosci.* 20, 513–515. doi: 10.1038/nn.4511

Lacadie, C. M., Fulbright, R. K., Rajeevan, N., Constable, R. T., and Papademetris, X. (2008). More accurate Talairach coordinates for neuroimaging using non-linear registration. *Neuroimage* 42, 717–725. doi: 10.1016/j.neuroimage.2008.04.240

Lerner, Y., Honey, C. J., Silbert, L. J., and Hasson, U. (2011). Topographic mapping of a hierarchy of temporal receptive windows using a narrated story. *J. Neurosci.* 31, 2906–2915. doi: 10.1523/jneurosci.3684-10.2011

Liu, J., Liao, X., Xia, M., and He, Y. (2018). Chronnectome fingerprinting: identifying individuals and predicting higher cognitive functions using dynamic brain connectivity patterns. *Hum. Brain Mapp.* 39, 902–915. doi: 10.1002/hbm.23890

Liu, L., Yan, X., Li, H., Gao, D., and Ding, G. (2020). Identifying a supramodal language network in human brain with individual fingerprint. *Neuroimage* 220:117131. doi: 10.1016/j.neuroimage.2020.117131

Luo, W., and Constable, R. T. (2022). Inside information: systematic within-node functional connectivity changes observed across tasks or groups. *Neuroimage* 247:118792. doi: 10.1016/j.neuroimage.2021.118792

Mueller, S., Wang, D., Fox, M. D., Yeo, B. T., Sepulcre, J., Sabuncu, M. R., et al. (2013). Individual variability in functional connectivity architecture of the human brain. *Neuron* 77, 586–595. doi: 10.1016/j.neuron.2012.12.028

Price, C. J. (2010). The anatomy of language: a review of 100 fMRI studies published in 2009. *Ann. N. Y. Acad. Sci.* 1191, 62–88. doi: 10.1111/j.1749-6632.2010.05444.x

Salehi, M., Greene, A. S., Karbasi, A., Shen, X., Scheinost, D., and Constable, R. T. (2020). There is no single functional atlas even for a single individual: functional parcel definitions change with task. *Neuroimage* 208:116366. doi: 10.1016/j.neuroimage.2019.116366

Sareen, E., Zahar, S., Ville, D. V., Gupta, A., Griffa, A., and Amico, E. (2021). Exploring MEG brain fingerprints: evaluation, pitfalls, and interpretations. *Neuroimage* 240:118331. doi: 10.1016/j.neuroimage.2021.118331

Schaefer, A., Kong, R., Gordon, E. M., Laumann, T. O., Zuo, X. N., Holmes, A. J., et al. (2018). Local-global parcellation of the human cerebral cortex from intrinsic functional connectivity MRI. *Cereb. Cortex* 28, 3095–3114. doi: 10.1093/cercor/bhx179

Shen, X., Tokoglu, F., Papademetris, X., and Constable, R. T. (2013). Groupwise whole-brain parcellation from resting-state fMRI data for network node identification. *Neuroimage* 82, 403–415. doi: 10.1016/j.neuroimage.2013.05.081

Van De Ville, D., Farouj, Y., Preti, M. G., Liegeois, R., and Amico, E. (2021). When makes you unique: temporality of the human brain fingerprint. *Sci. Adv.* 7:eabj0751. doi: 10.1126/sciadv.abj0751

Yan, C., and Zang, Y. (2010). DPARSF: a MATLAB Toolbox for "Pipeline" data analysis of resting-state fMRI. *Front. Syst. Neurosci.* 4:13. doi: 10.3389/fnsys.2010.00013

Yeo, B. T., Krienen, F. M., Sepulcre, J., Sabuncu, M. R., Lashkari, D., Hollinshead, M., et al. (2011). The organization of the human cerebral cortex estimated by intrinsic functional connectivity. *J. Neurophysiol.* 106, 1125–1165. doi: 10.1152/jn.00338.2011

Yeshurun, Y., Nguyen, M., and Hasson, U. (2021). The default mode network: where the idiosyncratic self meets the shared social world. *Nat. Rev. Neurosci.* 22, 181–192. doi: 10.1038/s41583-020-00420-w

frontiers | Frontiers in Human Neuroscience

TYPE Original Research
PUBLISHED 17 November 2022
DOI 10.3389/fnhum.2022.972375

OPEN ACCESS

EDITED BY
Stephen José Hanson,
Rutgers, The State University
of New Jersey, United States

REVIEWED BY
Juan Chen,
South China Normal University, China
Wen Li,
Florida State University, United States
Jie Zhang,
Fudan University, China

*CORRESPONDENCE
Yiying Song
songyiying@bnu.edu.cn

SPECIALTY SECTION
This article was submitted to
Cognitive Neuroscience,
a section of the journal
Frontiers in Human Neuroscience

RECEIVED 18 June 2022
ACCEPTED 04 November 2022
PUBLISHED 17 November 2022

CITATION
Hao X, Chen Z, Huang T, Song Y,
Kong X and Liu J (2022) Dissociation
of categorical and coordinate spatial
relations on dynamic network
organization states.
Front. Hum. Neurosci. 16:972375.
doi: 10.3389/fnhum.2022.972375

Dissociation of categorical and coordinate spatial relations on dynamic network organization states

Xin Hao[1,2], Zhencai Chen[3], Taicheng Huang[4], Yiying Song[5]*, Xiangzhen Kong[6] and Jia Liu[4]

[1]Key Laboratory of Adolescent Cyberpsychology and Behavior (CCNU), Ministry of Education, Wuhan, China, [2]School of Psychology, Central China Normal University, Wuhan, China, [3]Department of Psychology, Jiangxi University of Chinese Medicine, Nanchang, China, [4]Department of Psychology, Tsinghua University, Beijing, China, [5]Beijing Key Laboratory of Applied Experimental Psychology, Faculty of Psychology, Beijing Normal University, Beijing, China, [6]Department of Psychology and Behavioral Sciences, Zhejiang University, Hangzhou, China

Humans can flexibly represent both categorical and coordinate spatial relations. Previous research has mainly focused on hemisphere lateralization in representing these two types of spatial relations, but little is known about how distinct network organization states support representations of the two. Here we used dynamic resting-state functional connectivity (FC) to explore this question. To do this, we separated a meta-identified navigation network into a ventral and two other subnetworks. We revealed a Weak State and a Strong State within the ventral subnetwork and a Negative State and a Positive State between the ventral and other subnetworks. Further, we found the Weak State (i.e., weak but positive FC) within the ventral subnetwork was related to the ability of categorical relation recognition, suggesting that the representation of categorical spatial relations was related to weak integration among focal regions in the navigation network. In contrast, the Negative State (i.e., negative FC) between the ventral and other subnetworks was associated with the ability of coordinate relation processing, suggesting that the representation of coordinate spatial relations may require competitive interactions among widely distributed regions. In sum, our study provides the first empirical evidence revealing different focal and distributed organizations of the navigation network in representing different types of spatial information.

KEYWORDS

categorical spatial relation, coordinate spatial relations, network organization, functional connectivity, dynamics

Introduction

Understanding spatial relations is hard for artificial intelligence, but easy for human being. Spatial relationships are critical to the formation of cognitive maps in navigation. We can use flexible representations to encode spatial relations either categorically, such that concerns the spatial layout formed by relative positions of objects (e.g., a house located in the left of the oak); or as coordinates, such that refers to the spatial locations in terms of metric units (e.g., a house located 2.5 m from the oak) (Kosslyn, 1987). The categorical spatial relationships capture abstract or general relations among object, such as "under"; by contrast, the coordinate spatial relationships reflect the exact metric or precise distance between objects. As evidenced in other domains, such as number (Feigenson et al., 2004; Pica et al., 2004) and color (Kay and Regier, 2003), there are profound distinctions between categorical and coordinate representations (Holden et al., 2010). Do the representations of categorical and coordinate spatial relations have distinct underlying neural substrates? Large majority of relevant neuroimaging studies concentrated on discovering the hemispheric lateralization dissociation between the two types of spatial relation representations in the prefrontal or parietal cortex, which based on making very basic task designs by using lines, crosses, or dots (Kosslyn et al., 1989; Trojano et al., 2002; Slotnick and Moo, 2006; van der Ham et al., 2009, 2013). However, a fundamental question remaining unclear is how distinct neural substrates in the large-scale navigational system underpinned the categorical and coordinate spatial relations.

Until now less attention has been paid to direct comparison between categorical and coordinate spatial relations representation under navigational system, and mix results are reported. The only known studies identify greater activation in the parietal cortex in the categorical condition, and higher activation in the medial temporal lobe (MTL) and dorsal striatum in the coordinate condition during spatial navigation (Baumann et al., 2012; Baumann and Mattingley, 2014); however, another study finds that the anterior temporal gyrus processes the categorical spatial information, and the left angular and inferior frontal gyrus processes more coordinate spatial information (Amorapanth et al., 2010). Importantly, neuropsychological studies provide some insight about some brain regions are conjointly and others distinctly recruited in the categorical and coordinate spatial relations. Within the scope of categorical/coordinate distinction, these shared and distinct activation regions mainly restrict to a small number of navigation-related regions of interest. On the one hand, the MTL has been found to play a central role in representing both categorical and coordinate spatial relations. For categorical spatial relations, patients with hippocampal damage are impaired in recognizing the relative relations among mountains (Hartley et al., 2007; Urgolites et al., 2017), and bilateral posterior hippocampus (HIP) are activated more highly for correct than incorrect recognition of ordinal location relations (Hannula and Ranganath, 2008). In addition, a recent study demonstrates greater activation in the left parahippocampal gyrus and retrosplenial cortex for processing of spatial relations than locations (Blacker and Courtney, 2016). Similarly, for coordinate spatial relations, the activation in either anterior or posterior HIP has been found correlated with the Euclidean distance (Evensmoen et al., 2013; Sherrill et al., 2013; Howard et al., 2014) path distance (Howard et al., 2014) and environment size (Baumann and Mattingley, 2013), and closer locations/items have higher neural pattern similarity in the HIP (Nielson et al., 2015; Deuker et al., 2016). On the other hand, compared with categorical spatial relations, more distributed regions beyond the MTL have been demonstrated to represent the coordinate spatial relations. For example, the medial prefrontal and medial posterior parietal regions show increased activation with closer distance to the goal (Spiers and Maguire, 2007; Viard et al., 2011), and the PCUN, insula, and anterior cingulate cortex show higher activation with further distance to the goal (Viard et al., 2011). In addition, distance-related adaptation effect is observed in the left inferior insula, anterior superior temporal sulcus, and right inferior temporal sulcus (Morgan et al., 2011). Taken together, existing evidence seems to suggest that the representation of categorical spatial relations mainly converges on the MTL, while the representation of coordinate spatial relations may also involve other spatial-related regions beyond the MTL (Ekstrom and Yonelinas, 2020).

Notably, it is increasingly recognized that different functions of the MTL may arise from its distinct intrinsic connectivity profiles with diverse cortical regions (Mahon and Caramazza, 2011; Sormaz et al., 2017). Yet, limited studies investigated the neural differences based on the intrinsic functional connectivity (FC) nature of the spatial relations. One suggestive study shows higher resting-state FC between the HIP and lingual gyrus is related to better ordinal relations memory (Sormaz et al., 2017). However, it remains unclear how different intrinsic connectivity patterns among the MTL and other spatial-related regions support representations of categorical and coordinate spatial relations in spatial navigation, respectively. Based on previous findings, we hypothesize that (1) the representation of categorical spatial relations would be mainly related to interactions within the MTL regions and (2) the representation of coordinate spatial relations would be related to more distributed interactions among navigation-related regions.

To test these two hypotheses, we used the meta-identified navigation network across the brain with the Neurosynth (Yarkoni et al., 2011), and decomposed it into a ventral subnetwork containing the MTL and other two subnetworks with a modularity analysis (Hao et al., 2016; Kong et al., 2016). Then, we characterized the intrinsic FC within the ventral subnetwork and that between the ventral and other subnetworks. Recent studies adopting dynamic FC approach

have unveiled the time-varying nature of resting-state FC, indicating some degree of multi-stability for dynamic FC with multiple typical network states recurring during resting-state (Hutchison et al., 2013; Allen et al., 2014). The recurring FC states may manifest endogenous neural dynamics that are believed to underlie the flexibility of cognition and behavior, with different FC states relating to different cognitive functions (Shine et al., 2016). That is, representation of categorical and coordinate spatial relations may be associated with different dynamic FC states of the navigation network. Therefore, we calculated the FC matrices of all sliding time windows during resting-state and clustered them into typical dynamic FC states within the ventral subnetwork and between the ventral and other subnetworks, respectively. After MRI scanning, we used an ordinal scene recognition task to measure representation of categorical spatial relations, and distance test to measure representation of coordinate spatial relations. Finally, we correlated properties of the typical dynamic FC states with behavioral performances in the two tasks to examine whether and how distinct dynamic network states were associated with representations of categorical and coordinate spatial relations.

Materials and methods

Participants

Two hundred and twenty-six students (age range: 19–24; mean age = 21.66, *SD* = 1.00 years, 108 males) were recruited from Beijing Normal University, Beijing, China to participate in this study. This sample size is comparable with previous work (Wang et al., 2016; Hao et al., 2021) and exceeds prior fMRI studies in most cases. None of the participants reported a history of neurological or psychiatric disorders. This study is part of an ongoing project (Gene Environment Brain and Behavior) (Kong et al., 2017; Zhen et al., 2017). All experiments were in accordance with the ethical standards of the Institutional Review Board of Beijing Normal University and written informed consent was obtained from each participant before the experiment. One participant was excluded due to more than 0.2 mm in mean framewise displacements of the head motion.

Behavior tasks

The behavior tasks were tested outside of the MRI scanner in a separate behavioral session, after the participants underwent MRI scanning.

Assessment of categorical spatial relations

We assessed the participants' ability to represent categorical spatial relations with an ordinal scene recognition task adapted from Hartley et al. (2007). The stimuli were all computer-generated landscapes, with four mountains varying in shape and size surrounded by a distant semicircular mountain range (**Figure 1**). There were 20 trials which were randomly mixed in the task. In the study phase of each trial, participants were required to study an image at the center of the screen for 2 s. Then after a delay of 2 s with fixation, two images from a novel viewpoint were presented in the test phase, including one target image which preserved all topographic information from the study image and one non-target image with the locations of two mountains exchanged with each other. The location of the target image on the left or right was randomized. The participants were asked to identify the target image as quickly and accurately as possible, by pressing "F" when the target image was on the left and "J" when the target image was on the right. Critically, the categorical spatial position among the

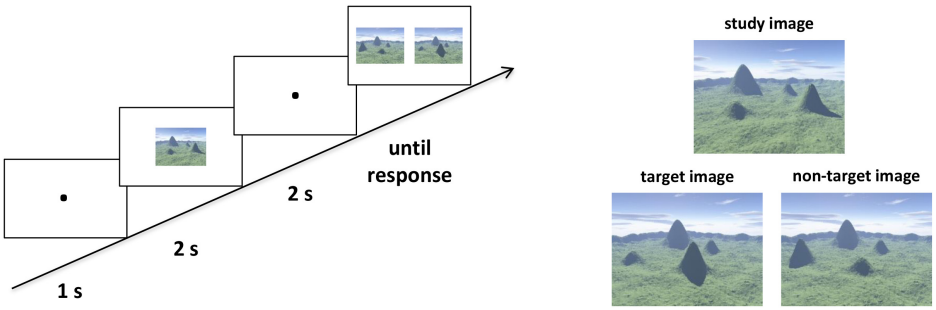

FIGURE 1
The ordinal scene recognition task to assess categorical spatial relations. **Left panel:** Example of a single trial. The participants were asked to identify the target image as quickly and accurately as possible in the test phase. **Right panel:** Examples of the study and test images. Two images were presented in the test phase, one of which was the target image and the other was the non-target image. The target image preserved all ordinal information from the study image but with a novel viewpoint. For the non-target image, the locations of two mountains were exchanged to the study image.

four mountains extracted from the study images, which were interrupted in the non-target images. Then, we averaged the reaction times (RTs) of the correct trials for each participant. For visualization and enhancing readability, we converted these RTs into speed values using the classic formula: $speed_i$ = (Max–RT_i)/(Max–Min), where *i* refer to each participant, and Max and Min correspond to the maximum and minimum RT across all participants (Hao et al., 2017). The speed values were used as the ordinal scene recognition scores.

Assessment of coordinate spatial relations

According to the Lopez et al. (2020), we assessed the ability to represent coordinate spatial relations with the distance test. For the most noticeable way to assess the mentally represented distances is to compare the landmarks with each other (Lopez et al., 2020). The participant was presented with two well-known landmarks (i.e., buildings or statues) in the Beijing Normal University campus and required to choose the one closer to the building where the experiment was conducted (i.e., the starting point). It's reasonable that coordinate judgments were made when representing distances metrically. Specifically, we used two surveys, which measured both the optimal path distance and straight-line Euclidean distance. For the optimal path distance survey, the participant was asked to select the optimal routes and avoid dead ends to assess the distances between the starting point and the landmarks; while in the Euclidean distance survey, the participant was asked to estimate the straight-line distances between the starting point and the landmarks. Each survey contained nine items, including eighteen prominent landmarks. Before the formal test, participants were provided with two practice items to familiarize with the task and were given feedback on each item. No feedback was provided in the formal test. We averaged the number of correct items of the path distance and Euclidean distance surveys as the distance score for each participant.

All participants had lived in the campus for more than 2 years at the time of the test. To ensure that all participants were familiar with the landmarks, they underwent a familiarity testing, in which they rated their degree of familiarity with each landmark on a scale ranging from one "very unfamiliar" to seven "very familiar." The high mean score (6.10 $\pm$ 0.70) indicates relatively very familiar to all landmarks for each participant.

Image acquisition and preprocessing

MRI scanning was conducted on a Siemens 3T scanner (MAGENTOM Trio, a Tim system) with a 12-channel phased-array head coil at Beijing Normal University Imaging Center for Brain Research, Beijing, China. T2*-weighted functional images in resting state were acquired using a gradient-echo, echo-planar imaging (EPI) sequence (TR = 2 s, TE = 30 ms, FA = 90°, number of slices = 33, voxel size = 3.125 mm × 3.125 mm × 3.6 mm, number of volumes = 240). During resting state scans, the participants were instructed to close their eyes, keep still, remain awake, and not think about anything systematically. Of note, each participant was asked whether he/she had fallen asleep during the scanning when the scan was finished. Those who reported having fallen asleep were required to rescan the resting-state imaging. In addition, high-resolution T1-weighted structure images were acquired using a magnetization-prepared rapid gradient-echo (MPRAGE) sequence (TR/TE/TI = 2,530/3.39/1,100 ms, FA = 7°, matrix = 256 × 256, voxel size = 1 mm × 1 mm × 1.33 mm, number of volumes = 128) for each participant.

For each participant, image preprocessing was conducted using FSL (FMRIB software Library[1]). Steps included the removal of the first four volumes for image stabilization, head motion correction (by aligning each volume to the middle volume of the image with MCFLIRT), spatial smoothing (with a Gaussian kernel of 6 mm full-width at half-maximum), grand-mean intensity normalization, and the removal of linear trend. Next, a band-pass temporal filter (0.01–0.1 Hz) was applied to reduce low-frequency drifts and high-frequency noise. Then, the physiological noise (such as cardiac and respiratory cycles), and nuisance signals from the white matter, global gray matter average, cerebrospinal fluid, six head motion correction parameters, and first derivatives of these signals were regressed out (Fox et al., 2005; Biswal et al., 2010). The residual time series obtained were registered to the MNI standard space with using FLIRT and then used for the dynamic FC analyses. The strength of the intrinsic FC between two regions was estimated using the Pearson's correlation coefficients of the residual rs-fMRI time series.

Functional organization of the navigation network

Considering the complexity of navigation system, we used a meta-analysis approach named Neurosynth (Yarkoni et al., 2011), to identify 23 highly navigation-relevant regions involving in navigation (Hao et al., 2021). After the preprocessing, we first computed the Fisher *z*-transformed Pearson correlation coefficients between the residual time series of each pair of the defined regions for each participant. To detect how interconnected regions formed functionally module structure in the navigation network, we conducted a modularity analysis on the averaged correlation matrix across participants. Specifically, we used the community Louvain algorithm in

1 http://www.fmrib.ox.ac.uk/fsl

the brain connectivity toolbox (version 2017-01-15, Rubinov and Sporns, 2010). For the Louvain algorithm, we choose the default resolution parameter gamma = 1 and executed it in the MATLAB. Considering the conceptual advantages of unequal importance of positive and negative weights, we adopted an asymmetric modularity measure to avoid biased thresholding of the networks. Then, we ran the algorithm 1,000 times and obtained the auto-generated optimal community structure with a module partition number of three. Further spatial examination found that one of the modules contained most of well-established navigational specific regions in the MTL (e.g., the hippocampal formation and retrosplenial complex) (Ekstrom et al., 2017; Qiu et al., 2019), which was labeled as the ventral subnetwork. The other two modules contained a set of general cognitive regions in frontal and parietal cortex (e.g., the inferior parietal lobe and middle frontal gyrus).

Dynamic functional connectivity state clustering and statistics

We characterized the dynamic FC by using sliding time-window correlation among the identified regions in navigation network. For each participant we constructed a tapered window by convolving a rectangular window (width = 50 s/25 TRs) in steps of 1 TR, which resulting in 212 windows during rs-fMRI scanning. We chose the typical window size between 30 and 60 s, which was found to well balance the susceptibility to spurious fluctuations for short window lengths and categorical insensitivity to variability for long window lengths in empirical studies (Allen et al., 2014; Leonardi and Van De Ville, 2015; Zalesky and Breakspear, 2015). Following previous classic work, tapering window shape was suggested to better suppress spurious correlations and reduce sensitivity to outliers in categorically short time segments. The weighted Pearson correlation was adopted to calculate the FC for reducing the noise induced by the limited number of data points available in each time window (Zalesky et al., 2014). To estimate the dynamic FC within ventral subnetwork (dWNC), we computed the correlations between each pair of regions within the ventral subnetwork for each time window. Similarly, to characterize the dynamic FC between ventral and other subnetworks (dBNC), we extracted the correlations between each region in the ventral subnetwork and each region in the other subnetworks. Finally, all time windows were concatenated across all participants, resulting in 47700 (212 × 225) FC windows for dWNC and dBNC, respectively.

To detect the representative FC patterns for the dWNC, we applied the *k*-means clustering method on the concatenated FC matrix consisting of all participants' time windows (Lloyd, 1982; Allen et al., 2014; Nomi et al., 2016). Following previous work in dynamics, the *k*-means algorithm was evaluated across values of *k* ranging from 2 to 10 using the silhouette metric, which measures how similar a FC window is to its own cluster compared to other clusters (Hutchison and Morton, 2015). The *k*-means clustering was repeated for 500 times with random initialization of centroid positions and produced the highest silhouette score with the value of $k = 2$. As a result, each time window for dWNC was assigned to one of the two typical dynamic FC states (clusters) for further analyses. Further, we calculated the frequency (i.e., the proportion of all 212 windows assigned to a particular state) and mean duration (i.e., the average number of consecutive windows assigned to a particular state) to describe each typical dynamic FC state. Likewise, we clustered the time windows for dBNC across all participants into two typical FC states and described their frequencies and mean durations in the same way.

Behavioral correlation with dynamic functional connectivity states

The most essential nature of these typical dynamic states is their FC strength. Thus, we calculated the mean FC strength of each typical dynamic FC state for each participant, which was the averaged FC value for all windows assigned to a particular state. First, to examine how dynamic organization within the ventral subnetwork was related to representations of categorical and coordinate spatial relations, we conducted partial correlation analyses between the mean FC strength of each typical dWNC FC state and scores in the ordinal scene recognition test and the distance test, respectively. The same correlation analyses were performed between the mean FC strength of each typical dBNC FC state and two behavioral scores to examine how dynamic interactions between subnetworks supported representations of the two types of spatial relations. Several confounding factors were controlled. First, age and gender were included as control variables. Second, the framewise displacement (FD; *mean* = 0.09, *SD* = 0.03) (Power et al., 2012) was included as a control variable for head motion. Third, the familiarity of all landmarks was added as a control variable when performing the correlation analyses regarding the distance test.

Results

In the present study, we used the Neurosynth-defined navigation network with 23 regions widely distributed in the medial temporal, parietal, and frontal cortex (Hao et al., 2021), which was aligned to another meta-analysis studies (Boccia et al., 2014, 2017; Ekstrom et al., 2017; Gona and Scarpazza, 2019). To refine the potential differences in navigation organization underlying between the representations of categorical and coordinate relations, we conducted a modularity analysis on the averaged FC matrix of the navigation network and obtained

an optimized structure of three modules (**Figure 2**), with a modularity index (Q) of 0.50, indicating a strong modular structure in the navigation network (Newman and Girvan, 2004). The three modules almost fit well with three distinct pathways in the dorsal visual stream that mainly targets to the MTL involved in navigation, and projects to the prefrontal and premotro cortex involved in spatial working memory and visually guided action, respectively (Kravitz et al., 2011). Most important, the ventral subnetwork included bilateral HIP, parahippocampus gyrus (PHG), retrosplenial complex (RSC), lingual gyrus (LING), fusiform gyrus (FFG), and the right middle occipital gyrus (MOG), which were well-known navigational regions reported in previous studies (Epstein and Kanwisher, 1998; Maguire et al., 1998; Spiers and Maguire, 2006; Epstein, 2008; Epstein et al., 2017). Other subnetworks were widely characterized in many cognitions with general function, including bilateral superior parietal gyrus (SPG), Inferior parietal lobe (IPL), precuneus (PCUN), the right angular gyrus (ANG), superior frontal gyrus (SFG), and left precentral gyrus (PreCG), middle frontal gyrus (MFG), supplementary motor area (SMA), and a third module including the left MOG. Further examination found that the left MOG module consisted of multiple clusters, including some inferior parietal lobule voxels, a few superior parietal lobule voxels in Juelich Histological atlas and some superior lateral occipital cortex (LOC) voxels in Harvard-Oxford cortical structural atlas.

Next, we explored the representative states for dWNC using a clustering method. Stable clustering of all concatenated dWNC FC matrices was obtained, showing the highest silhouette value when $k = 2$. The resulting two clustering FC matrices represented the centroids of all matrices assigned to each cluster and putatively reflected the two typical FC states within the ventral subnetwork. As shown in **Figure 3**, we found that the two FC states showed different FC strength among the ventral regions, that is, one state showed relative weak FCs (mean = 0.28; $SD = 0.051$; named as Weak State), while the other showed strong FCs (mean = 0.62; $SD = 0.05$; named as Strong State; Weak vs. Strong, $t_{224} = -101.65$, $p < 0.001$). Notably, both the Weak and Strong State showed FC strength significantly higher than 0 (Weak State: $t_{224} = 83.32$, $p < 0.001$; Strong State: $t_{224} = 185.94$, $p < 0.001$), indicating functional integration within ventral subnetwork. Then, the Weak State had a higher frequency than the Strong State (Weak State: 0.54, Strong State: 0.46; $t_{224} = 3.62$, $p < 0.001$). Finally, the Weak State showed longer mean duration (12.34 ± 6.51 windows) than the Strong State (10.05 ± 4.36 windows; $t_{224} = 3.85$, $p < 0.001$).

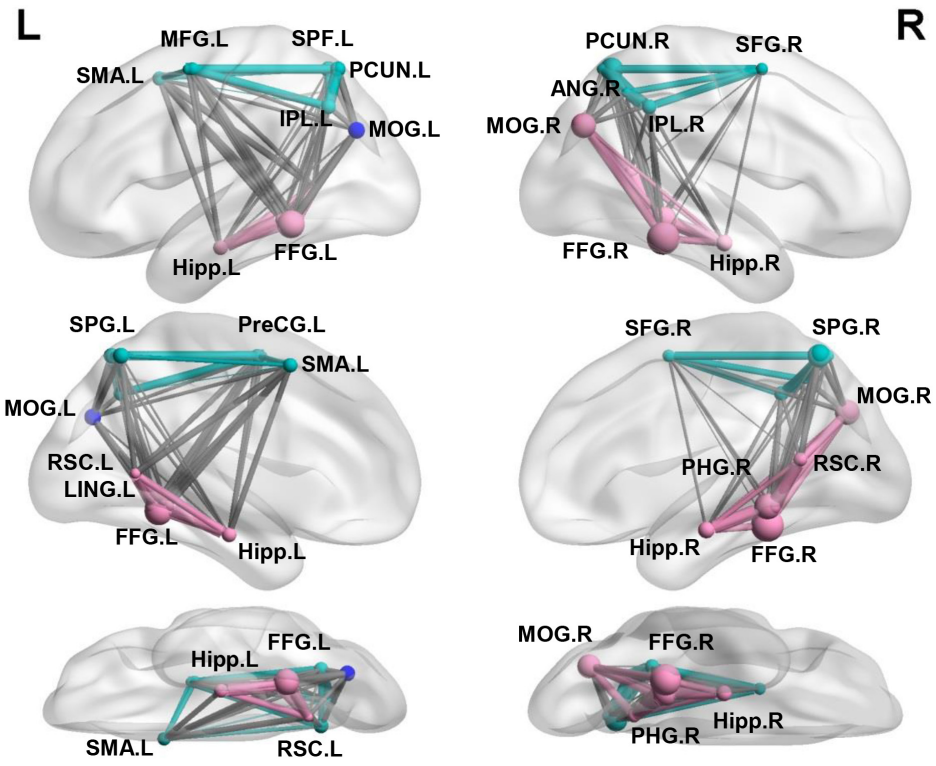

FIGURE 2
Separating the navigation network into the ventral and other two subnetworks. Three modules identified using modular analysis: ventral subnetwork (red) including most well-established regions for navigation and other two subnetworks (green and blue) including multiple regions in the dorsal parietal-frontal lobe.

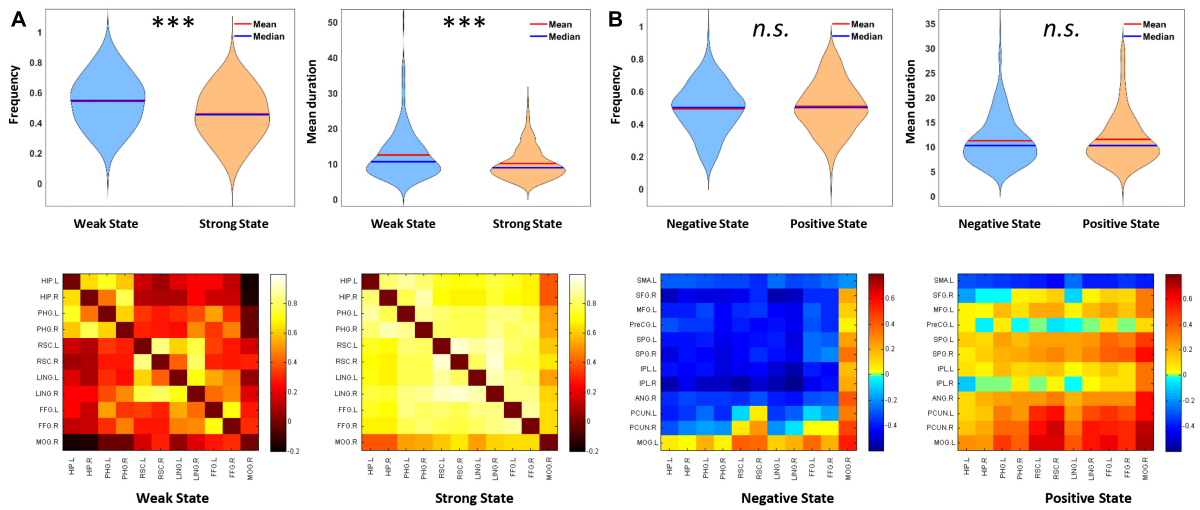

FIGURE 3
Properties of representative dynamic functional connectivity (FC) states within the ventral subnetwork (dWNC) and those between ventral and other subnetworks (dBNC). **(A)** Weak State and Strong State for dWNC. Weak State showed higher frequency, longer mean duration, and weaker FC strength than Strong State. **(B)** Negative State and Positive State for dBNC. The two states showed no difference in frequency or mean duration. Error bars indicate SEM. ***$p < 0.001$.

Similarly, we adopted clustering analysis and revealed two typical states for all concatenated dBNC matrices. Specifically, one state showed significantly negative FCs between the ventral and other subnetworks (mean = −0.18, $SD = 0.06$; $t_{224} = -48.48$, $p < 0.001$; named as Negative State), indicating competitive interactions between subnetworks. In contrast, another state showed significantly positive FC (mean = 0.13, $SD = 0.05$; $t_{224} = 36.47$, $p < 0.001$; named as Positive State), indicating cooperative interactions between subnetworks. Apparently, two typical states showed significantly different mean FC strengths ($t_{224} = -66.54$, $p < 0.001$). There is no significant difference between the Negative and Positive States in frequency (Negative State: 0.49, Strong State: 0.51; $t_{224} = -0.75$, $p = 0.45$) or mean duration (Negative State: 11.22 ± 4.86 windows, Positive State: 11.51 ± 5.12 windows; $t_{224} = -0.57$, $p = 0.57$).

After depicting these typical states, we then explore how the mean FC strength of each typical dynamic FC state associates with behavioral performance of categorical and coordinate spatial relations. The descriptive statistics of behavioral tests were summarized in Table 1. There was no correlation between the speed scores and distance scores ($r = -0.09$, $p = 0.20$). On the one hand, for the dWNC, we examined how Weak State or Strong State were relevant to individual differences in representation of categorical spatial relations. To do this, we assessed the participants' representation of categorical spatial relations by using an ordinal scene recognition task. We found the mean FC strength of the Weak State, not the Strong State, had a significant negative correlation with speed scores (0.71 ± 0.18), after controlling for age, gender, head motion (Weak State: $r = -0.19$, $p = 0.016$, Bonferroni correction; Strong State: $r = -0.05$, $p = 0.42$; Figure 4). These results suggested that weak integration among the ventral regions during resting-state was an optimal state for representation of categorical spatial relations. Next, we checked the association between dWNC FC states and participants' ability to represent coordinate spatial relations. We didn't find any correlations between distance scores and mean FC strength of the Weak State or Strong State (Weak State: $r = 0.02$, $p = 0.78$; Strong State: $r = 0.02$, $p = 0.76$). To sum up, these results confirm hypothesize 1, that is, representation of categorical spatial relations was related to weak dynamic integration within the ventral subnetwork.

On the other hand, we investigated whether the FC states of dBNC were associated with the representation of coordinate spatial relations. We found that the mean FC

TABLE 1 Demographic information and descriptive statistics of behavioral tests.

n		226
Sex (M/F)		108/118
Age		21.66 ± 1.00
Categorical spatial relations		
Ordinal scene recognition task	RT (s)	2.84 ± 1.077
	Speed	0.71 ± 0.183
	ACC	0.79 ± 0.136
Coordinate spatial relations		
Sense of distance score		5.28 ± 0.925
Path distance		6.19 ± 1.564
Euclidean distance		4.37 ± 2.139
Familiarity		6.10 ± 0.704

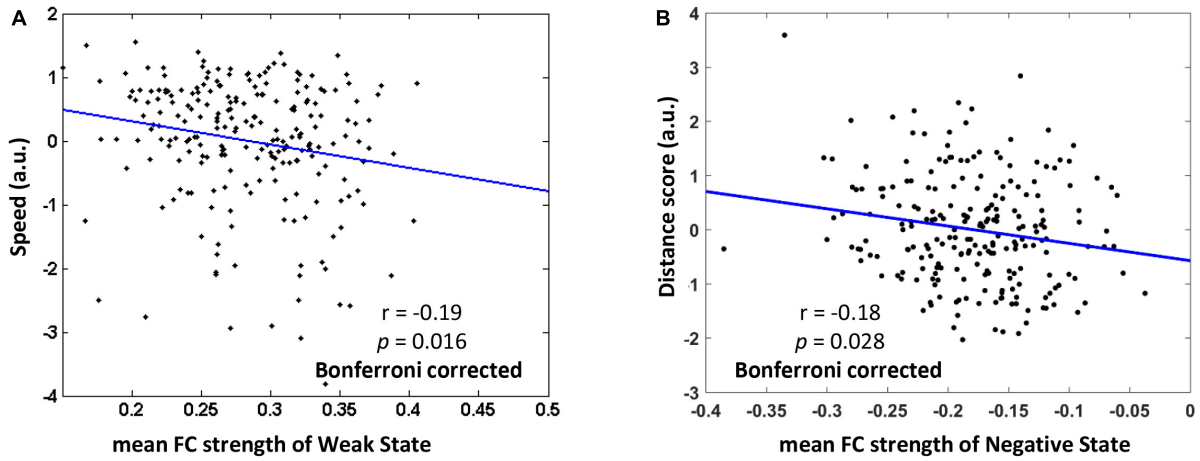

FIGURE 4
The relationship between mean functional connectivity (FC) strength of typical FC states and behavioral performance of representing categorial and coordinate spatial relations (Bonferroni correction). **(A)** Weaker mean FC of Weak State within the ventral subnetwork was related to higher speed in ordinal scene recognition based on representation of categorical spatial relations. **(B)** Stronger negative FC of Negative State between the ventral and other subnetworks was associated with higher distance scores based on representation of coordinate spatial relations. The speed score and distance score were standardized.

strength of the Negative State, rather than the Positive State, was negatively correlated with the distance scores (5.28 ± 0.93), after controlling for age, gender, head motion, familiarity with landmarks (Negative State: $r = -0.18$, $p = 0.028$, Bonferroni correction; Positive State: $r = -0.11$, $p = 0.11$). These results suggested that stronger competitive interaction between the ventral and other subnetworks during resting-state was an optimal state for representation of coordinate spatial relations. Further, we checked the relationship between dBNC states and the representation of categorical spatial relations. We didn't find the mean FC strength of the Negative State or Positive State had correlation with speed scores (Negative State: $r = 0.14$, $p = 0.16$; Positive State: $r = 0.06$, $p = 0.35$). In sum, these results confirmed hypothesize 2, that is, representation of coordinate spatial relations was related to dynamic interactions between the ventral and other subnetworks.

Discussion

In the current study, we investigated the dissociable dynamic FC states underlying the representations of categorical and coordinate spatial relations in the large-scale organization of navigation network. First, we separated the navigation network into a ventral subnetwork containing the MTL regions and other two subnetworks with a modularity analysis. Then, we identified the Weak State and Strong State for dynamic FC within the ventral subnetwork and found that the Weak State was related to the performance of ordinal scene recognition based on categorical relations, suggesting that the representation of categorical spatial relations was related to weak integration among focal regions within the ventral subnetwork. In contrast, we identified the Negative State and Positive State for dynamic FC between the ventral and other subnetworks and found that the Negative State was associated with the distance test scores assessing coordinate relations, suggesting that the representation of coordinate spatial relations may require competitive interactions among widely distributed regions between the ventral and dorsal subnetworks. Overall, our study provides the first empirical evidence at the network level revealing dissociation of focal and distributed organizations of the navigation network in representing different types of spatial information, which may illuminate the mechanisms for understanding scenes containing multiple objects.

Importantly, our study revealed dynamic organizations of the navigation network during resting-state. First, we revealed two opposite FC states for interactions between the ventral and other two subnetworks, a positive state and a negative state. Previous studies using static FC methods reported only positive connectivity between the ventral and dorsal networks. For instance, the RSC was functionally connected with widespread parieto-frontal regions including the posterior cingulate cortex, the PCUN, and SFG (Boccia et al., 2017). Intriguingly, for the first time we revealed that FCs between the ventral and other subnetworks alternated between a positive and a negative state, suggesting that cooperative interactions between subnetworks are accompanied by periods of competitive interactions between them during resting-state. While the positive state may promote efficient communication between the subnetworks, the negative state may constrain the information flow between them, contributing to the functional specialization of the ventral subnetwork. Additionally, we revealed a weak state and a strong

state for FCs within the ventral subnetwork. Previous findings have reported wide-spread positive resting-state FCs among ventral subnetwork regions, such as the HIP, parahippocampal place area, RSC, and occipital place area (Kong et al., 2016; Silson et al., 2016; Boccia et al., 2017). Our results enriched previous findings by showing that integration within the ventral subnetwork also alternated between two typical states with different FC strength, a strong state and a weak state, each potentially exploited to varying degrees by navigational behaviors. While the strong state indicated highly synchronized activity among the ventral subnetwork regions, the weak state exhibited loose synchronization activity among the regions.

Further, identification of different dynamic FC states is critical to reveal the association between spatial relation representations and organizations of the navigation network, since our results indicated that spatial relation representations were associated with FC states of only some but not all time periods during resting-state. Specifically, representation of categorical spatial relations was only associated with the Weak State, but not the Strong State, within the ventral subnetwork; in contrast, representation of coordinate spatial relations was only related to the Negative State, but not the Positive State, between the ventral and other subnetworks. The associations between spatial relationship representations and specific dynamic FC states were concealed when FCs of all time windows were taken as static and invariant.

The dissociation of representations of categorical and coordinate spatial relations lies in two aspects. First, representation of categorical spatial relations was mainly related to the ventral subnetwork, while representation of coordinate spatial relations was related to interactions between the ventral and other subnetworks. Although some studies have suggested the potential dissociable neural bases between the hippocampal formation and parietal cortex underlying representations of the two types of spatial relations, accumulating research showed different results and indicated the dissimilarity might didn't be confined to the specific regions. Broad regions were found be involved in the two kinds of spatial relations. The MTL has been found to play a central role in representing both categorical and coordinate spatial relations (Howard et al., 2014; Blacker and Courtney, 2016; Deuker et al., 2016; Urgolites et al., 2017), and the prefrontal and posterior parietal regions are also involved in coordinate spatial relations (Spiers and Maguire, 2007; Morgan et al., 2011; Viard et al., 2011). Our results extended previous studies by comparing the dynamic FC nature of the two types of spatial relations from the network organization level. Representation of categorical spatial relations has been considered as an integrated cognitive process including extracting environment layout in the PPA, encoding location information in the HIP, and updating viewpoint information in the RSC. It's reasonable that the dynamic cooperation of ventral navigation regions supports the representation of categorical spatial relations. In contrast, representation of coordinate spatial relations requires precise distance information between landmarks, possibly involving both spatial processing and high-level cognitive functions such as executive control and attention modulation, which may be supported by dynamic communication between the ventral and dorsal subnetworks.

Another dissociation of representations of the two types of spatial relations lies in that weak integration among the ventral regions during resting-state was optimal for representation of categorical spatial relations, while competitive interaction between the ventral and other subnetworks was optimal for representation of coordinate spatial relations. It can be speculated that the moderate integration among the ventral regions may support an optimal balance between effective communications among these regions and maintenance of independent function of individual regions. In contrast, the competitive interactions between the ventral and other subnetworks are important for precise representation of coordinate spatial relations. In line with this result, we have found in a previous study that stronger integration of the IPS with other regions in the navigation network was associated with poor ability of executive control (Hao et al., 2017). Thus, we speculated that competitive interactions between the ventral and parietal-frontal subnetworks might be related to better ability of executive control or other high-level cognitive functions, which brings better representation of coordinate spatial relations.

Our study revealed different dynamic network organization states in relation to the representations of categorical and coordinate spatial relations. It is worth noting that the distinction of allocentric and egocentric spatial processing constitutes another vital classification, which concerns about the frame of reference with respect to navigator or environment. The allocentric-egocentric dichotomy may partly overlap with the categorical-coordinate dichotomy. It will be still necessary for future studies to further determine the relationship between the two dichotomy systems (Jager and Postma, 2003; Baumann and Mattingley, 2014; Ruotolo et al., 2019). Several important issues are unaddressed for future research. First, the present study characterized dynamic organizations of the navigation network by clustering FC states of all time windows into typical FC states, and future study needs to examine how more quantitative characteristics in dynamic network organization, such as flexibility and module allegiance, are related to spatial relation representation (Chai et al., 2016). Noteworthy, although we didn't find any sub-modules for the ventral network in the weak state, it still inspires further studies to explore the functional significance of possible sub-modules in the ventral network with more sensitive measures. Second, Deco et al. (2011) propose that dynamic network configuration is constrained by the underlying stable anatomical skeleton, and it's important to explore the link between anatomical structure and resting-state functional dynamics. Third, the negative correlation between the ventral and dorsal subnetworks should

be interpreted with caution, considering the debate that global signal regression may introduce artifactual anti-correlations (Fox et al., 2005; Murphy et al., 2009; Cole et al., 2010; Murphy and Fox, 2017). Forth, the role of MOG module seems to be special. Further research would be valuable to examine the temporal variability at the nodal level and subnetwork level in an integrated manner (Zhang et al., 2016; Sun et al., 2019), which helps to better reveal the functional specificity of navigation network regions. Finally, the dynamic FC patterns revealed in our study provide new insights than constant connectivity patterns in conventional analysis, and future studies with the dynamic approach in developing brain may provide new understanding of brain maturation and plasticity.

Data availability statement

The raw data supporting the conclusions of this article will be made available by the authors, without undue reservation.

Ethics statement

The studies involving human participants were reviewed and approved by Institutional Review Board of Beijing Normal University. The patients/participants provided their written informed consent to participate in this study.

Author contributions

XH and YS designed the experiments and wrote the manuscript. XH, ZC, and XK conducted the experiments. XH and TH analyzed the data. XH, YS, and JL supervised the project. All authors contributed to the article and approved the submitted version.

Funding

This study was funded by the National Natural Science Foundation of China (31872786, 31861143039, and 32200864), the Natural Science Foundation of Hubei Province of China (2020CFB363), the MOE (Ministry of Education in China) Project of Humanities and Social Sciences (21YJC190005), the Open Research Fund of the Key Laboratory of Adolescent Cyberpsychology and Behavior (CCNU) (2019A01), and the Fundamental Research Funds for the Central Universities (CCNU22QN020).

Conflict of interest

The authors declare that the research was conducted in the absence of any commercial or financial relationships that could be construed as a potential conflict of interest.

Publisher's note

References

Allen, E. A., Damaraju, E., Plis, S. M., Erhardt, E. B., Eichele, T., and Calhoun, V. D. (2014). Tracking whole-brain connectivity dynamics in the resting state. *Cereb. Cortex* 24, 663–676. doi: 10.1093/cercor/bhs352

Amorapanth, P. X., Widick, P., and Chatterjee, A. (2010). The neural basis for spatial relations. *J. Cogn. Neurosci.* 22, 1739–1753. doi: 10.1162/jocn.2009.21322

Baumann, O., and Mattingley, J. B. (2013). Dissociable representations of environmental size and complexity in the human hippocampus. *J. Neurosci.* 33, 10526–10533. doi: 10.1523/JNEUROSCI.0350-13.2013

Baumann, O., and Mattingley, J. B. (2014). Dissociable roles of the hippocampus and parietal cortex in processing of coordinate and categorical spatial information. *Front. Hum. Neurosci.* 8:73. doi: 10.3389/fnhum.2014.00073

Baumann, O., Chan, E., and Mattingley, J. B. (2012). Distinct neural networks underlie encoding of categorical versus coordinate spatial relations during active navigation. *Neuroimage* 60, 1630–1637. doi: 10.1016/j.neuroimage.2012.01.089

Biswal, B. B., Mennes, M., Zuo, X.-N., Gohel, S., Kelly, C., Smith, S. M., et al. (2010). Toward discovery science of human brain function. *Proc. Natl. Acad. Sci. U.S.A.* 107, 4734–4739. doi: 10.1073/pnas.0911855107

Blacker, K. J., and Courtney, S. M. (2016). Distinct neural substrates for maintaining locations and spatial relations in working memory. *Front. Hum. Neurosci.* 10:594. doi: 10.3389/fnhum.2016.00594

Boccia, M., Nemmi, F., and Guariglia, C. (2014). Neuropsychology of environmental navigation in humans: Review and meta-analysis of FMRI studies in healthy participants. *Neuropsychol. Rev.* 24, 236–251. doi: 10.1007/s11065-014-9247-8

Boccia, M., Sulpizio, V., Nemmi, F., Guariglia, C., and Galati, G. (2017). Direct and indirect parieto-medial temporal pathways for spatial navigation in humans: Evidence from resting-state functional connectivity. *Brain Struct. Funct.* 222, 1945–1957. doi: 10.1007/s00429-016-1318-6

Chai, L. R., Mattar, M. G., Blank, I. A., Fedorenko, E., and Bassett, D. S. (2016). Functional network dynamics of the language system. *Cereb. Cortex* 26, 4148–4159. doi: 10.1093/cercor/bhw238

Cole, D. M., Smith, S. M., and Beckmann, C. F. (2010). Advances and pitfalls in the analysis and interpretation of resting-state FMRI data. *Front. Syst. Neurosci.* 4:8. doi: 10.3389/fnsys.2010.00008

Deco, G., Jirsa, V. K., and McIntosh, A. R. (2011). Emerging concepts for the dynamical organization of resting-state activity in the brain. *Nat. Rev. Neurosci.* 12, 43–56. doi: 10.1038/nrn2961

Deuker, L., Bellmund, J. L., Schröder, T. N., and Doeller, C. F. (2016). An event map of memory space in the hippocampus. *Elife* 5:e16534. doi: 10.7554/eLife.16534

Ekstrom, A. D., and Yonelinas, A. P. (2020). Precision, binding, and the hippocampus: Precisely what are we talking about? *Neuropsychologia* 138:107341. doi: 10.1016/j.neuropsychologia.2020.107341

Ekstrom, A. D., Huffman, D. J., and Starrett, M. (2017). Interacting networks of brain regions underlie human spatial navigation: A review and novel synthesis of the literature. *J. Neurophysiol.* 118, 3328–3344. doi: 10.1152/jn.00531.2017

Epstein, R. A. (2008). Parahippocampal and retrosplenial contributions to human spatial navigation. *Trends Cogn. Sci.* 12, 388–396. doi: 10.1016/j.tics.2008.07.004

Epstein, R. A., and Kanwisher, N. (1998). A cortical representation of the local visual environment. *Nature* 392, 598–601. doi: 10.1038/33402

Epstein, R. A., Patai, E. Z., Julian, J. B., and Spiers, H. J. (2017). The cognitive map in humans: Spatial navigation and beyond. *Nat. Neurosci.* 20, 1504–1513. doi: 10.1038/nn.4656

Evensmoen, H. R., Lehn, H., Xu, J., Witter, M. P., Nadel, L., and Håberg, A. K. (2013). The anterior hippocampus supports a coarse, global environmental representation and the posterior hippocampus supports fine-grained, local environmental representations. *J. Cogn. Neurosci.* 25, 1908–1925. doi: 10.1162/jocn_a_00436

Feigenson, L., Dehaene, S., and Spelke, E. (2004). Core systems of number. *Trends Cogn. Sci.* 8, 307–314. doi: 10.1016/j.tics.2004.05.002

Fox, M. D., Snyder, A. Z., Vincent, J. L., Corbetta, M., Van Essen, D. C., and Raichle, M. E. (2005). The human brain is intrinsically organized into dynamic, anticorrelated functional networks. *Proc. Natl. Acad. Sci. U.S.A.* 102, 9673–9678. doi: 10.1073/pnas.0504136102

Gona, C., and Scarpazza, C. (2019). Where is the "where" in the brain? A meta-analysis of neuroimaging studies on spatial cognition. *Hum. Brain Mapp.* 40, 1867–1886. doi: 10.1002/hbm.24496

Hannula, D. E., and Ranganath, C. (2008). Medial temporal lobe activity predicts successful relational memory binding. *J. Neurosci.* 28, 116–124. doi: 10.1523/JNEUROSCI.3086-07.2008

Hao, X., Huang, T., Song, Y., Kong, X., and Liu, J. (2021). Development of navigation network revealed by resting-state and task-state functional connectivity. *Neuroimage* 243:118515. doi: 10.1016/j.neuroimage.2021.118515

Hao, X., Huang, Y., Li, X., Song, Y., Kong, X., Wang, X., et al. (2016). Structural and functional neural correlates of spatial navigation: A combined voxel-based morphometry and functional connectivity study. *Brain Behav.* 6:e00572. doi: 10.1002/brb3.572

Hao, X., Wang, X., Song, Y., Kong, X., and Liu, J. (2017). Dual roles of the hippocampus and intraparietal sulcus in network integration and segregation support scene recognition. *Brain Struct. Funct.* 223, 1473–1485. doi: 10.1007/s00429-017-1564-2

Hartley, T., Bird, C. M., Chan, D., Cipolotti, L., Husain, M., Vargha-Khadem, F., et al. (2007). The hippocampus is required for short-term topographical memory in humans. *Hippocampus* 17, 34–48. doi: 10.1002/hipo.20240

Holden, M. P., Curby, K. M., Newcombe, N. S., and Shipley, T. F. (2010). A category adjustment approach to memory for spatial location in natural scenes. *J. Exp. Psychol. Learn. Mem. Cogn.* 36:590. doi: 10.1037/a0019293

Howard, L. R., Javadi, A. H., Yu, Y., Mill, R. D., Morrison, L. C., Knight, R., et al. (2014). The hippocampus and entorhinal cortex encode the path and Euclidean distances to goals during navigation. *Curr. Biol.* 24, 1331–1340. doi: 10.1016/j.cub.2014.05.001

Hutchison, R. M., and Morton, J. B. (2015). Tracking the brain's functional coupling dynamics over development. *J. Neurosci.* 35, 6849–6859. doi: 10.1523/JNEUROSCI.4638-14.2015

Hutchison, R. M., Womelsdorf, T., Allen, E. A., Bandettini, P. A., Calhoun, V. D., Corbetta, M., et al. (2013). Dynamic functional connectivity: Promise, issues, and interpretations. *Neuroimage* 80, 360–378. doi: 10.1016/j.neuroimage.2013.05.079

Jager, G., and Postma, A. (2003). On the hemispheric specialization for categorical and coordinate spatial relations: A review of the current evidence. *Neuropsychologia* 41, 504–515. doi: 10.1016/S0028-3932(02)00086-6

Kay, P., and Regier, T. (2003). Resolving the question of color naming universals. *Proc. Natl. Acad. Sci. U.S.A.* 100, 9085–9089. doi: 10.1073/pnas.1532837100

Kong, X., Song, Y., Zhen, Z., and Liu, J. (2017). Genetic variation in S100B modulates neural processing of visual scenes in Han Chinese. *Cereb. Cortex* 27, 1326–1336. doi: 10.1093/cercor/bhv322

Kong, X., Wang, X., Pu, Y., Huang, L., Hao, X., Zhen, Z., et al. (2016). Human navigation network: The intrinsic functional organization and behavioral relevance. *Brain Struct. Funct.* 222, 749–764. doi: 10.1007/s00429-016-1243-8

Kosslyn, S. M. (1987). Seeing and imagining in the cerebral hemispheres: A computational approach. *Psychol. Rev.* 94, 148–175. doi: 10.1037/0033-295X.94.2.148

Kosslyn, S. M., Koenig, O., Barrett, A., Cave, C. B., Tang, J., and Gabrieli, J. D. (1989). Evidence for two types of spatial representations: Hemispheric specialization for categorical and coordinate relations. *J. Exp. Psychol. Hum. Percept. Perform.* 15, 723–735. doi: 10.1037/0096-1523.15.4.723

Kravitz, D. J., Saleem, K. S., Baker, C. I., and Mishkin, M. (2011). A new neural framework for visuospatial processing. *Nat. Rev. Neurosci.* 12, 217–230. doi: 10.1038/nrn3008

Leonardi, N., and Van De Ville, D. (2015). On spurious and real fluctuations of dynamic functional connectivity during rest. *Neuroimage* 104, 430–436. doi: 10.1016/j.neuroimage.2014.09.007

Lloyd, S. (1982). Least squares quantization in PCM. *IEEE Trans. Inform. Theory* 28, 129–137. doi: 10.1109/TIT.1982.1056489

Lopez, A., Postma, A., and Bosco, A. (2020). Categorical & coordinate spatial information: Can they be disentangled in sketch maps? *J. Environ. Psychol.* 68:101392. doi: 10.1016/j.jenvp.2020.101392

Maguire, E. A., Burgess, N., Donnett, J. G., Frackowiak, R. S., Frith, C. D., and O'Keefe, J. (1998). Knowing where and getting there: A human navigation network. *Science* 280, 921–924. doi: 10.1126/science.280.5365.921

Mahon, B. Z., and Caramazza, A. (2011). What drives the organization of object knowledge in the brain? *Trends. Cogn. Sci.* 15, 97–103. doi: 10.1016/j.tics.2011.01.004

Morgan, L. K., MacEvoy, S. P., Aguirre, G. K., and Epstein, R. A. (2011). Distances between real-world locations are represented in the human hippocampus. *J. Neurosci.* 31, 1238–1245. doi: 10.1523/JNEUROSCI.4667-10.2011

Murphy, K., and Fox, M. D. (2017). Towards a consensus regarding global signal regression for resting state functional connectivity MRI. *Neuroimage* 154, 169–173. doi: 10.1016/j.neuroimage.2016.11.052

Murphy, K., Birn, R. M., Handwerker, D. A., Jones, T. B., and Bandettini, P. A. (2009). The impact of global signal regression on resting state correlations: Are anti-correlated networks introduced? *Neuroimage* 44, 893–905. doi: 10.1016/j.neuroimage.2008.09.036

Newman, M. E., and Girvan, M. (2004). Finding and evaluating community structure in networks. *Phys. Rev. E* 69:026113. doi: 10.1103/PhysRevE.69.026113

Nielson, D. M., Smith, T. A., Sreekumar, V., Dennis, S., and Sederberg, P. B. (2015). Human hippocampus represents space and time during retrieval of real-world memories. *Proc. Natl. Acad. Sci. U.S.A.* 112, 11078–11083. doi: 10.1073/pnas.1507104112

Nomi, J. S., Farrant, K., Damaraju, E., Rachakonda, S., Calhoun, V. D., and Uddin, L. Q. (2016). Dynamic functional network connectivity reveals unique and overlapping profiles of insula subdivisions. *Hum. Brain Mapp.* 37, 1770–1787. doi: 10.1002/hbm.23135

Pica, P., Lemer, C., Izard, V., and Dehaene, S. (2004). Exact and approximate arithmetic in an Amazonian indigene group. *Science* 306, 499–503. doi: 10.1126/science.1102085

Power, J. D., Barnes, K. A., Snyder, A. Z., Schlaggar, B. L., and Petersen, S. E. (2012). Spurious but systematic correlations in functional connectivity MRI networks arise from subject motion. *Neuroimage* 59, 2142–2154. doi: 10.1016/j.neuroimage.2011.10.018

Qiu, Y., Wu, Y., Liu, R., Wang, J., Huang, H., and Huang, R. (2019). Representation of hu man spatial navigation responding to input spatial information and output navi gational strategies: An ALE meta-analysis. *Neurosci. Biobehav. Rev.* 103, 60–72. doi: 10.1016/j.neubiorev.2019.06.012

Rubinov, M., and Sporns, O. (2010). Complex network measures of brain connectivity: Uses and interpretations. *Neuroimage* 52, 1059–1069. doi: 10.1016/j.neuroimage.2009.10.003

Ruotolo, F., Ruggiero, G., Raemaekers, M., Iachini, T., van der Ham, I. J. M., Fracasso, A., et al. (2019). Neural correlates of egocentric and allocentric frames of reference combined with metric and non-metric spatial relations. *Neuroscience* 409, 235–252. doi: 10.1016/j.neuroscience.2019.04.021

Sherrill, K. R., Erdem, U. M., Ross, R. S., Brown, T. I., Hasselmo, M. E., and Stern, C. E. (2013). Hippocampus and retrosplenial cortex combine path integration signals for successful navigation. *J. Neurosci.* 33, 19304–19313. doi: 10.1523/JNEUROSCI.1825-13.2013

Shine, J. M., Bissett, P. G., Bell, P. T., Koyejo, O., Balsters, J. H., Gorgolewski, K. J., et al. (2016). The dynamics of functional brain networks: Integrated network states during cognitive task performance. *Neuron* 92, 544–554. doi: 10.1016/j.neuron.2016.09.018

Silson, E. H., Steel, A. D., and Baker, C. I. (2016). Scene-selectivity and retinotopy in medial parietal cortex. *Front. Hum. Neurosci.* 10:412. doi: 10.3389/fnhum.2016.00412

Slotnick, S. D., and Moo, L. R. (2006). Prefrontal cortex hemispheric specialization for categorical and coordinate visual spatial memory. *Neuropsychologia* 44, 1560–1568. doi: 10.1016/j.neuropsychologia.2006.01.018

Sormaz, M., Jefferies, E., Bernhardt, B. C., Karapanagiotidis, T., Mollo, G., Bernasconi, N., et al. (2017). Knowing what from where: Hippocampal connectivity with temporoparietal cortex at rest is linked to individual differences in semantic and topographic memory. *Neuroimage* 152, 400–410. doi: 10.1016/j.neuroimage.2017.02.071

Spiers, H. J., and Maguire, E. A. (2006). Thoughts, behaviour, and brain dynamics during navigation in the real world. *Neuroimage* 31, 1826–1840.

Spiers, H. J., and Maguire, E. A. (2007). A navigational guidance system in the human brain. *Hippocampus* 17, 618–626. doi: 10.1002/hipo.20298

Sun, J., Liu, Z., Rolls, E. T., Chen, Q., Yao, Y., Yang, W., et al. (2019). Verbal creativity correlates with the temporal variability of brain net-works during the resting state. *Cereb. Cortex* 29, 1047–1058. doi: 10.1093/cercor/bhy010

Trojano, L., Grossi, D., Linden, D. E., Formisano, E., Goebel, R., Cirillo, S., et al. (2002). Coordinate and categorical judgements in spatial imagery. An fMRI study. *Neuropsychologia* 40, 1666–1674. doi: 10.1016/S0028-3932(02)00021-0

Urgolites, Z. J., Hopkins, R. O., and Squire, L. R. (2017). Medial temporal lobe and topographical memory. *Proc. Natl. Acad. Sci. U.S.A.* 114, 8626–8630. doi: 10.1073/pnas.1708963114

van der Ham, I. J., Raemaekers, M., van Wezel, R. J., Oleksiak, A., and Postma, A. (2009). Categorical and coordinate spatial relations in working memory: An fMRI study. *Brain Res.* 1297, 70–79. doi: 10.1016/j.brainres.2009.07.088

van der Ham, I. J., van Zandvoort, M. J., and Postma, A. (2013). Lateralization of spatial relation processing in natural scenes. *Behav. Neurol.* 26, 175–177. doi: 10.1155/2013/519205

Viard, A., Doeller, C. F., Hartley, T., Bird, C. M., and Burgess, N. (2011). Anterior hippocampus and goal-directed spatial decision making. *J. Neurosci.* 31, 4613–4621. doi: 10.1523/JNEUROSCI.4640-10.2011

Wang, X., Zhen, Z., Song, Y., Huang, L., Kong, X., and Liu, J. (2016). The hierarchical structure of the face network revealed by its functional connectivity pattern. *J. Neurosci.* 36, 890–900. doi: 10.1523/JNEUROSCI.2789-15.2016

Yarkoni, T., Poldrack, R. A., Nichols, T. E., Van Essen, D. C., and Wager, T. D. (2011). Large-scale automated synthesis of human functional neuroimaging data. *Nat. Methods* 8, 665–670. doi: 10.1038/nmeth.1635

Zalesky, A., and Breakspear, M. (2015). Towards a statistical test for functional connectivity dynamics. *Neuroimage* 114, 466–470. doi: 10.1016/j.neuroimage.2015.03.047

Zalesky, A., Fornito, A., Cocchi, L., Gollo, L. L., and Breakspear, M. (2014). Time-resolved resting-state brain networks. *Proc. Natl. Acad. Sci. U.SA.* 111, 10341–10346. doi: 10.1073/pnas.1400181111

Zhang, J., Cheng, W., Liu, Z., Lei, X., Yao, Y., Ben, B., et al. (2016). Neural, electrophysiological and anatomical basis of brainnetwork variability and its characteristic changes in mental disorders. *Brain* 139, 2307–2321. doi: 10.1093/brain/aww143

Zhen, Z., Kong, X., Huang, L., Yang, Z., Wang, X., Hao, X., et al. (2017). Quantifying the variability of scene-selective regions: Interindividual, interhemispheric, and sex differences. *Hum. Brain Mapp.* 38, 2260–2275. doi: 10.1002/hbm.23519

frontiers | Frontiers in Human Neuroscience

TYPE Perspective
PUBLISHED 24 November 2022
DOI 10.3389/fnhum.2022.1062487

OPEN ACCESS

EDITED BY
Pedro Antonio Valdes-Sosa,
University of Electronic Science and Technology of China, China

REVIEWED BY
Guido Nolte,
University Medical Center Hamburg-Eppendorf, Germany

*CORRESPONDENCE
Eli J. Müller
eli.muller@sydney.edu.au

†These authors have contributed equally to this work

SPECIALTY SECTION
This article was submitted to Cognitive Neuroscience, a section of the journal Frontiers in Human Neuroscience

RECEIVED 06 October 2022
ACCEPTED 10 November 2022
PUBLISHED 24 November 2022

CITATION
Müller EJ, Munn BR, Aquino KM, Shine JM and Robinson PA (2022) The music of the hemispheres: Cortical eigenmodes as a physical basis for large-scale brain activity and connectivity patterns.
Front. Hum. Neurosci. 16:1062487.
doi: 10.3389/fnhum.2022.1062487

The music of the hemispheres: Cortical eigenmodes as a physical basis for large-scale brain activity and connectivity patterns

Eli J. Müller[1,2,3*†], Brandon R. Munn[1,2,3†], Kevin M. Aquino[1,2], James M. Shine[3] and Peter A. Robinson[1,2]

[1]School of Physics, The University of Sydney, Sydney, NSW, Australia, [2]Center for Integrative Brain Function, The University of Sydney, Sydney, NSW, Australia, [3]Brain and Mind Center, The University of Sydney, Sydney, NSW, Australia

Neuroscience has had access to high-resolution recordings of large-scale cortical activity and structure for decades, but still lacks a generally adopted basis to analyze and interrelate results from different individuals and experiments. Here it is argued that the natural oscillatory modes of the cortex—cortical eigenmodes—provide a physically preferred framework for systematic comparisons across experimental conditions and imaging modalities. In this framework, eigenmodes are analogous to notes of a musical instrument, while commonly used statistical patterns parallel frequently played chords. This intuitive perspective avoids problems that often arise in neuroimaging analyses, and connects to underlying mechanisms of brain activity. We envisage this approach will lead to novel insights into whole-brain function, both in existing and prospective datasets, and facilitate a unification of empirical findings across presently disparate analysis paradigms and measurement modalities.

KEYWORDS

eigenmodes, resting state networks, principal components, independent components, brain dynamics, brain connectivity

1. Introduction

Recent technological advances have seen a huge increase in data recorded from the brain, and in their spatial and temporal resolution, revealing striking complexity of neural activity up to whole-brain scales. In response, neuroscientists have attempted to compactly characterize these data, often decomposing signals into statistically derived components that maximize statistical independence, explained variance, or fidelity to anatomical and cytological features. Methods such as independent component analysis (ICA), principal component analysis (PCA), and clustering (McKeown and Sejnowski, 1998; Fischl et al., 2004; Desikan et al., 2006; Triarhou, 2007; Thomas Yeo et al., 2011; Abeysuriya and Robinson, 2016; Shine et al., 2019) typically produce 5–20 robust large-scale spatial patterns (Van De Ven et al., 2004; Damoiseaux et al., 2006)

including the visual, attention, and default-mode 'resting state networks' (RSNs), and permit data classification and comparison between subjects and experiments. However, comparison between approaches and protocols is difficult, because of the lack of obvious compatibility of different experimental and data-processing choices, and most rely on 'black-box' statistical approaches that do not consider the sources or mechanisms behind the signals being analyzed. These factors limit their utility for understanding brain dynamics and one is motivated to seek a means to compactly represent large-scale brain activity and structure that is researcher- and protocol-independent, linked to physical mechanisms, and general enough to enable comparisons across different subjects and imaging modalities.

We argue that the natural oscillatory modes of the physical cortex (i.e., its spatial eigenmodes), analogous to the notes of a stringed instrument, represent the optimal basis set for the systematic decomposition of cortical neural activity. First, their physical interpretation as mutually independent 'notes' produced by the cortex provides an intuitive basis for understanding brain activity in a way that separates spatial and temporal structure. Furthermore, this basis provides a compact representation of neural dynamics with an ordering that is grounded in the physical structure of the brain and independent of stimuli. Second, if eigenmodes are the fundamental "notes" of the brain, one can then view the robust large-scale brain patterns identified by statistical means as akin to frequently played musical chords, each comprising a characteristic combination of notes. This viewpoint enables us to explain classical findings in whole-brain neuroimaging, such as the alternating engagement of the default-mode and attentional RSNs (Fox et al., 2005), as discussed below. Finally, eigenmodes provide insight into the structure of the cortex and how low-order modes can facilitate interareal communication in the absence of direct physical connection.

2. Notes of the cortex: Eigenmodes

The eigenmodes of a physical system typically comprise spatial patterns that oscillate at characteristic frequencies. For example, when a violin is plucked, or a drum is struck, natural frequencies are excited, each corresponding to a spatial pattern of displacement of the string or drumhead. Before being plucked, a violin string remains at rest in its equilibrium position, as seen in Figure 1A. Both ends of the string are fixed, so when it is plucked they remain stationary (they are termed zeros or nodes) while the rest of the string oscillates. The first three oscillatory modes are shown in Figure 1A, ordered by their number of zeros (and thus by spatial frequency). Significantly, each mode extends over the whole string and every point on the string is part of every mode. In the temporal domain, each spatial eigenmode generates a note whose frequency is determined by the string's physical properties, but constrained by its geometry because an integer number of half-wavelengths must fit exactly within its length.

Eigenmodes of any system are intrinsic to that system and are determined by its dynamics and geometry independently of any particular inputs or stimuli. Moreover, in a broad class of systems, eigenmodes are mutually independent and any arbitrary spatial pattern can be expressed as a weighted sum of eigenmodes. These properties make eigenmodes so useful that they have become ubiquitous throughout mathematics, science, and engineering, starting with Fourier's work more than 200 years ago (Fourier, 1822). Indeed, moving between coordinate-space and modal representations is essential to obtain maximal insight into almost any physical system.

In the case of the cortex, the closed cortical surface imposes a geometric constraint in two dimensions (2D) that determines the spatial structure of its eigenmodes. The resonant frequencies of brain rhythms are then set by a combination of this constraint and local dynamics, analogously to the case of the 1D violin string. Any pattern of brain excitation and structure can then be expressed in terms of these eigenmodes, including spontaneous and evoked brain activity (Nunez, 1989; Robinson et al., 2001; Gabay and Robinson, 2017; Mukta et al., 2020) and underlying brain connectivity (Robinson et al., 2014, 2016; Gao and Robinson, 2020).

The spatial structure of eigenmodes of the cortex (termed spatial eigenmodes for brevity) have been shown to be well approximated by assuming a governing wave equation and thus solving the Helmholtz equation on a cortical hemisphere (Nunez, 1989; Robinson et al., 2001; Pinotsis et al., 2013; Gabay and Robinson, 2017; Mukta et al., 2020).

$$\nabla^2 u(\mathbf{r}) = -k^2 u(\mathbf{r}), \tag{1}$$

where $\mathbf{r}$ denotes spatial location. In this approximation, spatial eigenmodes $u(\mathbf{r})$ of brain activity are eigenfunctions of the Laplace-Beltrami operator ∇^2 with eigenvalues k^2; this equation can be solved on cortical surfaces, such as ones estimated *via* MRI, using finite element methods (see Robinson et al., 2016; Gabay and Robinson, 2017 for mathematical details). Figure 1B shows examples of the spatial eigenmodes of an average cortical surface (Fischl, 2012).

As for other systems, cortical eigenmodes are mutually independent, so each provides independent spatial information. They are naturally ordered from low spatial frequency (globally uniform) to high spatial frequency (localized features), with the lowest modes having the longest-lived oscillations. When spontaneous or task-related activity with spatial structure given by a function $g(\mathbf{r})$, where $\mathbf{r}$ is position, is decomposed into a sum over modes, the coefficient c of a mode u is given by the following integral over all $\mathbf{r}$ in the cortex:

$$c = \int u(\mathbf{r}) g(\mathbf{r}) d\mathbf{r}, \tag{2}$$

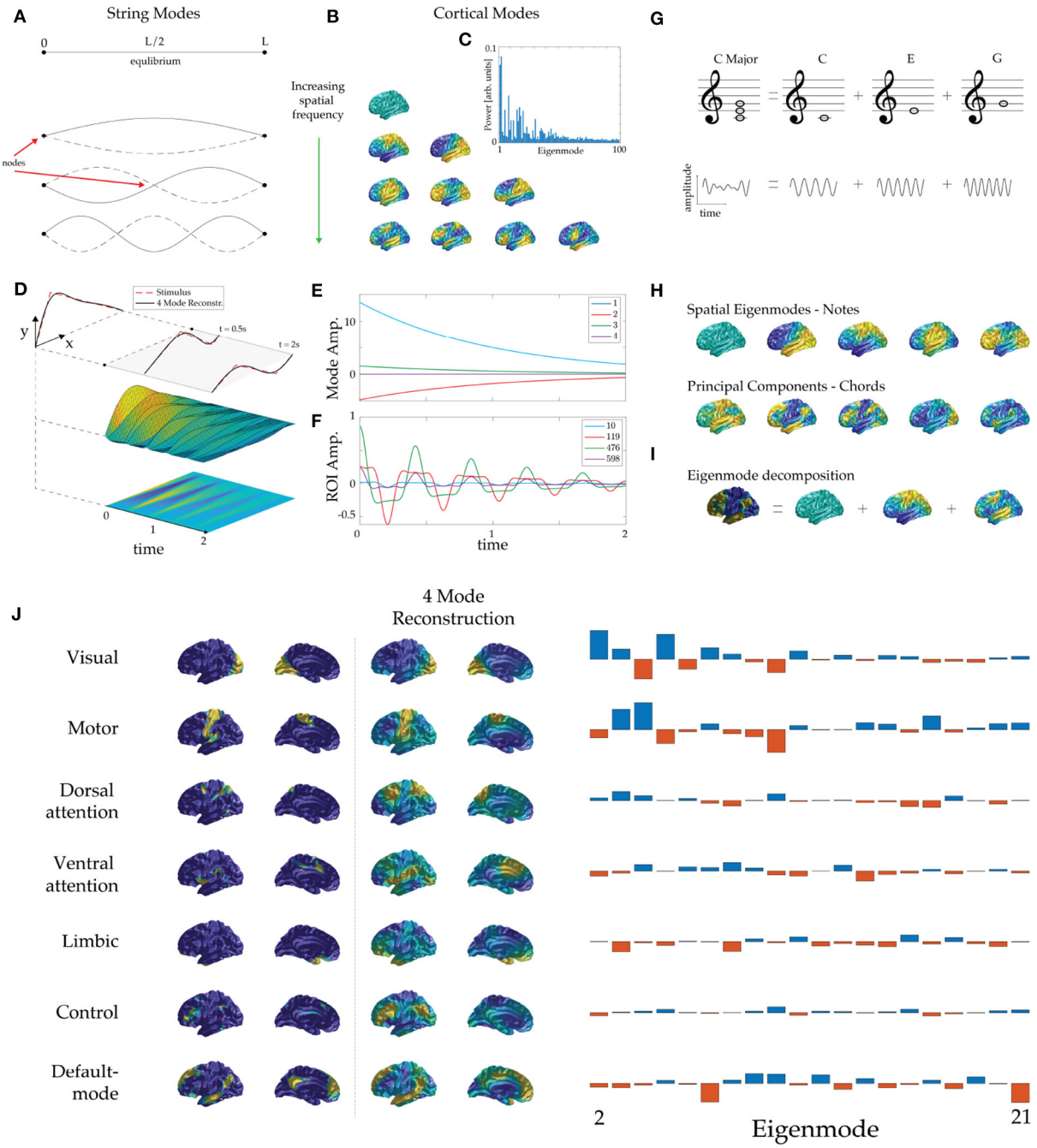

FIGURE 1
Eigenmode basis and dynamics. **(A)** Equilibrium position (top) and the lowest three eigenmodes of a violin string, ordered by increasing spatial frequency, showing zeros (nodes) and antinodes. (Note: we do not use "node" to denote an artificially discretized point on the cortex.) The solid dots indicate the clamped ends and solid and dashed curves show string positions half an oscillation apart in each case. **(B)** Lowest eigenmodes of an average cortical surface. Rows display cortical modes ordered by spatial frequency (more nodal lines) and warm and cool colors show positive and negative values relative to the mean at one extreme of an oscillation. **(C)** Human BOLD power (amplitude-squared) spectrum of eigenmodes during rest. The lower eigenmodes contribute the most power to ongoing neural activity. **(D)** Initial position of a plucked violin string and its mapping to the first four eigenmodes. **(E)** Subsequent evolution of mode amplitudes. **(F)** Subsequent evolution of displacement of several points along the violin string, analogous to regions-of-interest. **(G)** The C major chord is made up of a superposition of the notes C, E, and G, which have the frequency ratio 4:5:6; time series appear below. **(H)** Eigenmodes of the human cortex (top row) are analogous to "notes" of the cortex and statistically derived modes (bottom row, PCA modes here) are analogous to commonly recurring "chords" of cortical activity. **(I)** Analogously to music, cortical patterns can be decomposed into eigenmodes, whose amplitudes are its 'fingerprint'. In this example we approximate Margulies's principal "gradient" pattern (chord) (Margulies et al., 2016) *via* its dominant constituent eigenmodes (notes). (The term

(Continued)

FIGURE 1 (Continued)
gradient derives from the fact that it is calculated from quantities that have spatial gradients although it is not itself the gradient of any quantity.) **(J)** Eigenmode decomposition of the seven resting-state networks (RSNs) of Thomas Yeo et al. (2011). The first two columns show the RSNs formed by clustering correlations and weighted by the confidence of each point's attribution to its cluster to avoid spurious enhancement of high-order mode amplitudes by sharp edges. The third and fourth columns show each RSN reconstructed from its dominant four eigenmodes. The fifth column shows the modal amplitudes of each RSN, from which the dominant modes were identified.

which is termed the *projection* of g onto u. The lowest modes are found to dominate the dynamics (Nunez, 1989; Robinson et al., 2001; Wingeier et al., 2001; Mukta et al., 2020), as illustrated by the power spectrum of human blood-oxygen-level-dependent (BOLD) activity during rest in Figure 1C. This explains why only 5–20 robust spatial patterns are identified by statistical means. A useful feature of Equation (2) is that it integrates over short-scale noise, and hence tends to suppress it, thereby removing the main motivation for thresholding.

When stimuli enter the brain (or when a violin string is plucked), eigenmodes are excited with initial amplitudes given by Eq. (2), with $g(\mathbf{r})$ representing the initial stimulus. These amplitudes then decay at the damping rates appropriate to each mode (Mukta et al., 2020). Figure 1D illustrates the dynamics of a violin string that is plucked (i.e., release from an initial triangular shape) and its approximation by just the lowest four nonzero eigenmodes. We see that this provides a good approximation of the shape of the string, both then and at later times. Additionally, the subsequent temporal dynamics of the string is described by exponentially decreasing mode amplitudes, as shown in Figure 1E. In contrast, the time evolution of displacements of various points along the violin string—an analog of region-of-interest (ROI) time-series—gives a more complicated and obscure picture, as seen in Figure 1F. This result highlights the benefits of representing complex brain dynamics *via* its spatial eigenmodes and we expect these representations will expand functional insights.

3. Music of the cortex: Notes and chords

Music involves vibrational modes of instruments, excited at various frequencies and times. A chord such as C major has a complex periodic waveform that comprises superposed sine waves at the frequencies of the individual notes C, E, and G, as shown in Figure 1G. An electronic synthesizer constructs chords in just this way, but a musician plays chords directly, rather than exciting individual sine waves. Some chords are very common in particular pieces of music and thus may be more easily detected in statistical analyses than less common isolated notes. Each chord has a unique temporal signature but shares notes with other chords, establishing a fundamental interdependence. Hence, while chords provide a useful and efficient way to capture recurring musical motifs, an understanding of the underlying notes is essential to facilitate comparisons and groupings of chord families and links to the mechanisms by which instruments generate sound.

The above points lead to a direct analogy with the brain: if cortical eigenmodes correspond to its notes [Figure 1H (top)] then large-scale statistically detected patterns of recurrent brain activity can be viewed as its chords [Figure 1H (bottom)]. Frequently recurring patterns likely emerge from similar 'plucking' *via* related external stimuli or endogenous changes (e.g., large-scale neuromodulation). This view is consistent with the pervasive visual (sensory) and attentional (neuromodulatory) patterns seen in whole-brain imaging data (Thomas Yeo et al., 2011).

Any cortical pattern can be uniquely decomposed into eigenmodes, as illustrated in Figure 1I. Figure 1J (left) shows the seven widely cited RSNs of Yeo et al., where the confidence of each region's attribution to a particular RSN has been used to spatially smooth the patterns to remove artifactual sharp edges (Thomas Yeo et al., 2011). The reconstruction of each RSN using the four dominant (highest amplitude) eigenmodes in each case is shown, reflecting differing combinations of eigenmodes [Figure 1J (right)]. Interestingly, the default mode RSN and the dorsal attention RSN project with opposite sign onto the dominant low spatial frequency modes (eigenmodes 2–4; i.e., those with a single nodal line), so when any of these three eigenmodes oscillates, the default-mode and the dorsal-attention RSNs will oscillate 180° out of phase, thus providing a simple mechanistic explanation for the finding that these RSNs are temporally anticorrelated (Greicius et al., 2003; Fox et al., 2005).

We expect that eigenmode analysis will facilitate further such mechanistic insights into patterns of whole brain activity detected *via* various imaging methods (Atasoy et al., 2016). Furthermore, eigenmodes may explain a similar axis of separation that has been demonstrated in functional-MRI data using diffusion embedding (Margulies et al., 2016). Follow-up work by Raut et al. (2021) has also shown that a very similar spatial pattern is found in the oscillatory phase-shifts observed relative to subject arousal levels measured *via* respiratory variation. This phase relationship may be mechanistically interpreted in terms of physical eigenmodes; i.e., arousal is coincident with the promotion of a particular family of oscillatory eigenmodes.

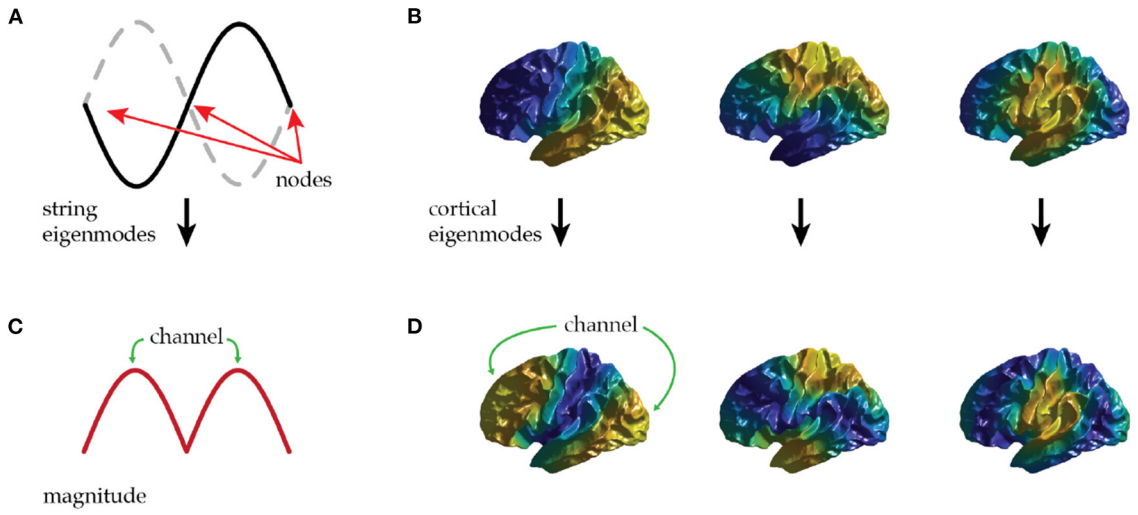

FIGURE 2
(A) The first non-uniform eigenmode of a string contains three zeros (nodes) and two antinodes that oscillate in antiphase. **(B)** The first three non-uniform eigenmodes of the cortex—each has a single nodal line. **(C)** The local amplitude (magnitude) of the first non-uniform eigenmode of a string shows a possible communication channel between each antinode. **(D)** The local amplitude of the first three non-uniform cortical eigenmodes supports communication along rostrocaudal, dorsoventral, and mediolateral axes.

4. Modal communication channels

Spatial eigenmodes offer a potential channel to mediate communication between distant brain regions. Equation (2) shows that modes are most easily excited where $|u(\mathbf{r})|$ is largest; i.e., at antinodes; likewise, their influence on local activity is largest at antinodes. Hence, each mode provides a channel for preferential communication between regions centered on its antinodes, as illustrated in Figures 2A,C for the second mode of a violin string.

Applying this idea to the lowest cortical modes, we see that the first (uniform) mode mediates communication approximately equally between all regions of the cortex, thus providing a means for any region to access the typical level of excitation of the brain as a whole. The next three modes have a single nodal line each with a pair of antinodes. Figures 2B,D shows that these are aligned along the rostrocaudal axis, the dorsoventral axis, and the mediolateral axis of the brain hemisphere. Each of these modes can thus preferentially mediate communication along one of these principal axes. Oscillatory activity transmitted in this way may provide a large-scale analog of the communication-through-coherence mechanism originally introduced at short scales by invoking roughly 40 Hz gamma oscillations to preferentially excite responses at particular phases (Fries, 2005). Here we argue that modal oscillations could also enhance responses at particular spatial locations defined by the antinodes of spatial cortical eigenmodes.

To illustrate these points, consider the first mode in Figure 2B with rostro-caudal orientation. This mode's antinodes are in prefrontal cortex and posterior sensory cortex, with a nodal line running through somatomotor cortex. This provides a communication channel between sensory and prefrontal regions that only weakly involves intermediate zones. These intermediate zones thus interact little with this mode. The analogy with a violin string is helpful in seeing that this is not problematic, the second mode seen in Figure 1A peaks at two points (Figure 1C) with a zero at the center, despite the string being continuous through the zeros.

Neural activity is dominated by only a few low order eigenmodes, as shown in Figure 1C. These modes are continuous, accessible everywhere in the brain, and integrate over fine scale structure and inputs. We thus speculate these dominant modes play an important role in supporting cognition and states of consciousness by providing channels for communication between distal cortical regions that do not necessarily possess direct physical connections.

Finally, the spatial patterns of the eigenmodes suggest a novel stimulation strategy to effectively and deliberately manipulate large-scale cortical activity— plucking a violin string near antinodes of a given eigenmode will have the greatest impact on the amplitude of that eigenmode. This suggests that systems for measurement or stimulation could usefully exploit eigenmode structures—particularly those of the low-order dominant eigenmodes. Indeed, key features of the empirically observed evoked response of the brain to spatially localized impulse stimuli are found to be well described by only a few eigenmodes (Mukta et al., 2020). This insight is relevant for transcranial magnetic stimulation and other

stimulation technologies used to probe cognition and treat pathologies. The power of systems that can excite low level eigenmodes may also help to explain how small but widely projecting neuromodulatory sources, such as the adrenergic locus coeruleus and nucleus basalis of Meynert (Shine et al., 2021; Wainstein et al., 2022), can have a large effect on cortical dynamics. We suggest that future experiments investigate how the neuromodulatory systems interact with cortical eigenmodes and that this may assist in optimizing cortical stimulation protocols.

5. Concluding remarks

In this manuscript we have outlined various advantages of a cortical eigenmode basis of the brain:

(i) Eigenmodes satisfy the main criteria for an optimal basis set in that they are readily interpretable and leverage the intuitive understanding of natural resonances or notes of the cortex—equivalent to notes of a string.

(ii) A key goal of neuroscience is to unify theories of brain activity, function, and structure. First and foremost this requires recordings and analysis of brain activity to be generalizable and thus comparable across recording sessions, different tasks, subjects, and measurement methods. In neuroimaging this has been approached *via* "resting-state networks" and popular parcellation schemes (Thomas Yeo et al., 2011; Gordon et al., 2016; Schaefer et al., 2018); however, as we discussed in previous sections, these are often constructed *via ad hoc* statistical measures, which limits interpretability and prevents standardization. In the worst case, each new approach requires the research community to establish mutual interpretability between it and all others—an overall burden that scales as the square of the total number of methods in use. However, much as English often serves as a common language through which other languages can be translated, eigenmodes provide a route by which only a single extra interpreter is required for each new method (or language, analogously) added. In other words, cortical eigenmodes can serve as a common basis through which to interrelate new findings and existing knowledge.

(iii) Eigenmodes are easily generalizable, independent of stimuli and experimental choices, and result from the brain's structure—avoiding the artificial warping and thresholding required for analyses *via* parcellations and artificially discretized networks. As such, eigenmodes remain applicable regardless of future improvements in resolution and accuracy of brain measurements and imaging.

(iv) Eigenmodes provide insight into the whole-brain function with parallel communication channels possible between cortical areas with no direct physical connection.

(v) Eigenmodes offer a simple explanation to the perplexing finding that the dorsal attention network and default mode network are anticorrelated. And further a cortical pattern revealed in fMRI data separating primary sensory and association areas, which has been recapitulated in oscillatory phase shifts tied to subject arousal, can be simply interpreted as an arousal evoked family of oscillatory cortical eigenmodes.

The eigenmodes in this work are considered purely for the cortex, and an identical set exists for each hemisphere. This presents an exciting opportunity to extend eigenmode analysis to subcortical loci including key structures such as the thalamus, hippocampus, and cerebellum.

The above advantages favor the wider adoption of eigenmodes in neuroscience that will provide both theoretical and empirical insight, as it has done for the fields of physics, mathematics, and engineering, thereby opening up exciting opportunities for future work.

Data availability statement

The original contributions presented in the study are included in the article/supplementary material, further inquiries can be directed to the corresponding author.

Author contributions

EM and BM contributed equally to all facets of this project. KA, JS, and PR contributed to concepts and writing of the manuscript. All authors contributed to the article and approved the submitted version.

Funding

This work was supported by the Australian National Health and Medical Research Council *via* Grant GNT1193857 and by the Australian Research Council Center of Excellence Grant CE140100007, and the Australian Research Council Laureate Fellowship Grant FL140100025.

Acknowledgments

We thank S. Sarkar for musical advice and J. Henderson for helpful discussions.

Conflict of interest

The authors declare that the research was conducted in the absence of any commercial or financial relationships that could be construed as a potential conflict of interest.

Publisher's note

References

Abeysuriya, R. G., and Robinson, P. A. (2016). Real-time automated EEG tracking of brain states using neural field theory. *J. Neurosci. Methods* 258, 28–45. doi: 10.1016/j.jneumeth.2015.09.026

Atasoy, S., Donnelly, I., and Pearson, J. (2016). Human brain networks function in connectome-specific harmonic waves. *Nat. Commun.* 7, 10340. doi: 10.1038/ncomms10340

Damoiseaux, J. S., Rombouts, S. A. R. B., Barkhof, F., Scheltens, P., Stam, C. J., Smith, S. M., et al. (2006). Consistent resting-state networks. *Proc. Natl. Acad. Sci. U.S.A.* 103, 13848–13853. doi: 10.1073/pnas.0601417103

Desikan, R. S., Ségonne, F., Fischl, B., Quinn, B. T., Dickerson, B. C., Blacker, D., et al. (2006). An automated labeling system for subdividing the human cerebral cortex on MRI scans into gyral based regions of interest. *Neuroimage* 31, 968–980. doi: 10.1016/j.neuroimage.2006.01.021

Fischl, B. (2012). FreeSurfer. *Neuroimage* 62, 774–781. doi: 10.1016/j.neuroimage.2012.01.021

Fischl, B., Van Der Kouwe, A., Destrieux, C., Halgren, E., Ségonne, F., Salat, D. H., et al. (2004). Automatically parcellating the human cerebral cortex. *Cereb. Cortex* 14, 11–22. doi: 10.1093/cercor/bhg087

Fourier, J. B. J., and Gaston D. (1822). *Théorie analytique de la chaleur. Vol. 504*. Paris: Didot.

Fox, M. D., Snyder, A. Z., Vincent, J. L., Corbetta, M., Van Essen, D. C., and Raichle, M. E. (2005). The human brain is intrinsically organized into dynamic, anticorrelated functional networks. *Proc. Natl. Acad. Sci. U.S.A.* 102, 9673–9678. doi: 10.1073/pnas.0504136102

Fries, P. (2005). A mechanism for cognitive dynamics: neuronal communication through neuronal coherence. *Trends Cogn. Sci.* 9, 474–480. doi: 10.1016/j.tics.2005.08.011

Gabay, N. C., and Robinson, P. A. (2017). Cortical geometry as a determinant of brain activity eigenmodes: neural field analysis. *Phys. Rev. E* 96, 032413. doi: 10.1103/PhysRevE.96.032413

Gao, X., and Robinson, P. A. (2020). Importance of self-connections for brain connectivity and spectral connectomics. *Biol. Cybern.* 114, 643–651. doi: 10.1007/s00422-020-00847-5

Gordon, E. M., Laumann, T. O., Adeyemo, B., Huckins, J. F., Kelley, W. M., and Petersen, S. E. (2016). Generation and evaluation of a cortical area parcellation from resting-state correlations. *Cereb. Cortex* 26, 288–303. doi: 10.1093/cercor/bhu239

Greicius, M. D., Krasnow, B., Reiss, A. L., and Menon, V. (2003). Functional connectivity in the resting brain: a network analysis of the default mode hypothesis. *Proc. Natl. Acad. Sci. U.S.A.* 100, 253–258. doi: 10.1073/pnas.0135058100

Margulies, D. S., Ghosh, S. S., Goulas, A., Falkiewicz, M., Huntenburg, J. M., Langs, G., et al. (2016). Situating the default-mode network along a principal gradient of macroscale cortical organization. *Proc. Natl. Acad. Sci. U.S.A.* 113, 12574–12579. doi: 10.1073/pnas.1608282113

McKeown, M. J., and Sejnowski, T. J. (1998). Independent component analysis of fMRI data: examining the assumptions. *Hum. Brain Mapp.* 6, 368–372. doi: 10.1002/(SICI)1097-0193(1998)6:5/6andlt;368::AID-HBM7andgt;3.0.CO;2-E

Mukta, K. N., Robinson, P. A., Pagès, J. C., Gabay, N. C., and Gao, X. (2020). Evoked response activity eigenmode analysis in a convoluted cortex *via* neural field theory. *Phys. Rev. E* 102, 1–10. doi: 10.1103/PhysRevE.102.062303

Nunez, P. L. (1989). Generation of human EEG by a combination of long and short range neocortical interactions. *Brain Topogr.* 1, 199–215. doi: 10.1007/BF01129583

Pinotsis, D. A., Hansen, E., Friston, K. J., and Jirsa, V. K. (2013). Anatomical connectivity and the resting state activity of large cortical networks. *Neuroimage* 65, 127–138. doi: 10.1016/j.neuroimage.2012.10.016

Raut, R. V., Snyder, A. Z., Mitra, A., Yellin, D., Fujii, N., Malach, R., et al. (2021). Accepted manuscript: global waves synchronize the brain's functional systems with fluctuating arousal. *Sci. Adv.* 7, 1–48. doi: 10.1126/sciadv.abf2709

Robinson, P. A., Loxley, P. N., O'Connor, S. C., and Rennie, C. J. (2001). Modal analysis of corticothalamic dynamics, electroencephalographic spectra, and evoked potentials. *Phys. Rev. E* 63, 1–13. doi: 10.1103/PhysRevE.63.041909

Robinson, P. A., Sarkar, S., Pandejee, G. M., and Henderson, J. A. (2014). Determination of effective brain connectivity from functional connectivity with application to resting state connectivities. *Phys. Rev. E* 90, 1–6. doi: 10.1103/PhysRevE.90.012707

Robinson, P. A., Zhao, X., Aquino, K. M., Griffiths, J. D., Sarkar, S., and Mehta-Pandejee, G. (2016). Eigenmodes of brain activity: neural field theory predictions and comparison with experiment. *Neuroimage* 142, 79–98. doi: 10.1016/j.neuroimage.2016.04.050

Schaefer, A., Kong, R., Gordon, E. M., Laumann, T. O., Zuo, X.-N., Holmes, A. J., et al. (2018). Local-global parcellation of the human cerebral cortex from intrinsic functional connectivity MRI. *Cereb. Cortex* 28, 3095–3114. doi: 10.1093/cercor/bhx179

Shine, J. M., Breakspear, M., Bell, P. T., Ehgoetz Martens, K., Shine, R., Koyejo, O., et al. (2019). Human cognition involves the dynamic integration of neural activity and neuromodulatory systems. *Nat. Neurosci.* 22, 289–296. doi: 10.1038/s41593-018-0312-0

Shine, J. M., Müller, E. J., Munn, B., Cabral, J., Moran, R. J., and Breakspear, M. (2021). Computational models link cellular mechanisms of neuromodulation to large-scale neural dynamics. *Nat. Neurosci.* 24, 765–776. doi: 10.1038/s41593-021-00824-6

Thomas Yeo, B. T., Krienen, F. M., Sepulcre, J., Sabuncu, M. R., Lashkari, D., Hollinshead, M., et al. (2011). The organization of the human cerebral cortex estimated by intrinsic functional connectivity. *J. Neurophysiol.* 106, 1125–1165. doi: 10.1152/jn.00338.2011

Triarhou, L. C. (2007). The Economo-Koskinas atlas revisited: cytoarchitectonics and functional context. *Stereotact. Funct. Neurosurg.* 85, 195–203. doi: 10.1159/000103258

Van De Ven, V. G., Formisano, E., Prvulovic, D., Roeder, C. H., and Linden, D. E. (2004). Functional connectivity as revealed by spatial independent component analysis of fMRI measurements during rest. *Hum. Brain Mapp.* 22, 165–178. doi: 10.1002/hbm.20022

Wainstein, G., Müller, E. J., Taylor, N., Munn, B., and Shine, J. M. (2022). The role of the locus coeruleus in shaping adaptive cortical melodies. *Trends Cogn. Sci.* 26, 527–538. doi: 10.1016/j.tics.2022.03.006

Wingeier, B. M., Nunez, P. L., and Silberstein, R. B. (2001). Spherical harmonic decomposition applied to spatial-temporal analysis of human high-density electroencephalogram. *Phys. Rev. E* 64, 9. doi: 10.1103/PhysRevE.64.051916

frontiers | Frontiers in Human Neuroscience

TYPE Methods
PUBLISHED 01 March 2023
DOI 10.3389/fnhum.2023.1001848

OPEN ACCESS

EDITED BY
Ruben Sanchez-Romero,
Rutgers University, United States

REVIEWED BY
Amirhossein Khalilian,
New York University, United States
Hae-Jeong Park,
Yonsei University, Republic of Korea

*CORRESPONDENCE
Sayan Nag
✉ sayan.nag@mail.utoronto.ca
Kamil Uludag
✉ kamil.uludag@rmp.uhn.ca

SPECIALTY SECTION
This article was submitted to Cognitive Neuroscience, a section of the journal Frontiers in Human Neuroscience

RECEIVED 24 July 2022
ACCEPTED 25 January 2023
PUBLISHED 01 March 2023

CITATION
Nag S and Uludag K (2023) Dynamic Effective Connectivity using Physiologically informed Dynamic Causal Model with Recurrent Units: A functional Magnetic Resonance Imaging simulation study.
Front. Hum. Neurosci. 17:1001848.
doi: 10.3389/fnhum.2023.1001848

Dynamic Effective Connectivity using Physiologically informed Dynamic Causal Model with Recurrent Units: A functional Magnetic Resonance Imaging simulation study

Sayan Nag[1,2]* and Kamil Uludag[1,2,3,4]*

[1]Techna Institute & Koerner Scientist in MR Imaging, University Health Network, Toronto, ON, Canada, [2]Department of Medical Biophysics, University of Toronto, Toronto, ON, Canada, [3]Center for Neuroscience Imaging Research, Institute for Basic Science, Suwon, Republic of Korea, [4]Department of Biomedical Engineering, Sungkyunkwan University, Suwon, Republic of Korea

Functional MRI (fMRI) is an indirect reflection of neuronal activity. Using generative biophysical model of fMRI data such as Dynamic Causal Model (DCM), the underlying neuronal activities of different brain areas and their causal interactions (i.e., effective connectivity) can be calculated. Most DCM studies typically consider the effective connectivity to be static for a cognitive task within an experimental run. However, changes in experimental conditions during complex tasks such as movie-watching might result in temporal variations in the connectivity strengths. In this fMRI simulation study, we leverage state-of-the-art Physiologically informed DCM (P-DCM) along with a recurrent window approach and discretization of the equations to infer the underlying neuronal dynamics and concurrently the dynamic (time-varying) effective connectivities between various brain regions for task-based fMRI. Results from simulation studies on 3- and 10-region models showed that functional magnetic resonance imaging (fMRI) blood oxygenation level-dependent (BOLD) responses and effective connectivity time-courses can be accurately predicted and distinguished from faulty graphical connectivity models representing cognitive hypotheses. In summary, we propose and validate a novel approach to determine dynamic effective connectivity between brain areas during complex cognitive tasks by combining P-DCM with recurrent units.

KEYWORDS

dynamic effective connectivity, neuroscience, graphical models, BOLD fMRI, causality

1. Introduction

Functional Magnetic Resonance Imaging (fMRI) non-invasively measures neural activity indirectly *via* changes in the hemodynamic response (i.e., changes in cerebral blood flow and volume). Local blood brain flow increases when the neuron increases its activity in the presence of a stimulus or intrinsically to support the increased metabolic demand and subsequently oxygenated blood displaces deoxygenated blood (Buxton et al., 2004; Stefanovic et al., 2004; Uludağ et al., 2004). This leads to a rise in the blood oxygenation level-dependent (BOLD)

response during stimulation before the response typically falls to a post-stimulus undershoot below the initial baseline and ultimately returns to baseline. The BOLD signal is not only used to map task-correlated brain activity or study brain physiology in individual voxels but also used to study functional and effective connectivity (Friston, 2011; Goldenberg and Galván, 2015; Kuhnke et al., 2021; Underwood et al., 2021). Functional connectivity is another term for instantaneous BOLD signal correlations during resting-state of remote voxels and brain areas (van den Heuvel and Pol, 2010; Friston, 2011; Shakil et al., 2016). However, functional connectivity methods typically are not utilized to infer causal relationships between these voxels (Friston, 2011). In contrast, effective connectivity utilizes causal connectivity graphs on the neuronal level representing a specific cognitive hypothesis for a task and a local generative model numerically describing the underlying BOLD signal physiology (Friston, 2011).

One prominent approach for effective connectivity is the Dynamic Causal Model (DCM) (Friston et al., 2003; Stephan et al., 2008; Moran et al., 2009; Havlicek et al., 2015). The basic idea behind DCM is to treat the brain as a nonlinear dynamical system and the observations (e.g., whole-brain fMRI signals) as indirect reflections of the signal of interest (e.g., the local neuronal activity and their connections). Using Bayesian model inversion (Ulrych et al., 2001; Friston et al., 2003), the local neuronal, effective connectivity values, and the vascular parameters can be estimated (Friston et al., 2003; Havlicek et al., 2015). The variants of DCM include stochastic DCM (Daunizeau et al., 2009), non-linear DCM (Stephan et al., 2008), spectral DCM (Moran et al., 2009) and physiologically informed DCM (P-DCM) (Havlicek et al., 2015). The P-DCM is the state-of-the-art model, which is inspired by experimental observations about the physiological underpinnings of the fMRI signal. It overcomes the limitations of earlier DCMs, such as inaccurate modeling of the initial overshoot and the post-stimulus undershoot, observations which are typically present in the time courses of task-based fMRI BOLD signals.

Dynamic Causal Model studies typically consider the causal interactions between brain areas to be fixed for an entire experimental run. However, experimental conditions can change with time within a run, for example when a subject is watching a movie, and consequently it is expected that the connectivity strengths between disparate brain regions also vary with time. In the recent years, more and more studies utilize these time-varying stimuli to study cognitive processes in the human brain (see, for example, Finn, 2021). To capture the dynamic nature of functional connectivity in resting-state, Dynamic Functional Connectivity (DFC) studies using sliding windows were proposed (Chang and Glover, 2010; Kiviniemi et al., 2011; Jones et al., 2012; Shakil et al., 2016). This is done by finding the statistical correlations amongst different brain area-specific resting-state fMRI BOLD time-series (Cribben et al., 2012; Handwerker et al., 2012; Calhoun et al., 2014; Monti et al., 2014; Shakil et al., 2016). However, as this analysis is done on the level of observations and, hence, does not utilize a generative model of the BOLD signal, DFC does not provide an assessment of the underlying neuronal mechanisms reflected in the fMRI BOLD responses (Stephan et al., 2010; Friston, 2011).

In this study, we propose a P-DCM based Dynamic Effective Connectivity approach the for modeling underlying neuronal dynamics in task-based fMRI. Our approach consists of sliding (recurrent) overlapping windows to capture the entire extent of fMRI BOLD time-series in a sequential manner. For each window, we have used discretized P-DCM with different parameter sets (i.e., connectivity variables, neuronal and vascular parameters) for different windows following a recurrence (from the previous window). Finally, for each such recurrent unit, we perform model inversion (parameter estimation) until convergence.

2. Methods

To determine time varying connectivity, we combined two approaches: discretized Physiologically informed Dynamic Causal Model (*d*P-DCM) and Recurrent Unit (RU).

2.1. *discretized* Physiologically informed Dynamic Causal Model (*d*P-DCM)

Physiologically informed Dynamic Causal Model (P-DCM) for fMRI was introduced by Havlicek et al. (2015) to describe the link between hidden neuronal activity and measured BOLD signals, overcoming the physiological limitations of previous Dynamic Causal Models (DCMs). The drawbacks of previous models included inaccurate modeling of initial overshoot and post-stimulus undershoot, which are temporal features typically observed in task-based fMRI BOLD signals.

The DCM approaches consist of a forward generative model and a backward model or inference (Friston et al., 2003; Havlicek et al., 2015). The P-DCM forward model (see Havlicek et al., 2015) consists of a two-state excitatory-inhibitory neuronal model which incorporates adaptive neuronal dynamics, capable of reproducing local field potential time courses as observed with invasive electrophysiology; neurovascular coupling is described as a feed-forward mechanism, and cerebral blood flow and volume can be uncoupled; and finally, Havlicek et al. also derived new parameters for the BOLD signal equation. Importantly, it has been shown that the different physiological assumptions of P-DCM compared with previous DCM approaches can lead to different estimated effective connectivity values (please see Havlicek et al., 2017b, for details).

To utilize RUs, we used a *discretized* version of P-DCM. For simplicity, instead of locally linearize the matrix exponential (Ozaki, 1992), we have used the Euler's method.

$$\frac{dz(t)}{dt} = \frac{z(t+\Delta t) - z(t)}{\Delta t} \tag{1}$$

Where $z \in \{x_E, x_I, a, f, v, q\}$, x_E the excitatory and x_I the inhibitory neuronal response, a the vasoactive signal, f the normalized cerebral blood flow response, v the normalized cerebral blood volume response, q the normalized deoxyhemoglobin content and Δt the difference between two adjacent time-points.

2.1.1. Neuronal component

The neuronal component estimates excitatory and inhibitory neuronal dynamics by modeling intra-regional and inter-regional neuronal interactions. The discretized neuronal component consisting of both excitatory (x_E) and inhibitory neuronal states (x_I)

is given as (here and below, please see Havlicek et al., 2015, for the corresponding continuous variable equations):

$$x_E(t+\Delta t) = (1-\sigma\Delta t)\cdot x_E(t) - (\mu\Delta t)\cdot x_I(t) + (c\Delta t)\cdot u(t) \quad (2a)$$

$$x_I(t+\Delta t) = (\lambda\Delta t)\cdot x_E(t) + (1-\lambda\Delta t)\cdot x_I(t) \quad (2b)$$

Equation 2a refers to the excitatory neuronal dynamics and 2b refers to the inhibitory neuronal dynamics. σ denotes the self-connectivity whose magnitude determines the temporal scaling of the neuronal dynamics. λ is the inhibitory gain factor that controls relative amplitude of the inhibitory activity with respect to the excitatory activity and the temporal smoothness. μ represents the inhibitory-excitatory connection, which regulates the temporary imbalance of the excitatory activity due to the inhibition. λ and μ are also deciding the rate, at which the activity of excitatory neuronal response drops from its initial peak to the plateau level and its return from the post-stimulus dip to the baseline value.

A discretized version of the multivariate form of the two-state connectivity equation (Havlicek et al., 2015) based on the neuronal component (described in the equations 2a and 2b) is given as:

$$\mathbf{X}_E(t+\Delta t) = (\mathbf{I}+\Delta t\boldsymbol{\psi})\mathbf{X}_E(t) + (\Delta t\boldsymbol{\psi}^-)\mathbf{X}_I(t) + (\Delta t\mathbf{C})\mathbf{U}_d(t) \quad (2c)$$

$$\mathbf{X}_I(t+\Delta t) = (\Delta t\boldsymbol{\mathfrak{C}})\mathbf{X}_E(t) + (\mathbf{I}-\Delta t\boldsymbol{\mathfrak{C}})\mathbf{X}_I(t) \quad (2d)$$

for which

$$\left.\begin{array}{c}\boldsymbol{\psi}_{ij} = \mathbf{A}_{ij} + \sum_{m=1}^{M}\mathbf{B}_{ij}^{(m)}u_m(t),\\ \boldsymbol{\psi}_{ij}^- = 0,\\ \boldsymbol{\mathfrak{C}}_{ij} = 0,\end{array}\right\} \forall\, i \neq j,$$

$$\left.\begin{array}{c}\boldsymbol{\psi}_{ii} = -\sigma e^{\left(\widetilde{\sigma}+\sum_{m=1}^{M}b_{ii}^{(m)}u_m(t)\right)},\\ \boldsymbol{\psi}_{ii}^- = -\mu e^{\left(\widetilde{\mu_i}+\sum_{k=1}^{K}b_{\mu i}^{(k)}u_{\mu k}(t)\right)},\\ \boldsymbol{\mathfrak{C}}_{ii} = \lambda e^{\left(\widetilde{\lambda_i}+\sum_{l=1}^{L}b_{\lambda i}^{(l)}u_{\lambda l}(t)\right)}\end{array}\right\}$$

A is the connectivity matrix [whose off-diagonal elements encode connections between regions whereas diagonal elements encode self-connections (Havlicek et al., 2015)], **B** denotes the matrix consisting of the additive modulatory effects controlled by modulatory inputs $u_m(t)$, and $\boldsymbol{\psi}$ is the total connectivity matrix. The direct input stimulus matrix is given as $\mathbf{U}_d(t)$. The context dependent inputs are represented as $u_{\mu\ k}(t)$ and $u_{\lambda\ l}(t)$, which are scaled by region-specific parameters $b_{\mu\ i}^{(k)}$ and $b_{\lambda\ i}^{(l)}$, and together they modulate the inhibitory-excitatory connections and inhibitory gain factors, respectively. These factors are encoded in the matrix given by $\boldsymbol{\mathfrak{C}}$. **I** is the identity matrix. In the above equations (derived from Havlicek et al., 2015), the parameters $\widetilde{\sigma},\widetilde{\mu},\widetilde{\lambda}$ represent self-connectivity, inhibitory-excitatory connection, and inhibitory gain, respectively, and σ, μ, λ are the corresponding constant scaling factors (please refer to Havlicek et al., 2015 for further details). Equations 2c and 2d can be represented in matrix form as follows:

$$\begin{bmatrix}\mathbf{X}_E(t+\Delta t)\\ \mathbf{X}_I(t+\Delta t)\end{bmatrix} = \begin{bmatrix}\mathbf{I}+\Delta t\boldsymbol{\psi} & \Delta t\boldsymbol{\psi}^-\\ \Delta t\boldsymbol{\mathfrak{C}} & \mathbf{I}-\Delta t\boldsymbol{\mathfrak{C}}\end{bmatrix}\begin{bmatrix}\mathbf{X}_E(t)\\ \mathbf{X}_I(t)\end{bmatrix} + \begin{bmatrix}\Delta t\mathbf{C}\\ 0\end{bmatrix}\mathbf{U}_d(t) \quad (2e)$$

$$\mathbf{X}(t+\Delta t) = \mathbf{W}_X\mathbf{X}(t) + \mathbf{W}_U\mathbf{U}_d(t) \quad (2f)$$

In the equation 2f, **X** represents the excitatory and inhibitory neuronal variables stacked together in a matrix form, $\mathbf{W}_X$ and $\mathbf{W}_U$ represent the collective matrices of individual weight matrices of $\mathbf{X}(t)$ and $\mathbf{U}_d(t)$, respectively.

2.1.2. Feedforward neurovascular coupling (NVC) component

Neurovascular coupling is the relationship between local neuronal activity and subsequent changes in CBF occurring through a complex sequence of coordinated events involving neurons, glia, and vascular cells. That is, neuronal excitation/inhibition leads to arterial vasodilation/vasoconstriction associated with increased/decreased CBF (Zonta et al., 2003; Uludağ et al., 2004; Lauritzen, 2005; Devor et al., 2007; Attwell et al., 2010)—with the result that the CBF time course is a smoothed version of the neuronal activity. Considering the constraint of linear relationship between synaptic activity and blood flow, the discretized version of feedforward NVC component can be given as:

$$a(t+\Delta t) = (1-\varphi\Delta t)\cdot a(t) + (\Delta t)\cdot x_E(t) \quad (3a)$$

$$f(t+\Delta t) = (\phi\Delta t)\cdot a(t) + (1-\chi\Delta t)\cdot f(t) + \chi\Delta t \quad (3b)$$

Here, $a(t)$ is the time-varying vasoactive signal responsible for transforming the excitatory neuronal response $x_E(t)$ to the CBF response $f(t)$. The set of equations 3a and 3b acts as a positively constrained low-pass filter of the neuronal dynamics as regulated by vasoactive signal decay (φ), vasoactive signal gain (ϕ) and blood inflow signal decay (χ).

The above set of equations in matrix form can be written as:

$$\begin{bmatrix}a(t+\Delta t)\\ f(t+\Delta t)\end{bmatrix} = \begin{bmatrix}1-\varphi\Delta t & 0\\ \phi\Delta t & 1-\chi\Delta t\end{bmatrix}\begin{bmatrix}a(t)\\ f(t)\end{bmatrix} + \begin{bmatrix}\Delta t\\ 0\end{bmatrix}x_E(t) + \begin{bmatrix}0\\ \chi\Delta t\end{bmatrix} \quad (3c)$$

2.1.3. Hemodynamic component

The CBF response $f(t)$ acts as an input to the post-capillary vessels, which are represented by an expandable venous balloon. The system of equations governing the hemodynamics describes the interaction between blood inflow $f(t)$, blood outflow $f_{out}(t)$, blood volume $v(t)$ and deoxyhemoglobin content $q(t)$ as they flow through the venous balloon. The discretized version of the set of equations is given as:

$$v(t+\Delta t) = v(t) + \Delta t\cdot\left[\frac{f(t)-f_{out}(v,t)}{t_{MTT}}\right] \quad (4a)$$

$$q(t+\Delta t) = q(t)\cdot\left[1-\frac{\Delta t\cdot f_{out}(v,t)}{t_{MTT}\cdot v(t)}\right] + \Delta t\cdot\frac{f(t)\cdot E(f)}{t_{MTT}\cdot E_0} \quad (4b)$$

$$E(f) = 1-(1-E_0)^{1/f} \quad (4c)$$

These equations are following mass balance principles: The blood volume $v(t)$ depends on the difference between the blood inflow $f(t)$ and the blood outflow $f_{out}(t)$. The deoxyhemoglobin

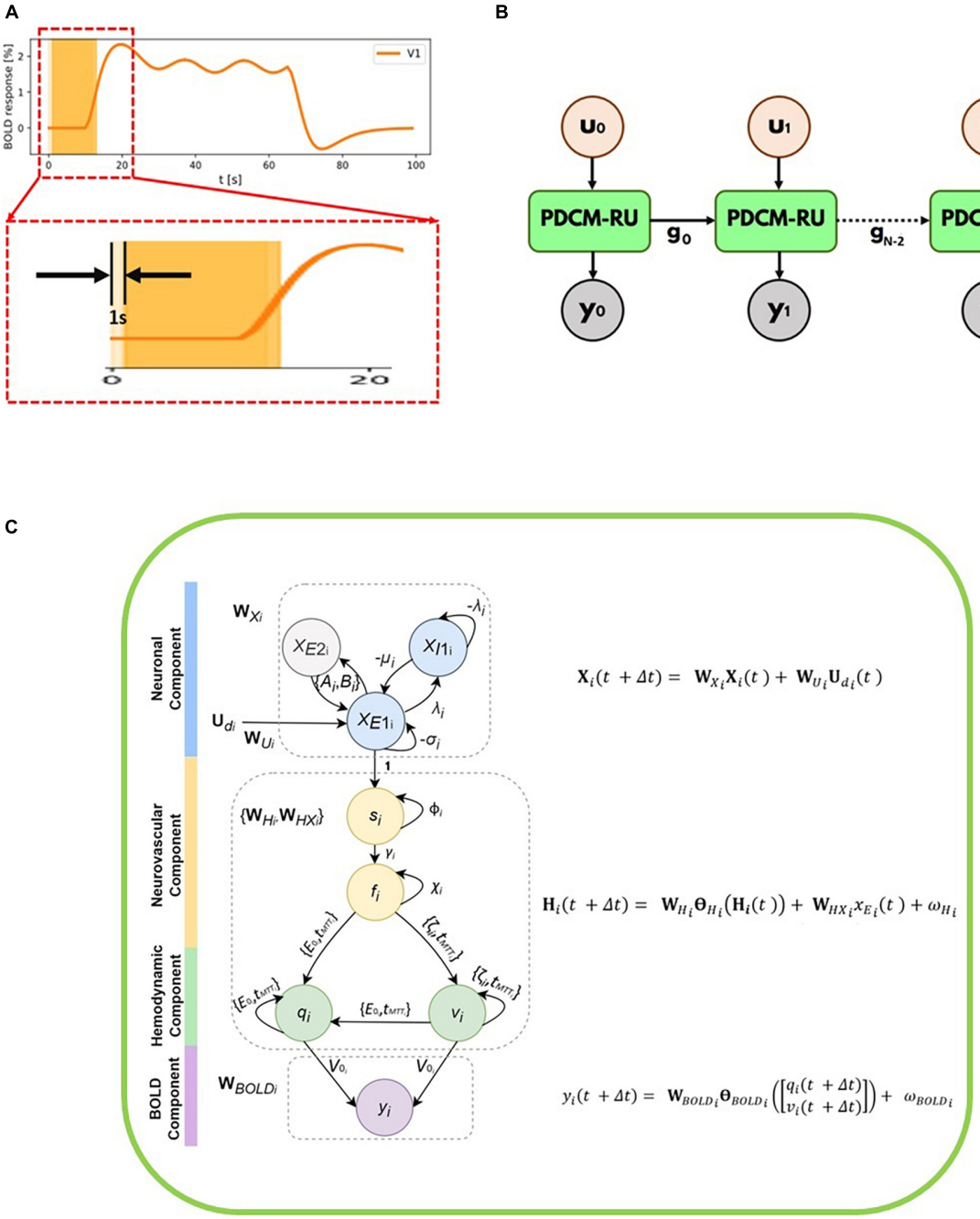

FIGURE 1
(A) Simulated BOLD fMRI time-courses for R1 along with two overlapping windows each of 12 s duration which moves from left to right. The time course between 0 and 20 seconds has been magnified to show the overlap of two successive windows. The stride of each overlapping window is 1 s. **(B)** Unfolded version of the *discretized* Physiologically informed Dynamic Causal Model (*d*PDCM)-recurrent unit (RU) architecture through time. For i^{th} window for which the input is u_i and the output is y_i. The set of hidden variables from the 0^{th} window, g_0 are being fed to the next window. Thus, a recurrence is followed and the same unit with different parameter values is being repeated time and again till the final window. **(C)** Overall schematic representation of each *d*P-DCM recurrent unit consisting of neuronal, neurovascular, hemodynamic, and blood oxygenation level-dependent (BOLD) components. These components include respective latent variables, whose states are updated according to the associated equations (shown on the right, also refer to Equation 8). x_{E2i} and x_{E1i} refer to excitatory populations from regions 1 to 2, respectively. These regions are connected at the excitatory level. For each region, an inhibitory population exists, given by x_{I1i}. Neuronal responses are the resultant of neuronal activity (due to the application of input stimulus) generated at the neuronal component. These excitatory responses induce vasoactive signals s_i, which increase the blood flow f_i. Changes in blood flow cause changes in blood volume (v_i) and deoxyhemoglobin content (q_i). Finally, these two hemodynamic states together yield BOLD response y_i.

content $q(t)$ depends on the difference between the delivery rate of deoxyhemoglobin into the venous compartment and the rate of clearance of deoxyhemoglobin from the tissue. The scaling factor t_{MTT} denotes the mean transit time that blood takes to pass through the veins. $E(f)$ represents the oxygen extraction fraction and E_0 is the net oxygen extraction at rest. [Please note that it is easy to use a different relationship between E and f. However, for consistency with previous papers (Havlicek et al., 2015), we employ equation (4c)

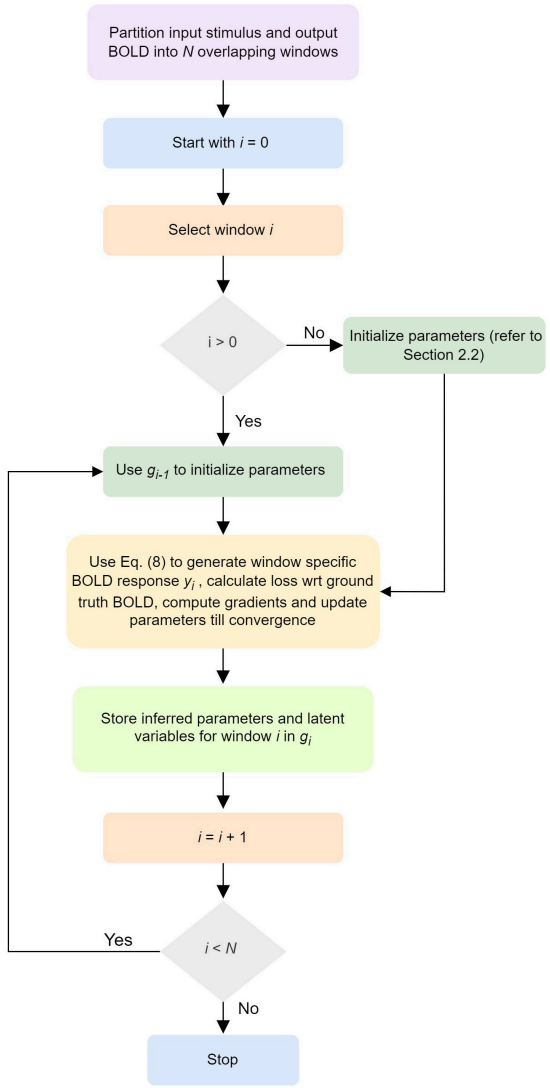

FIGURE 2
Workflow of *discretized* Physiologically informed Dynamic Causal Model (*d*P-DCM)-recurrent unit (RU).

for this relationship]. In addition to this steady-state relationship, some studies indicate a tight temporal association (but not necessarily mechanistic coupling) between CBF and cerebral metabolic rate of oxygen ($CMRO_2$) (Buxton and Frank, 1997; Masamoto et al., 2008; Zappe et al., 2008; Havlicek et al., 2017a).

2.1.4. Balloon model with viscoelastic effect

Instead of using the steady state flow-volume relationship as used in the earlier versions of DCMs as in Friston et al. (2003), Stephan et al. (2008), Havlicek et al. (2015) considered the original balloon model with viscoelastic effect. It was experimentally revealed in Mandeville et al. (1998) that the steady-state power law relationship does not adequately describe the temporal properties of the CBF-CBV relationship (see Uludağ and Blinder, 2018, for a recent review). The post-stimulus BOLD undershoot, for example, is primarily due to slow recovery of venous CBV to baseline rather than a metabolic effect [(Buxton, 2012), but see van Zijl et al. (2012) for opposing view]. Considering the dynamic viscoelastic effect term leads to:

$$f_{out}(v,t) = v(t)^{\frac{1}{\alpha}} + \tau \cdot \frac{dv(t)}{dt}$$

$$= \frac{1}{\tau + t_{MTT}} \cdot \left(t_{MTT} \cdot v(t)^{\frac{1}{\alpha}} + \tau \cdot f(t) \right) \tag{5a}$$

Here, α is Grubb's exponent, which describes the stiffness of the vessel. The value of α was experimentally found to be about 0.38 (Grubb et al., 1974; Chen and Pike, 2009) but lower values have also been found, especially for short stimuli (see Uludağ and Blinder, 2018, for an overview). τ indicates the viscoelastic time constant, which controls the duration of transient adjustment of the shape of the venous balloon. The value of the viscoelastic time constant τ is non-zero and thus cerebral blood outflow follows a different curve than the inflow, resulting in a temporal uncoupling of CBF and CBV.

Combining equations 4a, 4b, 4c, and 5 in matrix form we get,

$$\begin{bmatrix} v(t+\Delta t) \\ q(t+\Delta t) \end{bmatrix} =$$

$$\begin{bmatrix} 1 & 0 & \left(\frac{\Delta t}{t_{MTT}} - \frac{\tau \Delta t}{\tau + t_{MTT}}\right) & -\frac{t_{MTT}\Delta t}{\tau + t_{MTT}} & 0 & 0 & 0 \\ 0 & 1 & 0 & 0 & \frac{t_{MTT}\Delta t}{t_{MTT}(\tau + t_{MTT})} & \frac{\tau \Delta t}{t_{MTT}(\tau + t_{MTT})} & \frac{\Delta t}{t_{MTT}} \end{bmatrix}$$

$$\begin{bmatrix} v(t) \\ q(t) \\ f(t) \\ v(t)^{\frac{1}{\alpha}} \\ \frac{q(t)v(t)^{\frac{1}{\alpha}}}{v(t)} \\ \frac{q(t)f(t)}{v(t)} \\ \left(\frac{1-(1-E_0)^{\frac{1}{f(t)}}}{E_0}\right) f(t) \end{bmatrix} \tag{5b}$$

Combining equations 3c and 5b we get,

$$\begin{bmatrix} a(t+\Delta t) \\ f(t+\Delta t) \\ v(t+\Delta t) \\ q(t+\Delta t) \end{bmatrix} =$$

$$\begin{bmatrix} 1-\varphi \Delta t & 0 & 0 & 0 & 0 & 0 \\ \phi \Delta t & 1-\chi \Delta t & 0 & 0 & 0 & 0 \\ 0 & \left(\frac{\Delta t}{t_{MTT}} - \frac{\tau \Delta t}{\tau + t_{MTT}}\right) & 1 & 0 & -\frac{t_{MTT}\Delta t}{\tau + t_{MTT}} & 0 \\ 0 & 0 & 0 & 1 & 0 & \frac{t_{MTT}\Delta t}{t_{MTT}(\tau + t_{MTT})} \end{bmatrix}$$

$$\begin{bmatrix} 0 & 0 \\ 0 & 0 \\ 0 & 0 \\ \frac{\tau \Delta t}{t_{MTT}(\tau + t_{MTT})} & \frac{\Delta t}{t_{MTT}} \end{bmatrix}$$

$$\begin{bmatrix} a(t) \\ f(t) \\ v(t) \\ q(t) \\ v(t)^{\frac{1}{\alpha}} \\ \frac{q(t)v(t)^{\frac{1}{\alpha}}}{v(t)} \\ \frac{q(t)f(t)}{v(t)} \\ \left(\frac{1-(1-E_0)^{\frac{1}{f(t)}}}{E_0}\right) f(t) \end{bmatrix} + \begin{bmatrix} \Delta t \\ 0 \\ 0 \\ 0 \end{bmatrix} x_E(t) + \begin{bmatrix} 0 \\ \chi \Delta t \\ 0 \\ 0 \end{bmatrix} \quad (5c)$$

The above equation 5c can be further simplified in matrix form to:

$$\mathbf{H}(t + \Delta t) = \mathbf{W}_H \boldsymbol{\theta}_H(\mathbf{H}(t)) + \mathbf{W}_{HX} x_E(t) + \omega_H \quad (5d)$$

for which

$$\mathbf{H}(t) = \begin{bmatrix} a(t) \\ f(t) \\ v(t) \\ q(t) \end{bmatrix} \quad (5e)$$

and

$$\boldsymbol{\theta}_H(\mathbf{H}(t)) = \left[a(t)\ f(t)\ v(t)\ q(t)\ v(t)^{\frac{1}{\alpha}}\ \frac{q(t)v(t)^{\frac{1}{\alpha}}}{v(t)}\ \frac{q(t)f(t)}{v(t)}\ \left(\frac{1-(1-E_0)^{\frac{1}{f(t)}}}{E_0}\right) f(t) \right]^T \quad (5f)$$

$\mathbf{W}_H$ is weight matrix of the neurovascular coupling, hemodynamic and Balloon model parameters collectively given by $\mathbf{H}$ (Equation 5e), $\mathbf{W}_{HX}$ is the column matrix connecting the excitatory neuronal response x_E with $\mathbf{H}$ and ω_H is the constant term. $\boldsymbol{\theta}_H(\mathbf{H}(t))$ is the column matrix consisting of the combination of the variables as shown in the equation 5f.

2.1.5. BOLD signal component

The BOLD signal $y(t)$ is determined by $v(t)$ and $q(t)$.

$$y(t) = V_0 \left[k_1 \cdot (1 - q(t)) + k_2 \cdot \left(1 - \frac{q(t)}{v(t)}\right) + k_3 \cdot (1 - v(t)) \right] \quad (6a)$$

$$k_1 = 4.3 \cdot \vartheta_0 \cdot E_0 \cdot TE, \quad (6b)$$
$$k_2 = \varepsilon \cdot r_0 \cdot E_0 \cdot TE,$$
$$k_3 = 1 - \varepsilon$$

Here, V_0 is the resting venous blood volume fraction and k_1, k_2, k_3 are dimensionless constants, which are dependent on the physiological properties of brain tissue and acquisition parameters of the Gradient Echo (GE) sequence. ε refers to the ratio of intra- to extravascular fMRI signal contributions. ϑ_0 symbolizes the field-dependent frequency offset at the outer surface of the magnetized blood vessel for fully deoxygenated blood. r_0 is the regression slope of the relation between the variations in intravascular signal relaxation rate and alterations in oxygen saturation. TE denotes the echo time (in ms). The first term in the equation 6a describes the relationship of the extravascular signal and the deoxyhemoglobin content, the second term of the intravascular signal and the ratio between deoxyhemoglobin content and venous blood volume, and the third term depicts the volume-weighted balance between extravascular and intravascular signals. The values of the parameters in Equation (6b) for various field strengths can be found in Havlicek et al. (2015).

The above equation 6a can be written in the following matrix form:

$$y(t) = \begin{bmatrix} -V_0 k_1 & -V_0 k_2 & -V_0 k_3 \end{bmatrix} \begin{bmatrix} q(t) \\ \frac{q(t)}{v(t)} \\ v(t) \end{bmatrix} + V_0(k_1 + k_2 + k_3) \quad (6c)$$

$$y(t) = \mathbf{W}_{BOLD} \boldsymbol{\theta}_{BOLD} \left(\begin{bmatrix} q(t) \\ v(t) \end{bmatrix} \right) + \omega_{BOLD} \quad (6d)$$

In total, the discretized P-DCM (*d*P-DCM) can be represented using the following set of equations:

$$dP - DCM = \quad (7)$$
$$\begin{cases} \mathbf{X}(t + \Delta t) = \mathbf{W}_X \mathbf{X}(t) + \mathbf{W}_U \mathbf{U}_d(t) \\ \mathbf{H}(t + \Delta t) = \mathbf{W}_H \boldsymbol{\theta}_H(\mathbf{H}(t)) + \mathbf{W}_{HX} x_E(t) + \omega_H \\ y(t + \Delta t) = \mathbf{W}_{BOLD} \boldsymbol{\theta}_{BOLD} \left(\begin{bmatrix} q(t + \Delta t) \\ v(t + \Delta t) \end{bmatrix} \right) + \omega_{BOLD} \end{cases}$$

2.2. Time varying calculations of the model parameters

We have partitioned the time-series (including the inputs and the observed/measured BOLD fMRI responses) into N number of overlapping windows. Each such overlapping window i of duration M seconds moves from left to right as demonstrated in the **Figure 1A**. Please note that for illustration purposes the window size (M) is chosen to be 12 s in the **Figure 1A**. However, it can be easily adjusted and optimized for any given signal-to-noise ratio of the time series. The time course between 0 and 20 s has been magnified to show the overlap of two successive windows centered at 6th second and 7th second, respectively. Considering the total number of samples in a window being T, we have $M = T\Delta t$. Thus, for every second, we have $T/M = 1/\Delta t$ samples (sampling frequency). The stride of these overlapping windows has been set to 1 s.

An unfolded version of the P-DCM-Recurrent Unit architecture through time is shown in the **Figure 1B**. For i^{th} window, the input stimulus to the unit is u_i and the output fMRI BOLD response from the unit is y_i. Each unit corresponds to one window and has four sub-units (components), namely, neuronal, neurovascular Coupling, hemodynamic and BOLD signal components (**Figure 1C**).

Every unit has two operations: (a) Forward Model and (b) Backward Model or Model Inference. In the Forward model, the model parameters and variables are initialized, and the fMRI BOLD response of the model is computed. To reduce the error between the calculated response and the observed fMRI BOLD response, we use model inference (as a part of the generative modeling technique) to update the parameters iteratively using gradient descent (Curry,

1944) until convergence is achieved (typically for 200 iterations or predefined tolerance threshold, usually 10^{-6}). The unit has a similar structure to that of a vanilla Recurrent Neural Network (RNN) (Rumelhart et al., 1985), in which the same unit is being used again and again but with different set of inputs to get different sets of hidden variables and outputs. Please note that in the Forward modeling step, for the first window, we follow zero-mean initializations of the connectivity parameters as recommended by Friston et al. (2003), Havlicek et al. (2015). This has been done owing to the following reasons: (i) to ensure stability of the system (Friston et al., 2003), (ii) we compare task modulation with control condition, and therefore only the changes in baseline connectivity are of interest.

For any window i, we employ a dP-DCM-RU, which takes in input stimuli (for that window) and fits output BOLD responses (for the same window). In doing so, latent (e.g., neuronal, hemodynamic, vascular) responses are generated and parameters (e.g., connectivity) are inferred. Therefore, for any window i ($i \in \{0, 1, 2, \ldots, N-1\}$), this set can be represented as: $g_i = \{\mathbf{X}_i, \mathbf{H}_i, \mathbf{W}_{Xi}, \mathbf{W}_{Ui}, \mathbf{W}_{Hi}\mathbf{W}_{HXi}\mathbf{W}_{BOLDi}\}$(see **Figures 1B, C** and Equation 8 below). The values of these parameters serve as the starting values or initializations for the next, i.e., $(i+1)^{th}$ window. In other words, the parameters for window $(i+1)$ are initialized with the predicted values for its previous window i, preserving continuity between adjacent windows. It is to be noted that before performing model inversion, we do zero-padding with half-window length on each end of the data so that we can cover the entire extent of the actual signal. Therefore, the computed connectivity at every window is centered at that window.

The output of each dP-DCM recurrent unit is the fMRI BOLD response. A recurrence is being followed because the same unit with different parameter values repeatedly performs the same task or operation (on input sequences) till the final window.

Dynamic effective connectivity is estimated using overlapping windows. That is, partitioning the time-series (including the inputs and the observed/measured BOLD fMRI responses) into N number of overlapping windows such that $\forall\, i \in \{0, 1, 2, \ldots, N-1\}$, we get:

$$dP - DCM_i = \tag{8}$$

$$\begin{cases} \mathbf{X}_i(t+\Delta t) = \mathbf{W}_{Xi}\mathbf{X}_i(t) + \mathbf{W}_{Ui}\mathbf{U}_{di}(t) \\ \mathbf{H}_i(t+\Delta t) = \mathbf{W}_{Hi}\boldsymbol{\theta}_{Hi}(\mathbf{H}_i(t)) + \mathbf{W}_{HXi}x_{Ei}(t) + \omega_{Hi} \\ y_i(t+\Delta t) = \mathbf{W}_{BOLDi}\boldsymbol{\theta}_{BOLDi}\left(\begin{bmatrix} q_i(t+\Delta t) \\ v_i(t+\Delta t) \end{bmatrix}\right) + \omega_{BOLDi} \end{cases}$$

A schematic illustrating the updates of the neuronal, neurovascular, hemodynamic, and BOLD variables (following the above Equation 8) in each dPDCM recurrent unit has been shown in the **Figure 1C**. Our proposed workflow has also been demonstrated in **Figure 2** in a nutshell.

3. Simulations set-up and results

To check the face validity of the approach, first, we simulated connectivity profiles for 3- and 10-region graphical models (representing cognitive hypotheses), to show the ability of dP-DCM-RU to estimate dynamic effective connectivity and to distinguish different causal functional graphs using model evidence for a simple and a complex case, respectively.

3.1. Three-region model

3.1.1. Case a: Time-varying connectivity

This model comprises three regions (R1, R2, and R3) (as shown in **Figure 3A**). A sinusoidal input u is applied to R1 which then activates R2 and R3. Area-specific time-varying fMRI BOLD responses, given as a percentage signal change are shown in the **Figure 3B**. The colored boxes correspond to the recurrent window size for each of these time courses.

3.1.1.1. Forward simulation

In this example, we have considered a fast-varying connection from R1 to R2 and a slow-varying connection from R1 to R3. The assumed connectivity time courses between R1 and R2 and between R1 and R3 are shown in **Figure 4A** (colored plots). **Supplementary Table 1A** shows the piece-wise continuous functions used to simulate the connectivity values. The effective connectivity as a function of time (t) is denoted as $eff\_conn(t)$. Using the simulated connectivity pattern, we get the corresponding area-specific fMRI BOLD responses as shown in the **Figure 4B** (colored plots). The value of Δt is 1/32s for all simulations (Wang et al., 2018). For all other parameters of the model, we please see **Supplementary Table 1B** (also please refer to **Supplementary Table 1A** of Havlicek et al., 2015).

3.1.1.2. Model inversion

For this model inversion, we assume the same connectivity graph as was used for the forward simulation. In **Figure 4**, the black dashed lines represent the predicted estimates from the model on top of the colored ground truth (i.e., forward simulated) values. It can be noticed that for both connectivity time courses (**Figure 4A**) and fMRI BOLD responses (**Figure 4B**) the fitting is highly accurate, with slight inaccuracies in the effective connectivity estimates during the initial rise and during return to baseline, indicating that sharp increases or decreases are smoothed out in the BOLD signal and model inversion.

The Normalized Root Mean Squared Error [NRMSE (Shcherbakov et al., 2013)][1] value averaged over the two connections (R1 and R2, R1 and R3) is 2.14% and the NRMSE value averaged over the fMRI BOLD responses from the three regions (R1, R2, and R3) is 0.91%. We have repeated the above simulation set-up for a higher frequency input and have done corresponding model inversion, whose results have been provided in the **Supplementary Section 1.1.1**.

3.1.1.3. Model comparison

To show a noticeable difference in performance between two models during model comparison, we have considered an additional scenario. In this scenario, we have considered 2 competing hypotheses models m_1 and m_2 as shown in **Figures 5A**, B. In m_1, *driving* input u_1 (in red) is applied to R1, which is connected to both R2, and R3. Feedback connection exists from R2 to R1, which is influenced by *modulatory* input u_2 (in purple). In m_2, driving input u_1 is applied to R1, which is connected to R2, which in turn is connected to R3. Feedback connection exists from R3 to R2. Connection from R2 to R3 is modulated by input u_2. Hypothesis model m_1 has been used for generating the ground truth BOLD data.

1 NRMSE is defined as the ratio of Root Mean Squared Error (RMSE) to the difference between the maximum and minimum values of the ground truth data (Shcherbakov et al., 2013).

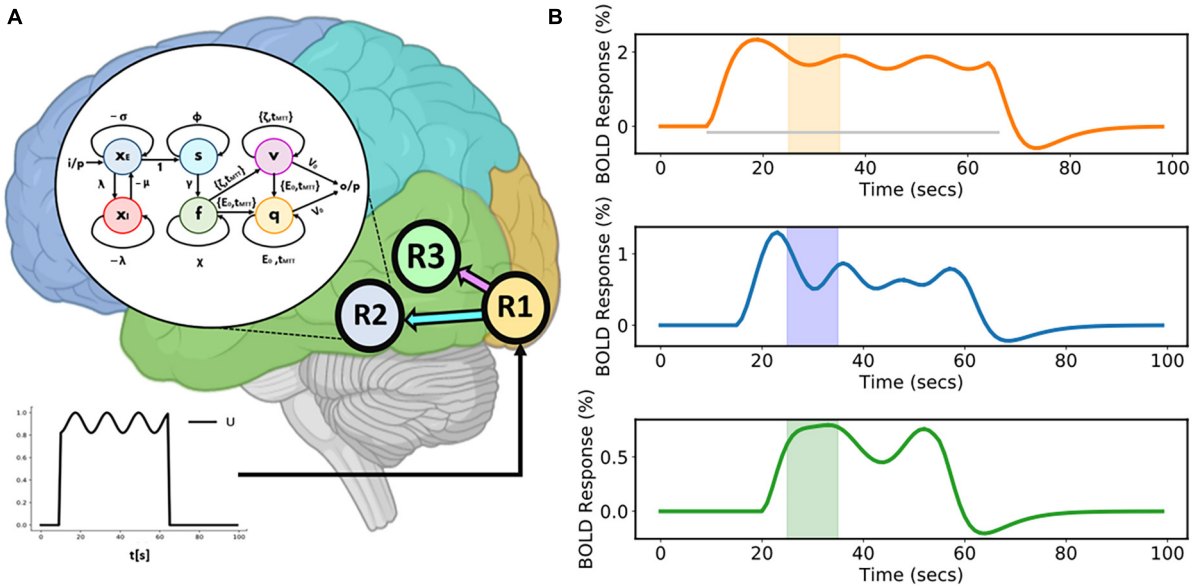

FIGURE 3
Three-region model and corresponding area-specific simulated functional magnetic resonance imaging (fMRI) blood oxygenation level-dependent (BOLD) responses. **(A)** Three-region model for which connections exist from Region 1 (R1) to Region 2 (R2) and from Region 1 (R1) to Region 3 (R3). The sinusoidal input *u* is applied to R1 and then activity propagates to both R2 and R3. The model inside the white circle (with black border) shows the internal sample model representation of R2. **(B)** Corresponding area-specific simulated fluctuating fMRI BOLD time courses with windows centered at the 30th second. The gray horizontal line represents the duration of the input stimulus.

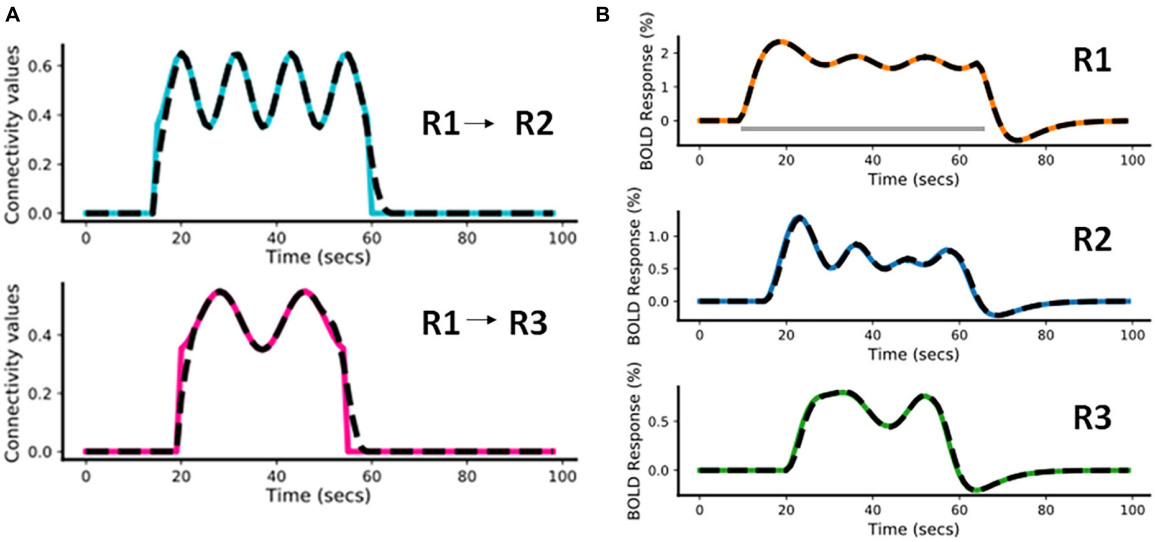

FIGURE 4
Predicted estimates along with the ground truth values for Case a. The black dashed lines represent the predicted responses and the colored time courses are the ground truth values. **(A)** Connectivity time courses, **(B)** area-specific functional magnetic resonance imaging (fMRI) blood oxygenation level-dependent (BOLD) time courses each expressed as a percentage change in response. The gray horizontal bar represents the stimulus duration.

3.1.1.3.1. Predictions using m_1 and m_2

In Figures 5A, B, the black dashed lines represent the predicted estimates from the model on top of the colored ground truth (simulated) values.

For m_1, it can be noticed that the fitting of the BOLD responses is accurate for all three regions (Figure 5A). The NRMSE value for this reconstructed fMRI BOLD time-series with respect to the ground truth time-series is 1.45%. For m_2, the errors of the predicted BOLD responses are higher compared to those of m_1 (Figure 5B). This can be attributed to the absence of feedback connection from R2 to R1 in model m_2. The NRMSE value[2] thus has increased to 10.31%. Hence, in terms of accuracy, m_1 performed better than m_2, ΔNRMSE

2 In noiseless cases, as in some of the current simulations, Free Energy (Friston et al., 2003) formulation cannot be utilized. Instead, NRMSE values between the fits (with respect to ground truth) obtained using different models can be used to indicate, which model is more accurate than the other. NRMSE is independent of the signal strength or amplitude and therefore, a more robust indicator of accuracy (while comparing different models) than RMSE.

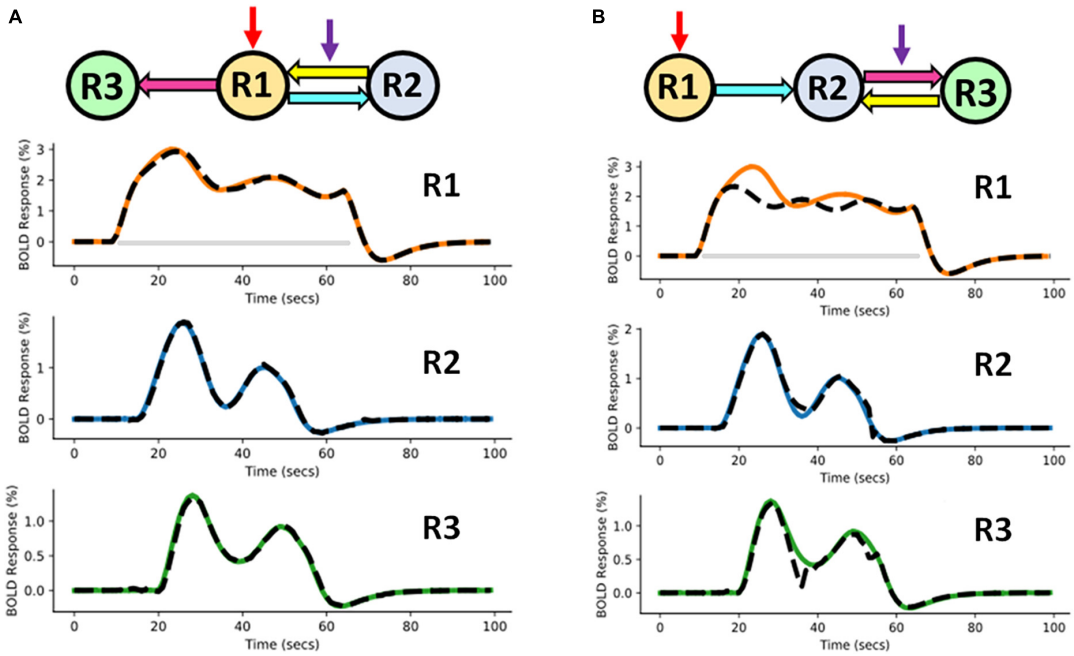

FIGURE 5
Competing hypotheses models **(A)** m_1 (ground truth model) and **(B)** m_2 (randomly chosen model) along with the corresponding area-specific functional magnetic resonance imaging (fMRI) blood oxygenation level-dependent (BOLD) responses. The black dashed lines represent the predicted responses and the colored time courses are the ground truth values. The red and purple arrows represent direct and modulatory inputs, respectively.

(= NRMSE_{m2}–NRMSE_{m1} = 8.86%) is high. This demonstrates that our method is able to adequately distinguish between two cognitive hypotheses.

In addition to the above m_2, we have the also evaluated performances of 10 more three-region models with randomly chosen configurations (**Supplementary Section 1.1.2**). ΔNRMSE values of these models with respect to m_1 (**Supplementary Figure 2**) clearly show that m_1 is superior in terms of performance and m_2 is one of the less inferior models in the group (m_2–m_{12}).

3.2. 10-region model

In a typical fMRI experiment, more than three brain areas are active. Thus, to demonstrate scalability, we evaluated a 10-region model as shown in the **Figure 6** (center). The connectivity graph for the forward simulation is illustrated in the **Supplementary Figure 4** (colored plots). Two time-varying inputs u_1 and u_2 (see **Supplementary Figure 3**) are applied to R1 and R2, respectively (see **Figure 6** for the time courses). There is a delay of 20 s between these two inputs (see **Supplementary Figure 3**). Activity then propagates from R1 and R2 to the remaining regions.

3.2.1. Forward simulation

The assumed connectivity time courses are shown in the **Supplementary Figure 4** (colored plots). Using the model and the connectivity time courses, we get the corresponding area-specific fMRI BOLD responses.

3.2.2. Model inversion

In both **Figure 6** and **Supplementary Figure 4**, the black dashed lines represent the predicted estimates from the model on top of the colored ground truth (simulated) values. The prediction has a low NRMSE value (averaged over all the 10 regions) of 1.17%. The predicted connectivity time courses are also shown in **Supplementary Figure 4**. As can be seen, the predictions follow the ground truth time courses very closely for all brain areas.

3.2.3. Model comparison

For model comparison purposes, we additionally performed model inversion for randomly selected model m_2 as shown in **Figure 7** (center).

3.2.3.1. Prediction using m_2

In **Figure 7**, the black dashed lines represent the predicted estimates from the model on top of the colored ground truth (simulated) values. Please notice that for fMRI BOLD responses the reconstruction and hence the fitting is good in the earlier brain areas, such as R1 and R2, but the discrepancies become more pronounced and errors larger for the later brain areas. The predicted connectivity time-courses are shown in **Supplementary Figure 5**. The NRMSE value (averaged over all the regions) for this reconstructed fMRI BOLD time-series with respect to the ground truth time-series is 25.75%. Hence, in terms of accuracy, m_1 performed better than m_2, ΔNRMSE (= NRMSE_{m2}–NRMSE_{m1} = 24.58%) is high showing that our method can sufficiently differentiate between two cognitive hypotheses. Additionally, we have also considered another 10-region model with reciprocal connections and have performed corresponding model inversion with a randomly chosen configuration as shown in the **Supplementary Section 3**, confirming that m_1 can be distinguished from a model with erroneous connectivity graphs.

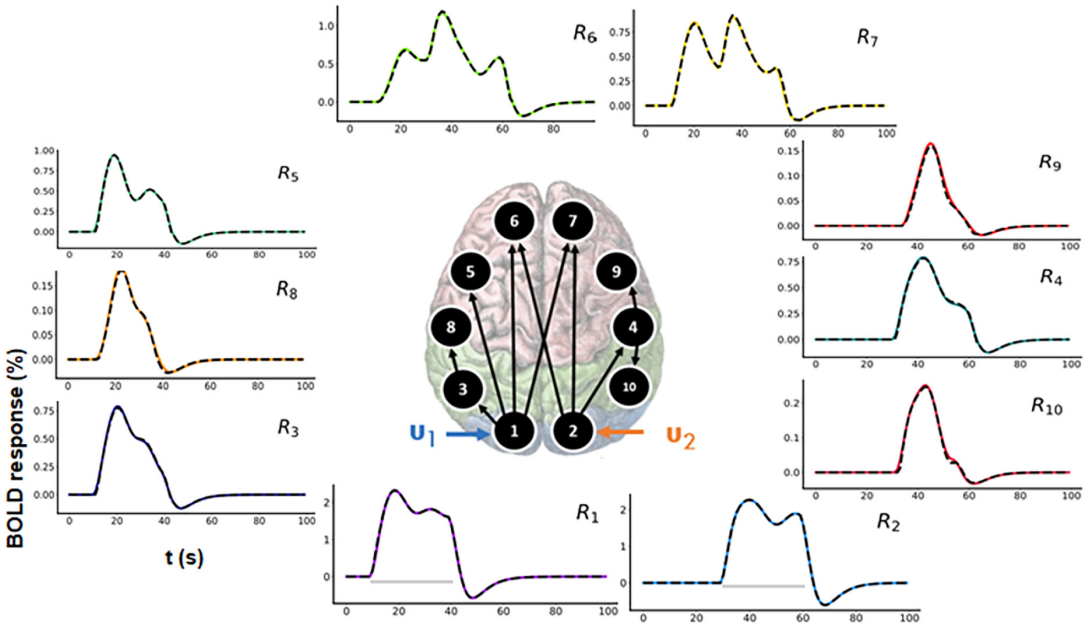

FIGURE 6
Functional magnetic resonance imaging (fMRI) blood oxygenation level-dependent (BOLD) time courses for 10-region model where connections exist between R1 to R3, R3 to R8, R1 to R5, R1 to R6, R1 to R7, R2 to R6, R2 to R4, R4 to R9, and R4 to R10. Two time-varying inputs u_1 and u_2 are applied to R1 and R2, respectively. The black dashed lines represent the predicted responses, and the colored lines represent the simulated time courses.

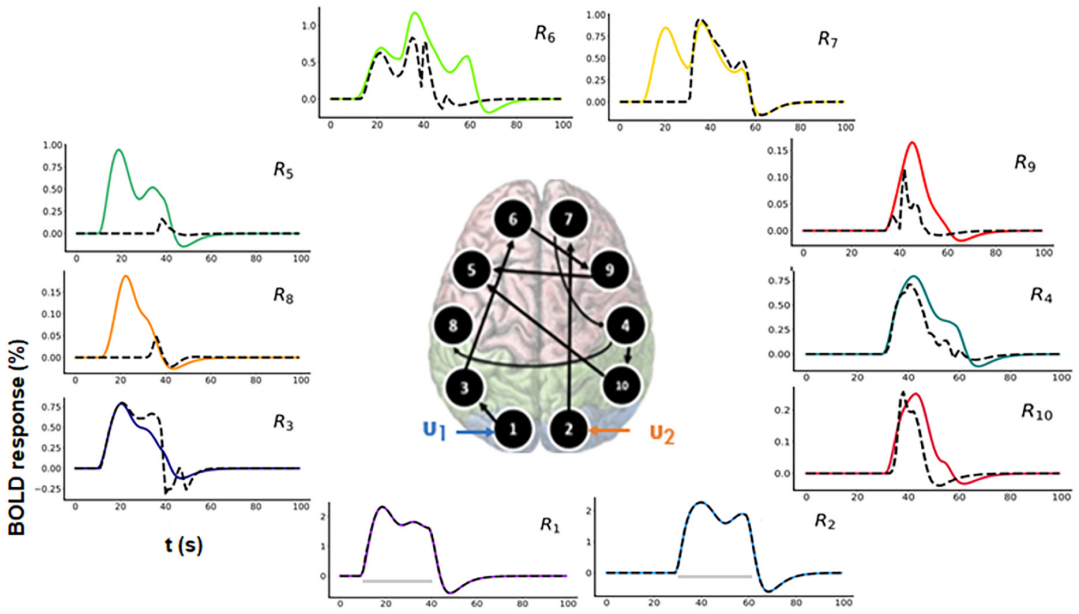

FIGURE 7
Predicted area-specific functional magnetic resonance imaging (fMRI) blood oxygenation level-dependent (BOLD) time courses along with the ground truth values for m_2 which is a randomly chosen model. The black dashed lines represent the predicted responses and the colored time courses are the ground truth values. There are fitting inconsistencies for R3, R4, R5, R6, R7, R8, R9, and R10 fMRI BOLD time courses.

4. fMRI BOLD time courses with measurement noise

In this case, we have used two models- a Three-region model (from "section 3.1.1 Case a: Time-varying connectivity") as a simple model and a 10-region model (from "section 3.2.1 Forward simulation") as a complex model. Here, the fMRI BOLD time courses are noisy with measurement or physical noise being present. Measurement or physical noise is an external noise which gets added to the signal while it is being acquired. For simulation purposes, this measurement noise used by us is a zero mean gaussian random noise with varying levels of standard deviation. Contrast-to-Noise Ratio (CNR) values were computed with respect to the ground truth values for fMRI BOLD responses. It is worth noting that we have

defined CNR as the ratio between the standard deviation of the signal and the standard deviation of the noise (Definition four of CNR, Welvaert and Rosseel, 2013) and this definition is consistent with the previous DCM works (Friston et al., 2003; Frässle et al., 2017)[3].

The extracted fMRI time series stem from Principal Component Analysis (PCA) over numerous voxels in local volumes of interest which suppresses noise (Frässle et al., 2017). Therefore, as outlined in Frässle et al. (2017), the typical CNR levels (SNR in DCM terminology, see footnote 3 for further clarification) of fMRI time series used for DCM are three or more. It is to be noted that this value is highly dependent on the tasks and brain areas investigated. That is, for some tasks and/or brain areas, DCM and its variants and the derived connectivity values are unreliable. This is already true for DCM estimating only one connectivity profile for a run and even more so for estimation of time-varying connectivity. Please note that this is also true for estimation of time-varying functional connectivity using resting-state. That is, it is not our claim that our approach (and no other statistical approach) will work for any task and/or brain area or any MRI acquisition parameters (such as field strength, sequence, etc.) but only if certain conditions, such as CNR levels, are met that time-varying effective connectivity can be estimated using our approach. Therefore, we have conducted the simulations for 3- and 10-region models with different CNR values [CNR = (1, 3, 5, 10, 20)] and repetition times [TR = (4, 2, 1, 0.25, 0.1 s)]. In each case, we resampled (*via* linear interpolation) the timeseries to sampling frequency of 32 Hz resulting in an increase in the number of samples[4]. Using our method, we did model inversions for each of these settings for both three-region and 10-region models. We compared the estimated effective connectivity time courses to those of the simulated ground truth using Normalized Root Mean Squared Error (NRMSE), expressed as a percentage (%) as shown in **Figure 8**. We repeated the above setup for 10 runs with newly sampled noise and reported the mean and standard deviations (s.d.) of the NRMSE values over these 10 runs in **Figure 8**.

We make the following two major observations for both three-region (**Figure 8A**) and 10-region (**Figure 8B**) models:

(i) The respective NRMSE values decrease with increase in the CNR levels for each TR setting. Moreover, at any TR value we observe that the standard deviations decrease with an increase in the CNR level, as expected. This indicates that the reliability of predictions increases toward high CNR values (i.e., when the data is less noisy).

(ii) The corresponding NRMSE values decrease with a decrease in the TR value for each CNR level. Notably, at any CNR level, the standard deviations also typically decrease with a decrease in the TR value (i.e., when the sampling rate is high) indicating more reliable predictions.

3 There exist several definitions of SNR and CNR: SNR is typically defined as the ratio of the mean of the fMRI signal to the standard deviation during baseline. However, the one that is predominantly used in the DCM literature is given as the ratio between the standard deviation of the signal and the standard deviation of the noise. This definition is the same as the Definition 4 of CNR in Welvaert and Rosseel, 2013. Therefore, following Welvaert and Rosseel, 2013, we will be using CNR terminology in our paper.

4 We have used linear interpolation technique for upsampling/resampling. Other interpolation/resampling methods (cubic, spline, etc.) and resampling frequencies have not been explored and it is beyond the scope of the current paper.

5. Discussion

The fMRI signal is an indirect reflection of neuronal activity, mediated by neurovascular coupling and hemodynamics. Generative models describe the biophysical basis underlying fMRI and present a framework to interpret empirical observations. Through model inversion, generative models enable investigations of underlying neuronal dynamics and functional integration in the brain. One such state-of-the-art generative model is the Physiologically informed Dynamic Causal Modeling (P-DCM, Havlicek et al., 2015). Most existing DCM studies (Friston et al., 2003; Stephan et al., 2008; Moran et al., 2009; Havlicek et al., 2015) typically consider the effective connectivity to be static for a cognitive task within an experimental run. However, experimental conditions can vary with time, especially in cases of complex stimuli, e.g., movie, music, etc. Consequently, the connectivity strengths between disparate brain regions involved in processing these complex stimuli may fluctuate with time. Please note that in the conventional DCM framework (Friston et al., 2003; Stephan et al., 2008; Moran et al., 2009), it may also be possible to model dynamic connectivity by utilizing dynamic **B** or **C** matrices (please refer to Equations 2a–f for definition of **B** and **C**). However, such an approach requires prior knowledge of the time-varying connectivity profiles and just estimates the strength of these dynamic connectivity predictors. In contrast, our method does not require prior knowledge of connectivity profiles.

In the recent years, there has been an increasing number of studies to elucidate the dynamic (functional) connectivity in fMRI by investigating the temporal correlations of resting-state BOLD fluctuations in distributed brain areas (Cribben et al., 2012; Handwerker et al., 2012; Calhoun et al., 2014; Monti et al., 2014). In such Dynamic Functional Connectivity (DFC) studies, one of the predominant methods is to employ a sliding window-based approach to find the time-varying correlations (Chang and Glover, 2010; Kiviniemi et al., 2011; Jones et al., 2012). However, lacking a generative model, the correlations between the areas are determined on the level of observations but not on the level of the underlying causes (Stephan et al., 2010). In contrast, DCM accounts for the indirect nature of the BOLD signal and fits BOLD signals in the different ROIs using a system of differential equations (Friston et al., 2003; Stephan et al., 2008; Havlicek et al., 2015, Havlicek et al., 2017b).

In this paper, we have introduced *discretized* Physiologically Informed Dynamic Causal Model with Recurrent Units (*d*P-DCM-RU) to characterize dynamic effective connectivity of various brain regions during tasks. This method is a combination of two approaches, namely, a Euler based discretization technique and a recurrent sliding window approach for dynamically modeling fMRI BOLD responses and for exploring the causal interactions between different neuronal populations. To validate, we have carried out simulations with 3- and 10-region models. To that end, we have decomposed effective connectivity into static and dynamic components. The static component acts as a baseline component and the dynamic component varies with time sinusoidally. However, please note that our recurrent window-based parameter estimation method can predict any connectivity profiles.

For the Three-region model, we have considered two different connectivity graphs. Using the first example, we have simulated *noiseless* time-varying effective connectivity between the regions. The results show that the fits of fMRI BOLD responses and the effective connectivity have low error values, compared to the ground truth

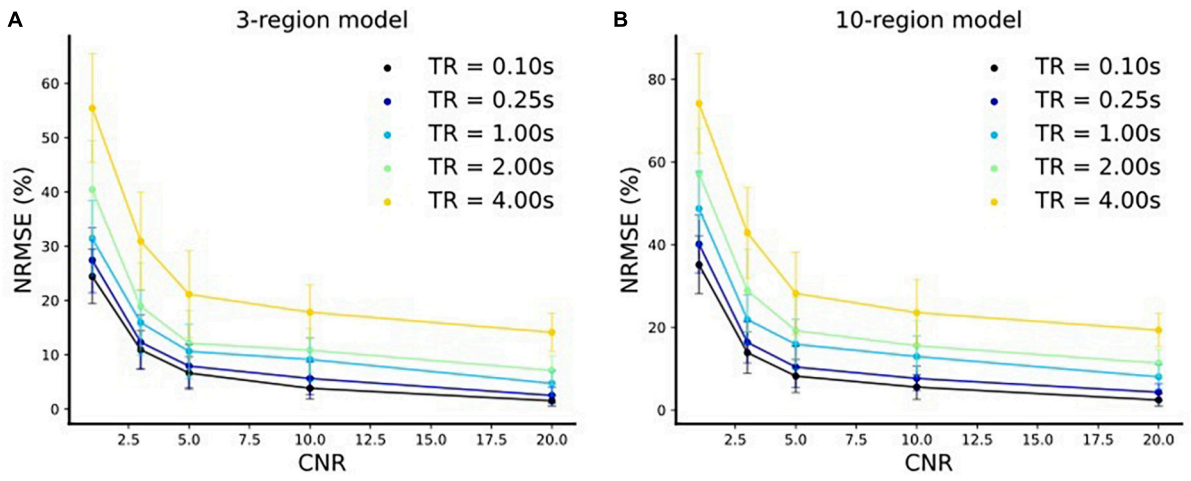

FIGURE 8
Normalized Root Mean Squared Error (NRMSE) (mean ± s.d.) expressed as a % vs. CNR for. **(A)** Three-region model and **(B)** 10-region model for five different repetition time (TR) settings.

(i.e., forward simulated) BOLD responses. This is not a trivial result as even assuming the correct connectivity graphs does not guarantee model invertibility due to potential ill-posed problem.

To show a noticeable difference in performance between models during model comparison, we have selected another example scenario (Three-region model) with feedback from R2 to R1 modulated by an input (i.e., the ground truth model, m_1) and 11 randomly chosen models for comparison. Results show that the randomly chosen models did not perform well in terms of fitting accuracy values (given by NRMSE) relative to the ground truth model (m_1). The results indicate a clear distinction between the hypothesis models and demonstrates that the *d*P-DCM-RU approach does not necessarily guarantee a good fit to any BOLD signal and is therefore capable of distinguishing models.

Typically, more than three brain regions are active during a complex cognitive task. Therefore, to illustrate a more complex case, we have performed simulations for a 10-region model (also see 10-region model example with reciprocal connections in the **Supplementary Section 3**). Results clearly suggested that the method was able to predict effective connectivity with low error values and to fit fMRI BOLD responses with high accuracy. We did model a competing 10-region connectivity graph (hypothesis model) for comparison. Model inversion results demonstrated that this randomly chosen hypothesis model was unable to reconstruct fMRI BOLD signals accurately leading to large deviation values from the ground truth fMRI BOLD responses, in particular, in areas most distant from the input areas. In this 10-region example ("section 3.2 10-region model"), we did not provide any delay between the input and connectivity (e.g., R1 to other regions). However, the window/duration of connectivity and input do not necessarily have to match. That is, connectivity from a certain brain region to another brain region may change from baseline value later than the input depending on the experiment (for such an example, please refer to "section 3.1.1 Case a: Time-varying connectivity").

In addition, we have considered noisy scenarios by adding measurement noise (see "section 4 fMRI bold time courses with measurement noise"). We have conducted simulations for 3- and 10-region models with different Contrast-to-Noise Ratio (CNR) values [CNR = (1, 3, 5, 10, 20)] and repetition times [TR = (4, 2, 1, 0.25, 0.1 s)]. We observed that the connectivity prediction error decreases and the reliability of predictions increases with an increase in CNR and a decrease in TR values, respectively (see **Figure 8**). Depending on the threshold for accuracy used, estimation of dynamic connectivity using our method may be prohibited (the same argument also applies for dynamic functional connectivity calculation). In the cases of low CNR and high TR values, standard denoising procedures may be used, which may lead to less erroneous and more reliable parameter estimates.

One of the foremost limitations of DCM in general is that they are restricted to a fixed number of regions because of their computational demand (Frässle et al., 2017). In particular, the number of coupling parameters (i.e., connectivities) grows quadratically with the number of nodes, and therefore the computational time required to invert these models grows exponentially with the number of free parameters (Seghier and Friston, 2013; Frässle et al., 2017). Since our method is based on the P-DCM framework, the above problem also persists in our case. Additionally, the windowing scheme makes the approach even more computationally intensive. Furthermore, higher-order integrators are potentially slow in practice and computational (memory) requirements become even larger because of explicit Jacobian-based update schemes, which are evaluated numerically at each time point (Friston et al., 2003). Therefore, to increase computational speed and reduce memory, we utilize the lower-order Euler method. However, a disadvantage of the Euler method compared to higher order ODE solvers is lower numerical accuracy. Nevertheless, the numerical errors can be kept low for small step size Δt values. Following Wang et al. (2018), we have assessed the impact of different step sizes for the three-region model. As illustrated in the **Supplementary Figure 10**, NRMSE is the lowest (with a value of 0.82%) for Δt = 1/32 s and it increases (more than linearly) with step-size (e.g., for Δt = 1/4 s, NRMSE = 19.97%). Hence, we selected Δt = 1/32 s for all our simulations.

Another challenge for *d*P-DCM-RU is the selection of optimal window size. If the window sizes are too large, then the transients may not be captured, whereas too small window sizes may lead to overfitting of the model (Sakoğlu et al., 2010; Shakil et al., 2016).

We investigated the effect of window sizes on the (three-region) model performance given in terms of NRMSE (%). **Supplementary Figure 11** shows that for a window size of 5 s, NRMSE is low (1.45%), whereas model performance substantially degrades for a window size of 11 s (NRMSE increases to 22.68%). However, the window size can be easily adjusted to the complexity of the experimental design. A 5 s window size worked well for varying connectivity chosen in our simulations (**Supplementary Figure 11**). Please note that—as the BOLD signal can be represented as a smoothing kernel—very fast neuronal dynamics cannot be recovered by fMRI for any window size, independent of acquisition speed and analysis method (Polimeni and Lewis, 2021).

Park et al. (2018), Zarghami and Friston (2020) have proposed dynamic functional connectivity estimation frameworks for resting state fMRI (rs-fMRI). Park et al. (2018) utilized discrete cosine transform eigenvariates and Hierarchical Parametric Empirical Bayes (PEB) approach (Friston et al., 2016) to model dynamic functional connectivity at two levels. In the first level, they have inverted a spectral DCM (spDCM) separately for each window to obtain (within-window) connectivity parameters. Subsequently, in the second level they have applied PEB to estimate between-window effects on these connectivity parameters. Motivated by the nonlinear dynamical systems theory, Zarghami and Friston (2020) proposed a hybrid generative framework consisting of Hidden Markov Model (HMM), PEB and spDCM (discrete and continuous hierarchical models) to explain metastable dynamics in the brain via modeling the temporal evolution of different connectivity states. Their paradigm utilized the variational message passing technique, for which the HMM provided Bayesian model averages for the intermediate PEB level, which successively supplied priors to each spDCM. In this manner, by assigning an itinerant prior to the state-transition matrix, they estimated the transition and state-dependent effective connectivity parameters. On the contrary, our approach ("section 2.2 Time varying calculations of the model parameters") neither requires "two-level" connectivity estimation nor involves a "hybrid" generative approach. Furthermore, these previous studies have typically considered larger window sizes for their estimations, which they have shown to work well for rs-fMRI. It is important to note that in contrast to our approach, these works do not capture the entire temporal extent of connectivity dynamics (i.e., connectivity values do not exist for all time-points) and are only suitable for tracking slow dynamics (Park et al., 2018, Zarghami and Friston, 2020). Furthermore, our method considers the stride of the overlapping windows to be 1 s and, therefore, covers the entire extent of the signal (in the order of seconds), and is able to track relatively faster dynamics (as demonstrated in **Figure 4**, where we have considered slow and fast varying connectivities). Finally, our work deals with task-based fMRI and not rs-fMRI.

Another recent work (Wang et al., 2018) utilizing Recurrent Neural Networks (RNNs) (Rumelhart et al., 1985; Hochreiter and Schmidhuber, 1997) proposed a biophysically interpretable DCM-RNN. Although both *d*P-DCM-RU and DCM-RNN take inspiration from the recurrence concept as in RNNs, DCM-RNN differs from *d*P-DCM-RU in many aspects: In their method, they have used Truncated Backpropagation Through Time (TBPTT) for computing parameter updates, whereas we have simply used gradient descent as done in standard DCM implementations (Havlicek et al., 2015). Their definition of recurrence is the same as in standard RNNs utilizing segmented batches. Therefore, they have used multiple batches in *parallel* (as in deep learning) and updated model parameters *via* TBPTT. To ensure that the gradients obtained by TBPTT are reliable, each of these segments has to be sufficiently long and the sampling time has to be sufficiently small. Since they use parallel batches for parameter update, the gradients may often not be accurate (Wang et al., 2018). This is because each of those batches does not represent the characteristic of the whole signal. Due to this batch *parallel* processing, they can only estimate *static* connectivity. In our case, the recurrence lies between the successive P-DCM units. We do *sequential* processing of each such unit estimating time-varying connectivity parameters. Furthermore, unlike DCM-RNN, we have used the state-of-the-art DCM model, i.e., P-DCM (Havlicek et al., 2015) in our framework instead of Single-State DCM (S-DCM) (Friston et al., 2003). Finally, the authors of DCM-RNN claimed that their model can be extended for complex paradigms such as movie watching using representations of the complex stimuli. However, at this stage their model cannot estimate dynamic connectivity without further modifications.

One of the major DCM steps is to conduct a Model Selection (using group Bayes factor) between several alternative competing models to establish which model accounts best for the experimental observations. After selection of the optimal model, making further inferences about its parameter estimates (e.g., connectivity) is typically not done in DCM studies and usually some statistical values (e.g., mean) of the parameter estimates for the group is reported (Stephan et al., 2009). However, inferences about model parameters can still be made with either a fixed effects or a random effects approach. For fixed effects parameter inference, a common way is to use Bayesian average (for example "DCM average" function in SPM) (Friston et al., 1994). For random effects parameter inference, subject-specific parameter estimates can be used with a classical frequentist test, such as a paired *t*-test (between model parameters) or repeated measures ANOVA in case of multiple sessions per subject (Stephan et al., 2009).

It is important to note that our proposed method is not necessarily restricted to block designs. Naturalistic stimulus typically comprises block (e.g., fluctuation of light intensity) and event-related (e.g., presence of face for a limited period of time) components. However, that due to sluggishness of the hemodynamic response, very fast events may not be detected, similarly as in standard fMRI data and analysis. Please note that our approach can be used with arbitrary time-varying inputs and the choice of sinusoidal inputs (in our simulations) is for illustrative purposes and can easily be modified.

In our approach, the estimates from the previous window serve as the initial values (and not constraints) for the next window. Therefore, the model gets a good starting point which makes it easier to optimize. However, for any window, model inversion is performed independently, therefore, an estimation error in the previous window will unlikely be reflected in the next window. Furthermore, for optimization we have resorted to using the conventional gradient based scheme, i.e., gradient descent. Although gradient descent can potentially be slow, it has a better generalization performance (Zhou et al., 2020). Alternatively, one can use momentum based (Sutskever et al., 2013) or adaptive algorithms (Kingma and Ba, 2015) to further speed up performance while maintaining accuracy (Ruder, 2016). Nonetheless, we have not explored different optimization algorithms and strongly feel that it is beyond the scope of the current paper since this is a general topic for all DCM and model inversion approaches and not specific to our paper. To summarize, when a subject is

exposed to a complex stimulus (e.g., watching a movie), human brains show dynamic effective connectivity between remote areas on the neuronal level, which can be indirectly measured using fMRI and which can be effectively recovered using the *d*-PDCM-RU approach. In the future, we will demonstrate the validity of our method in clinical and cognitive neuroscience studies.

Data availability statement

The original contributions presented in this study are included in the article/**Supplementary material**, further inquiries can be directed to the corresponding authors.

Author contributions

SN and KU made substantial contributions to the conceptualization, methodology, design of the experiments, data analysis, visualization, and drafting the manuscript. Both authors provided final approval of the submitted version of the manuscript.

Funding

This study was supported by the Institute for Basic Science, Suwon, Republic of Korea (IBS-R015-D1) to KU.

Acknowledgments

We thank Labeeb Talukder and Shawn Carere for their constructive feedbacks on the manuscript.

Conflict of interest

The authors declare that the research was conducted in the absence of any commercial or financial relationships that could be construed as a potential conflict of interest.

Publisher's note

All claims expressed in this article are solely those of the authors and do not necessarily represent those of their affiliated organizations, or those of the publisher, the editors and the reviewers. Any product that may be evaluated in this article, or claim that may be made by its manufacturer, is not guaranteed or endorsed by the publisher.

Supplementary material

The Supplementary Material for this article can be found online at: https://www.frontiersin.org/articles/10.3389/fnhum.2023.1001848/full#supplementary-material

References

Attwell, D., Buchan, A. M., Charpak, S., Lauritzen, M., MacVicar, B. A., and Newman, E. A. (2010). Glial and neuronal control of brain blood flow. *Nature* 468, 232–243.

Buxton, R. B. (2012). Dynamic models of BOLD contrast. *Neuroimage* 62, 953–961.

Buxton, R. B., and Frank, L. R. (1997). A model for the coupling between cerebral blood flow and oxygen metabolism during neural stimulation. *J. Cereb. Blood Flow Metab.* 17, 64–72. doi: 10.1097/00004647-199701000-00009

Buxton, R. B., Uludağ, K., Dubowitz, D. J., and Liu, T. T. (2004). Modeling the hemodynamic response to brain activation. *Neuroimage* 23, S220–S233.

Calhoun, V. D., Miller, R., Pearlson, G., and Adalı, T. (2014). The chronnectome: Time-varying connectivity networks as the next frontier in fMRI data discovery. *Neuron* 84, 262–274. doi: 10.1016/j.neuron.2014.10.015

Chang, C., and Glover, G. H. (2010). Time–frequency dynamics of resting-state brain connectivity measured with fMRI. *Neuroimage* 50, 81–98.

Chen, J. J., and Pike, G. B. (2009). BOLD-specific cerebral blood volume and blood flow changes during neuronal activation in humans. *NMR Biomed.* 22, 1054–1062.

Cribben, I., Haraldsdottir, R., Atlas, L. Y., Wager, T. D., and Lindquist, M. A. (2012). Dynamic connectivity regression: Determining state-related changes in brain connectivity. *Neuroimage* 61, 907–920.

Curry, H. B. (1944). The method of steepest descent for non-linear minimization problems. *Q. Appl. Math.* 2, 258–261.

Daunizeau, J., Friston, K. J., and Kiebel, S. J. (2009). Variational Bayesian identification and prediction of stochastic nonlinear dynamic causal models. *Phys. D* 238, 2089–2118. doi: 10.1016/j.physd.2009.08.002

Devor, A., Tian, P., Nishimura, N., Teng, I. C., Hillman, E. M., Narayanan, S. N., et al. (2007). Suppressed neuronal activity and concurrent arteriolar vasoconstriction may explain negative blood oxygenation level-dependent signal. *J. Neurosci.* 27, 4452–4459. doi: 10.1523/JNEUROSCI.0134-07.2007

Finn, E. S. (2021). Is it time to put rest to rest? *Trends Cogn. Sci.* 25, 1021–1032.

Frässle, S., Lomakina, E. I., Razi, A., Friston, K. J., Buhmann, J. M., and Stephan, K. E. (2017). Regression DCM for fMRI. *Neuroimage* 155, 406–421.

Friston, K. J. (2011). Functional and effective connectivity: A review. *Brain Connectiv.* 1, 13–36.

Friston, K. J., Harrison, L., and Penny, W. (2003). Dynamic causal modelling. *Neuroimage* 19, 1273–1302.

Friston, K. J., Holmes, A. P., Worsley, K. J., Poline, J. P., Frith, C. D., and Frackowiak, R. S. (1994). Statistical parametric maps in functional imaging: A general linear approach. *Hum. Brain Mapp.* 2, 189–210.

Friston, K. J., Litvak, V., Oswal, A., Razi, A., Stephan, K. E., Van Wijk, B. C., et al. (2016). Bayesian model reduction and empirical Bayes for group (DCM) studies. *Neuroimage* 128, 413–431. doi: 10.1016/j.neuroimage.2015.11.015

Goldenberg, D., and Galván, A. (2015). The use of functional and effective connectivity techniques to understand the developing brain. *Dev. Cogn. Neurosci.* 12, 155–164.

Grubb, R. L. Jr., Raichle, M. E., Eichling, J. O., and Ter-Pogossian, M. M. (1974). The effects of changes in PaCO2 cerebral blood volume, blood flow, and vascular mean transit time. *Stroke* 5, 630–639. doi: 10.1161/01.str.5.5.630

Handwerker, D. A., Roopchansingh, V., Gonzalez-Castillo, J., and Bandettini, P. A. (2012). Periodic changes in fMRI connectivity. *Neuroimage* 63, 1712–1719.

Havlicek, M., Ivanov, D., Poser, B. A., and Uludag, K. (2017a). Echo-time dependence of the BOLD response transients–a window into brain functional physiology. *Neuroimage* 159, 355–370. doi: 10.1016/j.neuroimage.2017.07.034

Havlicek, M., Ivanov, D., Roebroeck, A., and Uludağ, K. (2017b). Determining excitatory and inhibitory neuronal activity from multimodal fMRI data using a generative hemodynamic model. *Front. Neurosci.* 11:616. doi: 10.3389/fnins.2017.00616

Havlicek, M., Roebroeck, A., Friston, K., Gardumi, A., Ivanov, D., and Uludag, K. (2015). Physiologically informed dynamic causal modeling of fMRI data. *Neuroimage* 122, 355–372.

Hochreiter, S., and Schmidhuber, J. (1997). Long short-term memory. *Neural Comput.* 9, 1735–1780.

Jones, D. T., Vemuri, P., Murphy, M. C., Gunter, J. L., Senjem, M. L., and Machulda, M. M. (2012). Non-stationarity in the "resting brain's" modular architecture. *PLoS One* 7:e39731. doi: 10.1371/journal.pone.0039731

Kingma, D. P., and Ba, J. (2015). "Adam: A method for stochastic optimization," in *Proceedings of the international conference on learning representations (ICLR)*, Ithaca, NY.

Kiviniemi, V., Vire, T., Remes, J., Elseoud, A. A., Starck, T., Tervonen, O., et al. (2011). A sliding time-window ICA reveals spatial variability of the default mode network in time. *Brain Connectiv.* 1, 339–347. doi: 10.1089/brain.2011.0036

Kuhnke, P., Kiefer, M., and Hartwigsen, G. (2021). Task-dependent functional and effective connectivity during conceptual processing. *Cereb. Cortex* 31, 3475–3493.

Lauritzen, M. (2005). Reading vascular changes in brain imaging: Is dendritic calcium the key? *Nat. Rev. Neurosci.* 6, 77–85. doi: 10.1038/nrn1589

Mandeville, J. B., Marota, J. J., Kosofsky, B. E., Keltner, J. R., Weissleder, R., Rosen, B. R., et al. (1998). Dynamic functional imaging of relative cerebral blood volume during rat forepaw stimulation. *Magn. Reson. Med.* 39, 615–624.

Masamoto, K., Vazquez, A., Wang, P., and Kim, S. G. (2008). Trial-by-trial relationship between neural activity, oxygen consumption, and blood flow responses. *Neuroimage* 40, 442–450. doi: 10.1016/j.neuroimage.2007.12.011

Monti, R. P., Hellyer, P., Sharp, D., Leech, R., Anagnostopoulos, C., and Montana, G. (2014). Estimating time-varying brain connectivity networks from functional MRI time series. *Neuroimage* 103, 427–443.

Moran, R. J., Stephan, K. E., Seidenbecher, T., Pape, H. C., Dolan, R. J., and Friston, K. J. (2009). Dynamic causal models of steady-state responses. *Neuroimage* 44, 796–811.

Ozaki, T. (1992). A bridge between nonlinear time series models and nonlinear stochastic dynamical systems: A local linearization approach. *Stat. Sin.* 2, 113–135.

Park, H. J., Friston, K. J., Pae, C., Park, B., and Razi, A. (2018). Dynamic effective connectivity in resting state fMRI. *Neuroimage* 180, 594–608.

Polimeni, J. R., and Lewis, L. D. (2021). Imaging faster neural dynamics with fast fMRI: A need for updated models of the hemodynamic response. *Prog. Neurobiol.* 207:102174. doi: 10.1016/j.pneurobio.2021.102174

Ruder, S. (2016). An overview of gradient descent optimization algorithms. *arXiv* [Preprint]. arXiv:1609.04747.

Rumelhart, D. E., Hinton, G. E., and Williams, R. J. (1985). *Learning internal representations by error propagation*. San Diego, CA: Institute for Cognitive Science, University of California.

Sakoğlu, Ü, Pearlson, G. D., Kiehl, K. A., Wang, Y. M., Michael, A. M., and Calhoun, V. D. (2010). A method for evaluating dynamic functional network connectivity and task-modulation: Application to schizophrenia. *Magn. Reson. Mater. Phys. Biol. Med.* 23, 351–366. doi: 10.1007/s10334-010-0197-8

Seghier, M. L., and Friston, K. J. (2013). Network discovery with large DCMs. *Neuroimage* 68, 181–191. doi: 10.1016/j.neuroimage.2012.12.005

Shakil, S., Lee, C. H., and Keilholz, S. D. (2016). Evaluation of sliding window correlation performance for characterizing dynamic functional connectivity and brain states. *Neuroimage* 133, 111–128.

Shcherbakov, M. V., Brebels, A., Shcherbakova, N. L., Tyukov, A. P., Janovsky, T. A., and Kamaev, V. A. E. (2013). A survey of forecast error measures. *World Appl. Sci. J.* 24, 171–176.

Stefanovic, B., Warnking, J. M., and Pike, G. B. (2004). Hemodynamic and metabolic responses to neuronal inhibition. *Neuroimage* 22, 771–778.

Stephan, K. E., Kasper, L., Harrison, L. M., Daunizeau, J., den Ouden, H. E., Breakspear, M., et al. (2008). Nonlinear dynamic causal models for fMRI. *Neuroimage* 42, 649–662.

Stephan, K. E., Penny, W. D., Daunizeau, J., Moran, R. J., and Friston, K. J. (2009). Bayesian model selection for group studies. *Neuroimage* 46, 1004–1017.

Stephan, K. E., Penny, W. D., Moran, R. J., den Ouden, H. E., Daunizeau, J., and Friston, K. J. (2010). Ten simple rules for dynamic causal modeling. *Neuroimage* 49, 3099–3109.

Sutskever, I., Martens, J., Dahl, G., and Hinton, G. (2013). "On the importance of initialization and momentum in deep learning," in *Proceedings of the international conference on machine learning*, (New York, NY: PMLR), 1139–1147. doi: 10.3390/brainsci10070427

Ulrych, T. J., Sacchi, M. D., and Woodbury, A. (2001). A Bayes tour of inversion: A tutorial. *Geophysics* 66, 55–69.

Uludağ, K., and Blinder, P. (2018). Linking brain vascular physiology to hemodynamic response in ultra-high field MRI. *Neuroimage* 168, 279–295. doi: 10.1016/j.neuroimage.2017.02.063

Uludağ, K., Dubowitz, D. J., Yoder, E. J., Restom, K., Liu, T. T., and Buxton, R. B. (2004). Coupling of cerebral blood flow and oxygen consumption during physiological activation and deactivation measured with fMRI. *Neuroimage* 23, 148–155. doi: 10.1016/j.neuroimage.2004.05.013

Underwood, R., Tolmeijer, E., Wibroe, J., Peters, E., and Mason, L. (2021). Networks underpinning emotion: A systematic review and synthesis of functional and effective connectivity. *Neuroimage* 243:118486. doi: 10.1016/j.neuroimage.2021.118486

van den Heuvel, M. P., and Pol, H. E. H. (2010). Exploring the brain network: A review on resting-state fMRI functional connectivity. *Eur. Neuropsychopharmacol.* 20, 519–534.

van Zijl, P. C., Hua, J., and Lu, H. (2012). The BOLD post-stimulus undershoot, one of the most debated issues in fMRI. *Neuroimage* 62, 1092–1102. doi: 10.1016/j.neuroimage.2012.01.029

Wang, Y., Wang, Y., and Lui, Y. W. (2018). Generalized recurrent neural network accommodating dynamic causal modeling for functional MRI analysis. *Neuroimage* 178, 385–402. doi: 10.1016/j.neuroimage.2018.05.042

Welvaert, M., and Rosseel, Y. (2013). On the definition of signal-to-noise ratio and contrast-to-noise ratio for fMRI data. *PLoS One* 8:e77089. doi: 10.1371/journal.pone.0077089

Zappe, A. C., Uludağ, K., Oeltermann, A., Uğurbil, K., and Logothetis, N. K. (2008). The influence of moderate hypercapnia on neural activity in the anesthetized nonhuman primate. *Cereb. Cortex* 18, 2666–2673. doi: 10.1093/cercor/bhn023

Zarghami, T. S., and Friston, K. J. (2020). Dynamic effective connectivity. *Neuroimage* 207:116453.

Zhou, P., Feng, J., Ma, C., Xiong, C., and Hoi, S. C. H. (2020). Towards theoretically understanding why sgd generalizes better than adam in deep learning. *Adv. Neural Inf. Process. Syst.* 33, 21285–21296.

Zonta, M., Angulo, M. C., Gobbo, S., Rosengarten, B., Hossmann, K. A., Pozzan, T., et al. (2003). Neuron-to-astrocyte signaling is central to the dynamic control of brain microcirculation. *Nat. Neurosci.* 6, 43–50. doi: 10.1038/nn980

Frontiers in
Human Neuroscience

Bridges neuroscience and psychology to understand the human brain

The second most-cited journal in the field of psychology, that bridges research in psychology and neuroscience to advance our understanding of the human brain in both healthy and diseased states.

Discover the latest Research Topics

See more →

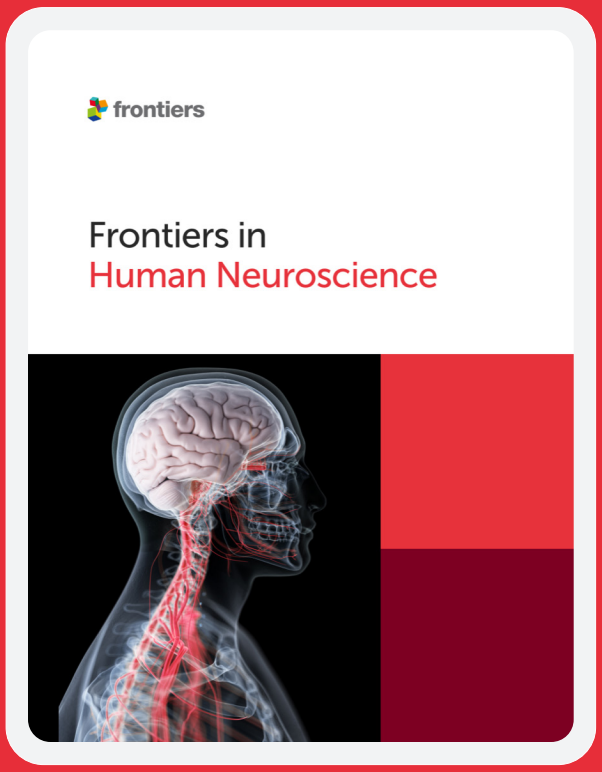

Frontiers

Avenue du Tribunal-Fédéral 34
1005 Lausanne, Switzerland
frontiersin.org

Contact us

+41 (0)21 510 17 00
frontiersin.org/about/contact